UNIVERSITÉ FRANÇOIS – RABELAIS DE TOURS

ÉCOLE DOCTORALE SANTÉ, SCIENCES BIOLOGIQUES ET CHIMIE DU VIVANT

INSTITUT DE RECHERCHE SUR LA BIOLOGIE DE L'INSECTE

THÈSE présentée par :

Thomas STEINMANN

soutenue le : 06 mars 2017

pour obtenir le grade de : **Docteur de l'université François – Rabelais de Tours**

Discipline/ Spécialité : Sciences de la Vie et de la Santé

MÉTROLOGIE OPTIQUE EN DYNAMIQUE DES FLUIDES APPLIQUÉE À L'ÉCOLOGIE PHYSIQUE DES INSECTES

THÈSE dirigée par :

M. CASAS Jérôme	Professeur, Université François Rabelais de Tours

RAPPORTEURS :

M. BRÜCKER Christoph	Professeur, City, University of London
M. DAVID Laurent	Professeur, Université de Poitiers

JURY :

M. LESIGNE Emmanuel	Professeur, Université François Rabelais de Tours
M. ROBERT Daniel	Professeur, University of Bristol
M. BRÜCKER Christoph	Professeur, City, University of London
M. DAVID Laurent	Professeur, Université de Poitiers
M. CASAS Jérôme	Professeur, Université François Rabelais de Tours

Remerciements

Avant tout, je voudrai remercier Jérôme Casas, mon directeur de thèse, pour m'avoir fait confiance, pour m'avoir soutenu, guidé et encouragé lors de la rédaction de ce manuscrit. Au delà de l'aide que vous m'avez apporté pour l'élaboration de ce mémoire, je tenais à vous remercier pour votre disponibilité ainsi que pour votre soutien au cours de ces 13 années de travail. J'ai beaucoup appris de nos diverses interactions scientifiques. J'ai également grandement apprécié nos nombreux échanges qui allaient bien souvent au delà des considérations scientifiques et techniques.

Je tiens aussi à remercier les membres de jury : Christoph Brücker, Laurent David, Emmanuel Lesigne et Daniel Robert d'avoir accepté de lire et d'évaluer mon travail.

Je tiens particulièrement à remercier Philippe Roingeard et l'école doctorale santé, sciences biologiques et chimie du vivant de l'Université François Rabelais pour avoir accepté et soutenu mes démarches de postulation au diplôme de docteur.

Je remercie également Jean Paul Monge et David Giron, à la direction passée et actuelle de l'IRBI, pour avoir soutenu ma démarche et pour tout le travail que vous effectuez tous les jours pour nous permettre de faire le notre dans les meilleurs conditions. Merci aussi à Christelle Suppo, directrice de l'équipe Ecologie Quantitative pour son soutien.

J'ai eu le plaisir d'interagir et de collaborer scientifiquement avec de nombreuses personnes qui m'auront toutes inspiré. Je remercie chaleureusement et dans le désordre, Jean Philippe Christidès, pour ton soutien technique, scientifique et ta bonne humeur, Olivier Dangles, pour ton aide précieuse lors de mes premières rédactions, Gijs Krijnen, pour l'accueil à Tewnte et les nombreux échanges passés et futurs, Claudio Lazzari, pour toutes nos discussions intéressantes, pour tes astuces, ton savoir faire et tes connaissances encyclopédiques de la physiologie des insectes, Sylvain Pincebourde, pour ta bonne humeur, tes conseils et ton aide précieuse, Fabrice Vannier, pour ton aide et pour nos discussions, Dominique Pierre pour tous tes conseils

J'ai aussi rencontré beaucoup de plus jeunes scientifiques que je souhaite remercier, merci à Fabienne Dupuy, Erica Morley, Brice Bathellier, Ales Skorjanc, Harmen Droogendijk. Je remercie aussi Miguel Piñeirua pour son aide sur Latex. Je remercie mes stagaires, Précillia Cochard et Antoine Cribellier.

Merci à tous les membres de l'IRBI. Et plus particulièrement, je souhaite remercier les amis que je me suis fait au cours de ces années au laboratoire, ils sont nombreux et je ne peux qu'en oublier : Arnold, Franck et Rebecca, Wilfried, Jonathan, Robin, Simon et Elfie, Laurianne, Antoine Guiguet, Antoine Humeau, Jérémy Gévar, Jérémy Gauthier, Julien, Germain, Mourad. Merci aussi aux gestionnaires du laboratoire, Nadine, Sylvie, Aïcha et Marjorie pour tout ce que vous faites pour nous simplifier la vie.

Au delà de l'IRBI, j'ai eu la chance de rendre visite à des physiciens, je remercie Elie Raphaël, Michael Benzaquen, Maxence Arutnik de l'ESPCI pour les fructueux échanges et les interactions et Frédéric Moisy et Marc Rabaud pour leur accueil au FAST. Merci aussi à Antoine Ruyter du GREMAN, pour ses conseils sur l'AFM et son accueil.

Je remercie ma famille, mes soeurs et mes parents, qui ont toujours soutenu leurs enfants. Ils nous auront permis de nous réaliser, en nous faisant toujours passer avant tout le reste.

Je te remercie, Faustine, pour ton soutien de tous les jours, ta patience, ton pragmatisme, ton optimisme, tes corrections, nos discussions scientifiques, ton intérêt ... je n'aurais jamais entrepris cette démarche si tu ne m'avais pas inspiré et aidé. Merci d'avoir cru en moi.

Enfin, je finirais par remercier Sela, qui est arrivée dans notre vie et qui nous apporte chaque jour le plus grand des bonheurs.

Résumé

La capacité à percevoir des courants dans un fluide s'est développée chez de nombreuses espèces animales, dans des contextes écologiques très variés qui couvrent aussi bien les interactions proies-prédateurs, la sélection sexuelle ou l'orientation dans un environnement. Parmi ces espèces animales, les grillons détectent les courants d'air générés notamment lors de l'attaque de leurs prédateurs à l'aide de deux organes appelés "cerques", situés à l'arrière de leur abdomen et recouverts de poils mécano-sensoriels. Ces senseurs sont considérés comme les détecteurs les plus sensibles du monde animal. Il leur suffit de capter l'énergie d'un dixième d'un photon pour déclencher un potentiel d'action au niveau du neurone sensoriel.
Ce manuscrit présente à la fois le développement des outils de mesures sans contact adaptés à ces questions d'écologie sensorielle ainsi que les méthodes numériques simulant les processus physiques à l'œuvre. L'étude du fonctionnement des senseurs a nécessité l'adaptation des méthodes de mesures non intrusives de très grande précision tel que la Vélocimétrie par Imagerie de Particules (PIV). La couche limite oscillante dans laquelle évoluent les poils a été visualisée et a servi à déterminer la réponse de poils modélisés par des systèmes oscillatoires du second ordre. Le couplage visqueux entre poils a été lui aussi caractérisé en adaptant la PIV à des mesures à très petites échelles sur des poils biomimétiques micro-electro-mécanique (MEMS). Les mesures des perturbations générées lors des attaques d'araignées, principales prédatrices des grillons, nous ont aidé à valider des modélisations numériques, réalisées à l'aide des techniques de dynamique des fluides computationnelles (CFD) par résolution des équations de Navier Stokes via la méthode des éléments finis (FEM).
La mise au point et l'utilisation de techniques de métrologie optique en dynamique des fluides semi-visqueux et l'analyse des données nous permettent de revisiter la sensibilité extrême du système sensoriel du grillon et de placer ces mesures dans un contexte plus large, d'écologie sensorielle. En particulier, nous montrons que ces soies sont placées en groupe compact et exercent entre elles un fort couplage aérodynamique visqueux, qui réduit fortement leur sensibilité "de groupe". Ce fort couplage interroge l'intérêt d'avoir des récepteurs aussi performants individuellement, s'ils perdent leur sensibilité lorsqu'ils fonctionnent en réseau. Finalement, les réactions des poils à des mouvements de fluides générés par un piston mimant les attaques réelles d'araignées ont pu être déterminées à l'aide d'une caméra rapide, puis simulées et validées après avoir développé un modèle mécanique du poil répondant à des stimuli transitoires.

Mots clefs : écologie sensorielle, écologie physique, Vélocimétrie par imagerie de particules (PIV), poils filiformes, couche limite, bioinspiration, biomimétisme, écoulements visqueux, interaction proie-prédateur, biomécanique

Abstract

Flow sensing is used by a vast number of animals in various ecological contexts, from prey-predator interactions to mate selection, and orientation to flow itself. Among these animals, crickets use hundreds of filiform hairs on two cerci as an early warning system to detect remote potential predators. Over the years, the cricket hairs have been described as the most sensitive sensor in the animal kingdom. The energy necessary for the emission of an action potential by its sensory neuron was estimated to be a tenth of the energy of a photon.

This PhD thesis aims to describe recent technological advances in the measurement and model of flows around biological and artificial flow sensors in the context of organismal sensory ecology. The study and understanding of the performance of sensory systems requires a high spatial precision of non-intrusive measurement methods. Thus, non-contacting measurement methods such as and Particle Image Velocimetry (PIV), originally developed by aerodynamics and fluid mechanics engineers, have been used to measure flows of biological relevance. The viscous oscillatory boundary layer surrounding filiform hairs has been visualized and used as input to model the mechanical response of these hairs, described as second order mechanical systems. The viscous hydrodynamic coupling occurring within hair canopy was also characterized using PIV measurements on biomimetic micro-electro-mechanical systems (MEMS) hairs, mimicking biological ones. Using PIV, we have also measured the air flow upstream of hunting spiders. We prove that this flow is highly conspicuous aerodynamically, due to substantial air displacement detectable up to several centimeters in front of the running predator. This disturbance of upstream air flows were also assessed by computational fluid dynamics (CFD) with the finite elements method (FEM).

The development of non-intrusive measurement and CFD methods and their application to the analysis of the biological flow involved in cricket sensory ecology allowed us to revisit the extreme sensitivity of cricket filiform hairs. We predicted strong hydrodynamic coupling within natural hair canopies and we addressed why hairs are packed together at such high densities, particularly given the exquisite sensitivity of a single hair. We also proposed a new model of hair deflection during the arrival of a predator, by taking into account both the initial and long-term aspects of the flow pattern produced by a lunging predator. We conclude that the length heterogeneity of the hair canopy mirrors the flow complexity of an entire attack, from launch to grasp.

Keywords : sensory ecology, physical ecology, Particle Image Velocimetry (PIV), filiform hairs, boundary layer flow, biomimetism, bioinspiration, viscous flow, prey-predator interaction, biomechanics

Table des matières

Table des figures

Chapitre 1

Introduction Générale

Préambule à un mémoire de thèse sur travaux en VAE

Ce mémoire de thèse sur travaux a été rédigé dans le cadre de l'obtention d'un diplôme de docteur par validation des acquis de l'expérience. Il consiste en une compilation de travaux, réalisés aux cours des treize dernières années, dans l'équipe d'écologie physique du Professeur Jérôme Casas au sein de l'Institut de Recherche sur la Biologie de l'Insecte (IRBI) à TOURS. J'ai été affecté dans cette équipe d'écologues en 2003 en tant qu'ingénieur d'étude CNRS en métrologie optique où je me suis attaché dès lors à développer d'un coté des outils de mesures sans contact adaptés à des question d'écologie sensorielle des insectes, et de l'autre, dans une moindre mesure, des méthodes numériques simulant les processus physiques à l'œuvre. Les mesures biomécaniques et physiques à la petite échelle des insectes requièrent la mise en place de techniques non intrusives de très grande précision et l'application d'outils d'analyses théoriques et numériques spécifiques. Ces outils de mesures et de modélisation ont servi à comprendre comment les propriétés à la fois des signaux, des récepteurs sensoriels et de l'environnement physique des insectes pouvaient influencer un signal et sa perception. C'est dans cette perspective que j'ai adapté à des mesures biologiques, des techniques comme l'Anémométrie Laser Doppler (**LDA**) et la Vélocimétrie par Imagerie de Particules (**PIV**), historiquement développées pour et par les ingénieurs hydrodynamiciens, et déjà présentes au laboratoire.

L'originalité de mon affectation de physicien expérimental dans un groupe d'écologues et l'originalité de ma démarche de postuler au titre de docteur via une thèse sur travaux par VAE ont influencé la structuration de ce mémoire. Dans une thèse classique, la porte d'entrée scientifique est définie par un sujet précis. Lors de la constitution de ce mémoire, ma démarche a consisté à synthétiser, à posteriori, des travaux composites réalisés au cours de plus de dix années de travail en grande partie centrées autour d'un parc d'instruments. Il n'était cependant pas garanti à l'avance que les résultats scientifiques qui se sont accumulés, au fil de nos études sur ce système sensoriel, nous permettent de faire émerger une structure cohérente, propre à l'élaboration d'un mémoire de thèse classique. Cette introduction a donc une structure originale, qui reflète l'originalité de cette double démarche. Les objectifs et différentes parties de la thèse seront introduits et définis au fur et à mesure de la description du contexte scientifique global.

1.1 Perception des écoulements dans le monde vivant

La plupart des décisions comportementales prises par un organisme sont conditionnées par la capacité de son système nerveux à se représenter son environnement direct. Ce sont ses organes sensoriels qui jouent le rôle d'interface entre son système nerveux et son environnement physique, en transmettant la plupart de ces informations nécessaires à cette représentation. Ces organes sensoriels périphériques et les réseaux neuronaux associés ont évolué pour traiter des informations complexes, en adaptant leur propriétés aux caractéristiques les plus cruciales des stimuli sensoriels qu'ils avaient besoin de détecter (Wehner (1987), von der Emde et Warrant (2015)). De tous les sens disponibles dans le monde du vivant, la capacité à percevoir des courants dans un fluide s'est développée chez de nombreuses espèces animales, des araignées aux mammifères marins, en passant par les poissons, les chauves-souris ou encore les insectes (Bleckmann *et al.* (2014)). Ainsi des structures sensorielles diverses et variées sont utilisées par les animaux pour sentir les écoulements, et ceci dans divers contextes écologiques. Ces derniers couvrent aussi bien les interactions proies-prédateurs, la sélection sexuelle que l'orientation spatiale dans un environnement. Ces capteurs hydrodynamiques (ou aérodynamiques) mesurent la plupart du temps un écoulement relatif du fluide par rapport au corps de l'animal (Bleckmann *et al.* (1994)). Les systèmes parmi les mieux étudiées sont entre autres les poils sensoriels des grillons (Shimozawa *et al.* (2003)), les poils sensoriels des crustacés (Wiese (1976)), les lignes latérales des poissons et des amphibiens (Bleckmann et Zelick (2009)) et les vibrisses des mammifères aquatiques (Hanke *et al.* (2014)). Une étude a même très récemment prédit et mesuré les réponses mécaniques des macro-vibrisses des rats soumises à des écoulements d'air (Yu *et al.* (2016b), Yu *et al.* (2016a)). Leurs résultats suggèrent que les vibrisses des mammifères terrestres seraient des senseurs multimodaux, ayant sûrement un rôle important dans la capacité de ces animaux à percevoir le vent dans leur environnement.

Bien qu'ayant une origine anatomique différente, on constate une certaine convergence évolutive des caractéristiques fonctionnelles de ces systèmes sensoriels, et ceci à travers différents embranchements. Ils sont, dans tous les cas, caractérisés par la présence d'un prolongement kératiné ou cuticulaire qui pourra facilement être défléchie par un écoulement et qui sera en outre innervé et affleurant à la cuticule ou à la peau. Ce sont les cellules sensorielles innervant ces structures qui vont traduire leur déformation par des stimuli nerveux transmis au système nerveux central de l'animal.

1.2 Le système cercal des grillons

Parmi les arthropodes terrestres capables de percevoir ainsi leur environnement, on peut distinguer les Blattopteroïdes et les Orthoptéroïdes, comme les blattes, sauterelles, mantes religieuses ou grillons qui ont la particularité de percevoir les courants d'air, générés notamment lors de l'attaque de leurs prédateurs ou lors du vol, à l'aide de deux organes appelés "cerques", situés à l'arrière de leur abdomen et recouverts de poils mécano-sensoriels (Figure 1.1.A). Chez les criquets, certains neurones moteurs initiateurs du vol, présents dans le ganglion mesothoracique, reçoivent des signaux provenant du système cercal (Boyan *et al.* (1986)). Il a aussi été

montré que le système cercal des blattes pouvait leur servir à détecter les changements de vitesse du fluide, relative à leur corps, causés par des déplacements angulaires rapides durant le vol (Fraser (1977)). C'est en outre la stimulation de leurs organes sensoriels qui est à l'origine d'un comportement de fuite chez ces insectes (Gras et Hörner (1992)). Chez le grillon notamment, l'ablation des cerques a montré le rôle prédominant de ces organes dans le déclenchement de la fuite des grillons (Kanou *et al.* (2006), Dupuy *et al.* (2011)). Ces derniers fuient en général en sautant dans direction opposée au stimulus généré par leur prédateur comme observé chez plusieurs espèces (Tauber et Camhi (1995), Kanou *et al.* (2006)).

1.2.1 Morphologie et neurophysiologie du réseau de senseurs

Chez le grillon, *Gryllus bimaculatus*, les cerques peuvent être recouverts de 400 à 500 poils filiformes dont la taille peut varier entre 30 et 1500 μm (Shimozawa et Kanou (1984a)), et on peut en compter jusqu'à 2000 chez *Acheta domesticus* (Edwards et Palka (1974)). La diversité des structures cercales a été analysée par Desutter-Grandcolas *et al.* (2010) chez 18 espèces d'un groupe de grillons tropicaux, les Eneopterinae. Ces auteurs ont déterminé que les cerques de ces espèces pouvaient être recouverts d'entre 100 et 900 poils et que les plus longs pouvaient mesurer jusqu'à 2500 μm. Ces poils filiformes sont insérés individuellement dans une structure cuticulaire de forme ovale appelée "chaussette", et sont soutenus à leur base par la membrane de jonction, une suspension flexible composé de résiline (Edwards et Palka (1974)) (Figure 1.1.c et d). Il est suggéré que la forme ovale de cette chaussette, associée à la forme ovale de la base du poil, va contraindre le poil à fléchir dans un plan préférentiel (Gnatzy et Tautz (1980)). La répartition des poils n'est pas homogène sur tout le long du cerque, ils sont plus densément implantés dans la partie proximale du cerque (Dangles *et al.* (2008)) (Figure 1.1.b) et la répartition des directionnalités n'est pas non plus homogène et semble présenter une assez faible variation inter-individuelle (Miller *et al.* (2011)).

La déviation de ces poils filiformes par les courants d'air va activer les récepteurs mécano-sensoriels situés dans la chaussette, sous le poil. Chez le grillon, à chaque poil est associé un seul neurone sensoriel (Figure 1.1.e). Les dendrites de ces neurones vont être activées quand la flexion du poil fournira assez d'énergie au piquet cuticulaire situé à sa base pour lui permettre de compresser le corps tubulaire (Figure 1.1.e) (Gnatzy et Tautz (1980), Dupuy (2009)). Ces neurones sensoriels se projettent dans le ganglion abdominal terminal pour former une représentation spatiale neuronal de la provenance du stimulus (Landolfa et Miller (1995)). On sait par ailleurs que les interneurones sensorielles primaires, directement reliés à cette carte neuronale, possèdent une sélectivité d'activation qui dépendra de paramètres pertinents contenus dans le stimulus faisant dévier les poils. Ces interneurones génèreront ainsi des potentiels d'action à des fréquences qui dépendent de la valeur de ces paramètres, comme la fréquence et la vitesse de l'écoulement (Shimozawa et Kanou (1984a)).

1.2.2 Réponse mécanique du poil filiforme

De nombreuses études sur le rôle fonctionnel de ces senseurs ont montré que la diversité des réponses mécaniques des poils de différentes longueurs à divers stimuli permettent aux grillons

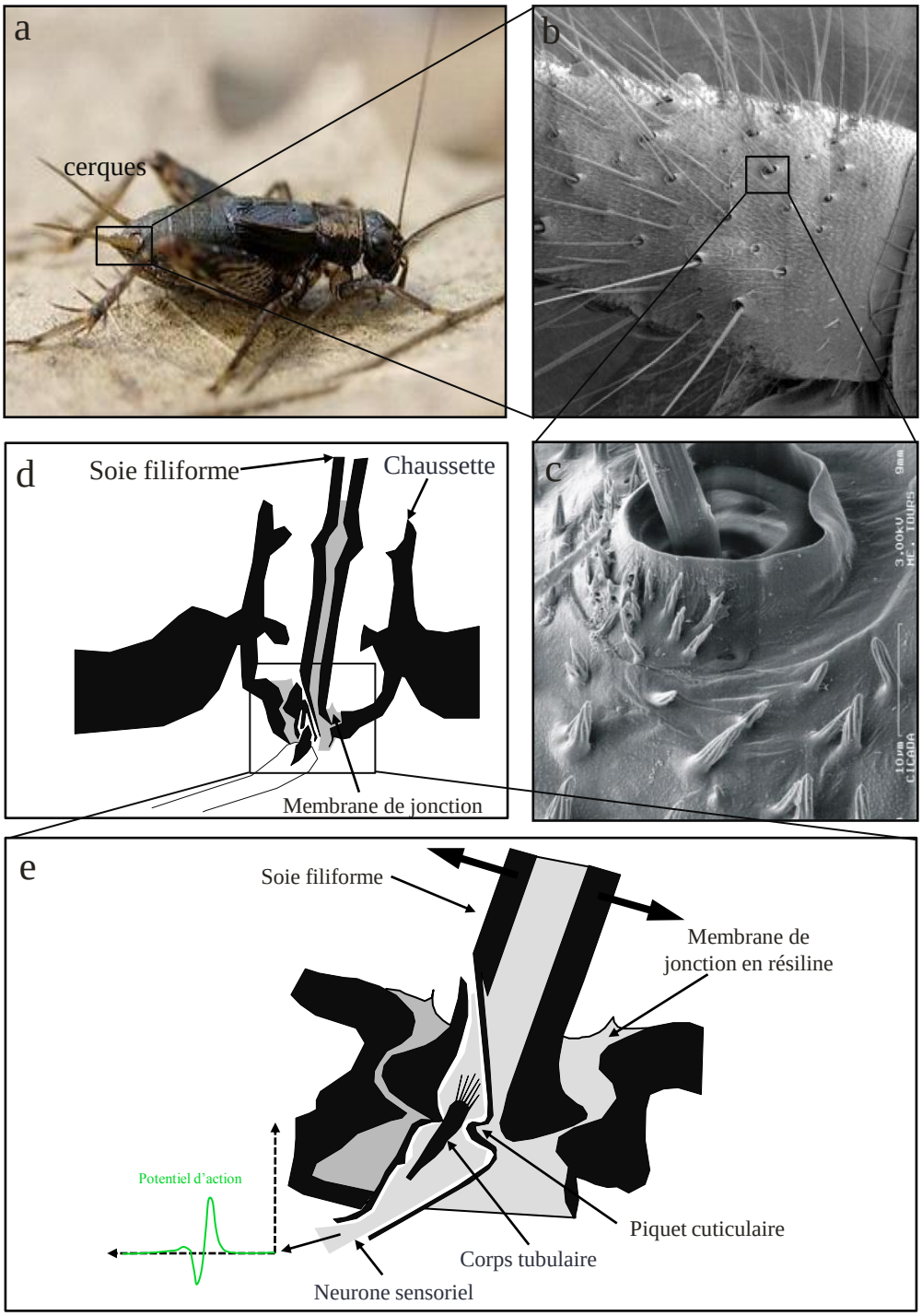

FIGURE 1.1: **Fonctionnement du système cercal des grillons**. (a) Les cerques du grillon (ici *Nemobius sylvestris*) se situent au bout de son abdomen, (b) ils sont recouverts de centaines de soies filiformes, (c) et (d) au repos, le poil filiforme flotte au centre de sa chaussette et est maintenu en place par une membrane de jonction. (e) Chaque poil est associé à un seul neurone sensoriel dont le corps cellulaire se trouve à la base du poil. Lors d'une stimulation, l'axe du poil fléchi, ce qui engendre une rotation de la base du poil et le piquet cuticulaire compresse le corps tubulaire. Lorsqu'un angle de déflexion minimal est atteint, la force de compression du corps tubulaire sera suffisante pour générer un potentiel récepteur dépolarisant dans les dendrites (Gnatzy et Tautz (1980))

de discriminer à la fois l'intensité et la fréquence de ces stimuli (Tautz (1979), Shimozawa et Kanou (1984a), Humphrey *et al.* (1993)). La biomécanique du mouvement de ces poils dans un fluide oscillant a fait l'objet de nombreux travaux de recherche au cours des dernières décennies, et plusieurs modèles ont été mis au point (Fletcher (1978), Shimozawa et Kanou (1984b), Humphrey *et al.* (1993), Bathellier *et al.* (2012)). Dans tous ces modèles, le poil est défini comme étant un pendule inversé soutenu par une base viscoélastique. Ce modèle mécanique peut être décrit par quatre paramètres (Shimozawa *et al.* (2003), Humphrey *et al.* (1993)) : (i) le moment d'inertie qui représente la répartition de la masse le long du poil, (ii) la constante de raideur du "ressort" de sa suspension qui fournit le couple de rappel du poil vers sa position de repos, (iii) la résistance à la torsion à l'intérieur de la suspension et (iv) le coefficient de trainée visqueuse du poil dans l'air. Shimozawa et Kanou (1984a) sont les premiers à avoir mesuré la vitesse minimale de l'écoulement oscillatoire permettant de stimuler une réponse de l'interneurone 10-2 chez *Gryllus bimaculatus*. Cette vitesse "seuil" a été estimé à 30 μm/s. Connaissant ce seuil, stimulant ensuite des poils de différentes longueurs par des flux oscillatoires contrôlés et utilisant ces modèles viscoélastiques pour ajuster les déviations théoriques sur les déflexions mesurées, ils ont pu déterminer l'angle minimal nécessaire à un neurone sensoriel pour générer un potentiel d'action (Shimozawa et Kanou (1984b)). Ce seuil a été estimé à 0,002° pour des longs poils filiformes de 1000 μm. En estimant l'énergie dont dispose la cellule réceptrice pour stimuler la transduction d'un potentiel d'action comme étant l'énergie mécanique consommée par la résistance de la suspension, Shimozawa *et al.* (2003) ont réussi à déterminer la sensibilité énergétique de ce neurone sensoriel. Ils ont établi qu'il leur suffisait de capter dans l'air l'énergie d'un dixième d'un photon pour déclencher un potentiel d'action au niveau du neurone sensoriel à leur base. Individuellement ces senseurs sont donc considérés comme les détecteurs les plus sensibles du monde animal (Shimozawa *et al.* (2003)). Kämper et Kleindienst (1990) ont aussi mesuré les oscillations des poils filiformes de différentes espèces de grillons, *Acheta domestica, Gryllus bimaculatus* et *Phaeophilacris spectrum*, dans des champs sonores de basse fréquence. Ils ont notamment prouvé que ces poils réagissaient le plus fortement à des fréquences comprises entre 40 et 100 Hz, et qu'à ces fréquences le déplacement du bout du poil pouvait être deux fois plus rapide que le déplacement de l'air qui l'entourait. Shimozawa *et al.* (1998) ont suggéré que les poils filiformes étaient optimisés pour transmettre le maximum d'énergie du poil aux neurones récepteurs situés au niveau de l'articulation. Ils ont estimé que les valeurs du coefficient de trainée visqueuse dans l'air et du coefficient de friction à la base de l'articulation devaient être en quelque sorte liés. Cette adéquation des caractéristiques mécaniques, connue sous le nom d'adaptation d'impédance, leur assurerait une transmission optimale de l'énergie contenue dans l'air. Cette observation n'a cependant été expérimentalement validée qu'en 2012 par Bathellier *et al.* (2012), qui ont prouvé que les poils filiformes réagissaient à la limite physique de leur capacité à transmettre l'énergie contenu dans le fluide et ceci dans une bien plus large gamme de fréquences que celle précédemment estimée.

1.3 Écologie physique de la perception des écoulements

Au fil des années et des études, une incroyable quantité de connaissances a été accumulée concernant principalement le réseau neuronal des grillons. (Dangles *et al.* (2006a)). La littérature concernant les aspects neurophysiologiques du fonctionnement de cet organe sensoriel est à présent tellement fournie que le système cercal du grillon (et de son homologue chez les blattes) est un des systèmes sensoriels les plus étudiés et les plus connus du monde animal. Ainsi, le grillon et son système cercal ont atteint le statut de "star" des livres de premier cycle. Ces connaissances sont le fruit de recherches conduites, pour la plupart en laboratoire, par des équipes de physiologistes, de neurophysiologistes ou d'ingénieurs. L'interprétation correcte du rôle fonctionnel des propriétés biomécaniques des réseaux de poils filiformes nécessite pourtant de replacer l'étude de ces organismes dans un contexte écologique plus vaste. On définit de manière générale l'écologie physique comme l'étude interdisciplinaire de phénomènes biologiques et écologiques dans une perspective physique (Dangles et Casas (2010)). Le but premier de cette discipline d'interface est de comprendre comment les organismes se sont adaptés aux contraintes imposées par leur environnement physique et ont réussi à utiliser les mécanismes physiques pour satisfaire les processus biologiques nécessaires à leur survie.

1.3.1 Du 'textbook cricket' à l'étude sur le terrain

Dans leur étude réalisée en milieu naturel, Dangles *et al.* (2006a) ont mis en évidence que la pression de prédation était beaucoup plus importante chez les jeunes grillons juvéniles que chez les adultes. Ces résultats les ont amené à focaliser leurs études sur l'aspect ontogénique du fonctionnement du codage du système cercal du grillon (Dangles *et al.* (2006c)). Ils ont ainsi prouvé qu'en se développant, le système cercal du grillon développait une sensibilité globale aux signaux dont la fréquence était comprise entre 150 et 180 Hz. Cette sensibilité est conditionnée par l'augmentation, au fil de la croissance, du nombre de longs poils et l'apparition de nouveaux poils sensoriels. Cette démarche intégrative consistant à lier la compréhension de l'écologie de la vie d'un organisme et le rôle fonctionnel de ses organes sensoriels était à l'époque inédite chez le grillon. Roeder (Roeder (1966), Roeder (1970)) s'intéressait déjà au lien entre la neurophysiologie de la perception d'un organisme et son environnement écologique, en appliquant cette démarche à l'étude des mécanismes d'évitement acoustique des chauves-souris chez leurs proies, les papillons nocturnes. Il montra l'adéquation entre la distribution spectrale des intensités ultrasonores générées par les chauves souris en milieu naturel, et la sensibilité fréquentielle des tympans de papillons nocturnes. Cette démarche a été théorisée dans l'article de référence 'Matched filters' de Wehner (1987). Elle est aussi à la base du travail de McHenry *et al.* (2008) sur l'écologie physique de la perception des écoulements chez les poissons. Elle est aussi au cœur des travaux de Jiang et Kiorboe (2011) et de Kjellerup et Kiorboe (2012) sur l'écologie du plancton et de ceux de Koehl (2003), sur le rôle fonctionnel de la morphologie des chémorécepteurs des homards. Ces quelques exemples ne représentent bien sûr pas un examen exhaustif des nombreuses études sur l'écologie sensorielle des animaux. Ce domaine de recherche en pleine expansion a donné lieu très récemment à l'écriture d'un ouvrage (von der Emde et

Warrant (2015)) qui illustre les divers champs d'application de cette démarche d'écologie sensorielle, allant du traitement des informations sensorielles impliquées dans l'olfaction chez les insectes, à la neurophysiologie de l'audition chez les vertébrés.

1.3.2 Rôle fonctionnel de la structure et du nombre

C'est en suivant cette démarche que nous avons décidé d'étudier l'importance de la fonction des soies sensorielles du grillon dans la structuration des cerques qui les supportent, et ceci en essayant de comprendre comment leur aspect tridimensionnel influencera la perception des mouvements d'air. Il faudra, pour ce faire, caractériser précisément les écoulements autour de ces structures sans s'en remettre à des modèles trop simplificateurs (**Chapitre 3**). Les poils filiformes sont, en outre, placés en groupe compact et suspectés d'exercer entre eux un fort couplage aérodynamique visqueux, pouvant réduire fortement leur sensibilité individuelle. On est en droit de s'interroger dans ce cas, sur l'intérêt d'avoir des récepteurs aussi performants individuellement, puisqu'ils perdent leur sensibilité lorsqu'ils fonctionnent en réseau. La mesure de l'influence d'un mécano-senseur individuel sur ses proches voisins, et la caractérisation de l'étendue spatiale du couplage visqueux entre les poils, pourraient ainsi nous permettre d'en connaitre davantage sur les propriétés émergentes du fonctionnement mécanique en réseau (**Chapitre 4**).

1.3.3 Hypersensibilité et hydrodynamique de la prédation

D'un point de vue évolutif, la sélection d'un mécanisme sensoriel aussi performant a probablement été conditionnée par une importante pression de prédation. Les grillons des bois (*Nemobius sylvestris*) constituent par exemple des proies de premier choix pour les araignées loups (*Pardosa lugubris*) qui partagent leur environnement (Dangles *et al.* (2006a)). Ces prédateurs chassent dans la litière de feuilles des forêts et ont développé pour cela deux types de stratégies, l'embuscade et l'attaque très rapide (Dangles *et al.* (2006b)). Ces stratégies furent semble-t-il adoptées pour contrecarrer les formidables capacités de perception des mouvements d'air du grillon. Il apparait alors primordial de comprendre quels sont ces signaux transportés dans l'air et quels vitesses d'écoulements sont générées par les prédateurs des grillons. Cependant, compte tenu de la faible capacité de diffusion des particules dans l'air, la visualisation de ces écoulements par imagerie de particules et leur corrélation à des comportements d'attaques ou de fuites représente un véritable challenge technologique (Dangles et Casas (2010)). Les écoulements traduisant la présence de proies ou de prédateurs ont été historiquement beaucoup plus étudiés chez les animaux aquatiques et ceci pour deux raisons : (i) il était techniquement beaucoup plus facile d'effectuer ces mesures dans l'eau, la diffusion des particules d'ensemencement y étant plus élevée et (ii) ces écoulements étaient plus appréhendables, moins rapide et plus visible dans l'eau. La perception des flux et leur rôle primordial dans la compréhension du fonctionnement d'un organisme a été particulièrement bien étudié dans l'eau et ceci dans le contexte écologique des stratégies de fourragement du mésozooplancton (Visser (2001), Jiang *et al.* (2002), Jiang et Kiorboe (2011), Kjellerup et Kiorboe (2012)). Ces auteurs ont caractérisé aussi bien théoriquement qu'expérimentalement les structures hydrodynamiques et les forces visqueuses créées et ressenties par ces petits organismes, à des échelles très proches des échelles

d'interaction des grillons et de leurs prédateurs. Ainsi, à l'image de ces études sur les copépodes, il est apparu comme essentiel de comprendre les phénomènes physiques qui conditionnent la stratégie de prédation de l'araignée. En supposant que la pression de sélection imposée par ce prédateur soit forte, la caractérisation des écoulements générés lors de la prédation devrait nous permettre de comprendre comment la sensibilité de perception du grillon influence les distances et vitesses d'attaques de son principal prédateur. (**Chapitre 5 et 6**)

1.3.4 Rôle fonctionnel de la diversité morphologique

Comme rappelé en début d'introduction, cette évolution se serait effectuée en faisant correspondre les propriétés de leur structures périphériques et de leurs circuits neuronaux sensoriels, associés aux caractéristiques du stimulus sensoriel le plus crucial qu'ils avaient besoin de détecter (Wehner (1987), von der Emde et Warrant (2015)). Ainsi, la prise en compte des caractéristiques fréquentiels et des amplitudes des écoulements générés lors de la prédation nous permettra de comprendre quel est le rôle fonctionnel de la diversité morphologique des senseurs individuels du grillon. Si les capacités sensorielles hors du commun des grillons ont conditionné des comportements de prédation spécifiques chez leurs prédateurs, on s'attendrait légitimement à ce que les stimuli générés lors de l'attaque des prédateurs conditionnent à leur tour, d'une manière ou d'une autre, la morphologie des soies sensorielles de la proie, et plus généralement le fonctionnement global de son système sensoriel (**Chapitre 7 et 8**).

1.4 Mesures laser en biologie animale

On le comprend à la lecture du sous-chapitre précédent, la réponse à ces questions écologiques nécessite bien souvent la compréhension fine et précise des processus physiques en dynamiques des fluides impliqués dans les interactions entre les animaux et leur environnement biotique et abiotique. En raison de leur croissante accessibilité, les techniques de mesure laser qui furent initialement restreintes à des applications d'ingénierie en mécanique des fluides sont maintenant également utilisées dans les domaines de la locomotion et de l'écologie sensorielle. Parmi ces techniques de métrologie laser, la vélocimétrie par imagerie de particules (PIV) a été souvent adaptée aussi bien dans l'eau que dans l'air. Ce sont plus particulièrement des physiologistes, spécialistes du vol ou de la locomotion aquatique, qui ont exploité le potentiel de cette technique pour décrire les écoulements et caractériser avec précision les champs de vitesses turbulente autour du corps d'un animal. La PIV classique bidimensionnelle consiste à acquérir à l'aide d'une caméra (rapide ou classique) des images successives d'une section d'un fluide préalablement ensemencée et illuminée par une intense lumière. La section illuminée est, la plupart du temps, parallèle au plan image de la caméra et les sources lumineuses, éclairant les particules traçantes, sont bien souvent des laser (à émission impulsionnelle ou continue). On obtient ainsi des images des positions successives des particules dans un plan de l'écoulement. On corrèle ensuite des sous-régions de ces images successives entre elles pour y extraire la vitesse locale de déplacement des particules.

1.4.1 Vélocimétrie par imagerie de particules en hydrodynamique de la locomotion

Dès 1984, Spedding et Rayner (1984) ont photographié l'évolution des écoulements dans le sillage de pigeons entrainés à voler à travers un nuage de bulles d'hélium de 3 mm, éclairées par 4 flashs déclenchés séquentiellement (Figure 1.2.b). Cette étude constitue sûrement l'une des premières adaptations de la vélocimétrie par imagerie de particule à la biologie de la locomotion. On doit aussi aux pionniers Weis-Fogh, Lightill et Ellington la compréhension du rôle primordial des phénomènes instationnaires dans la création de la portance à l'aide du vol battu chez les petits animaux et plus particulièrement chez les insectes. Ils ont très tôt prédit l'existence de tourbillons tridimensionnels dans le sillage de ces insectes (Weis-fogh (1972)), ainsi que la présence de tourbillons de bords des ailes (Leading Edge Vortex - LEV), caractéristiques du vol battu, permettant aux insectes d'emmagasiner de la portance. Il aura pourtant fallu attendre 1996 pour qu'Ellington C. P. *et al.* (1996) visualisent en premier ces tourbillons de bords d'ailes, en photographiant la déviation de fils de fumée à proximité des insectes (Figure 1.2.c). Dickinson *et al.* (1999) seront ensuite parmi les premiers à appliquer la PIV pour caractériser la présence et le rôle prédominant de la recapture du sillage tourbillonnaire par les ailes des insectes afin d'accroître leurs forces de portance aérodynamique. Leur étude est réalisé cependant sur une aile artificielle d'insecte (de 8 cm de chorde) dans un réservoir rempli d'huile ensemencée par de petites bulles d'air. La compréhension des phénomènes hydrodynamiques inhérents à la locomotion dans l'eau a aussi très tôt bénéficié d'outils de mesures sans contact. Blickhan *et al.* (1992) ont utilisé l'anémométrie laser Doppler (LDA) pour montrer que l'écoulement dans le sillage du déplacement d'un poisson se compose d'une chaîne d'anneaux tourbillonnaires peu déformés. La PIV a aussi été utilisée très tôt par Müller *et al.* (1997) pour analyser qualitativement et quantitativement la structure du sillage derrière un poisson. Drucker et Lauder (1999) sont aussi parmi les premiers à caractériser avec une précision accrue les vortex dans les sillages des poissons à l'aide de la PIV (Figure 1.2.d). Par la suite, le développement croissant des capacités des caméras rapides, de la mémoire des ordinateurs et des intensités des sources laser ont permis aux ingénieurs d'accroître encore plus les résolutions, aussi bien spatiales que temporelles, de ces techniques. Ces sauts technologiques successifs ont poussé toujours plus loin le développement des outils nécessaires à la compréhension des phénomènes tridimensionnels instationnaires dans ce contexte particulier de la locomotion animale. Ainsi en 2005, Bomphrey *et al.* (2005) produisirent la première analyse par PIV du LEV caractéristique de l'écoulement autour d'une aile de papillon (*Manduca sexta*). Mis également en valeur à l'aide de mesures PIV, c'est le même mécanisme qui permet aux colibris de se maintenir en vol stationnaire (Warrick *et al.* (2009)) (Figure 1.2.e). La perspective de déterminer toutes les forces et moments agissant sur les ailes des animaux, en déterminant les géométries tridimensionnelles des structures tourbillonaires a motivé grandement l'application des techniques tomographiques. L'utilisation de ces techniques à la pointe de la technologie ne se fait cependant pas sans d'importantes difficultés. Composées de quatre caméras synchronisées à l'émission d'un puissant laser impulsionnel, elles nécessitent une calibration très précise et produisent des matrices tridimensionnelles. Néanmoins en 2012, Bomphrey *et al.* (2012), innovent de nouveau, en appliquant cette technique de PIV

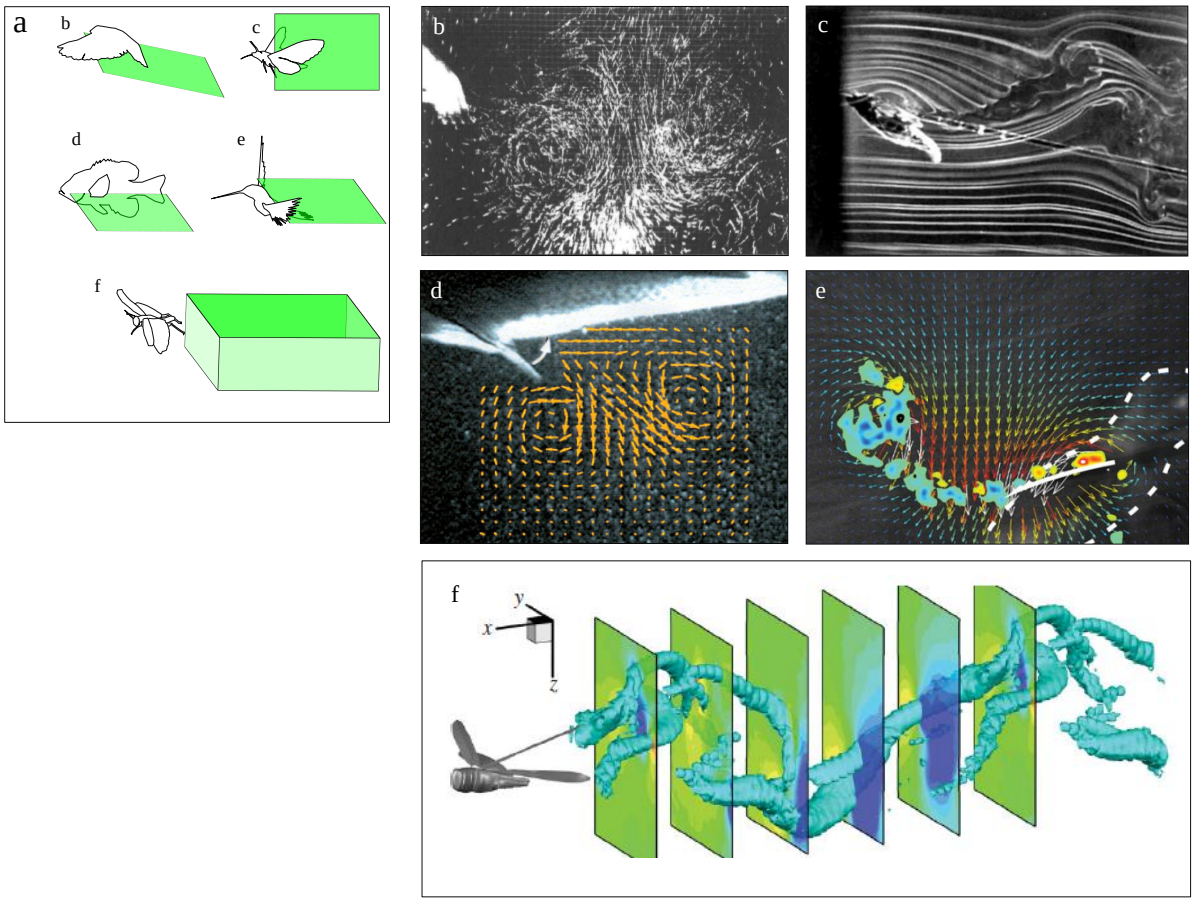

FIGURE 1.2: **Illustration des techniques expérimentales appliquées l'étude de l'aérodynamique et de l'hydrodynamique de la locomotion animale**. (a) Schéma synthétique des positions relatives des animaux et des plans ou volumes laser utilisés pour illuminer l'écoulement. (b) Ecoulement dans le sillage d'un pigeon (*Columbia livia*) visualisé par PIV (Spedding et Rayner (1984)). (c) Visualisation des lignes d'écoulement dans le sillage d'un papillon (*Manduca sexta*) en vol stationnaire (Ellington C. P. *et al.* (1996)). (d) Détermination par PIV des vitesses d'écoulement dans une coupe horizontale du tourbillon annulaire généré dans le sillage d'un crapet arlequin (*Lepomis macrochirus*) lors de sa nage (Drucker et Lauder (1999)). (e) Détermination par PIV des vitesses d'écoulement dans les vortex de bords d'aile (LEV) et sillage derrière un colibri (*Selasphorus rufus*) en vol stationnaire (Warrick *et al.* (2009)). (f) Visualisation tridimensionnelle par tomo-PIV des tourbillons générés dans le sillage d'un criquet (*Schistocerca gregaria*) (Bomphrey *et al.* (2012)).

tomographique à l'étude des tourbillons générés dans le sillage des criquets pèlerins (*Schistocera gragaria*) (Figure 1.2.f). Encore plus récemment, Henningsson *et al.* (2015) mirent au point une expérience comportant six caméras rapides haute résolution pour estimer l'empreinte aérodynamique du sillage derrière ces mêmes criquets pèlerins, mais cette fois ci dans un très grand volume illuminé (20 × 24 × 4 cm). La compréhension des mécanismes aérodynamiques impliqués dans le vol des chauves-souris aura aussi bénéficié, durant ces dix dernières années, des progrès technologiques des techniques de vélocimétrie laser, comme rapporté dans la récente review de Hedenström et Johansson (2015).

1.4.2 Métrologie optique en écologie sensorielle des animaux aquatiques

En parallèle des formidables développements des techniques de métrologie optique appliquées à la locomotion animale (nage et vol), on a vu se développer des applications spécifiques de ces techniques en écologie sensorielle, et plus particulièrement en milieu aquatique. Dès 1977, Strickler (1977) avait déjà adapté la strioscopie (ou photographie Schlieren) pour déterminer le sillage de traînée résultant de la propulsion de copépodes. Ce même auteur étudia la structure de l'écoulement autour de la tête et de la bouche d'un copépode lors de son alimentation et détermina le champ de vitesse en étudiant le déplacement des micro algues par prise successives d'images (Strickler (1982)). Un peu plus tard, Bleckmann *et al.* (1991) ont utilisé LDA pour déterminer la distribution spectrale des champs d'écoulements hydrodynamiques causés par le déplacement des poissons, grenouilles et crustacés, et ont discuté de la capacité de détection des événements hydrodynamiques à haute fréquence chez les poissons. Plus récemment, en utilisant également la PIV, Hanke *et al.* (2000) ont constaté la présence de vortex structurés dans sillage d'un poisson pendant au moins 30 s après son passage (Figure 1.3.b). Ces mesures ont permis à ces auteurs de discuter de l'avantage potentiel pour les prédateurs piscivores d'être en mesure de détecter et d'analyser les sillages générés par leurs proies. En 2002, Engelmann *et al.* (2002) ont adapté la technique de PIV classique pour la visualisation de l'écoulement le long de la ligne latérale d'un poisson afin de comprendre l'influence de la viscosité sur le fonctionnement de ce senseur. Chagnaud *et al.* (2006), après avoir généré artificiellement des anneaux tourbillonnaires ressemblant aux stimuli hydrodynamiques que les poissons pourraient rencontrer dans leurs milieux naturels, ont analysé la corrélation entre les réponses neuronales à ces anneaux tourbillonnaires et les champs de vitesse correspondants obtenus par PIV. Denissenko *et al.* (2007) ont mis en lumière la façon dont un stimulus hydrodynamique peut être affecté par la forme du corps d'un animal en étudiant notamment le flux généré par le système olfactif actif de l'écrevisse rouge (Figure 1.3.d). Ces animaux se servent de leurs membres propulseurs antérieurs pour générer des motifs d'écoulements distincts qui peuvent être utilisés pour l'acquisition de l'odeur. Catton *et al.* (2007) ont quantifié les champs d'écoulements générés par les copépodes captifs et libres (Figure 1.3.c). Ils montrèrent que la zone, dans laquelle la vitesse d'écoulement était suffisamment élevée pour induire une réaction de fuite, était 11 fois plus grande que l'organisme. Ainsi, les prédateurs peuvent être en mesure de percevoir un signal qui est spatialement étendu bien au-delà de la taille du corps. Dans Windsor *et al.* (2010b) et Windsor *et al.* (2010a), les auteurs ont étudié le champ d'écoulement impliqué dans la percep-

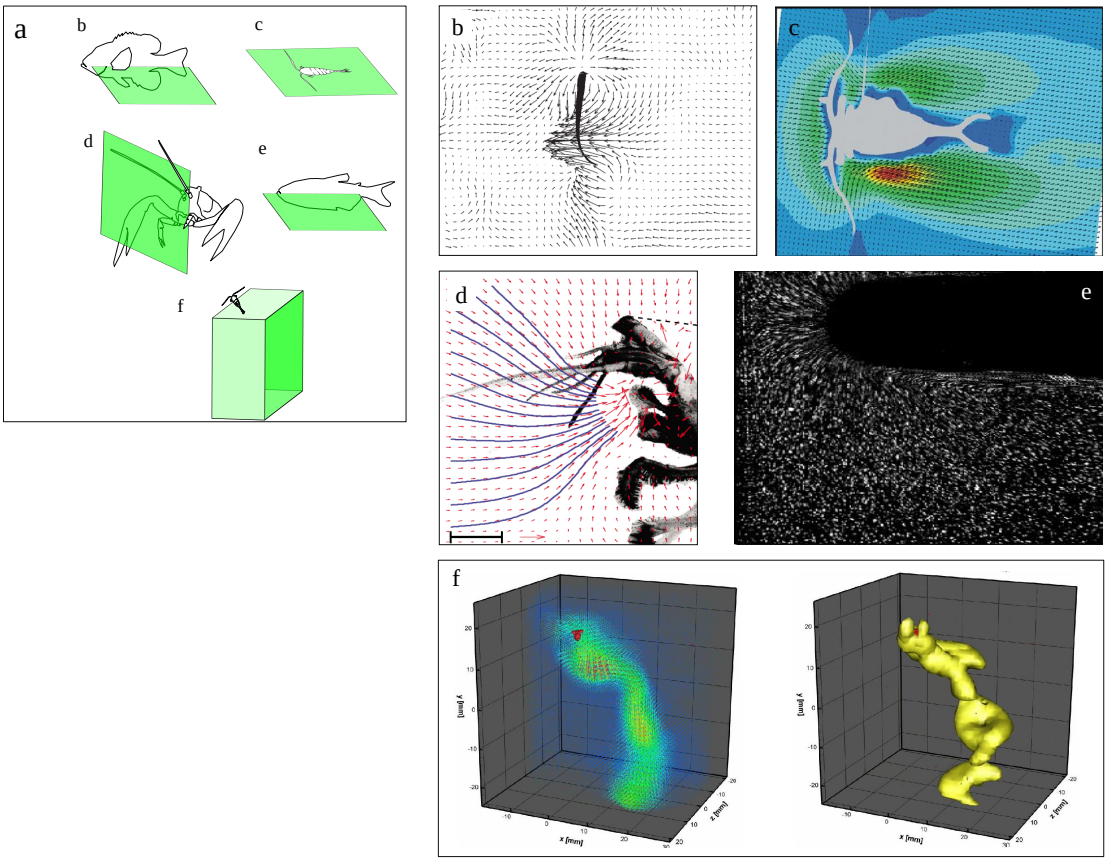

FIGURE 1.3: **Illustration des techniques expérimentales appliquées l'étude de l'écologie sensorielle des animaux aquatiques**. (a) Schéma synthétique des positions relatives des animaux et des plans ou volumes laser utilisés pour illuminer l'écoulement. (b) Visualisation par PIV du champ de vitesses horizontales de l'écoulement constituant la signature hydrodynamique laissée dans son sillage par un poisson rouge (*Carrassius auratus*) (Hanke *et al.* (2000)). (c) Détermination par PIV du champ de vitesses horizontales autour d'un copépode dans un écoulement (Catton *et al.* (2007)). (d) Détermination par PIV du champ de vitesses dans le plan de symmétrie verticale d'une écrevisse (*Astacus leptodactylus*) lors de la génération active d'un écoulement par ses flagelles (Denissenko *et al.* (2007)). (e) Visualisation par PIV du mouvement des particules le long de la ligne latérale d'un tetra aveugle (*Astyanax fasciatus*) (Windsor *et al.* (2010a)). (f) Détermination par tomo-PIV du champ tridimensionnel de vitesses dans le sillage d'une daphnie (*Daphnia magna*) (Michaelis (2014)).

tion hydrodynamique chez les poissons aveugles des grottes mexicaines, lorsque ces derniers se dirigeaient vers un mur ou glissaient parallèlement à lui (Figure 1.3.e). Ils ont suggéré que la nature des champs d'écoulement autour d'un poisson est telle qu'une forme d'imagerie hydrodynamique peut être utilisée par ces derniers pour détecter des surfaces proches.

1.4.3 Vélocimétrie laser à petite échelle dans les liquides

A une très petite échelle et dans l'eau, divers animaux utilisent aussi des réseaux de poils pour diverses tâches telles que l'alimentation, les échanges gazeux, l'odorat, et la nage. Dès 1981, Tautz *et al.* (1981) mesura, à l'aide de la vibrométrie laser Doppler (LDV) la vibration basse fréquence d'antennes d'écrevisses. Plus tard, Weissburg (2000) démontra l'utilité des techniques

de Fluoresence Induite par émission Laser (LIF), dans l'étude des jets d'odeurs et de leur transport convectif. Cette technique LIF, qui permet de faire des mesures de concentrations, aura aussi permis à Webster *et al.* (2003) de déterminer l'impact de la turbulence dans la capacité des animaux à percevoir des panaches d'odeurs, dans un contexte de chimiotaxie (voir la review de Webster et Weissburg (2009)). Koehl (2004) a utilisé la PIV pour étudier l'écoulement, à travers des modèles physiques à grande échelle, des appendices alimentaires de capture de copépodes. Plus récemment, la PIV a été adaptée à petite échelle pour montrer que c'était la morphologie et la cinématique de l'antennule de la langouste qui facilitait l'échantillonnage des odeurs (Reidenbach *et al.* (2008)). McHenry *et al.* (2008) ont montré, à l'aide de mesures PIV, l'importance de la couche limite superficielle autour des organes récepteurs cutanés, les neuromastes, dans la réponse mécanique de la ligne latérale des poissons. Ils ont prouvé que la variation de l'épaisseur de cette couche limite, avec la fréquence des écoulements, impliquait une forte hétérogénéité fréquentielle de la quantité d'énergie disponible au niveau des neuromastes. Ils définirent ainsi cette couche limite comme le premier filtre physique conditionnant la réponse globale de la ligne latérale.

Pour les petits organismes évoluant à très petits nombres de Reynolds, la caractérisation de l'écoulement tridimensionnel et la mesure des cinématiques tridimensionnelles des organes moteurs et de la direction du corps à très haute cadence est très difficile (Miller et Bergsten (2012)). Cependant les récents progrès de la PIV tomographique, qui avaient déjà fait leur preuve en permettant la caractérisation des écoulements tourbillonnaires dans le sillage des insectes, ont montré leur applicabilité à ces problèmes d'écologie sensorielle des arthropodes marins. Ainsi, en focalisant plusieurs caméras rapides sur des petits volumes d'une zone éclairée, Murphy *et al.* (2012) ont quantifié les perturbations hydrodynamiques tridimensionnelles générées par la nage libre du zooplancton.

1.4.4 Vibrométrie et anémométrie à petite échelle dans l'air

Dans l'air aussi, la mesure des écoulements basses fréquences et la caractérisation de la vibration ou du mouvement de petites structures à ces basses fréquences et à petite échelle a été un véritable défi technologique. Plusieurs techniques de mesure de vitesse d'écoulement ont aussi été exploitées pour étudier l'écoulement autour des organes sensoriels des arthropodes terrestres, tant en termes de phase que de fréquence, mais c'est en partie l'adaptation d'outils acoustiques qui a permis les premières mesures. D'astucieuses méthodes furent développées pour caractériser les déplacements d'air ou les vibrations infinitésimales de soies sensorielles. En 1979, Tautz (1979) adapta un tube de Kundt, dispositif expérimental servant à générer des ondes stationnaires, pour faire fléchir des poils sensoriels de divers arthropodes et en mesurer les caractéristiques mécaniques. En 1984, Bennet-clarck (1984) développa un microphone sensible aux très faibles écoulements dans l'air et prouva son applicabilité à l'étude des sons et chants de petits insectes. Le dispositif, qui possédait pour l'époque une extrême sensibilité aux mouvements dans l'air, bénéficia d'un astucieux décalage de la gamme de fréquence de sensibilité d'un microphone classique de 100-5000 Hz à 5-500Hz. Cette technique sera très tôt adoptée par Kämper et Dambach (1985) pour mesurer les vibrations basse fréquence générées dans l'air par

les grillons lors de leur chant de cour. Ce même microphone sera ensuite utilisé pour déterminer les écoulements produit dans l'air par des prédateurs approchant leur proie (Gnatzy et Kämper (1990)). Ce système très utile pour caractériser les vibrations basse fréquence dans l'air avait cependant des limites. Son gros désavantage étant de grandement déformer les écoulements qu'il était censé mesurer. Ainsi à l'image des accéléromètres, ces instruments de mesures perturbent, par leur simple présence physique, les vibrations des structures qu'ils sont sensés caractériser, et ceci d'autant plus que les phénomènes physiques se produisent à des très petites échelles biologiques. En 1990, Kämper et Kleindienst (1990) ont imaginé une technique très novatrice permettant de déterminer avec précision la vibration d'un poil sensoriel. Ils ont focalisé sur un poil, la lumière d'une lampe de microscope à l'aide de deux lentilles pour en mesurer, à l'aide d'un microscope, l'ombre projetée sur un réseau linéaire de cellules CCD. Cet astucieux système leur permis de déterminer la vibration d'un poil avec une précision de 0.3 μm.

Dès la fin des années 70, la vibrométrie laser Doppler (LDV) fut adaptée à l'observation des vibrations des membranes tympanales des sauterelles (Tettigoniidae) (Michelsen et Larsen (1978)) et à l'étude des vibrations des alvéoles des ruches lors de la danse des abeilles (Michelsen *et al.* (1986)). Dans le milieu des années 90, la popularisation des appareillages de LDV, beaucoup plus accessibles aux biologistes, révolutionna des champs entier de l'écologie physique et de l'écologie sensorielle des arthropodes. Les vibrations à la surface d'une feuille, générées par une larve de mineuse du pommier *Phyllonoructer madella* lors de son déplacement dans sa mine sous la surface, furent caractérises grâce à la LDV par Meyhöfer *et al.* (1994). Ils supposèrent que ces vibrations pouvaient être une des modalités de leur détection par leur parasitoïde *Sympiesis sericeicornis*. En 1998, Casas *et al.* (1998), toujours en utilisant la vibrométrie laser, déterminèrent que le parasitoïde générait lui aussi des vibrations à la surface de la feuille, détéctables par son hôte. Kumagai *et al.* (1998) adaptérent la LDV classique pour la mesure de la déviation des poils du grillon *Gryllus bimaculatus*. L'étude de la déviation de ces poils à différentes fréquences leur permirent de mesurer les caractéristiques mécaniques de ces poils sensoriels. Ils décrivirent ainsi le cerque de grillon comme un ensemble mécanique de filtres passe bande sur-atténués dont les fréquences de résonnances sont inversement proportionnelles à la longueur. En 1999, Göpfert *et al.* (1999) adaptèrent la vibrométrie laser à balayage (Scanning LDV) à l'étude des propriétés mécaniques des flagelles antennaires des moustiques *Aedes aegypti*. Ils focalisèrent leur faisceau laser en un point de 7 μm le long de l'antenne de moustique et furent capables de reconstruire, par moyennage de phase, les motifs de déflexion des antennes dans des champs oscillatoires variant de 300 à 3000 Hz. Utilisant de nouveau la vibrométrie laser à balayage et à échelle microscopique, Göpfert et Robert (2002) caractérisèrent la non linéarité de la réponse mécanique des segments antennaires sensibles aux vibrations de l'air, les arista de *Drosophila melanogaster*, lors de leur rotation dans un champ acoustique. Les vibrations des surfaces tympanales de papillons nocturnes *Agrotis exclamationis*, *Noctua pronuba*, *Xestia c-nigrum* et *Xestia triangulum* ont aussi été caractérisées par Windmill *et al.* (2007) à l'aide de la vibrométrie à balayage, pour en déterminer les réponses mécaniques dans des champs acoustiques ultrasonores et en déduire leur exceptionnelle sensibilité.

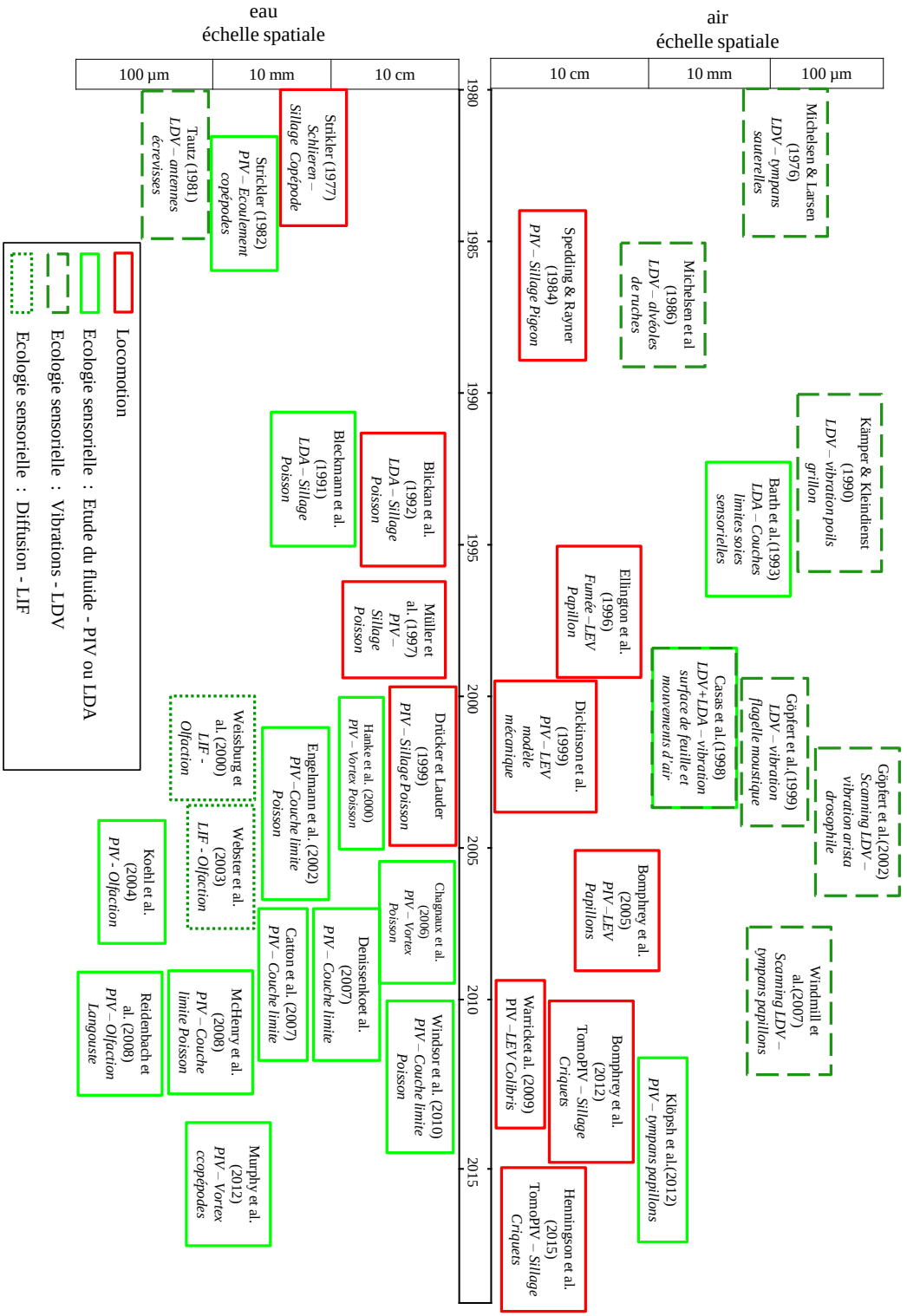

FIGURE 1.4: **Chronologie récapitulative et non exhaustive des applications des techniques de métrologie laser à la biologie animale**. Cette figure présente un recueil chronologique et non exhaustif des applications des techniques de PIV et LDA à la locomotion animale (en rouge) et à l'écologie sensorielle (en vert) des animaux terrestres et aquatiques. Y apparaissent également les applications des techniques LDV (vert tirets) et LIF (vert points), à l'écologie sensorielle des animaux aquatiques et terrestres.

1.4.5 Adaptation de la métrologie laser à l'écologie physique de la perception des écoulements chez les arthropodes terrestres

On l'a vu, de nombreuses techniques de mesures non intrusives ont été développées pour caractériser les écoulements dans les liquides d'un coté, et les vibrations de surfaces de l'autre, et ceci dans des contextes allant de la locomotion à la physique de la perception sensorielle. La figure 1.4 résume chronologiquement et non exhaustivement les diffèrentes études présentées dans les parties précédentes, les diffèrentes techniques utilisées (LIF, LDV, LDA, PIV) et les échelles étudiées aussi bien pour les organismes aquatiques que terrestres. Cette figure ne fait apparaître que très peu d'applications de la PIV ou de la LDA à petite échelle dans l'air. Dans l'air c'est l'adaptation d'outils acoustiques qui a permis les premières mesures de vitesses d'écoulements. A l'époque même où les physiologistes commençaient à quantifier des écoulements dans l'eau autour d'organes sensoriels à l'aide de la LDA ou de la PIV, la faible diffusion de la lumière par les particules d'ensemencement présentes dans l'air, couplée aux faibles capacités des photomultiplicateurs et des caméras analogiques, ne permettaient pas les mêmes prouesses dans l'air. Ainsi, peu de ces techniques ne furent réellement adaptées à l'étude des écoulements autour des senseurs de flux des arthropodes et notamment, à l'étude de soies sensorielles dans l'air. On peut tout au plus trouver une des rares caractérisations de l'écoulement autour de soies sensorielles dans une étude pionnière, où Barth *et al.* (1993) ont adapté la vélocimétrie laser doppler (LDA) à la détermination à très petite échelle de la couche limite de l'écoulement sur une patte d'araignée, où ils obtinrent ainsi une résolution de 300 μm. On constate aussi que, contrairement au grand nombre de mesures réalisées sur les signatures hydrodynamiques des animaux aquatiques trahissant leur présence, il y eu très peu d'études similaires sur les écoulements dans l'air, seul l'étude de Gnatzy et Kämper (1990) permis de caractériser les écoulements produits par des arthropodes terrestres prédateurs. Mais l'utilisation par ces auteurs d'un microphone assez volumineux, en lieu et place d'un anémomètre laser moins intrusif, pourrait avoir perturbé grandement le flux généré par ces prédateurs. En 2012, Klopsch *et al.* (2012) ont adapté la PIV à l'étude des champs de vitesse dans l'écoulement généré par une mouche libre de ses déplacements. Ils déterminèrent que les araignées *Cupiennius salei* pouvaient, à l'aide de leurs soies filiformes, détecter ses proies jusqu'à une distance de 4 cm.

Les travaux présentés dans ce mémoire décrivent l'application des techniques de métrologie laser à la caractérisation des écoulements impliqués dans la perception des mouvements d'air chez le grillon (Figure 1.5.A) et ceci à plusieurs échelles, (i) l'écoulement généré par une araignée prédatrice à l'échelle mesoscopique, (ii) l'écoulement autour des cerques de grillons à l'échelle macroscopique (Figure 1.5.B) et (iii) l'écoulement autour des soies de grillons à l'échelle microscopique (Figure 1.5.C et 1.5.D). Ces travaux se sont déroulés de 2004 à 2016, période qui a vu se succéder d'importantes avancées technologiques. Ces différentes technologies, issues de la mécanique des fluides expérimentale, n'ont pas été facilement adaptables à ces petites échelles de mesures, à nos géométries et problèmes tridimensionnels. Les poils de grillons sont, par exemple, implantés de tel façon sur le cerque qu'il est quasiment impossible de trouver un arrangement de poils permettant la focalisation de la nappe laser dans les deux plans de déflexion préférentiels des deux poils à la fois, nécessaire dans l'étude du couplage visqueux. C'est la raison pour

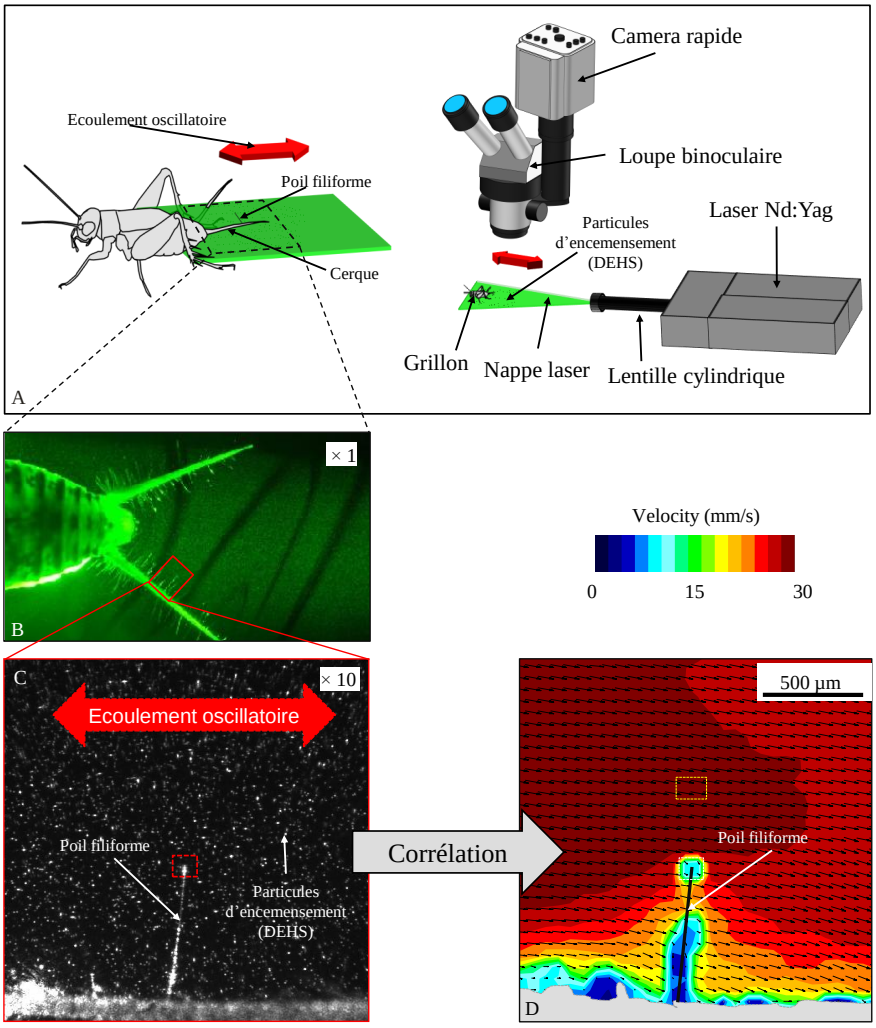

FIGURE 1.5: **Adaptation de la technique de vélocimétrie par imagerie de particules à l'étude d'un écoulement autour d'un poil filiforme de grillon**. (A) Le système de mesure se compose d'un laser impulsionnel (Nd :YAG, 30 mJ), d'une lentille cylindrique qui va transformer le faisceau laser en une fine nappe laser (d'une épaisseur de 50 μm à son point de focalisation). Dans une enceinte de mesure étanche, un écoulement oscillatoire généré par un couple de haut parleurs est ensemencé à l'aide de fines goutellettes d'huile (DEHS). Le spécimen d'étude est placé dans l'enceinte et orienté de telle sorte qu'un de ces cerques soit parallèle au plan laser. (B) La caméra rapide est placée sur une loupe binoculaire et peut assurer le cas échéant la visualisation de l'écoulement à l'échelle macroscopique ($\times$ 1). (C) En utilisant un plus fort grossissement ($\times$ 10), on peut imager localement la trajectoire des particules autour d'un poil filiforme. (D) On obtient ensuite la vitesse locale autour du poil par corrélation successives de sous-parties des images. Les vecteurs représentent les directions de l'écoulement et leur longueur est proportionnelle à la vitesse locale. Les couleurs représentent l'amplitude de la vitesse locale de l'écoulement.

laquelle nous avons développé l'utilisation d'un réseau de poils artificiels, afin de contrôler la géométrie d'implantation nous permettant alors de mesurer l'influence hydrodynamique d'un poil sur l'autre.

Ces adaptations ont en outre nécessité des ajustements, tant dans le choix de la puissance des sources lumineuses laser que dans le choix des caméras de visualisation et de leurs optiques respectives. Le travail sur des espèces vivantes fragiles et particulièrement petites nous a contraint à travailler avec des sources lumineuses moins puissantes mais plus concentrées et à réduire très fortement les champs de mesures traditionnelles pour travailler à des échelles macro voir micrométriques. La plupart des techniques expérimentales exposées dans ces travaux sont donc des développements technologiques spécifiques répondant à des cahiers des charges contraignants. Les choix des sources lasers, des optiques d'illumination, de la sensibilité des cameras, des optiques de visualisations ou encore des particules d'ensemencement et des traitements de surface se sont avérés primordiaux pour le succès des mesures (**Chapitre 2**).

1.5 Plan du mémoire

Le corps de ce mémoire s'ouvre sur le **chapitre 2**, chapitre technique qui présente en détail nos développements et adaptations de la PIV ainsi que la micro-PIV à l'étude des écoulements autour des organes sensoriels des grillons. Une application de la technique est détaillée dans le **chapitre 3**, qui présente les mesures des écoulements oscillatoires autour des structures cercales supportrices des poils tandis que le couplage visqueux entre poils est caractérisé dans le **chapitre 4**, à l'aide de l'estimation, toujours par PIV, des perturbations générées et ressenties par des tandems de poils biomimétiques micro-electro-mécanique (**MEMS**) servant de modèles physiques. La PIV a aussi été adaptée à l'étude des écoulements générés lors de l'attaque du prédateur principal du grillon, l'araignée loup (**chapitre 5**). Ces mesures sont confrontées à leurs modélisations par résolution des équations de Navier et Stokes incompressibles par la méthode des éléments finis dans le **chapitre 6**. Les performances relatives des senseurs de flux biomimétiques et de leurs homologues naturels sont comparées dans le **chapitre 7**. C'est la définition d'un facteur de mérite, tenant compte aussi bien de la sensibilité que de la rapidité de réponse d'un poil, qui nous permet de déterminer que le système sensoriel du grillon surpasse encore et toujours grandement son homologue biomimétique. Le **chapitre 8** décrit ensuite la validation expérimentale d'un modèle général simulant la réponse des poils de grillons dans des écoulements instationnaires. Enfin l'ensemble de ces résultats est discuté dans le **chapitre 9 (la discussion)** où, après avoir estimé l'implication de nos résultats sur la compréhension du fonctionnement global d'un réseau de senseurs et après avoir discuté les limites des modèles biomécaniques utilisés dans ce mémoire, nous conclurons sur le rôle essentiel de la caractérisation précise des couches limites tridimensionnelles instationnaires pour la compréhension du fonctionnement de senseurs d'écoulement. Tous ces chapitres ont fait l'objet de publications, à l'exception du chapitre 8 (soumis) et de la discussion en chapitre 9.

Chapitre 2

Techniques optiques laser en écologie sensorielle

Steinmann, T. & Casas, J. 2014 Laser-Based Optical Methods for the Sensory Ecology of Flow Sensing : From Classical PIV to Micro-PIV and Beyond. *In* Bleckmann, H., Mogdans, J. et Coombs, S. L., éditeurs : *Flow Sensing in Air and Water*, pages 31-62. Springer Berlin Heidelberg.

Résumé du chapitre

Ce chapitre présente un aperçu des techniques de vélocimétrie laser sans contact et discute leur applicabilité à un ensemble de problématiques d'écologie sensorielle. Une attention particulière est accordée à la Vélocimétrie par Imagerie de Particules (PIV) et aux techniques de mesures dérivées de cette PIV classique. L'investigation de phénomènes physiques opérant à diverses échelles spatiales implique en effet l'adaptation de la PIV utilisable uniquement à échelle mesoscopique.

Résultats

Nous présentons ainsi l'application de la PIV aux échelles macroscopiques des cerques de grillons et la mise au point d'une technique de micro-PIV. Celle-ci a la particularité d'utiliser un éclairage volumique des particules dans un fluide et nous permettant de visualiser leur déplacement autour des poils filiformes des grillons. Nous comparons ensuite les avantages et les limites de ces techniques.

Discussion

Nous concluons enfin que la technique micro-PIV, utilisée habituellement pour décrire des écoulements bidimensionnels dans des canaux très fins, est de fait mal adaptée aux exigences spécifiques de l'écologie sensorielle et de la physiologie sensorielle, ainsi qu'à la nature tridimensionnelle de la morphologique des organismes étudiés, malgrès une échelle répondant aux contraintes de la technique. Nous proposons, pour clore ce chapitre, une technologie mixte innovante qui exploite les avantages des deux techniques standard et micro- PIV, tout en contournant leurs principales limites.

Chapter 2
Laser-Based Optical Methods for the Sensory Ecology of Flow Sensing: From Classical PIV to Micro-PIV and Beyond

Thomas Steinmann and Jérôme Casas

Abstract This chapter presents an overview of techniques for laser-based, non-contact fluid flow measurements, and their application to real datasets. Particular consideration is given to particle image velocimetry (PIV)-techniques, from the usual macro-scale PIV, through meso-scale PIV, to micro-PIV, thereby spanning the range from decimeter to micrometer scales. We compare the advantages and limitations of these techniques. The specific requirements of sensory ecology and sensory physiology, as well as the 3D-morphological nature of the organisms studied led us to conclude that the techniques that are used in water are ill-suited for several key tasks when dealing with terrestrial organisms. We therefore propose an innovative mixed technology that exploits the advantages of both standard and micro-PIV techniques while avoiding their main limitations.

Keywords Particle image velocimetry, micro-PIV · Viscous boundary layer · Filiform hairs · Mechanoreceptors · Sensory ecology · Biomimetics · Flow sensing

2.1 Introduction

Flow sensing is used by a vast number of animals (see for example, the reviews of Casas and Dangles (2010) on insects, Engelmann et al. (2002) on fishes, Barth et al. (1993) on arachnids, Denissenko et al. (2007) on crustaceans, Sterbing-D'Angelo et al. (2011) on bats and Hanke et al. (2012) on seals).

T. Steinmann (✉) · J. Casas
Faculté des Sciences et Techniques, Institut de Recherche sur la Biologie de l'Insecte, IRBI UMR 7261 CNRS, Avenue Monge, Parc Grandmont 37200 Tours, France
e-mail: thomas.steinmann@univ-tours.fr

J. Casas
e-mail: jerome.casas@univ-tours.fr

H. Bleckmann et al. (eds.), *Flow Sensing in Air and Water*,
DOI: 10.1007/978-3-642-41446-6_2,

The ecological contexts in which flow sensing is relevant are varied: from prey–predator interactions to mate selection, and orientation to flow itself as illustrated in the works cited above. Flow sensing is used in air, water and most likely also in sand and hence in soil (Casas and Dangles 2010; Fertin and Casas 2006, 2007). Flow sensing is one of the several senses used by animals during orientation, and in some cases it is the dominant sense, for example for cave fishes (Windsor et al. 2010a, b). Thus, the study of flow sensing is a vibrant field of research for sensory ecologists and neuroethologists, and also for technologists working on biomimetic sensor design (Casas et al. 2013).

Studies on flow sensing, particularly those at small scale around single sensors, require high spatial precision and nonintrusive measurement methods. Thus, noncontacting measurement methods such as Laser Doppler Anemometry (LDA), Laser Doppler Vibrometry (LDV), and Particle Image Velocimetry (PIV), originally developed by aerodynamics and fluid mechanics engineers, have been used to measure flows of biological relevance. This chapter aims to describe recent technological advances in the measurement of flow around biological and artificial flow sensors in the context of organismal sensory ecology. We start with a description of the state of the art of the various techniques used for flow measurement at the scale of an organism or a sensing organ. We then describe two innovative techniques we have developed for greater spatial resolution, down to the single sensory hair: the first is relatively similar to the standard PIV technique as the particles in the fluid are illuminated by a thin light sheet; the second, micro-PIV, is relatively new to organismal biologists. It is, however, well known to microfluidic engineers, and is based on volumetric illumination. We compare the advantages and limitations of both techniques. In each case, we illustrate our reasoning with a figure or an example. Comprehensive considerations of parameter variations and extended theoretical development can be found in the references provided. The specific requirements of sensory ecology and sensory physiology, combined with the morphological nature of the organisms studied, led us to conclude that both techniques are ill-suited for several key questions. We therefore propose an innovative mixed technology that exploits the advantages of both standard and micro-PIV techniques and avoids their main limitations.

2.2 Classical PIV at the Scale of Bodies and Organs (10^{-2} m–10^{-3} m Resolution)

Due to their improved accessibility, laser-based measurement techniques that were originally restricted to applications in engineering and fluid mechanics are now also used in the fields of locomotion and sensory ecology. In particular, fish physiologists discovered the potential of these techniques to describe complex, unsteady, whole-field flows around an animal's body.

For instance, Bleckmann et al. (1991) used LDA to determine the spectral distribution of hydrodynamic flow fields caused by moving fish, frogs, and crustaceans, and discussed the possible biological relevance of the ability to detect high-frequency hydrodynamic events. Blickhan et al. (1992) used automatic particle tracking and LDA to show that the flow in the wake of a subundulatory swimmer consists of a chain of slightly deformed vortex rings. Two-dimensional PIV was used by Müller et al. (1997) to qualitatively and quantitatively analyze the structure of the wake behind a continuously swimming mullet. More recently, also using PIV, Hanke et al. (2000) found that the wake behind a swimming goldfish can show a vortex structure for at least 30 s. These authors discuss the possible advantage for piscivorous predators of being able to detect and analyze fish-generated wakes. In 2002, Engelmann and colleagues adapted the classical PIV technique for the visualization of the flow around a whole body covered by sensory organs to understand the influence of viscous hydrodynamics on the fish lateral line system (Engelmann et al. 2002).

Chagnaud et al. (2006) analyzed the correlation between neural responses to vortex rings and PIV data. Their artificially generated vortex rings resembled hydrodynamic stimuli that fish might encounter in their natural environments. Denissenko et al. (2007) shed some light on how a hydrodynamic stimulus can be affected by body shape by studying the flow generated by the active olfactory system of the red swamp crayfish. These animals use their anterior fan organs to generate distinct flow patterns that can be used for odor acquisition. The application of PIV to mapping biogenic and biologically relevant flows has been reviewed by Stamhuis et al. (2002).

Catton et al. (2007) quantified the flow fields generated by tethered and free swimming copepods. They report that the area in which the flow velocity was high enough to induce an escape response was 11 times the area of the organism's exoskeletal form. Thus, mechanoreceptive predators may be able to perceive a signal that is spatially extended well beyond the body size (Catton et al. 2007). Windsor et al. (2010a, b), studied the flow field involved in hydrodynamic imaging by blind Mexican cave fishes in open water, both when heading towards a wall and when gliding parallel to a wall. They suggested that the nature of the flow fields surrounding a fish is such that hydrodynamic imaging can be used by fish to detect surfaces at short range.

Wolf spiders live on the surface of leaf litter in forests, where they pursue their cricket prey using two different strategies. Casas et al. (2008) showed, using PIV, that these running spiders are, however, aerodynamically highly conspicuous due to substantial air displacement detectable up to several centimeters in front of them. The airflow in front of running spiders is thus a source of information for escaping prey, such as crickets and cockroaches. More recently, Klopsch et al. (2012) adapted PIV techniques to the study of the flow produced by a fly and sensed by a spider. Their findings led them to propose that the differences in the time of arrival and intensity of the fly signals at their different legs inform spiders about the direction of their prey.

2.2.1 Airflow Over a Cricket Body

The cricket *Nemobius sylvestris* uses hundreds of filiform hairs on two cerci as an early warning system to detect remote potential predators. The direction of the attacking predator can be estimated by arrays of hairs that have different directionalities (Landolfa and Jacobs 1995). However, the correct estimation of the direction of the incoming flow field can be biased by the flow perturbation around the cricket's body as a whole. We used PIV to investigate this flow. This technique is mainly used in experimental fluid mechanics to obtain time-resolved velocity measurements and related properties in fluids. The fluid is seeded with tracer particles which are assumed to follow the flow dynamics, and thus the motion of these seeding particles can be used to calculate the velocity of the flow. We will not describe this technique any further, as many books on this topic are available (Raffel et al. 1998; Adrian and Westerweel 2011).

Living crickets were placed in a glass container, with a single loudspeaker producing an oscillatory flow. The air inside the sealed glass box was seeded with 0.2 μm oil particles (Di-Ethyl-Hexyl-Sebacat) using an aerosol generator. The laser of the PIV system illuminated the airflow within the box. The laser sheet (width = 17 mm, thickness = 1 mm) was operated at low power (3 mJ at 532 nm) to minimize glare. A target area was then imaged onto the CCD array of a digital camera (696 × 512 pixels) using a lens (Macro-Nikkon 60 mm). The use of a macro lens allows us to obtain a ratio of the subject plane on the sensor plane of 1:1. Measurements were conducted at 25 °C, corresponding to an air kinematic viscosity of $\nu_{air} = 1.59 \times 10^{-5}$ m^2 s^{-1}. The far-field velocity was set to 10 cm/s and the flow frequency was 80 Hz. We used a stroboscopic principle to sample high frequency oscillatory flow signals with a PIV system limited to 20 Hz (Steinmann et al. 2006). We present here the results for an oscillatory flow parallel to the plane defined by the two cerci; the midline along the cricket abdomen was fixed at an angle of 0° to the direction of the flow.

We found that the orientation of the flow on the surface of a cercus differs from the orientation of the free field flow, i.e. the direction of an incoming flow around the two cerci is strongly altered, as illustrated by the streamlines in Fig. 2.1 (left). The directionality of each of the hairs on the two cerci is crucial as the incoming flow from different directions will trigger different patterns of activity across the whole cercal system (Miller et al. 2011). The projection of each hair into the central nervous system forms a functional map of the current air direction that translates the origin of the incoming flow as three-dimensional spatio-temporal activity patterns (Jacobs et al. 2008). Specifically, the flow direction is slightly shifted counter clockwise on the left cercus and clockwise on the right cercus, i.e. in opposite directions. This has important consequences for the overall computation of the direction of the incoming perturbation as these two effects might cancel each other.

We also observed that the flow amplitude was substantially lower close to the surface of the abdomen than further away (Fig. 2.1, right). The presence of the two

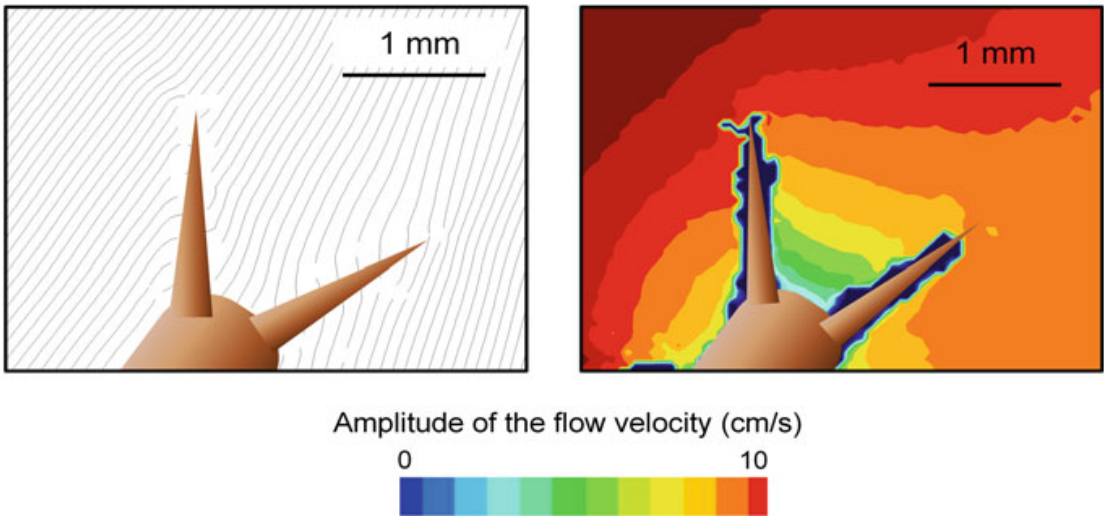

Fig. 2.1 Flow field around the rear of the wood cricket *Nemobius sylvestris*. On the *left*, streamlines represent the direction of airflow around the cricket's abdomen and cerci. The amplitude of the oscillatory flow in a cross section of the cricket's rear is shown on the *right*

cerci tends to decrease the amplitude of the flow field further, such that flow velocity at the bases of the cerci is considerably reduced. We can therefore conclude that there are substantial differences in the amount of energy available to the different hairs along a cercus.

In many cases, the intrinsic mechanical and neurophysiological properties of a sensory system reflect adaptation to ecologically relevant stimuli. We have illustrated how these stimuli can be greatly modified by the presence of the structure supporting the sensory organs. In addition to the cercus, which functions as a complex filter, the boundary layer over the body has significant implications for the ability of sensory organs to sense stimuli. Our findings agree with previous work with fish (Mc Henry et al. 2008) and crickets (Dangles et al. 2008). Thus, a complete understanding of the performance of a sensory system requires not only a knowledge of all the structural properties of the individual sensory elements but also the determination of the physical environment with exact quantification of the forces that drive these individual receptors.

2.2.2 *Structure of Acoustic Flow and Inter-Antennal Velocity Differences in Drosophila melanogaster*

The fruit fly *Drosophila melanogaster* has bilateral antennae of antisymmetric sensitivity. The arista, as well as the finuculus, two parts of the antenna, rotate about a central axis in response to acoustic stimuli. Acoustic communication is important during courtship, and takes place in the acoustic near field, where the small size of the dipole sound source (the male wing) and the rapid attenuation rate of particle velocity are expected to produce a highly divergent and localized sound

field. The small size of the male wing (considered as a dipole sound source) and the rapid attenuation rate of particle velocity produce a spatially divergent sound field of highly variable magnitude. Also, male and female *D. melanogaster* are not usually stationary during courtship, resulting in a variable directionality of the acoustic stimulus (Morley et al. 2012).

Using PIV, we examined the stimulus flow around the head of *Drosophila melanogaster* to identify the true geometry of the acoustic input into the antennae and its directional response. We found that the stimulus changes in both magnitude and direction as a function of its angle of incidence (Fig. 2.2).

Remarkably, directionality is substantial, with inter-antennal velocity differences that were up to 25 dB at 140 Hz [see explanations of the estimation of the intensity of inter-antennal differences in Morley et al. (2012)]. For an organism whose auditory receivers are separated by only 660 ± 51 μm (mean ± S.D.), this inter-antennal velocity difference is far greater than differences in intensity observed between tympanal ears for organisms of similar sizes.

Combining these measurements with a laser vibrometry analysis of the vibratory movement of the arista, Morley et al. (2012) demonstrated that the mechanical sensitivity of the antennae changes as a function of the angle of incidence of the acoustic stimulus, with peak responses along axes at 45 and 315° relative to the longitudinal body axis.

This work indicates not only that flies are able to detect a difference in signal intensity according to its direction, but also that the male song structure may not be the sole determinant of mating success; the male spatial position also makes a major contribution to female sound reception and therefore also, perhaps, to her decision making.

2.3 Macro-PIV at the Receptors Scale (10^{-4} m Resolution)

Rigorous understanding of the performance of a sensor generally requires studying the interaction between the input signal and the sensory organs. Airflow sensing by filiform hairs partially immerged in the boundary layer around the body has been extensively studied in arthropods, and especially spiders and crickets (Shimozawa and Kanou 1984; Humphrey et al. 1993; Barth et al. 1993; Bathellier et al. 2012). Filiform hairs can respond to air velocities as small as 0.03 mm s^{-1} (Shimozawa and Kanou 1984), making them one of the most sensitive biological sensors in the animal kingdom (Shimozawa et al. 2003). These outstandingly sensitive structures are used to detect the faintest oscillatory signals produced by the wing beats of prey and predators (Tautz and Markl 1979; Gnatzy and Heusslein 1986; Magal et al. 2006; Steinmann et al. 2006; Casas et al. 2008). The presence of hairs of different lengths allows spiders and crickets to fractionate both the intensity and frequency range of an airflow signal.

Several flow measurement techniques have been exploited to investigate the flow around a sensory hair, or sensory hair deflection, in terms of both phase and

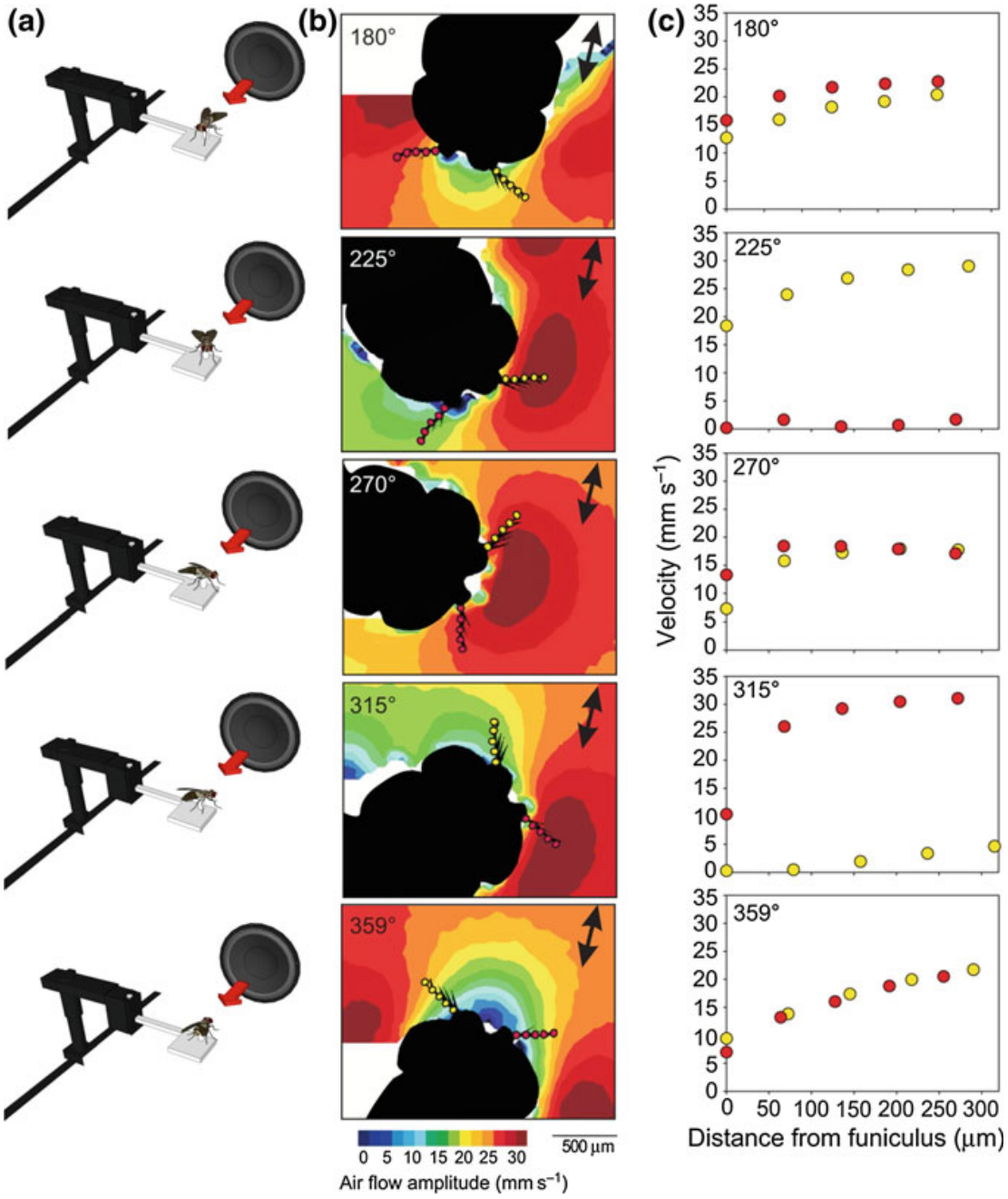

Fig. 2.2 **a** Orientation of Drosophila melanogaster to a 140 Hz sinusoidal stimulus produced by a loud speaker. **b** PIV velocity maps for five stimulus angles around the head of one individual fly. Points along the aristae correspond to positions at which velocity was determined. Large *black arrows* indicate the direction of the stimulus source. **c** Extracted velocity at five points along each arista for angles corresponding to those in (**a**). *Yellow* points represent the *left arista*, *red* points represent the *right arista*

frequency. In a pioneering study, Barth et al. (1993) adapted LDA to the study of the boundary layer of the flow over a spider leg. Kämper and Kleindienst (1990) and Shimozawa et al. (1998) adapted laser vibrometry to allow measurement of the deflection of cricket hairs.

In water, diverse animals use arrays of hair-like structures for important tasks such as feeding, gas exchange, smelling, and swimming. Koehl used both dynamically scaled physical models and a custom made PIV to study the flow through hairy food-capturing appendages (second maxillae) of calanoid copepods, which are abundant planktonic crustaceans (Koehl 2004). More recently, small-scale PIV has been used to show that antennule morphology and flicking kinematics facilitate odor sampling by the spiny lobster (Reidenbach et al. 2008). PIV has also been used to determine the fine-scale patterns of odor encounter by the antennules of mantis shrimps tracking odor plumes in both wave-affected and unidirectional flow conditions (Mead 2003). Mc Henry et al. (2008) presented direct PIV measurements of mechanical filtering by the boundary layer and fluid-structure interaction in the superficial neuromast of the fish lateral line system.

Following adaptation of PIV to small scales in water, we describe below how we adapted standard PIV protocols for the study of flow in air at a similar small scale. The major differences between macro-PIV and classical PIV are the use of a specialized optical system producing a particularly thin sheet of laser light and of a lens with five-times magnification.

2.3.1 Experimental Instrumentation

Various types of sample, including the cercus of *Nemobius sylvestris*, single 1,000 μm-long micro-electromechanical system (MEMS) hairs, and tandem 1,000 μm-long MEMS hairs on a plate of dimension 10×10 mm^2 (Krijnen et al. 2006) were placed in a glass container (dimensions: $10 \times 10 \times 10$ cm^3), with one loudspeaker (40 W) on one side connected to a signal generator. The seeding of air, the laser sheet generation and the imaging is explained in Sect. 2.2.1. The target area was then imaged onto the CCD array of a digital camera (696×512 pixels) using a binocular lens that allowed observation of a 2×2 mm^2 window around the substrate. The measurement technique is illustrated in Fig. 2.3. Far-field velocities were in the range 10–50 cm/s and flow frequencies 40–320 Hz. We used a stroboscopic principle to sample high frequency oscillatory flow signals with a PIV system limited to 20 Hz (Steinmann et al. 2006).

This technique allowed us to analyze the flow at a relatively high spatial resolution, higher than possible with standard PIV methods. We obtained a whole measurement field of $2{,}000 \times 2{,}000$ μm with a 5X magnification binocular objective lens. Given the camera resolution (696×512 pixels), the resolution can be 2.87 μm/pixels. Thus, selecting a 32-pixel correlation area, the spatial resolution is 100 μm. Using a time interval of 500 μs between two images and a sub-pixel interpolation, we were able to follow particle displacements of 0.287–100 μm. This methodology can thus resolve flows between 0.3 and 30 mm/s. The depth of field is given by the thickness of the laser light sheet and is estimated to be almost $\Delta z = 50$ μm at the focus point.

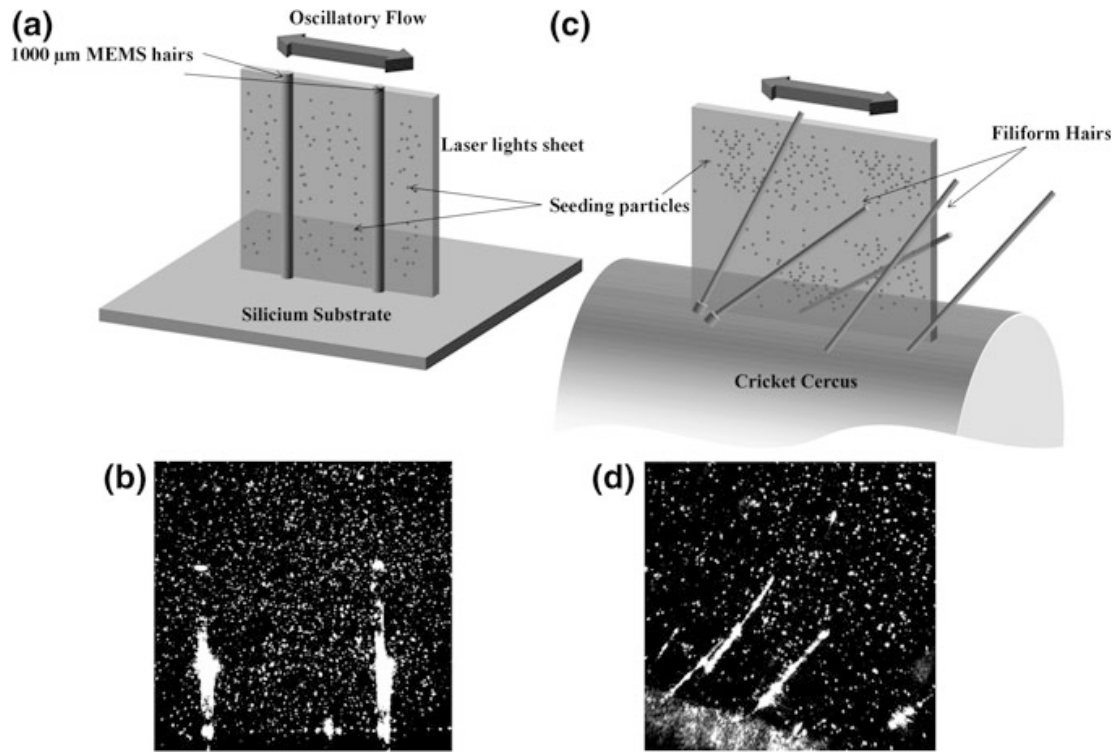

Fig. 2.3 Illustration of the macro-PIV principles. **a** PIV with a silicium substrate covered with MEMS hairs. **b** Raw PIV image of the seeding particles in the plane formed by the two MEMS hairs. **c** The same PIV technique adapted for the measurement of the oscillatory flow over a cricket cercus within the filiform-hair canopy. Filiform hairs are not always in the measurement plane, and sometimes cross it. **d** PIV images of the seeding particles in the light sheet plane. Hairs are in fact longer than can be observed on the image, but parts of their lengths are outside the light sheet

The quality of the measurement is greatly affected by the tracer concentration: if the concentration is too high, the discrimination of individual particles will be nearly impossible; if the concentration is too low, the particle density will not be sufficient for accurate estimation of the velocity at each point in the whole cross section of the flow. Indeed, the concentration must be lower than (Adrian and Westerweel 2011):

$$C_{\max} = \left(\frac{M}{d_i}\right)^2 \frac{1}{\Delta z}$$

where M is the magnification, d_i the particle diameter and Δz the laser light sheet thickness. As we will see in the next chapter on micro-PIV, there is a relationship between the signal-to-noise ratio (SNR) and the thickness of illumination (here referred to as the 'laser light sheet thickness', and also called 'the test section depth').

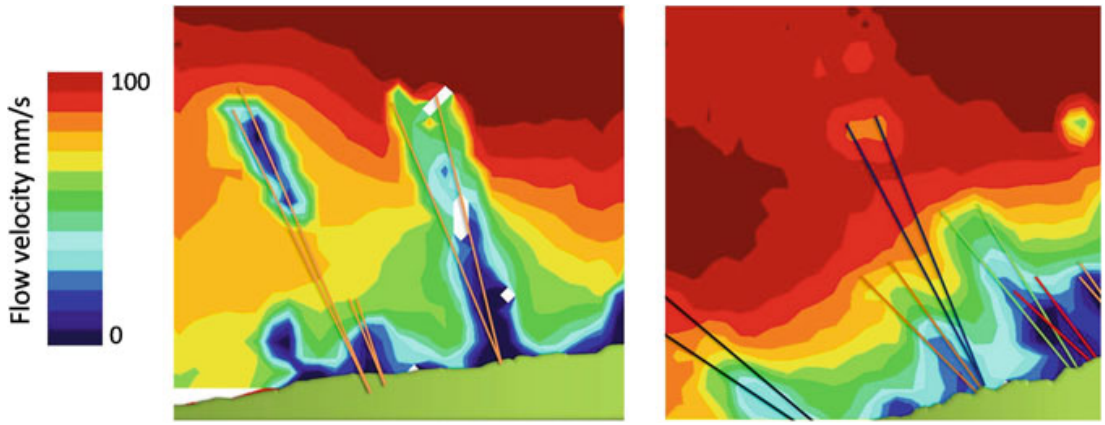

Fig. 2.4 Amplitude of an oscillatory flow over a canopy of cricket filiform hairs (Frequency = 80 Hz, Amplitude = 100 mm/s). Measurements from two different locations on the cercus are shown

2.3.2 Application of (Conventional) Macro-PIV to Airflow Sensing Organs

2.3.2.1 Cricket Hair Canopy

Figure 2.4 shows the velocity amplitudes of the oscillatory flow over a cricket cercus at two different locations. These findings reveal the complex arrangement of cricket filiform hairs and the corresponding flow patterns that result from the interactions between the boundary layers of different filiform hairs.

The mechanical constraints of the socket at the base of cricket filiform hairs cause a preferential plane of deflection, i.e. directionality. For a given direction of an incoming flow, only some hairs will oscillate in this flow direction, rather than in the plane of the laser sheet. Since it is impossible to determine the exact geometry and the plane of motion of the dense hair canopy in the immediate vicinity of the measurement plane, the interpretation of the flow patterns revealed by the PIV measurement is limited. The "out of plane" hairs probably have a large influence on the flow in the section of measurement. Nevertheless, it is still possible to extract some information about the ability of the hairs to follow the flow. The use of a stroboscopic technique to sample high frequency oscillatory flow allows simultaneous assessment of the dynamics of the flow velocity surrounding the cercus and the angle of displacement of the hairs (see Fig. 2.5).

Hairs of different sizes will be differently out of phase with the far-field flow. In the experiment illustrated, the small hair seems to have a phase advance of 26° with respect to the far-field flow. At a stimulus frequency of 80 Hz, as used here, a phase advance agrees well with the velocity of air within the boundary layer, in which the 260 μm-long hair is totally immersed, being phase advanced by $\pi/4$ (Kumagai et al. 1998; Steinmann et al. 2006). By contrast, the longer hairs (430 and 1,070 μm) were not totally immersed in this boundary layer and were

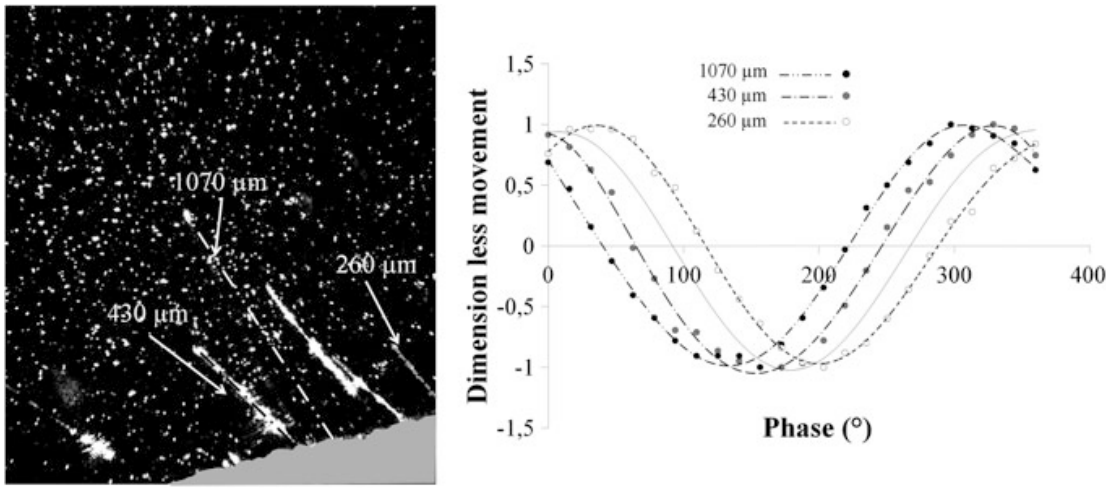

Fig. 2.5 (*Left*) Position and size of 3 filiform hairs, of length of 430, 1,070, 260 µm. (*Right*) Comparison of the phase differences between the far-field flow (*gray line*) and the three hairs. The *gray line* represents the phase of the far-field flow measured 1,500 µm above the cercus surface. The movements of the hairs are dimensionless, their velocity being divided by their maximal velocity. The hair length refers to the visible length and is therefore subject to error

thus less subject to this phase advance: indeed, they showed a phase lag (−26° for the 430 µm-long hair and −51° for the 1,070 µm-long hair). At 80 Hz, such increases of the phase lag with the length of the hair are expected and are coherent with theory. Although they are interesting in themselves, these results cannot be easily generalized. Systematic experimental variation of parameters is not feasible, as it is nearly impossible to find appropriate spatial arrangements of hairs in rows and similarly unlikely that each hair of such rows moves within the plane.

2.3.2.2 Single Cricket Hairs

We applied the macro-PIV technique in combination with a novel compact theoretical framework to describe the cricket hair mechanics (Fig. 2.6). In a systematic fashion, we studied the ability of six hairs of different lengths (410–870 µm) to follow oscillatory flows between 30 and 300 Hz (Bathellier et al. 2012). We found that cricket air-motion sensing hairs (and those in spiders) work close to the physical limit of sensitivity and energy transmission across a broad range of relatively high frequencies. In this range of frequencies, the hairs closely follow the motion of the incoming flow because a minimum of energy is dissipated in their basal articulation. This frequency band depends on hair length, and is between about 40 and 600 Hz, which is beyond the frequency at which the angular displacement of the hair is maximal.

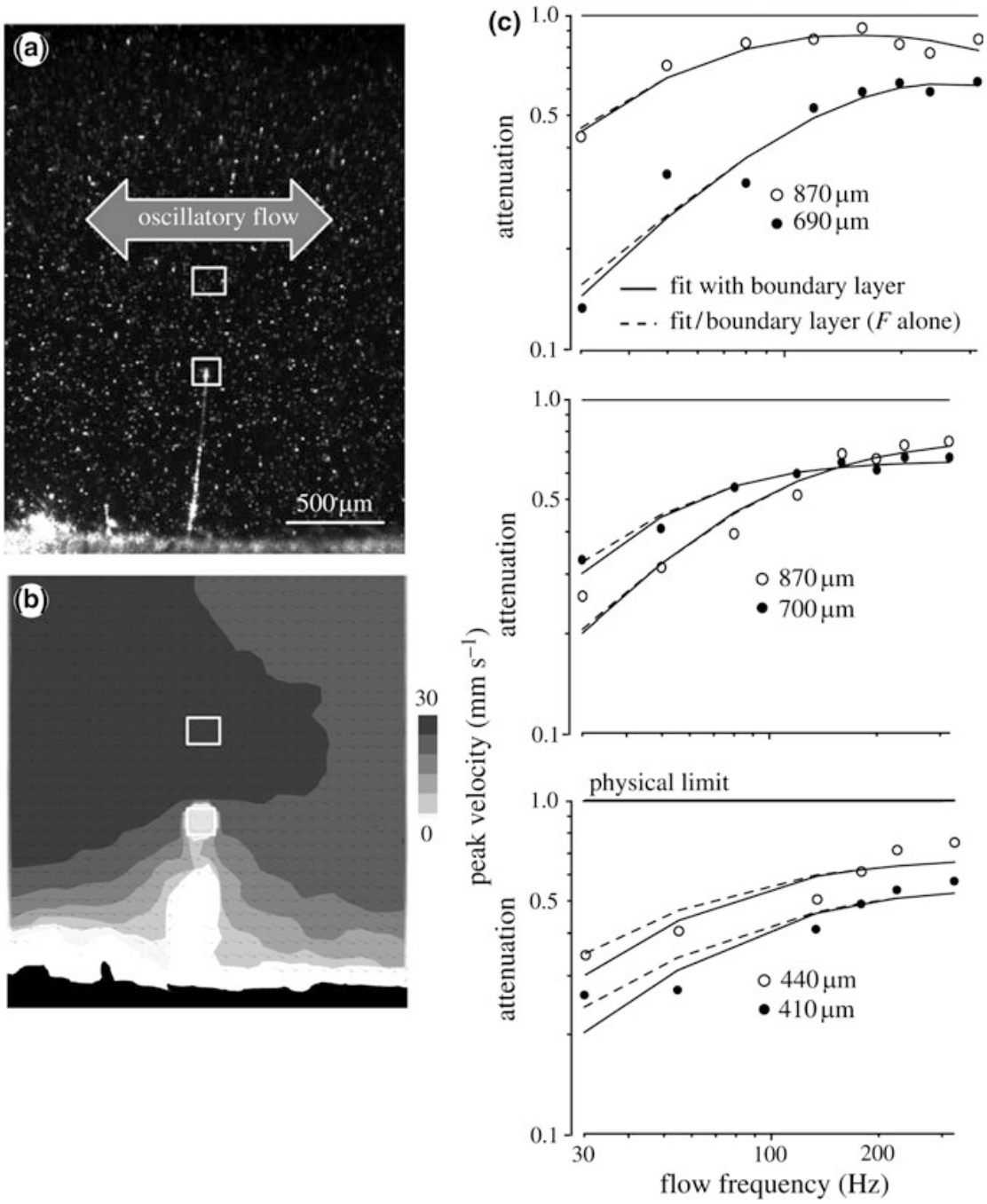

Fig. 2.6 Measurements of filiform hair motion in the cricket *Nemobius sylvestris*. **a** Picture of a cricket cercal hair in macro-PIV recording chamber. **b** Map of instantaneous air particle velocity (grey scale) and direction (*arrows*) for a 80 Hz oscillatory flow. The *white squares* represent the areas selected to compute the far-field flow velocity and the hair-tip velocity, respectively. **c** Deviation from the physical limit calculated by dividing the tip velocity of the hair measured by PIV by its physical limit, for six isolated cricket cercal hairs of different lengths. The solid lines represent the fit of the transfer function of a 2nd order mechanical system. In this model, the effect of the boundary layer was taken into account. It simply translates into a reduction of velocity close to the cercus surface (Bathellier et al. 2012)

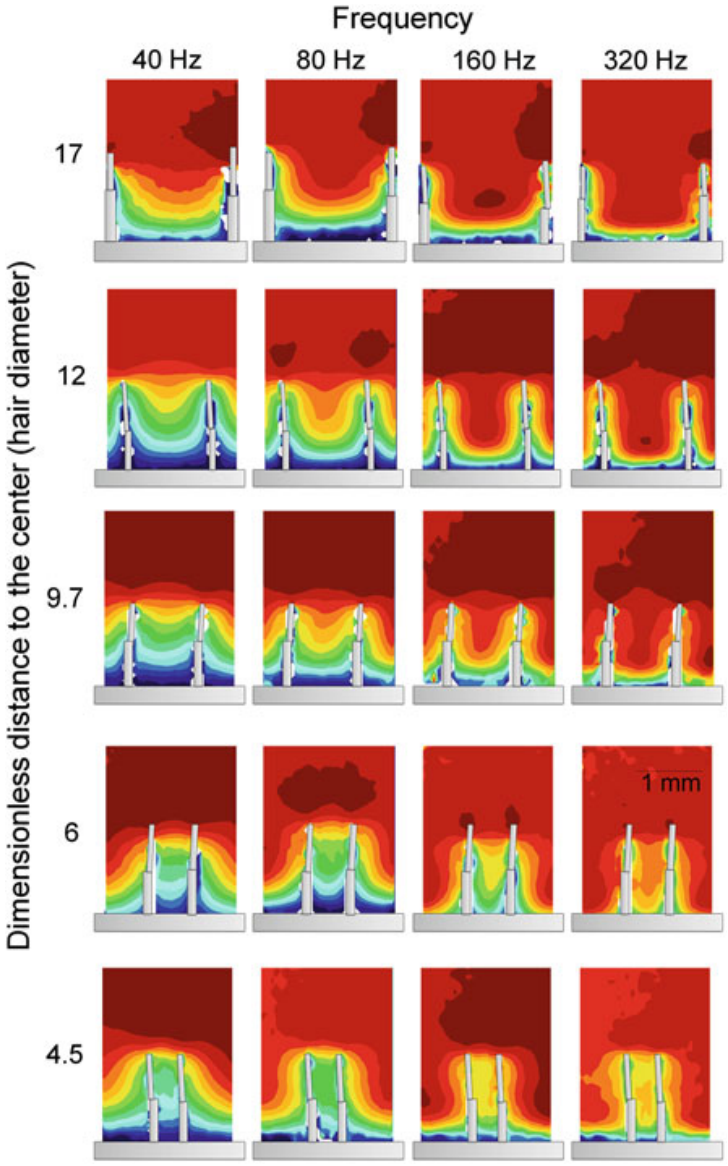

Fig. 2.7 Full-field data for flow in the vicinity of 1 mm-long MEMS hairs arranged in tandem, as a function of the frequency and inter-hair distance. Color code as in Fig. 2.6

2.3.2.3 The Use of MEMS Hairs as a Surrogate

Investigations of the flow around natural filiforms hairs suffer various limitations: it is difficult to select hairs of the desired lengths and to find tandem hairs with parallel planes of vibration. By using MEMS artificial sensors mimicking biological counterparts, it is however possible to reduce the various uncertainty factors. Indeed, all the MEMS hairs have a same, fixed length, and the use of MEMS technology enables very simple geometrical arrangements to be obtained, such as isolated hairs or tandem hairs with different spacing between the two members of the pair. By using flat plate substrates, all the nonsolvable problems arising from the 3D geometry of the cercus that supports the hairs in vivo can be avoided or minimized.

We used the PIV technique to measure the extent of flow perturbation by single and tandem hairs directly, using MEMS hairs as physical models (Fig. 2.7). Single

and tandem MEMS hairs with various inter-hair distances were subjected to oscillatory flows of diverse frequencies. Decreasing hair-to-hair distance markedly reduced flow velocity amplitude and increased the phase shift between the far-field flow and the flow between hairs. These effects were stronger for lower flow frequencies. We therefore predict strong hydrodynamic coupling within natural hair canopies exposed to natural stimuli, and the effects will vary depending on species, hair sizes, and hair densities (Casas et al. 2010).

2.3.3 Limitations of the Macro-PIV Technique

Kähler et al. (2012) reviewed the major sources of uncertainty of PIV near surfaces. They identified four major factors that determine the ability to resolve the flow in the hundreds of micrometers closest to the boundary layer: (1) the use of appropriate tracer particles that follow the fluid motion with sufficient accuracy, (2) the use of fluorescent particles or tangential illumination, such that reflection from the wall can be eliminated or avoided, (3) appropriate imaging of the particles with a lens or a microscope objective such that the particle signal can be suitably captured on a digital camera, and (4) satisfactory estimation of particle image displacement with digital particle imaging analysis methods. In our experiments, we had to deal with two of these four uncertainty factors, the imaging of individual particles and wall reflection. Indeed, one of the most important factors limiting the spatial resolution of the technique is diffraction: the recorded image of a tracer particle is generally greater than its theoretical magnified size (Meinhart et al. 2000). The size of the particle image is mostly determined by the diffraction of the optical system. Let d_i be the particle image diameter given by:

$$d_i = \sqrt{M^2 d_p^2 + d_{\text{Diff}}^2}$$

where M is the linear magnification of the binocular lens, d_p is the particle diameter (200 nm for DEHS oil droplets) and

$$d_{\text{Diff}} = 2.44(1 + M)\lambda \frac{1}{2\text{NA}}$$

where λ is the laser wavelength (532 nm) and NA is the numerical aperture of the optical system (binocular lens) and is 0.1 in our case.

It is also important to note that d_i is the size of the particle as projected onto the camera CCD sensors. Thus, the size of this particle in the measurement field will also depend on the size of the CCD sensor (see Fig. 2.8). As an example, with a 5X magnification, the field of view is 2,000 μm and consequently each pixel corresponds to 2,000/696 = 2.87 μm. At the measurement field scale, the particle image size is 3.24 pixels × 2.87 μm/pixels = 10 μm (Fig. 2.8).

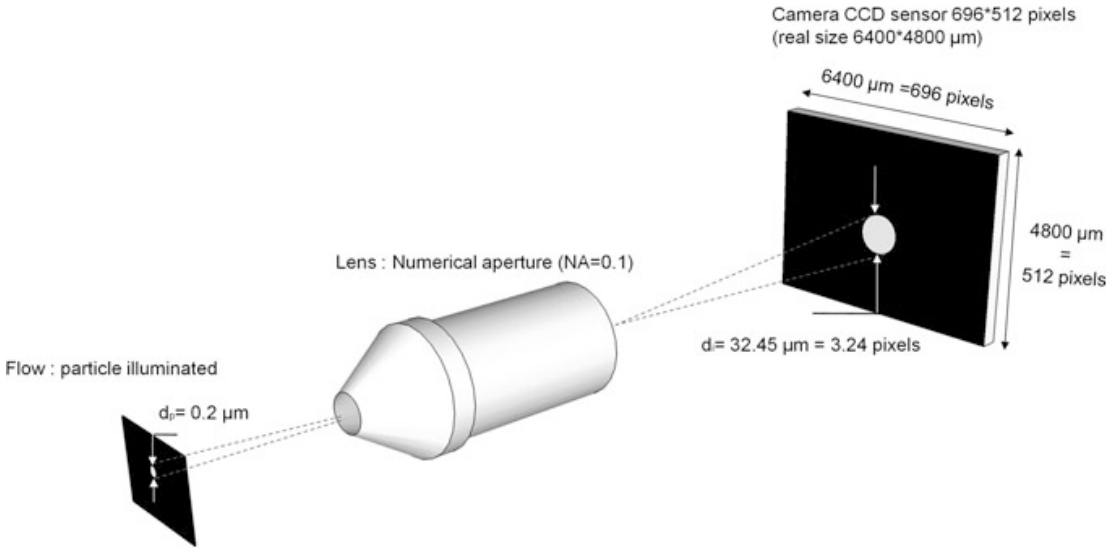

Fig. 2.8 Explanation of the estimation of the particle image size

Another limitation results from the large amount of light re-emitted by the surface of objects present in the flow. Biological sensory organs are generally very small, and therefore the capacity of the technique to resolve flows within a few hundred microns of the surface is crucial.

2.4 Micro-PIV at the Scale of Biological Receptors (10^{-5} m Resolution)

We have shown that the macro-PIV technique has limitations, in terms of spatial resolution, due to the small magnification factors of the optical system used. But even if magnification were to be increased, macro-PIV would still be limited by both the large diffraction of the optics and the substantial reflection from the surfaces of the objects studied. These constraints prevent visualization and quantification of the flows very close to receptors.

We will show in this section that using volume illumination provided by an epifluorescent microscope instead of the conventional optical light sheet allows the analysis of microscopic flows at the required scale (Santiago et al. 1998). In this methodology, the light, provided by a double pulsed monochromatic Nd:YAG laser (532 nm) is reflected by a dichroic mirror, travels through an objective lens that focuses on the point of interest, and illuminates a volume seeded with fluorescent particles. The emission from these particles at a specific wavelength (560 nm), along with the reflected laser light coming from surfaces or interfaces, shines back through the objective, the dichroic mirror and through a band pass filter that blocks the specific wavelength of the laser light (Wereley and Meinhart 2010).

The ability to observe and analyze a plane in macro-PIV is a consequence of the planar nature of the laser sheet that illuminates only a cross section of the flow.

By contrast, micro-PIV is a volume illumination technique, and exploits the ability of the objective lens to focus on a single plane, such that there is a two-dimensional plane in which particles can be viewed. Nevertheless, with this illumination method, the entire depth of the section is illuminated by a cone of light. Consequently, there is often background noise due to the emission from the out-of-focus particles added to the emission of individual particles in the focus plane; this can make discrimination difficult and low seeding concentrations have to be used. In the next section, we describe averaging analysis techniques that must be employed with this technique due to the low seeding. One consequence is that only steady flows can be investigated, in contrast to more conventional PIV techniques which can be used with unsteady or oscillatory flows. Adapted preprocessing techniques must also be used because the images tend to have a zero-displacement bias from background noise and low signal-to-noise ratios. Also, because of the low seeding particle density, high numerical aperture objectives are required to capture as much of the light emission as possible. The choice of optical material is therefore critical.

As far as we know, micro-PIV has rarely, if ever, been applied in the field of sensory ecology. The following section illustrates our attempts to apply this new technique to the visualization and quantification of the flows around single natural and biomimetic hairs with a resolution of 10 μm.

2.4.1 Experimental Instrumentation

The experimental micro-PIV apparatus consisted of a liquid delivery system composed of a syringe pump, a laser system, an epifluorescent microscope, an objective lens and an imaging system, and the cercus sample placed in a test section (a cavity with dimensions: 10 mm × 5 mm × 500 μm in PVC plate). Illumination was provided by a twin Nd:YAG laser system. The laser beams were directed onto the cercus using an objective lens (Olympus X20 or X40). The laser produces pulses of green light (532 nm) re-emitted by the fluorescent tracer particles at 560 nm. The tracer particle images were captured with a PCO Sensicam camera (696 × 512 pixels) and the images were transferred to a computer for processing. The camera and the laser were synchronized via an ILA PIV Synchronizer. The cercus was placed in a small waterproof Plexiglass box (500 μm depth) seeded with fluorescent particles (RhB-labeled beads of $d_p = 360$ nm). The box was open on both sides to allow a continuous flow.

2.4.1.1 Resolution of the Technique

This technique allowed us to acquire high-resolution tracer particle images. We obtained, with a 20X objective lens, a measurement field of 440 × 330 μm. With a 40X objective lens, the measurement field was 220 × 165 μm. The time

between two laser impulses was set at 500 µs, to resolve relatively high speed flows. Using the method described in Sect. 2.3.1, we determined that, for a 20X magnification, spatial resolution was 10 µm and flows between 0.13 and 13 mm/s could be studied.

2.4.1.2 Depth of Field and Measurement Depth

For 10 µm resolution in the focus plane, the depth of field and the measurement depth have to be limited to the same scale. However, the generation and alignment of a light sheet thinner than 50 µm is not possible, and therefore the use of volume illumination is the only feasible approach (Meinhart et al. 2000). In macro-PIV techniques, the depth of field is determined by the thickness of the laser light sheet, and the measurement depth by the positioning of the light sheet. By contrast, for volume illumination techniques, the depth of field and the measurement depth must be carefully determined.

The depth of field, which is the distance between the nearest and farthest objects that appear acceptably sharp can be calculated by Inoue and Spring (1997):

$$\delta_z = \frac{n\lambda}{\mathrm{NA}^2} + \frac{ne}{\mathrm{NAM}}$$

where n is the refractive index of the fluid between the objective lens and the test structure, λ is the wavelength of the incident light, NA is the numerical aperture of the objective lens, M is the total magnification of the microscope system, and e is the smallest resolvable distance on the image detector, i.e. the spacing between pixels. In the experimental setup we used, $n = 1$ for air, $\lambda = 532$ nm, NA $= 0.40$, $M = 20$, and $e = 0.64$ µm, resulting in a depth of field of $\delta_z = 3.4$ µm.

The measurement depth is the distance from the center of the object plane beyond which the particle image intensity is too low to contribute significantly to the measurement. It is given by Meinhart et al. (2000):

$$\delta_{z_m} = \frac{3n\lambda}{\mathrm{NA}^2} + \frac{2.16d_p}{\tan\,\theta} + d_p$$

where d_p is the tracer particle diameter (for RhB-labeled beads, $d_p = 360$ nm) and $\tan\,\theta = \mathrm{NA}/n$. With the optical settings we used, $\delta_{z_m} = 12.3$ µm.

For our experimental setup, the measurement depth was larger than the expected depth of field. We therefore had to keep the depth estimation criteria that gave the largest numerical result.

2.4.1.3 Air and Water Similitude

Micro-PIV has typically and historically been used in water, whereas cerci and hairs are naturally in air. At constant temperature (27 °C), the kinematic viscosity

of air is 20 times greater than that of water. The Stokes boundary layer thickness depends on this kinematic viscosity as follows:

$$\delta_{\mathrm{BL}} = \frac{4.64D}{Re^2}$$

where D is the diameter of the object being considered, i.e. the cercus or the hair diameter, and Re is the Reynold's Number defined thus:

$$Re = \frac{UD}{v}$$

where U is the velocity of the fluid and v is the kinematic viscosity of the fluid.

There is a simple relationship between the kinematic viscosity of air, v_{air}, and the kinematic viscosity of water, v_{water}:

$$v_{\mathrm{air}} = 20\ v_{\mathrm{water}} \text{ at } 27\ ^{\circ}\mathrm{C}$$

Consequently, at the same fluid velocity, the boundary layer thickness is 4.5 times smaller in water than in air. During our study, we therefore produced a continuous water flow of 2 mm/s which is equivalent to a 40 mm/s flow in air. The value of 40 mm/s is a biologically relevant value for crickets: it is the flow produced in front of a running spider (Casas et al. 2008).

2.4.2 *Application of the Micro-PIV Technique to Airflow Sensors in Crickets*

2.4.2.1 Study of Cercus Roughness and the Influence of Setae

The cricket cercus is covered with setae and small spines, up to a few tens of microns long, implanted at high density. The denticles covering shark skin reduce drag by decreasing the vorticity and shear stress in the boundary layer (Bechert and Bartenwerfer 1989; Bechert et al. 2000; Lee and Lee 2001). The drag reduction is proportional to the denticles size, but for larger denticles the proportionality breaks down, and the drag reduction eventually becomes a drag increase (Garcia Mayoral and Jimenez 2011). By analogy, we expected the spines on the cricket cercus to modify the boundary layer in the first hundreds of micron surrounding the cercus (Fig. 2.9).

Indeed, the modification of the boundary layer caused by the setae tends to extend to 150 μm above the cercus surface (Fig. 2.9b), a distance three times longer than the average length of the setae and long enough to be relevant to many sensory hairs. For a meaningful interpretation, these measurements of the biological system should be compared to the corresponding measures for a smooth cylinder surface. The experimental boundary conditions are, however, very difficult to estimate because they involve a superposition of the boundary layers of the

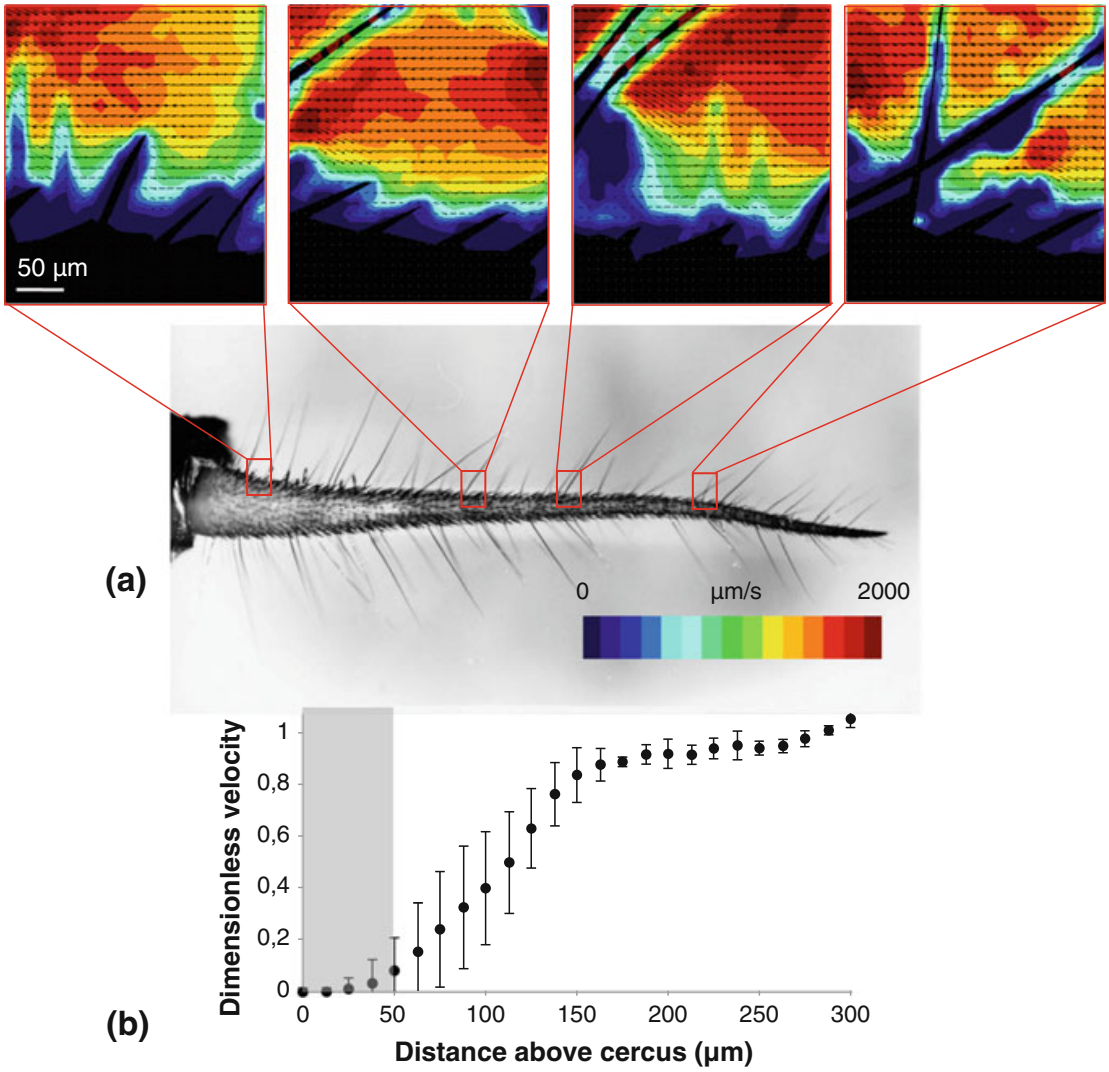

Fig. 2.9 Velocity fields of the flow in the first 500 µm around a cricket cercus acquired with the micro-PIV setup at four positions along a cricket cercus immersed in a water (**a**). Profile of the average flow over a vertical profile at the 4 positions. The distance is estimated from the base of the setae, and the average length of the setae is represented by the *grey box* (**b**). Velocities are normalized to the far-field velocity

channel test chamber with that of the cercus. Finally, the micro-PIV technique can only be used in water and water promotes adhesion of the seeding particles to the cercus surface and to each other (agglomeration).

2.4.2.2 Visualization and Quantification of the Flow Over a Single Hair

The micro-PIV technique was used to visualize and quantify the flow velocity over a single hair in steady flow at three different velocities: 150, 1,000, and 3,000 µm/s. Figure 2.10 shows the velocity field of a continuous flow along a cercus. The hair in the measurement plane had a 10 µm diameter. Two boundary layers can be seen, one around the cercus and the other around the hair. The flow was disturbed around

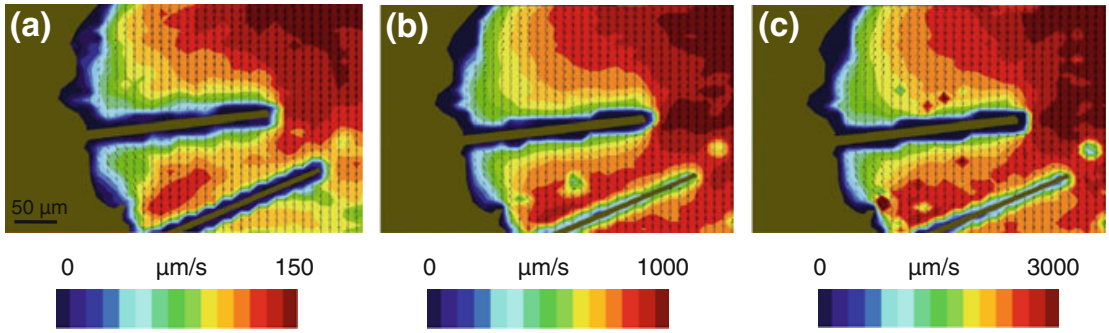

Fig. 2.10 Velocity field around a 10 µm-diameter cricket filiform hair (in the *middle* of each picture) in steady flows at three different velocities corresponding to three different regimes: $V = 150$ µm/s, $Re = 0.002$ (**a**), $V = 1{,}000$ µm/s, $Re = 0.015$ (**b**), $V = 3{,}000$ µm/s, $Re = 0.045$ (**c**)

the hair to a distance of roughly 15 times its diameter. Such strong disturbances over a long distance are comparable to what we observed previously for larger MEMS hairs, suggesting strong hydrodynamic coupling within natural hair canopies, depending on arthropod hair sizes and density (Casas et al. 2010).

2.4.2.3 Steady Flow Over a MEMS Hair

We adapted the micro-PIV technique for investigation of the steady flow along a single MEMS hair (Fig. 2.11). A set of 50 image pairs of the seeding particle flow in a cross section around a hair was obtained. After processing the micro-PIV images for reduction of noise, we used image pairs to compute the correlations to determine the local velocities of the particles. Figure 2.11d is the result of the averaging of the 50 velocity fields.

2.4.3 The Challenges for the Use of Micro-PIV in Sensory Ecology

It is clear that there are numerous problems associated with the adaptation of the micro-PIV technique to applications in sensory ecology, as illustrated above. The use of fluorescent particles and the background noise due to the volume illumination both limit the application of this technique to 2D flow in very simple setups. In most cases, the images are very noisy, such that it was not possible to identify individual particles. The reasons for this large amount of noise are numerous. We present here the three principal problems we had to face and suggest ways to solve them.

2.4.3.1 The Depth of the Micro Channel

Mielnik (2003) provides an estimated relationship between the SNR as function of the particle concentration and the depth of the test section. An increase of the

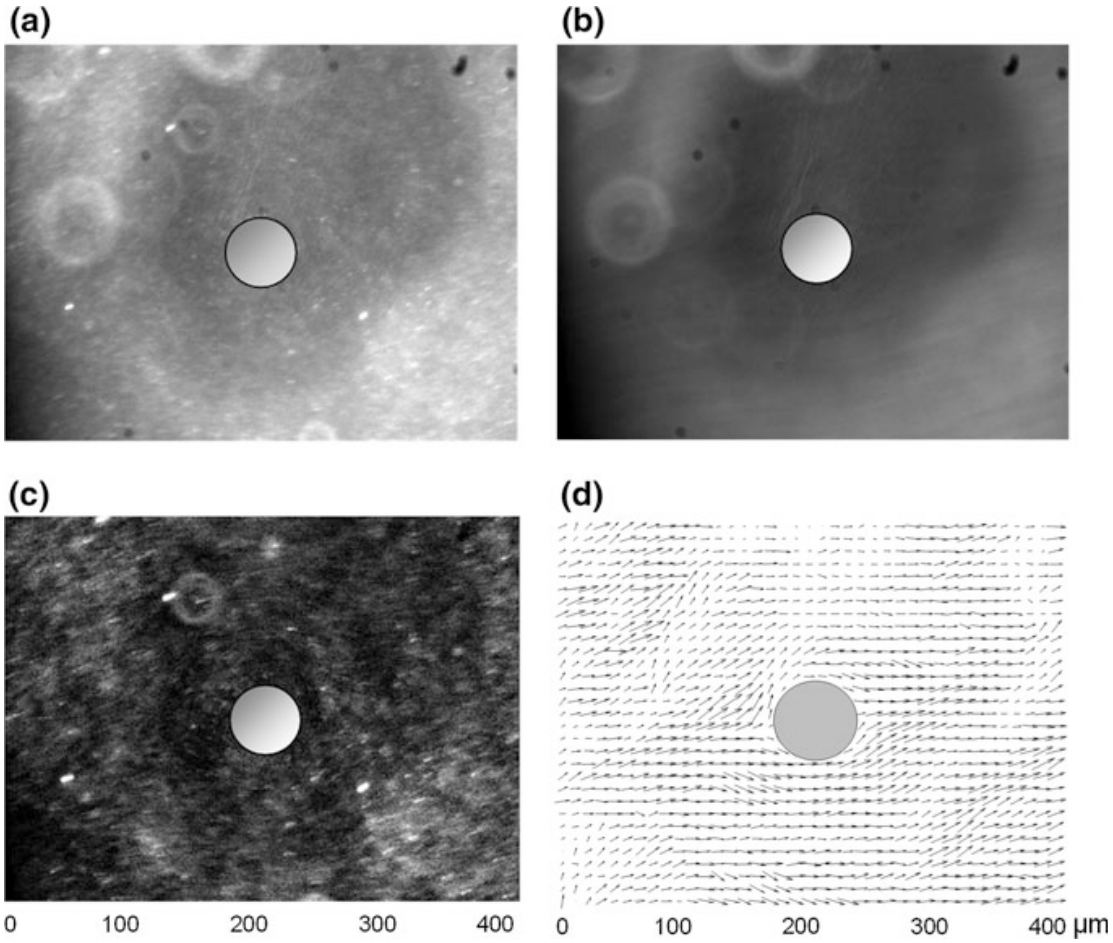

Fig. 2.11 Raw micro-PIV image of the particles around a MEMS hair (**a**), constant background extracted by estimating the minimal *gray* value by a technique of pixel-by-pixel sliding over time (**b**), pre-processed image (**c**) and velocity field around a hair in a viscous steady flow from the *left* (**d**)

micro channel depth or an increase of the particle concentration leads to a decrease of the SNR. The author estimated that test section depths larger than 200 µm would not allow a sufficient SNR, even at very low particle concentration (lower than 0.01 %). We concluded that the cercus was too thick (between 300 and 500 µm, which is thicker than most micro-channels) to provide good measurements because the SNR is very low. A solution to this problem could be to place a small cross section of the cercus in a very shallow micro-fabricated channel.

2.4.3.2 Particle Density

As explained by Mielnik (2003), a reduction of the particle density also leads to an increase of the SNR. Beyond a certain density, seeding particles are too few to provide enough information about the flow velocity at a sufficiently high spatial resolution. Micro-PIV experiment designs have to address this trade-off, lowering the particle density while generating sufficient information. The constraint imposed by the large section depth in our setup made it impossible to find a

suitable concentration. Mielnik et al. (2006) developed a novel seeding method, called Selective Seeding. The method involves selective seeding of a thin fluid layer within an otherwise particle-free flow. By analogy to the laser sheet in macro scale PIV, such particle sheets define both the depth and the position of the measurement plane, independent of the details of the optical setup.

It is also possible to make measurements in deep micro channels by confocal micro-PIV (Lima et al. 2007). This technique is based on confocal microscopy, in which pinhole apertures are used for spatial filtering and thus optical sectioning. As a result, it is possible to obtain a series of optical sectioning images at different focal planes, which provides 3D information of the fluid flow and reduces considerably the amount of background noise.

2.4.3.3 Contrast and Particle Fluorescence

The fact that individual particles are often not visible could also be due to insufficient fluorescence of the particles, or to poor transmission through the optical system of a given wavelength. We carried out experiments with three kinds of particles from micro-particles Gmbh: PS-Rhodamine B-particles (Diameter = 439 nm), MF-Rhodamine B-particles (Diameter = 366 nm), and PS-RhB-PEG-particles (Diameter = 448 nm). All these different particles absorb light at 560 nm and re-emit it at 584 nm. The results were similar for the three kinds of particles. We also tried different objective lenses, without improving the results.

2.4.3.4 Particles Agglomeration

We were able to increase the SNR by using a nonionic surfactant, polyvinyl alcohol, and alternatively by using seeding particles with a surface treatment (Polystyrene Rhodamine B particles, treated with Poly Ethylene Glycol). These two solutions greatly reduce both particle agglomeration and the sticking of particles to the walls of channels.

The noise has also been reduced computationally by subtracting a sliding minimum over time, for each pixel independently. The background noise stays the same over all images, while seeding particles move. This operation is executed with a window length of 30 images. For a particular pixel at a given position in image (n), the minimum over all images at that position is calculated and then subtracted from the pixel intensity in image (n) to obtain an enhanced processed image.

2.5 Conclusions: The Way Forward

This survey addresses micro-PIV in particular, as this technique had not previously been used in the field of sensory ecology. Being both novel and having unmatched accuracy, micro-PIV inevitably has great potential. However, our application of

this approach to the analysis of cricket sensory hairs has revealed several problems inherent to the technique. Solutions could often, but not always, be found.

Are these or similar problems encountered in other fields of application and how are they solved there? We performed a survey of the many papers published with micro-PIV technology to answer these questions (Appendix Table 2.1). As Wereley and Meinhart (2010) recently estimated, over 100 papers have been published annually reporting the use of this technique. Our survey shows that the problems we encountered are by no means rare. It also reveals that most of these studies were conducted in very small micro channels of thicknesses smaller than 500 μm, usually between 10 and 200 μm. Thus, one has to conclude that micro-PIV is a technique suitable for simple, essentially two-dimensional problems. This can be understood historically, as micro-PIV development was motivated by the need for a methodology to investigate microfluidic viscous flow phenomena. The broader utility of micro-PIV was demonstrated subsequently by applying it to flows in microchannels, micronozzles, BioMEMS, and flows around cells, still essentially 2D structures. Most sensory ecological issues associated with higher organisms are three-dimensional, and consequently micro-PIV is intrinsically not well adapted.

Combining the advantages of classical PIV and micro-PIV (see Appendix Table 2.2 for a comparison) would in many ways be a suitable solution for most of the problems and enable sensory ecologists to work at the receptor scale. There are indeed ways to adapt micro-PIV technology to suit the needs of sensory ecology. One very recent advance is to use confocal techniques (see Lima et al. 2007 and Patrick et al. 2010). However, this development is currently too expensive and sophisticated for most sensory ecology laboratories. Another possibility for channel depths larger than 1 mm is based on traditional laser light sheet illumination combined with long distance microscopic, rather than volume illumination. For an overview of this method see Kähler et al. (2006) and the most recent work by Alharbi and Sick (2010) and Eichler and Sattelmayer (2011). These authors explain that using a telecentric lens instead of a typical microscope solves the problem of the background noise caused by unfocused particles. The depth of focus of the optical system is then larger than the thickness of the laser light sheet, estimated to be 100 μm at a wavelength of 532 nm. More recently an innovative method for determining the three-dimensional location and velocity of particles was developed (Snoeyink and Wereley 2013). The wavefront from a particle is converted through a convex lens into a Bessel beam, the frequency and center of which can be directly related to the three-dimensional position of the particle.

In conclusion, one way forward would be to combine the thin laser sheet of classical and macro-PIV with telecentric lenses and fluorescent markers. Such a setup does not even need to be restricted to water environments, as Burgmann et al. (2011) were able to use fluorescent tracer particles to study small-scale wall-bounded gas flows. None of these ideas have been applied to, or tested in, sensory ecology. The study of flow sensing in organisms therefore has a bright future, but its students must be prepared to design their own tools, as off-the-shelf technology is generally unsuited to the models they study and the problems they face.

Appendix

Table 2.1 Summary of the different techniques, channel flow depth, and applications of micro-PIV from 20 papers on micro-PIV most pertinent to the scope of this review

Author	Year	Channel flow depth	Applications	Techniques	2D/3D	Velocity
Meinhart et al.	1999	30 μm	μ channel flow	NdYag laser	2D	
Cummings	2000	30 μm	Image processing	Argon ion Laser	2D	
Meinhart et al.	2000	90 μm	Inkjet print head	Nd YAG	2D	8 m/s
Kim et al.	2002	7 μm	μ channel, electroosmotic flow	Argon ion laser	2D	260 μm/s
Lee et al.	2002	690 μm	μ channel flow	Nd YAG laser	2D	
Devasenathipathy et al.	2003	50 μm	Electrokinetic flow		2D	
Devasenathipathy and Santiago	2003	107 μm	Silicon channel	Nd YAG laser	2D	20 mm/s
Meinhart and Wereley	2003	100 μm	AC electrokinetic flow	Mercury lamp	2D	110 μm/s
Sato et al.	2003					
Park et al.	2004					
Bitsch et al.	2005	30 μm	Blood flow in a capillary glass	LED	2D	4 mm/s
Liu et al.	2005	225 μm	Microcapillary flow	Nd YAG laser	2D	1 m/s
Boek et al.	2006	40 μm	Wormlike micellor fluid	Nd YAG laser	2D	4 mm/s
Bown et al.	2006	25 μm	DNA concentrator	Nd YAG laser	2D	5 μm/s
Curtin et al.	2006	233 μm	DNA, viscosity estimation	Nd YAG laser	2D	0.4 mm/s
Horiuchi et al.	2006	11 μm	μ channel, electroosmotic flow	Nd YAG laser	2D	100 μm/s
Kähler et al.	2006	Boundary layer of 5–7 mm	Wall-shear-stress and near-wall turbulence	Laser light sheet Nd: Yag laser	2D	5 m/s
Li and Olsen	2006	521 μm	Turbulent flow in μ channel	Nd YAG laser	2D	10 m/s
Lindken et al.	2006	200 μm	μ channel flow	NdYag laser, stereoscopy	3D	0.3 m/s
Mielnik and Saetran	2006	260 μm	Selective seeding	Sheet of seeding particles	2D	2 cm/s
Moghtaderi et al.	2006	300 μm	Baffle plate μ reactor	NdYag laser	2D	0.3 m/s
Sato and Hishida	2006					
Yan et al.	2006					

(continued)

Table 2.1 (continued)

Author	Year	Channel flow depth	Applications	Techniques	2D/3D	Velocity
Yang and Chuang	2005					
Bown and Meinhart	2006	436 μm	μ channel	3D, stereoscopy	3D	16 μm/s
Lima et al.	2007	100 μm	Confocal μPIV	NdYag Laser	2D	0.6 mm/s
Natrajan et al.	2006					
Pereira et al.	2007					
Walsh et al.	2007					
Kim et al.	2008	70 μm	Mixing and pumping	Continuous laser	2D	15 μm/s
Lee et al.	2009	50 μm	Fluid mechanics of blood sucking	Continuous Nd:YAG laser	2D	0.4 cm/s
Mansoor and Stoeber	2010	200 μm	Drying of polymer solutions	HeNe laser	2D	1 μm/s
Raghavan et al.	2009					
Alharbi and Sick	2010	44 mm	Study of boundary layers in internal combustion engines	1 mm laser light sheet	2D	1.5 m/s
Nguyen et al.	2010	200 μm	Improvement of measurement	Continuous DPSS laser	2D	
Poelma et al.	2010	250 μm	Study of outflow tract of embryonic chicken heart	Scanning μPIV	3D	4 cm/s
Wereley and Meinhart	2010		Review of recent advances in μPIV	Confocal imaging, particle image defocusing, stereo imaging…	2D, 3D	
Kloosterman et al.	2010	148 μm	Increasing depth of correlation	Diode-pumped Nd:YLF laser	2D	
Patrick et al.	2010	150 μm	Hemodynamics	Bidirectional scanning micro PIV	2D	45 μm/s
Rossi et al.	2011	Theoretical work	Image preprocessing use of depth of correlation	Particle image defocusing		
Wang et al.	2010	300 μm	Pulsed micro-flows for insulin infusion therapy	Nd Yag laser	2D	30 mm/s
Cierpka et al.	2011	200 μm	Comparative analysis	Astigmatism-μPTV, stereo-μPIV		75 mm/s
Eichler and Sattelmayer	2011	17.5 mm	Measurements of premixed flames	Long-distance micro-PIV	2D	

(continued)

Table 2.1 (continued)

Author	Year	Channel flow depth	Applications	Techniques	2D/3D	Velocity
Jin and Yoo	2011	100–140 μm	Droplet merging	Continuous laser/high speed camera	2D	4 cm/s
Nguyen et al.	2011	500 μm	Improvement of measurement	Volumetric-correlation PIV	3D	
Samarage et al.	2011	200 μm	Optimization of temporal averaging processes	Nd:Yag continuous laser	2D	
Sun et al.	2011	60 μm	Study of a microdiffuser	100 W Halogen lamp	2D	20 mm/s

Table 2.2 Advantages and limitations of both standard macro-PIV and micro-PIV techniques according to seven criteria

	Macro PIV standard thin laser light sheet/non fluorescent particles	Micro PIV Volume illumination/fluorescent particles	Mixed technique: Telecentric lens/thin laser light sheet/fluorescent particles
1. Glare and body surface reflexion	Standard illumination techniques lead to high reflection close to surfaces, and without fluorescent paint, there is a lack of information in the first 100 μm of the boundary layer	The greatest advantage of the use of fluorescent particles: investigation of the flow in the 100 μm closest to the receptor is possible	Use of fluorescent particles to reduce reflection of laser light close to the surface
2. Signal-to-noise ratio. Capacity of individual particle discrimination	The thin laser sheet thickness tends to reduce the background noise but the noise mainly depends on particle density: $C \ll \frac{1}{\Delta Z}\left(\frac{M}{di}\right)^2$	The biggest problem with the technique when applied to biological flows and particularly 3D problems: the SNR increases with the increase of test section depth	Thin laser sheet to reduce undesirable background noise
3. Limit of magnification	Depends on lens magnification, but the upper limit with a standard binocular lens is 5 times, which represents a field of view of 2,000 μm	Theoretically there is no limit of magnification. Practically a 20 times magnification is sufficient for a large number of applications and represents a field of view of 440 μm	Telecentric lens allowing a 10 times magnification leading to a field of view of 880 μm
4. Diffraction of the particles	Diffractive effects and particle image size on CCD sensor are large due to the low numerical aperture (di = 15 μm)	The high numerical aperture of a microscopic lens (0.4) limits the diffraction (di = 3 μm)	Telecentric lens with a numerical aperture of 0.21 leading to an estimated diffraction of 6 μm

(continued)

Table 2.2 (continued)

	Macro PIV standard thin laser light sheet/non fluorescent particles	Micro PIV Volume illumination/fluorescent particles	Mixed technique: Telecentric lens/thin laser light sheet/ fluorescent particles
5. Temporal resolution	At 5 times magnification and given the large SNR, real time and high frequency flow investigation is possible	To maintain a good SNR, the particle density needs to be low, and consequently often not high enough to provide good correlation or velocity fields without time averaging	High SNR expected even at high concentration, real time and high frequency possible
6. Working distance	Depends on lens but typically between 50 and 70 mm	The use of microscopic lens requires small working distances, generally a few mm. This constraint is hard to apply to the investigation of flows around 3D structures	Large working distance, allows the investigation of flows around 3D structures
7. Application fields (in the sensory ecological framework)	Steady and unsteady flows in air and water around 3D structures at a macro scale of a few millimeters	Steady flows in water around 2d structures at the scale of a few hundreds of microns (cells, protozoans, flows in vessels etc.)	The use of fluorescent particles constrains applications to steady and unsteady flows in water around 3D structures at a scale of a few hundreds of microns

The use of gray and white background colors respectively indicates for which criteria standard macro-PIV or micro-PIV perform better. The last column is for the new innovative mixed technique that exploits the advantages of both techniques

References

Adrian RJ, Westerweel J (2011) Particle image velocimetry. Cambridge University Press, Cambridge

Alharbi AY, Sick V (2010) Investigation of boundary layers in internal combustion engines using a hybrid algorithm of high speed micro-PIV and PTV. Exp Fluids 49:949–959. doi:10.1007/s00348-010-0870-8

Barth FG, Wastl U, Humphrey JAC, Devarakonda R (1993) Dynamics of arthropod filiform hairs II Mechanical properties of spider trichobothria (*Cupiennius salei* Keys). Philos Trans R Soc Lond B Biol Sci 340:445–461

Bathellier B, Steinmann T, Barth FG, Casas J (2012) Air motion sensing hairs of arthropods detect high frequencies at near-maximal mechanical efficiency. J R Soc Interface 9:1131–1143. doi:10.1098/rsif-2011-0690

Bechert DW, Bruse M, Hage W (2000) Experiments with three-dimensional riblets as an idealized model of shark skin. Exp Fluids 28:403–412. doi:10.1007/s003480050400

Bechert D, Bartenwerfer M (1989) The viscous flow on surfaces with longitudinal ribs. J Fluid Mech 206:105–129
Bitsch L, Olesen LH, Westergaard CH, Bruus H, Klank H, Kutter JP (2005) Micro particle-image velocimetry of bead suspensions and blood flows. Exp Fluids 39:505–511
Bleckmann H, Breithaupt T, Blickhan R, Tautz J (1991) The time course and frequency content of hydrodynamic events caused by moving fish, frogs, and crustaceans. J Comp Physiol A 168:749–757
Blickhan R, Krick C, Zehren D, Nachtigall W (1992) Generation of a vortex chain in the wake of a subundulatory swimmer. Naturwissenschaften 79:220–221
Boek ES, Padding JT, Anderson VJ, Briels WJ, Crawshaw JP (2006) Flow of entangled wormlike micellar fluids: mesoscopic simulations, rheology and μ-PIV experiments. J Non-Newton Fluid 146:11–21
Bown MR, Meinhart CD (2006) AC electroosmotic flow in a DNA concentrator. Microfluid Nanofluid 2:513–523. doi:10.1007/s10404-006-0097-4
Bown MR, MacInnes JM, RWK Allen (2006) Three-component micro-PIV using the continuity equation and a comparison of the performance with that of stereoscopic measurements. Exp Fluids 42:197–205. doi:10.1007/s00348-006-0229-3
Burgmann S, Van der Schoot N, Asbach C, Wartmann J, Lindken R (2011) Analysis of tracer particle characteristics for micro PIV in wall-bounded gas flows. La Houille Blanche 4:55–61. doi:10.1051/lhb/2011041
Casas J, Dangles O (2010) Physical ecology of fluid flow sensing in arthropods. Annu Rev Entomol 55:505–520. doi:10.1146/annurev-ento-112408-085342
Casas J, Liu C, Krijnen G (2013) Biomimetic flow sensors encyclopedia. Nanotechnology 2013:264–276
Casas J, Steinmann T, Dangles O (2008) The aerodynamic signature of running spiders. PLoS ONE 3:e2116. doi:10.1371/journal-pone-0002116
Casas J, Steinmann T, Krijnen G (2010) Why do insects have such a high density of flow-sensing hairs? Insights from the hydromechanics of biomimetic MEMS sensors. J R Soc Interface 7:1487–1495. doi:10.1098/rsif-2010-0093
Catton KB, Webster DR, Brown J, Yen J (2007) Quantitative analysis of tethered and free-swimming copepodid flow fields. J Exp Biol 210:299–310. doi:10.1242/jeb-02633
Chagnaud BP, Bleckmann H, Engelmann J (2006) Neural responses of goldfish lateral line afferents to vortex motions. J Exp Biol 209:327–342. doi:10.1242/jeb-01982
Cierpka C, Rossi M, Segura R, Mastrangelo F, Kähler CJ (2011) A comparative analysis of the uncertainty of astigmatism-μPTV, stereo-μPIV and μPIV. Exp Fluids 52:605–615. doi:10.1007/s00348-011-1075-5
Cummings EB (2000) An image processing and optimal nonlinear filtering technique for particle image velocimetry in microflows. Exp Fluids 29(1):S42–S50
Curtin DM, Newport DT, Davies MR (2006) Utilising μ-PIV and pressure measurements to determine the viscosity of a DNA solution in a microchannel. Exp Therm Fluid Sci 30:843–852
Dangles O, Steinmann T, Pierre D, Vannier F, Casas J (2008) Relative contributions of organ shape and receptor arrangement to the design of cricket's cercal system. J Comp Physiol A 194:653–663. doi:10.1007/s00359-008-0339-x
Denissenko P, Lukaschuk S, Breithaupt T (2007) The flow generated by an active olfactory system of the red swamp crayfish. J Exp Biol 210:4083–4091. doi:10.1242/jeb-008664
Devasenathipathy S, Santiago JG, Wereley ST, Meinhart CD, Takehara K (2003) Particle imaging techniques for microfabricated fluidic systems. Exp Fluids 34:504–514
Devasenathipathy S, Santiago JG (2003) Electrokinetic flow diagnostics. In: Breuer K (ed) Micro- and Nano-scale diagnostic techniques. Springer, New York, pp 113–144
Eichler C, Sattelmayer T (2011) Premixed flame flashback in wall boundary layers studied by long-distance micro-PIV. Exp Fluids 52:347–360. doi:10.1007/s00348-011-1226-8
Engelmann J, Hanke W, Bleckmann H (2002) Lateral line reception in still- and running water. J Comp Physiol A 188:513–526. doi:10.1007/s00359-002-0326-6

Fertin A, Casas J (2006) Efficiency of antlion trap construction. J Exp Biol 209:3510–3515. doi:10.1242/jeb-02401

Fertin A, Casas J (2007) Orientation towards prey in antlions: efficient use of wave propagation in sand. J Exp Biol 210:3337–3343. doi:10.1242/jeb-004473

García-Mayoral R, Jiménez J (2011) Drag reduction by riblets. Philos T Roy Soc A 369(1940):1412–1427. doi:10.1098/rsta-2010-0359

Gnatzy W, Heusslein R (1986) Digger wasp against crickets: I receptors involved in the antipredator strategies of the prey. Naturwissenschaften 73:212–215

Hanke W, Brücker C, Bleckmann H (2000) The ageing of the low-frequency water disturbances caused by swimming goldfish and its possible relevance to prey detection. J Exp Biol 203:1193–1200

Hanke W, Wieskotten S, Niesterok B, Miersch L, Witte M, Brede M, Leder A et al (2012) Hydrodynamic perception in pinnipeds. Note N Fl Mech Mul D 119:255–270. doi:10.1007/978-3-642-28302-4_16

Horiuchi K, Dutta P, Richards CD (2006) Experiment and simulation of mixed flows in a trapezoidal microchannel. Microfluid Nanofluid 3:347–358. doi:10.1007/s10404-006-0129-0

Humphrey JAC, Devarakonda R, Iglesias I, Barth FG (1993) Dynamics of arthropod filiform hairs: I mathematical modelling of the hair and air motions. Philos Trans R Soc Lond B Biol Sci 340:423–440

Inoué S, Spring KR (1997) Video microscopy. Plenum, Oxford

Jacobs GA, Miller JP, Aldworth Z (2008) Computational mechanisms of mechanosensory processing in the cricket. J Exp Biol 211:1819–1828. doi:10.1242/jeb-016402

Jin BJ, Yoo JY (2011) Visualization of droplet merging in microchannels using micro-PIV. Exp Fluids 52:235–245. doi:10.1007/s00348-011-1221-0

Kähler CJ, Scharnowski S, Cierpka C (2012) On the uncertainty of digital PIV and PTV near walls. Exp Fluids 52:1641–1656. doi:10.1007/s00348-012-1307-3

Kähler CJ, Scholz U, Ortmanns J (2006) Wall-shear-stress and near-wall turbulence measurements up to single pixel resolution by means of long-distance micro-PIV. Exp Fluids 41:327–341. doi:10.1007/s00348-006-0167-0

Kämper G, Kleindienst HU (1990) Oscillation of cricket sensory hairs in a low-frequency sound field. J Comp Physiol A 167:193–200

Kim MJ, Beskok A, Kihm KD (2002) Electro-osmosis-driven micro-channel flows: A comparative study of microscopic particle image velocimetry measurements and numerical simulations. Exp Fluids 33:170–180

Kim BJ, Yoon SY, Lee KH, Sung HJ (2008) Development of a microfluidic device for simultaneous mixing and pumping. Exp Fluids 46:85–95. doi:10.1007/s00348-008-0541-1

Kloosterman A, Poelma C, Westerweel J (2010) Flow rate estimation in large depth-of-field micro-PIV. Exp Fluids 50:1587–1599. doi:10.1007/s00348-010-1015-9

Klopsch C, Kuhlmann HC, Barth FG (2012) Airflow elicits a spider's jump towards airborne prey I Airflow around a flying blowfly. J R Soc Interface 9:2591–2602. doi:10.1098/rsif-2012-0186

Koehl MAR (2004) Biomechanics of microscopic appendages: functional shifts caused by changes in speed. J Biomech 37:789–795. doi:10.1016/j-jbiomech-2003-06-001

Krijnen G, Dijkstra M, van Baar J, Shankar S, Kuipers W, de Boer J, Altpeter D, Lammerink T, Wiegerink R (2006) MEMS based hair flow-sensors as model systems for acoustic perception studies. Nanotechnology 17:84–89. doi:10.1088/0957-4484/17/4/013

Kumagai T, Shimozawa T, Baba Y (1998) The shape of windreceptor hairs of cricket and cockroach. J Comp Physiol A 183:187–192

Landolfa G, Jacobs MA (1995) Direction sensitivity of the filiform hair population of the cricket cercal system. J Comp Physiol A 177:759–766

Lee SY, Wereley ST, Gui L, Qu W, Mudawar I (2002) Microchannel flow measurement using micro Particle Image Velocimetry. In: Proceedings of IMECE2002 ASME international mechanical engineering congress and exposition. New Orleans, Louisiana, 17–22 Nov 2002

Lee SJ, Kim BH, Lee JY (2009) Experimental study on the fluid mechanics of blood sucking in the proboscis of a female mosquito. J Biomech 42:857–864. doi:10.1016/j-jbiomech-2009-01-039

Lee SJ, Lee SH (2001) Flow field analysis of a turbulent boundary layer over a riblet surface. Exp Fluids 30:153–166. doi:10.1007/s003480000150

Li H, Olsen MG (2006) Micro PIV measurements of turbulent flow in square microchannels with hydraulic diameters from 200 μm to 640 μm. Int J Heat Fluid Flow 27:123–134. doi:10.1016/j-ijheatfluidflow-2005-02-003

Lima R, Wada S, Takeda M, Tsubota K, Yamaguchi T (2007) In vitro confocal micro-PIV measurements of blood flow in a square microchannel: the effect of the haematocrit on instantaneous velocity profiles. J Biomech 40:2752–2757. doi:10.1016/j-jbiomech-2007-01-012

Lindken R, Westerweel J, Wieneke B (2006) Stereoscopic micro particle image velocimetry. Exp Fluids 41:161–171. doi:10.1007/s00348-006-0154-5

Liu D, Garimella SV, Wereley ST (2005) Infrared micro-particle image velocimetry in silicon-based microdevices. Exp Fluids 38:385–392

Magal C, Dangles O, Caparroy P, Casas J (2006) Hair canopy of cricket sensory system tuned to predator signals. J Theor Biol 241:459–466. doi:10.1016/j-jtbi-2005-12-009

Mansoor I, Stoeber B (2010) PIV measurements of flow in drying polymer solutions during solvent casting. Exp Fluids 50:1409–1420. doi:10.1007/s00348-010-1000-3

McHenry MJ, Strother JA, van Netten SM (2008) Mechanical filtering by the boundary layer and fluid-structure interaction in the superficial neuromast of the fish lateral line system. J Comp Physiol A 194:795–810. doi:10.1007/s00359-008-0350-2

Mead KS (2003) Fine-scale patterns of odor encounter by the antennules of mantis shrimp tracking turbulent plumes in wave-affected and unidirectional flow. J Exp Biol 206:181–193. doi:10.1242/jeb-00063

Meinhart CD, Wereley ST, Gray MHB (2000) Volume illumination for two-dimensional particle image velocimetry. Meas Sci Technol 11:809–814

Meinhart CD, Wereley ST (2003) The theory of diffraction-limited resolution in microparticle image velocimetry. Meas Sci Technol 14:1047–1053

Meinhart CD, Wereley ST, Santiago JG (1999) PIV measurements of a microchannel flow. Exp Fluids 27:414–419

Mielnik MM (2003) Micro-PIV and its application to some BioMEMS related microfluidic flows. PHD Thesis. ISBN 82-471-6954-1

Mielnik MM, Saetran LR (2006) Selective seeding for micro-PIV. Exp Fluids 41(155–159):1007. doi:10/s00348-005-0103-8

Miller JP, Krueger S, Heys JJ, Gedeon T (2011) Quantitative characterization of the filiform mechanosensory hair array on the cricket cercus. PLoS ONE 6(11):e27873. doi:10.1371/journal-pone-0027873

Moghtaderi B, Shames I, Djenidi L (2006) Microfluidic characteristics of a multi-holed baffle plate micro-reactor. Int J Heat Fluid Fl 27:1069–1077. doi:10.1016/j-ijheatfluidflow-2006-01-008

Morley EL, Steinmann T, Casas J, Robert D (2012) Directional cues in Drosophila melanogaster audition: structure of acoustic flow and inter-antennal velocity differences. J Exp Biol 215:2405–2413. doi:10.1242/jeb-068940

Müller U, Heuvel B, Stamhuis E, Videler J (1997) Fish foot prints: morphology and energetics of the wake behind a continuously swimming mullet (*Chelon labrosus Risso*). J Exp Biol 200:2893–2906

Natrajan VK, Yamaguchi E, Christensen KT (2006) Statistical and structural similarities between micro and macroscale wall turbulence. Microfluid Nanofluid 3:89–100. doi:10.1007/s10404-006-0105-8

Nguyen CV, Carberry J, Fouras A (2011) Volumetric-correlation PIV to measure particle concentration and velocity of microflows. Exp Fluids 52:663–677. doi:10.1007/s00348-011-1087-1

Nguyen CV, Fouras A, Carberry J (2010) Improvement of measurement accuracy in micro PIV by image overlapping. Exp Fluids 49:701–712. doi:10.1007/s00348-010-0837-9

Park J, Choi C, Kihm K (2004) Optically sliced micro-PIV using confocal laser scanning microscopy (CLSM). Exp Fluids 37:105–119. doi:10.1007/s00348-004-0790-6

Patrick MJ, Chen CY, Frakes DH, Dur O, Pekkan K (2010) Cellular-level near-wall unsteadiness of high-hematocrit erythrocyte flow using confocal μPIV. Exp Fluids 50:887–904. doi:10.1007/s00348-010-0943-8

Pereira F, Lu J, Castaño-Graff E, Gharib M (2007) Microscale 3D flow mapping with μDDPIV. Exp Fluids 42:589–599. doi:10.1007/s00348-007-0267-5

Poelma C, Van der Heiden K, Hierck BP, Poelmann RE, Westerweel J (2010) Measurements of the wall shear stress distribution in the outflow tract of an embryonic chicken heart. J R Soc Interface 7:91–103. doi:10.1098/rsif-2009-0063

Raffel M, Willert C, Kompenhans J (1998) Particle image velocimetry, a practical guide. Springer, Berlin

Raghavan RV, Friend JR, Yeo LY (2009) Particle concentration via acoustically driven microcentrifugation: microPIV flow visualization and numerical modelling studies. Microfluidic Nanofluidic 8:73–84. doi:10.1007/s10404-009-0452-3

Reidenbach MA, George N, Koehl MAR (2008) Antennule morphology and flicking kinematics facilitate odor sampling by the spiny lobster, *Panulirus argus*. J Exp Biol 211:2849–2858. doi:10.1242/jeb-016394

Rossi M, Segura R, Cierpka C, Kähler CJ (2011) On the effect of particle image intensity and image preprocessing on the depth of correlation in micro-PIV. Exp Fluids 52(4):1063–1075. doi:10.1007/s00348-011-1194-z

Samarage CR, Carberry J, Hourigan K, Fouras A (2011) Optimisation of temporal averaging processes in PIV. Exp Fluids 52:617–631. doi:10.1007/s00348-011-1080-8

Santiago JG, Wereley ST, Meinhart CD, Beebe DJ, Adrian RJ (1998) A particle image velocimetry system for microfluidics. Exp Fluids 25:316–319. doi:10.1007/s003480050235

Sato Y, Hishida K (2006) Electrokinetic effects on motion of submicron particles in microchannel. Fluid Dyn Res 38:787–802. doi:10.1016/j-fluiddyn-2006-04-003

Sato Y, Inaba S, Hishida K, Maeda M (2003) Spatially averaged time-resolved particle-tracking velocimetry in microspace considering Brownian motion of submicron fluorescent particles. Exp Fluids 35:167–177. doi:10.1007/s00348-003-0643-8

Shimozawa T, Kanou M (1984) The aerodynamics and sensory physiology of range fractionation in the cercal filiform sensilla of the cricket *Gryllus bimaculatus*. J Comp Physiol A 155:495–505

Shimozawa T, Kumagai T, Baba Y (1998) Structural scaling and functional design of the cercal wind-receptor hairs of cricket. J Comp Physiol A 183:171–186

Shimozawa T, Murakami J, Kumagai T (2003) Cricket wind receptors: thermal noise for the highest sensitivity known. In: Barth FB, Humphrey JAC, Secomb T (eds) Sensors and sensing in biology and engineering. Springer, Berlin, pp 145–157

Snoeyink C, Wereley S (2013) A novel 3D3C particle tracking method suitable for microfluidic flow measurements. Exp Fluids 54:1453. doi:10.1007/s00348-012-1453-7

Stamhuis EJ, Videler JJ, Duren LAV, Mu UK (2002) Applying digital particle image velocimetry to animal-generated flows: traps, hurdles and cures in mapping steady and unsteady flows in Re regimes between 10–2 and 105. Exp Fluids 33:801–813. doi:10.1007/s00348-002-0520-x

Steinmann T, Casas J, Krijnen G, Dangles O (2006) Air-flow sensitive hairs: boundary layers in oscillatory flows around arthropod appendages. J Exp Biol 209:4398–4408. doi:10.1242/jeb-02506

Sterbing-D'Angelo S, Chadha M, Chiu C, Falk B, Xian W, Barcelo J, Zook JM et al (2011) Bat wing sensors support flight control. PNAS 108:11291–11296. doi:10.1073/pnas-1018740108

Sun C, Lee HC, Kao RX (2011) Diagnosis of oscillating pressure-driven flow in a microdiffuser using micro-PIV. Exp Fluids 52:23–35. doi:10.1007/s00348-011-1204-1

Tautz J, Markl H (1979) Caterpillars detect flying wasps by hairs sensitive to airborne vibration. Behav Ecol Sociobiol 4:101–110

Walsh PA, Walsh EJ, Davies MRD (2007) On the out-of-plane divergence of streamtubes in planar mini-scale flow focusing devices. Int J Heat Fluid Fl 28:44–53. doi:10.1016/j-ijheatfluidflow-2006-05-006

Wang B, Demuren A, Gyuricsko E, Hu H (2010) An experimental study of pulsed micro-flows pertinent to continuous subcutaneous insulin infusion therapy. Exp Fluids 51:65–74. doi:10.1007/s00348-010-1033-7

Wereley ST, Meinhart CD (2010) Recent advances in micro-particle image velocimetry. Annu Rev Fluid Mech 42:557–576. doi:10.1146/annurev-fluid-121108-145427

Windsor SP, Norris SE, Cameron SM, Mallinson GD, Montgomery JC (2010a) The flow fields involved in hydrodynamic imaging by blind Mexican cave fish (*Astyanax fasciatus*) Part I: open water and heading towards a wall. J Exp Biol 213:3819–3831. doi:10.1242/jeb-040741

Windsor SP, Norris SE, Cameron SM, Mallinson GD, Montgomery JC (2010b) The flow fields involved in hydrodynamic imaging by blind Mexican cave fish (*Astyanax fasciatus*), Part II: gliding parallel to a wall. J Exp Biol 213:3832–3842. doi:10.1242/jeb-040790

Yan DG, Yang C, Huang XY (2006) Effect of finite reservoir size on electroosmotic flow in microchannels. Microfluid Nanofluid 3:333–340. doi:10.1007/s10404-006-0135-2

Yang CT, Chuang HS (2005) Measurement of a microchamber flow by using a hybrid multiplexing holographic velocimetry. Exp Fluids 39:385–396. doi:10.1007/s00348-005-1022-4

Chapitre 3

Flux oscillatoires autour des cerques de grillons

Steinmann, T., Casas, J., Krijnen, G. & Dangles, O. 2006 Air-flow sensitive hairs : boundary layers in oscillatory flows around arthropod appendages. *Journal of Experimental Biology* 209, 4398408. (doi :10.1242/jeb.02506)

Résumé du chapitre

Ce chapitre présente une estimation des écoulements oscillatoires longitudinaux et transversaux autour des appendices antennaires des grillons et détaille une technique de meso-PIV stroboscopique. Nous y décrivons l'influence de la vitesse et de la fréquence de l'écoulement sur les paisseurs de couches limites, dans deux types de flux oscillatoires autour de cylindres qui simulent des cerques de 1 mm de diamètre.

Résultats

Nous montrons que les prédictions théoriques des profils de vitesses dans ces couches limites s'ajustent bien aux mesures, aussi bien pour les flux longitudinaux que transversaux. Il apparaît ainsi que l'écoulement transversal conduit à des vitesses de couches limites plus élevées que l'écoulement longitudinal et ceci sur une large gamme d'angles entre l'écoulement principal et le cylindre. Cette forte hétérogénéité spatiale des vitesses d'écoulements autour des structures suportrices est une source d'information riche pour les animaux possédant des senseurs d'écoulements renforcée par leur position sur un appendice.

Discussion

Nos résultats suggèrent que les grillons peuvent percevoir la provenance d'une source d'écoulement en positionnant leurs poils sensoriels tout autour de leurs cerques, profitant de ce fait de l'aspect tridimensionnel de l'écoulement perturbé. Nous concluons ce chapitre par une discussion sur les possibles implications de ces découvertes pour le design et la fabrication de senseurs biomimétiques.

The Journal of Experimental Biology 209, 4398-4408
Published by The Company of Biologists 2006
doi:10.1242/jeb.02506

Air-flow sensitive hairs: boundary layers in oscillatory flows around arthropod appendages

T. Steinmann[1], J. Casas[1,*], G. Krijnen[2] and O. Dangles[1]

[1]*Institut de Recherche sur la Biologie de l'Insecte–UMR CNRS 6035, Faculté des Sciences et Techniques, Université François Rabelais, Parc de Grandmont Avenue Monge, 37200 Tours, France and* [2]*MESA+ Research Institute, Transducers Science and Technology group Faculty of Electrical Engineering, University of Twente, PO Box 217, 7500 AE Enschede, The Netherlands*

*Author for correspondence (e-mail: jerome.casas@univ-tours.fr)

Accepted 22 August 2006

Summary

The aim of this work is to characterize the boundary layer over small appendages in insects in longitudinal and transverse oscillatory flows. The problem of immediate interest is the early warning system in crickets perceiving flying predators using air-flow-sensitive hairs on cerci, two long appendages at their rear. We studied both types of oscillatory flows around small cylinders using stroboscopic micro-particle image velocimetry as a function of flow velocity and frequency. Theoretical predictions are well fulfilled for both longitudinal and transverse flows. Transverse flow leads to higher velocities than longitudinal flow in the boundary layer over a large range of angles between flow and cylinder. The strong spatial heterogeneity of flow velocities around filiform-shaped appendages is a rich source of information for different flow-sensing animals. Our results suggest that crickets could perceive the direction of incoming danger by having air-flow-sensitive hairs positioned around their entire cerci. Implications for biomimetic flow-sensing MEMS are also presented.

Key words: viscous boundary layer, hair biomechanics, cercal system, cricket, flow sensing, sensor design.

Introduction

Boundary flows have been studied in a biological context for several decades, including fish swimming (Anderson et al., 2001), crustacean and moth olfaction (Koehl et al., 2001; Stacey, 2002) and fluid sensing in arthropods in air and water (Humphrey et al., 1993; Barth et al., 1993; Devarakonda et al., 1996; Humphrey et al., 2003a; Humphrey et al., 2003b). Air-flow sensing using filiform hairs partially immersed in the boundary layer around the body has been extensively studied in arthropods, especially in spiders and crickets (Shimozawa and Kanou, 1984; Humphrey and Devarakonda, 1993; Barth et al., 1993). Filiform hairs are among the most sensitive biological sensors in the animal kingdom (Shimozawa et al., 2003). These outstanding sensitive structures are used to detect approaching animals, in particular the oscillatory signals produced by the wing beats of prey and predators (Tautz and Markl, 1979; Barth et al., 1993; Gnatzy and Heusslein, 1986). According to the body of work performed to date, a variation of hair length is assumed to allow spiders and crickets to fractionate both the intensity and frequency range of an air flow signal.

The biomechanics of hair movement in an oscillating fluid has stimulated extensive research during the last few decades, and several models have been developed (Fletcher, 1978; Shimozawa and Kanou, 1984; Humphrey and Devarakonda, 1993). In all these models, a hair is defined as an inverted pendulum with a rigid shaft supported by a spring at its base. This mechanical model can be described by four parameters (Shimozawa et al., 2003; Humphrey et al., 2003): the moment of inertia that represents the mass distribution along the hair shaft; the spring stiffness which provides the restoring torque towards the resting position; the torsional resistance within the hair base; and the coupling resistance between the hair shaft and the air (see Appendix).

An important assumption of these models concerns the nature of the oscillating flow in the boundary layer over the cerci, as it greatly impacts the movement of hairs of different lengths. The boundary layer has been theoretically predicted and often experimentally confirmed on large structures for both longitudinal and transverse oscillatory flows (Raney et al., 1954; Bertelsen et al., 1973; Williamson, 1985; Obasaju et al., 1988; Justesen, 1991; Tatsuno and Bearman, 1990). These studies were, however, conducted for Reynolds and Strouhal numbers very different from those of biological relevance, with the exception of the studies by Holtsmark et al. (Holtsmark et al., 1954) and Wang (Wang, 1968). While the longitudinal flow

over arthropod appendages has been thoroughly characterised by Barth et al. (Barth et al., 1993), the transverse flow has been much less studied. Barth et al. characterized the boundary layer in longitudinal and transverse flows using laser Doppler anemometry (LDA) over a spider leg (Barth et al., 1993). However, only a few measurements were carried out and they were limited by the 300 μm resolution of the LDA system, hence missing out the region nearest to the substrate. Moreover, the influence of the source orientation on the boundary layer was not investigated.

The aim of the present work is to characterize, in a systematic way in terms of phase and frequency, the boundary layer over small antenna-like appendages in crickets in an oscillatory flow for both longitudinal and transverse flows. Situated at the rear end of crickets, these appendages of conical shape, called cerci, are equipped with hundreds of filiform hairs of varying length. We use stroboscopic micro-particle image velocimetry (μPIV) to carry out measurements on artificial cerci placed in oscillatory flows of varying frequencies and orientations with respect to the source. Thus, our work deals with the flow around a cricket cercus, and not with the flow around a single hair. Our results are compared to existing models for longitudinal and transverse flows. We discuss the implications of our findings in terms of hair length and angular hair location around the cercus to extract as much information as possible. The perspectives are in terms of cricket perception of attacking predators and in terms of biomimetic Micro-Electric-Mechanical Systems (MEMS) flow sensors.

Materials and methods

Air flow modelling around a cylinder

The signal emitted by a flying predator can be approximated by a spherical point source radiating an isotropic sinusoidal wave in all directions (Tautz and Markl, 1979) [see Sueur et al. (Sueur et al., 2005) for finer distinctions in the near-field region]. The far-field velocity of air particles is described by the equation:

$$U_\infty(t) = U_0 \sin(\omega t)\,, \tag{1}$$

where U_0 is the flow oscillation amplitude, and ω is the angular frequency (rad s^{-1}), with $\omega=2\pi f$, f being the frequency of flow oscillations (s^{-1}). A signal impacting the cylinder from any angle can be decomposed into longitudinal (V_l), radial (V_r) and circumferential (V_θ) components (Fig. 1A).

We first consider a flow oscillating parallel to a cylinder (longitudinal flow). To avoid end effects, the length of the cylinder (L) is supposed to be much larger than its diameter, D (L>10D). Under these conditions, the fluid velocity at time (t) can be expressed as a function of the distance to the cylinder (y) as follows:

$$V_1(t,y) = U_0 \left(\sin(\omega t) - \frac{\sin(\omega t-\beta y)e^{-\beta y}}{\left(1+\frac{2y}{D}\right)^{\frac{1}{2}}} \right), \tag{2}$$

where $\beta=(\omega/2\nu_{air})^{\frac{1}{2}}$ is the border effect factor (m^{-1}), $\nu_{air}=\mu_{air}/\rho_{air}$ is the kinematic viscosity of the fluid ($m^2\ s^{-1}$), μ_{air} is the dynamic viscosity of the fluid (Ns m^{-2}), ρ_{air} is the density of the fluid (kg m^{-3}) and D is the diameter of the cylinder (m) (Humphrey and Devarakonda, 1993).

Due to the viscosity effect, there is a phase displacement, φ, with the distance from the cylinder:

$$\varphi(y) = \arctan\left(\frac{\exp(-\beta y)\sin(\beta y)}{\sqrt{\frac{D+2y}{D}} - \exp(-\beta y)\cos(\beta y)} \right). \tag{3}$$

Second, we consider the flow oscillating perpendicular to a cylinder, theoretically described by Holtsmark et al. (Holtsmark et al., 1954). We compared our results to the first degree of this analytical approximation as we are interested in a simple semi-analytical solution of the Navier Stokes equation for modelling hair movement. This first-order solution corresponds to the oscillatory part of the solution. The circumferential component of the flow velocity, V_θ, triggers hair defection. The cylinder represents a cercus, not a hair on a cercus. This circumferential component is:

$$V_0(\theta,y,t) = -U_0 \sin\theta \left\{ -\left(1 - \frac{(D/2)^2}{(y+D/2)^2} C_r\right) \sin\omega t + (X_r - Zr)\sin\omega t + \left(X_i - Z_i + \frac{(D/2)^2}{(y+D/2)^2} C_i\right)\cos\omega t \right\}, \tag{4}$$

with

$$X = \frac{H_0(\epsilon y)}{H_0\left(\epsilon\frac{D}{2}\right)},\ Y = \frac{H_1(\epsilon y)}{H_0\left(\epsilon\frac{D}{2}\right)},\ Z = \frac{H_2(\epsilon y)}{H_0\left(\epsilon\frac{D}{2}\right)},\ C = Z\left(\frac{D}{2}\right). \tag{5}$$

X, Y, Z, C are complex numbers with X_i, Y_i, Z_i, C_i and X_r, Y_r, Z_r, C_r being their imaginary and real parts, respectively. H_n is the Hankel function of the first kind (Abramowitz and Stegun, 1965), y is the distance to the substrate (m), D is the diameter of the cylinder (m), $\epsilon=[i(\omega/\nu)]^{\frac{1}{2}}$, and θ is the angle between the cylinder and the flow (rad). The radial component of the flow, which is parallel to the hair and has no influence on its motion, is expressed as follows:

$$V_r(\theta,r,t) = U_0 \cos\theta \left\{ -\left(1 + \frac{(D/2)^2}{(y+D/2)^2} C_r\right) \sin\omega t + (X_r + Z_r)\sin\omega t - \left(X_i + Z_i - \frac{(D/2)^2}{(y+D/2)^2} C_i\right)\cos\omega t \right\}, \tag{6}$$

Eqns 4 and 6 show the existence of a phase lag δ between V_r and V_θ. This phase lag δ is given by:

$$\tan(\sigma-\delta) = \frac{-X_i + Z_i - \frac{(D/2)^2}{r^2} C_i}{1 - \frac{(D/2)^2}{r^2} C_r - X_r + Z_r}, \tag{7}$$

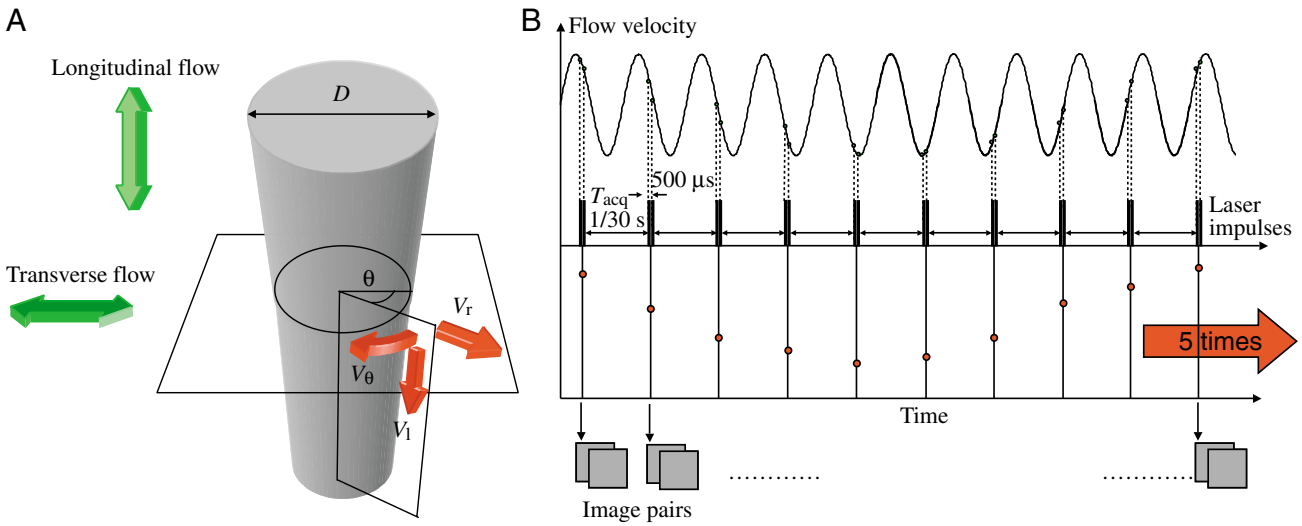

Fig. 1. (A) Longitudinal, circumferential and radial components of an oscillating flow acting on a hair perpendicular to a cylindrical substrate. (B) Principle of stroboscopic measurement of a flow oscillating at high frequency with a low-frequency sampling device. In this example, we take pairs of images (separated by 500 µs) at a frequency of 30 Hz of a flow oscillating at 33 Hz. The pseudo time increment is 3 ms and we need 10 pairs to sample a full period of the flow oscillations. We repeat this procedure five times and proceed then to a phase average.

σ being given by:

$$\tan(\sigma) = \frac{X_i + Z_i - \frac{(D/2)^2}{r^2} C_i}{X_r + Z_r - 1 - \frac{(D/2)^2}{r^2} C_r} \cdot \quad (8)$$

Therefore, the fluid far from the cylinder oscillates along a straight line whereas the fluid near the cylinder oscillates in an elliptic fashion (Holtsmark et al., 1954). We solved numerically the phase advance of V_θ with distance from the cylinder.

Experimental set-up

We used cylinders (D=1 mm, L=40 mm) made of steel, of identical base diameter but of a longer length than in real animals. This enabled us to avoid boundary effect at both extremities. These cylinders were stiff. They were held by a micromanipulator placed in a way to avoid vibrations produced by the loudspeakers.

Flow measurements were performed using two-dimensional PIV. It is now well established that PIV and LDA techniques are suitable for acoustical measurement (Campbell et al., 2000). Recently, these techniques have been used to characterize the laminar acoustic viscous boundary layer and the acoustic streaming in tube and wave guide (Castrejón-Pita et al., 2006). Artificial cylinders were placed in a cylindrical glass container (L=200 mm, D=100 mm), with two loudspeakers (40 W, 5 Ω; SP 45/4; Monacor, Brême, Germany) at both ends, connected to a sinusoidal signal generator (2 MHz; TG 230; Thurlby-Thandar, Huntingdon, Cambs, UK).

We checked for signal integrity at all frequencies in the centre of the container using an LDA system (FlowLite 1D 65X90; Dantec Dynamics A/S, Skovlunde, Denmark). At the central point, $U(\omega t)=U_0\sin(\omega t)$, with amplitude U_0=35 mm s^{-1}. The loudspeaker delivered good signals from 25 Hz upwards. Measurements were conducted at 25°C corresponding to an air kinematic viscosity, $\nu_{air}=1.56\times10^{-5}$ m^2 s^{-1}. The air inside the sealed glass box was seeded with 0.2 µm oil particles (Di-Ethyl-Hexyl-Sebacat, 0.5 L; TPAS, Dresden, Germany) using an aerosol generator (ATM 230; ACIL, Chatou, France). The laser of the PIV illuminated the flow produced by the wave through the glass (NewWave Research Solo PIV 2, 532 nm, 30 mJ, Nd:YAG, dual pulsed; Dantec Dynamics A/S). The laser sheet (width=17 mm, thickness at focus point=50 µm) was operated at low power (3 mJ at 532 nm) to minimize glare. A target area was then imaged onto the CCD array of a digital camera (Photron FastCam X1280 PCI 4K) using a stereomicroscope (LEICA M13, X10) that produced a 2×2 mm window around the substrate. In order to measure high-frequency and low-amplitude oscillatory movements, we set the CCD to capture a light pulse at 30 Hz in separate image frames every 500 µs, with a laser impulsion length of 4±1 ns (Fig. 1B). To reduce undesirable reflections, the cylinders were covered with fluorescent paint, which re-emits the light of the laser at another wavelength. We used a narrow band filter working at the laser wavelength λ=532 nm placed under the camera. Measurements were conducted for velocities U_0=35 mm s^{-1}, within the range of airborne vibration amplitude generated 10 cm in front of a flying predatory wasp (Tautz and Markl, 1979). Flow frequencies ranged from 30 to 180 Hz. For a cylinder diameter of 1 mm, the corresponding peak Reynolds number (Re) is 1.6 and the Strouhal numbers (St) range from 2.7 to 16.2.

Stroboscopic measurements

We used the stroboscopic principle to sample high-frequency sinusoidal signals (ranging from 30 Hz to 180 Hz)

with a PIV system limited to 30 Hz (Schram and Riethmuller, 2001). As explained in Fig. 1B, this consists of sampling a signal of period f_{flow} with a frequency (f_{acq}) slightly lower than a sub-multiple of the signal frequency. This technique gives us the following pseudo sampling time interval (t_{strob}):

$$t_{strob} = \text{mod}\,(T_{acq}, T_{flow})\,, \quad (9)$$

where T_{acq} is the inverse of the PIV sampling frequency, and T_{flow} is the inverse of the signal frequency. The number of sampling points, N, covering a full period of the signal is given by:

$$N = (T_{flow} / t_{strob})\,. \quad (10)$$

A numerical example is given in the legend of Fig. 1B. In a second example, let us assume we sample a 119 Hz signal at 30 Hz. The pseudo time interval is then t_{strob}=0.28 ms, corresponding to a phase of ωt_{strob}=0.2 rad=0.06π rad, giving N=33 sampling points per full period of signal. We repeated this measurement five times and proceeded to a phase average on the basis of 50 and 150 pair images in the first and second example, respectively. The estimation of the signal phase φ corresponding to each sample point is obtained through inference, not measurements. The known far-field velocity U_∞ and local velocity U_0 are used with the relationship φ=arcsin(U_∞/U_0).

Data acquisition

Flow measurements for both longitudinal and transverse flows were conducted for six frequencies (30, 60, 90, 120, 150 and 180 Hz). The two-dimensional (2-D) velocity vector fields were derived from sub-sections of the target area of the particle-seeded flow by measuring the movement of particles between two light pulses. Images were divided into small subsections (width, 70 μm; resolution, 32×32 pixels; covering rate, 50%) and cross-correlated with each other using a flow map software (Flow Manager 4.4; Dantec Dynamics A/S). The correlation produced a signal peak, identifying the common particle displacement. An accurate measurement of the displacement (and thus of the velocity) was achieved with sub-pixel interpolation.

We averaged five vector fields for each phase of the signal. For longitudinal flows, velocity profiles were obtained by averaging point measurements over 2 mm along the cylinder. For transverse flows, the velocity profile was extracted at five different angles (90, 60, 45, 30 and 15°) but not averaged along the length of the cylinder.

With subsection windows of 32×32 pixels, it is possible to obtain valid measurements down to 0.1 pixels (Mayinger and Feldman, 2001). In our set-up, this corresponds to 0.3 mm s^{-1}, equivalent to 1% of U_0.

Results

Frequency

Fig. 2 shows the frequency dependence of the velocity around a cylinder in transverse flow. It represents the

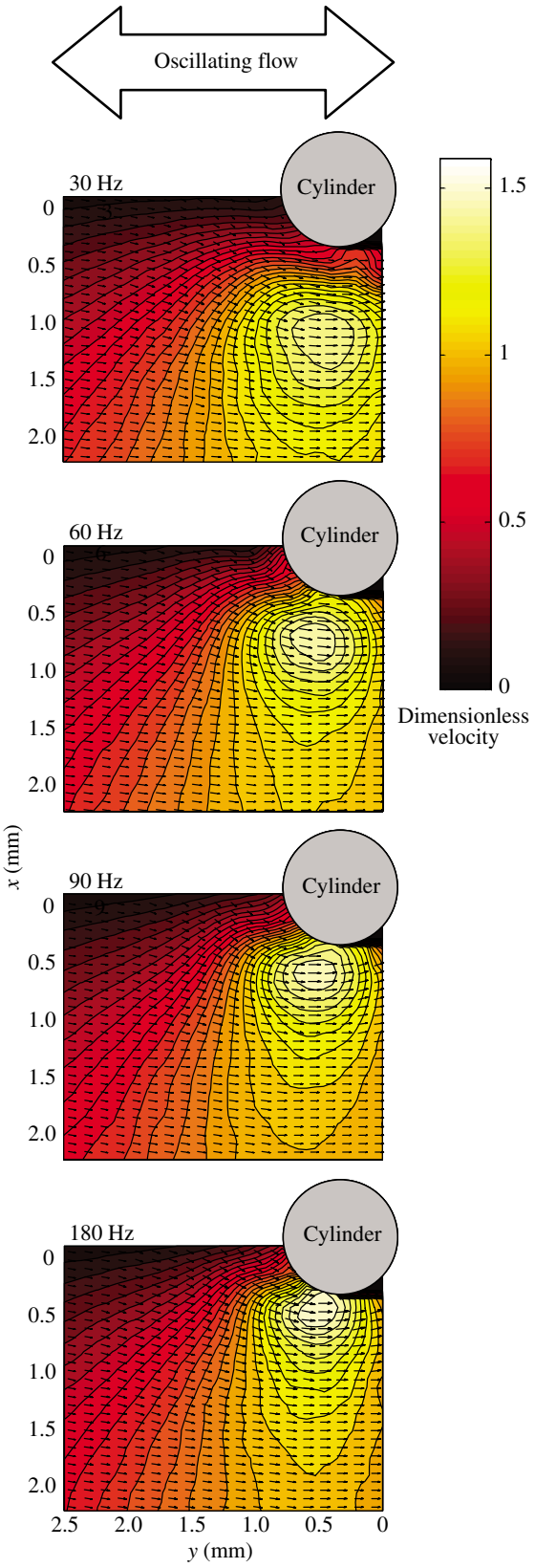

Fig. 2. Vector field of velocity amplitude around a cylinder of 1 mm diameter at four frequencies in transverse flow. Vectors are of constant length.

amplitude of the flow, i.e. the difference between the maximum velocity fields [measured at $\omega t=(\pi/2)$] and the minimum velocity fields [measured at $\omega t=-(\pi/2)$]. The boundary layer thickness around the cylinder is significantly reduced at high frequencies. From these measurements, we extracted the velocity profiles for five different circumferential θ angles (90, 60, 45, 30 and 15°) (Fig. 3), an angle θ of 0° being directly upwind. As predicted by theory, the flow velocity profiles vary as a function of the sine of this angle. At 30°, the curvature effects of the cylinder produce a noticeable peak in flow velocity, increasing at higher angles and levelling off at 90°. Maximal velocities also increase with flow frequency, from $1.4U_0$ at 30 Hz to $1.6U_0$ at 180 Hz.

In longitudinal flow, we measured significant changes in fluid velocity at a short distance above the cylinder (<0.5 mm) as a function of flow oscillation frequency (Fig. 3, grey line). For longitudinal flow, the velocity profiles match nicely with those predicted by theory both in terms of amplitude and distance of the maximal velocity above the cylinder. Measurements very close (70 μm) to the surface of the cylinder are ~50% higher than theoretical values. We do not know if it is due to a PIV uncertainty or a failing of the theory. The high light intensity in the focalisation part of the laser light sheet, which is then very near to the substrate, may heat the surface, leading to an increase of velocity (Brownian motion). The thickness of the boundary layer decreases with increasing flow frequency, as predicted by the theory.

The 90° and the 60° transverse flows produce higher velocities than the longitudinal one throughout the entire profile. This pattern is also observed for the 45° transverse flow but only within the first 1000 μm above the cylinder for a 30 Hz flow and within the first 700 μm for a 180 Hz flow. For all frequencies, the 30° and the 15° profiles are smaller than the longitudinal one, and the 45° profile is greater than the longitudinal one along the first 300 μm.

Phasing

Fig. 4 represents the temporal evolution of the velocity field around a cylinder in a transverse flow. The circulating zones typical of oscillatory flows are clearly visible. Particles trapped in this region rotate in antiphase on both sides of the cylinder (red arrows in Fig. 4). This is due to the interplay between their circumferential components, which are moving in phase, and their radial components, which are out of phase by $\pi/2$. We extracted the velocity profiles of the circumferential component of flow around the cylinder from the data represented in Fig. 4 and plotted them in Fig. 5. Hair movement, which we did not measure, is induced by this component. The phase is constant for each value of θ and is a function of y. Fig. 5 also shows the evolution of the velocity profile over a cylinder with time for a longitudinal flow. We obtained a good agreement between theory and measurement except at very small distances (<90 μm).

The phase displacement with distance from the cylinder is represented in Fig. 6. The fit with the theory is good. Phase displacement goes from $\pi/4$ close to the surface to 0 rad at the largest distances. There is therefore a phase advancement in the boundary layer. While the observed changes in amplitude between transverse and longitudinal flows are important, there is almost no phase lag between them.

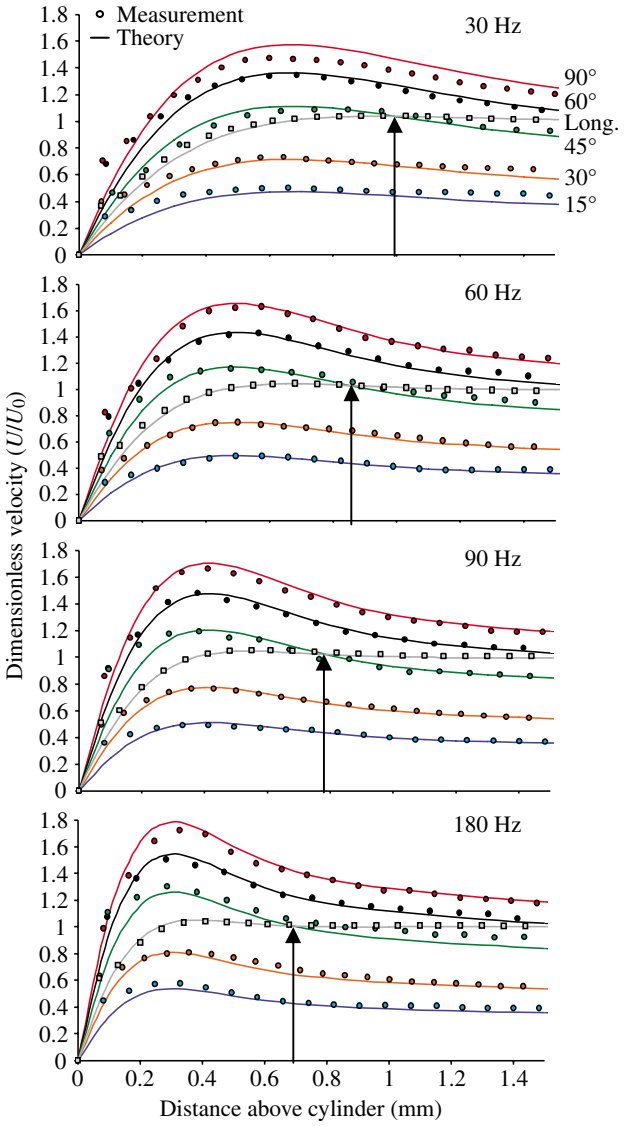

Fig. 3. Velocity profiles for longitudinal and transverse flows at four frequencies around a cylinder of 1 mm diameter. Holtsmark solutions for transverse flow (lines) and particle image velocimetry (PIV) measurements (points) at angles of 90° (red circles), 60° (black circles), 45° (green circles), 30° (orange circles) and 15° (blue circles). Humphrey solution for longitudinal flow (grey line) and corresponding PIV measurement (squares). The distance above the cylinder at which both components are equal is highlighted (arrow).

Discussion

Measurements versus models

This PIV study is one of the most comprehensive regarding flow velocities around cylinders of small diameters in

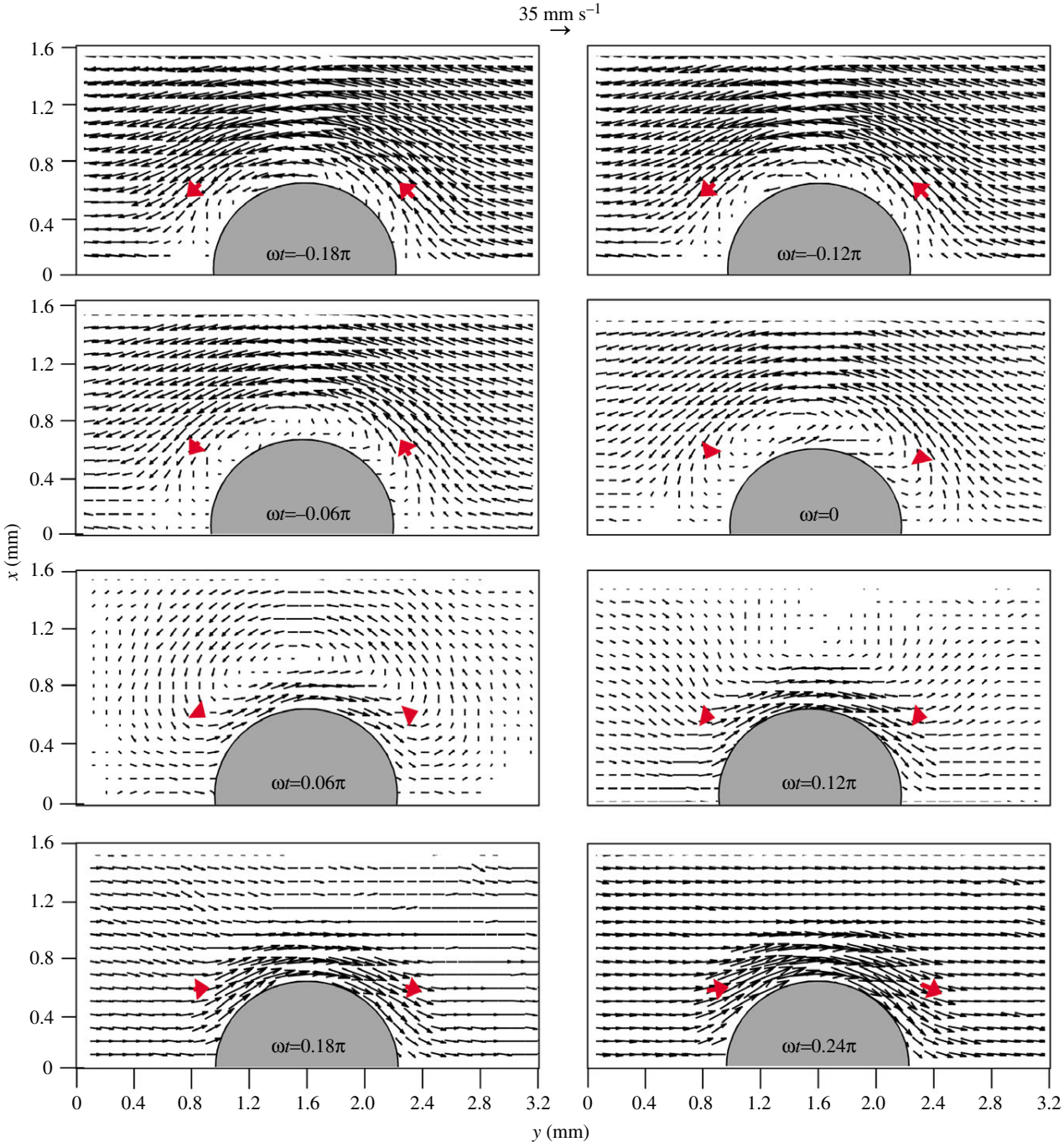

Fig. 4. Temporal evolution of the velocity field around a cylinder of 1 mm diameter in a 120 Hz transverse flow. The phase interval separating each vector field is 0.06 rad.

oscillatory flows at low *Re*. We could not use the approximation developed by Wang (Wang, 1968) and later used by Humphrey and Devarakonda [equation A.2.1 (Humphrey et al., 1993)] as the conditions for its application [$Re \times St \gg 1$ and $(Re/St) \ll 1$] did not apply for the full range of values we were interested in, particularly for the low frequencies [$Re \times St=3$ and $(Re/St)=0.4$ for $f=30$ Hz]. By contrast, the Holtsmark et al. model (Holtsmark et al., 1954) gives meaningful predictions over the full range of parameters. An exploration of the predictions of these different models indicates that the model of Wang, and its refinement by Humphrey et al., is valid from 180 Hz down to 90 Hz, but deteriorates at lower frequencies. As mentioned before, we compared the transverse measurement to the first approximation solution. The streaming motion to the hair movement was confirmed by visual examination of the film

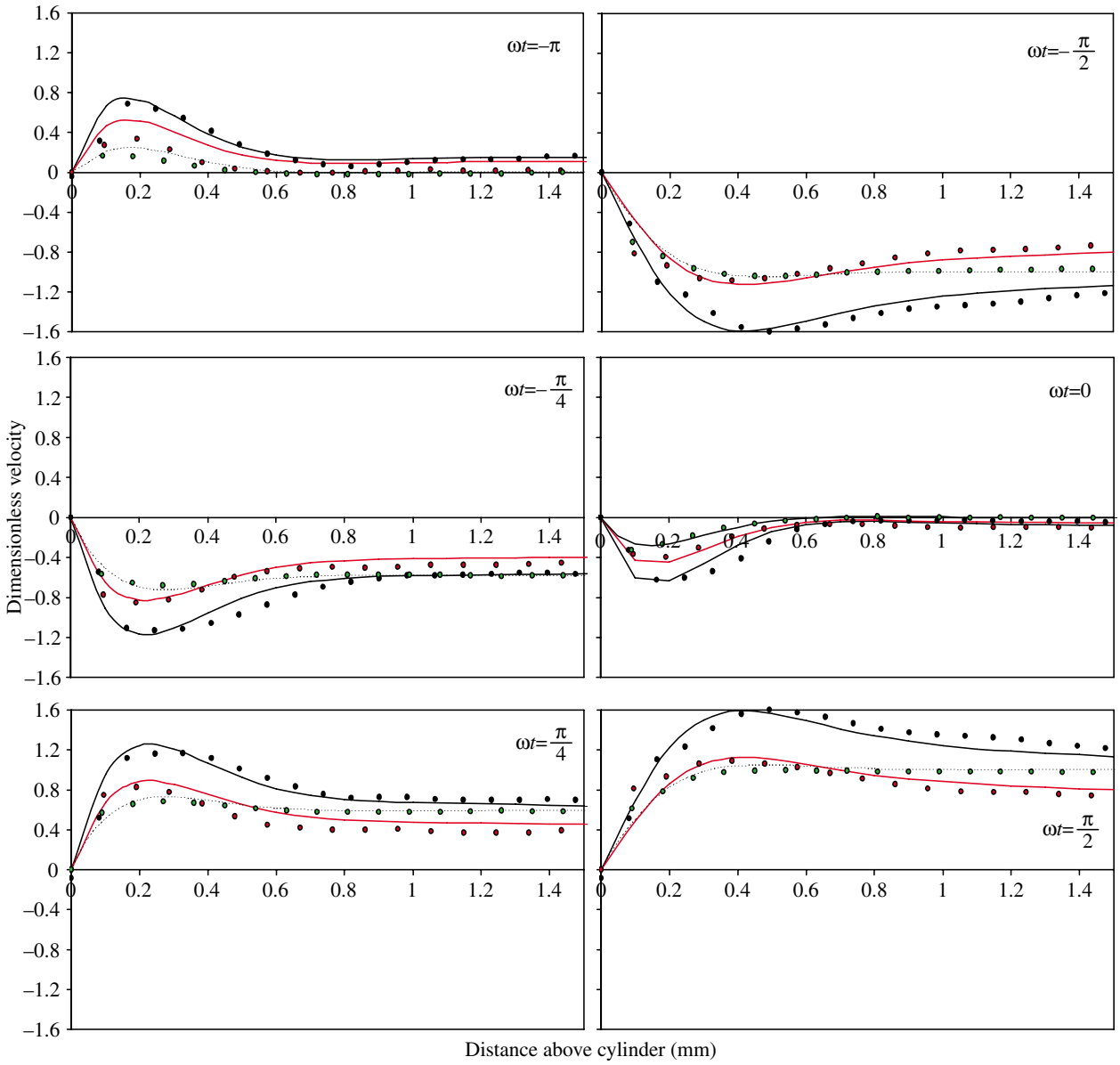

Fig. 5. Temporal evolution of the instantaneous velocity in longitudinal and transverse flows over a cylinder of 1 mm diameter at 120 Hz. Humphrey solution for longitudinal flow (dotted line) and particle image velocimetry (PIV) measurement (grey circles). Holtsmark solutions for transverse flow (lines) and PIV measurements (points) at angles of 90° (red circles) and 45° (black circles).

taken with the PIV camera, but we neglected it as its amplitude was estimated to be 2.5% of the amplitude of the far-field oscillatory flow (Holtsmark et al., 1954; Raney et al., 1954).

The match between model predictions for both longitudinal and transverse flows and experimental data is very good, except for the smallest measured distance from the cylinder. Reasons for this lack of fit may originate either from a breakdown of the many approximations made in the models or from experimental errors, as their weight is large at those small velocities. The slightest misalignment of the thin laser sheet with the tiny cylinder can indeed produce such a mismatch. Our results confirm the pioneer results obtained by Barth et al. (Barth et al., 1993) regarding the relative velocities in longitudinal and transverse flows around spider legs. In particular, these authors observed that velocities would be stronger in transverse flow than in longitudinal flow. We observed higher velocities for transverse flow as long as the θ angle is between 60° and 120°. As was previously predicted (Humphrey et al., 1993), the profiles are also quite different, transverse flows producing local velocities up to 1.6 times stronger than the far-field values. By contrast, the maximal amplification of the far-field value is only 1.1 for longitudinal flows.

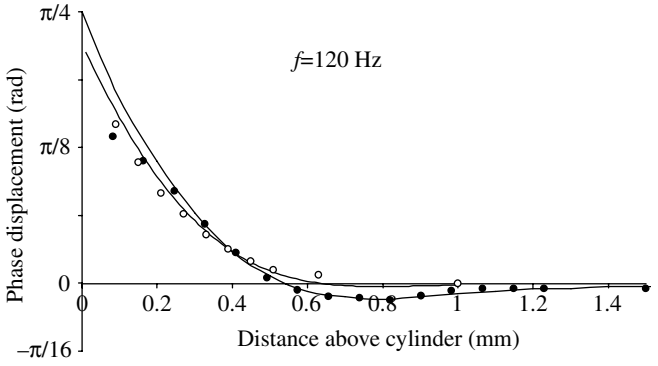

Fig. 6. Phase shift between far field and boundary layer flow as a function of distance from the cylinder at 120 Hz. Analytical solution (Eqn 3) of the phase displacement (dotted line) and particle image velocimetry (PIV) measurement (open circles) for a longitudinal flow. Numerical solution (line) and PIV measurement (filled circles) for a transverse flow at a circumferential angle of 90°.

Implications for air-flow sensing in animals and MEMS

The strong spatial heterogeneity of flow velocities around appendages in transverse flow is a rich source of information for flow-sensing animals, in particular for those using flow-sensing hairs. A single hair submitted to an air flow from any angle will experience longitudinal and transverse forces over its entire length. The relative importance of these air flow components will be a function of circumferential location θ and hair length. We distinguish between long (1500 μm) and short (300 μm) hairs in the following discussion, as they are known to differ in best-tuned frequencies and represent two extreme situations. We computed the drag torque (see Appendix) in order to understand the relative influence of the longitudinal and transverse components of any flow on hairs of different lengths (Fig. 7), the virtual mass torque being almost negligible. Long hairs experience boundary layer effects only on their bottom portion and are submitted to the far-field velocity over most of their remaining length. These far-field velocities decline with decreasing angle θ, so that the transverse drag torque acting on a long hair will also decline with decreasing angle and become inferior to the longitudinal one for an angle θ of 57°. Short hairs experiencing similar air flow are totally immersed in the boundary layer. The decline of transverse flow velocity with the angle is lower in the boundary layer, so that transverse drag torque will be higher than longitudinal drag torque over a larger range of θ angles, down to 37°.

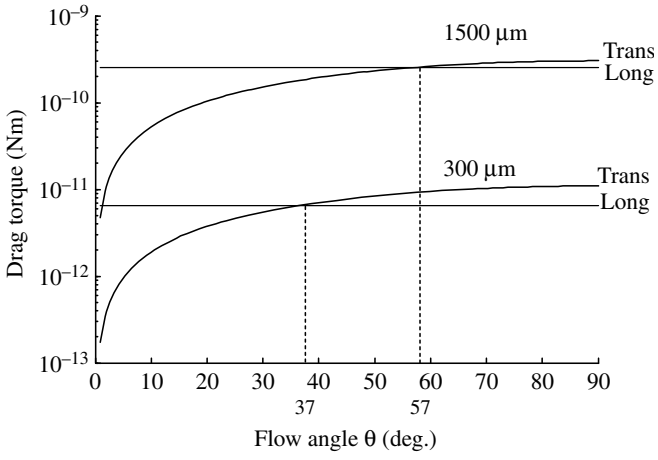

Fig. 7. Viscous drag torque for short and long hairs in transverse and longitudinal flows. Flow oscillations, f=120 Hz; flow velocity, V=35 mm s^{-1}; hair lengths, 1500 μm and 300 μm.

What are the consequences in terms of hair sensitivity as measured by the maximal amplitude of hair displacement? Whatever its position around the cylinder, a long hair shows high displacement values at low frequency. Hair displacement amplitude sharply declines from 80 Hz and reaches a negligible value at frequencies above 500 Hz (Fig. 8A). By contrast, short hairs do not show such strong frequency-dependent behaviour over the values of interest (Fig. 8B). For the air velocity and frequency used in Figs 7 and 8, the influence of the transverse component is greater than that of the longitudinal component in the angle interval of [90°, 50°] for long hairs. This interval is further extended to [90°, 37°] for short hairs. Thus, short hairs are more sensitive than long hairs to the transverse component of flow from almost any direction. This result

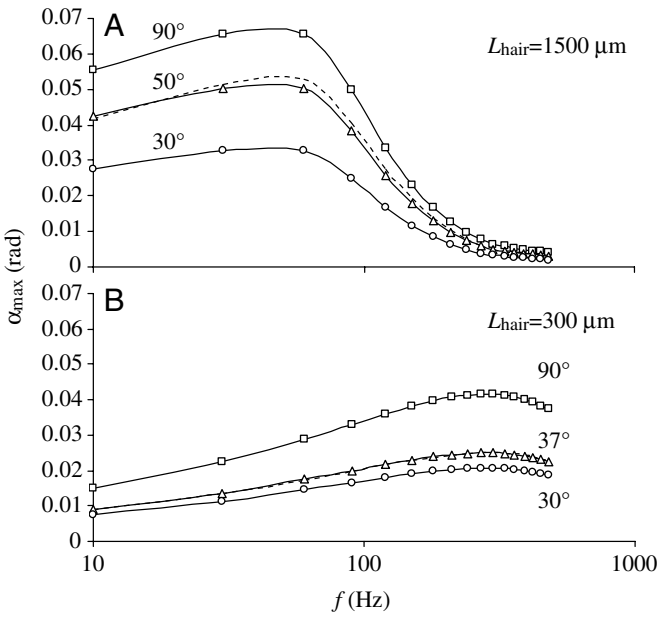

Fig. 8. Maximal hair displacement as a function of flow frequency (f_{flow}) and circumferential angle (θ). (A) Maximal hair displacement of long hairs positioned on a cylinder of 1 mm diameter, for attack angles of 90° (squares, transverse flow), 50° (triangles), 30° (circles) and 0° (broken line, longitudinal flow). (B) Maximal hair displacement of short hairs positioned on a cylinder of 1 mm diameter, for impact angles of 90° (squares, transverse flow), 37° (triangles), 30° (circles) and 0° (dotted line, longitudinal flow). For both computations, U_0=35 mm s^{-1}.

makes sense physically, as the largest differences between longitudinal and transverse flows are in the boundary layer, in which the small hairs are totally immersed. These considerations were tested at other frequencies (30 Hz and 180 Hz) and were found to be quite robust.

Our results have important implications for hair canopy arrangement in arthropods using air flow to sense prey or predators. First and foremost, the spatially heterogeneous information provided by a transverse flow around a cylinder implies that hairs should be placed all around a cylinder, maximising the chances to perceive a source coming from any angle. Indeed, an isotropic distribution of hairs ensures that some hair will always be perpendicular to the flow, thereby experiencing the smallest possible boundary layer, and hence the largest possible displacement. For similar reasons, hairs of the same length vibrate with different amplitudes around a cylinder depending on their radial location. Arthropods may therefore perceive the direction of an incoming air flow in a differentiated manner using the radial distribution of the canopy, very much as their hair lengths act as a Fourier transform for frequency decomposition through different natural frequencies. This directionality filter may help crickets to identify the direction of the approaching source.

The rich content of information in the spatially heterogeneous flow around a cylinder has escaped the attention of previous workers, who cited the great computational advantages of considering a cylinder of low curvature as a plate for the purpose of computation of hair movement. We now need to revisit both the hair biomechanical models and the neurocomputational models of danger perception in crickets on the basis of these results. Cricket air flow sensors have recently been a source of inspiration to build artificial air flow sensors (Dijkstra et al., 2005). Design guidelines for building flow-sensing MEMS arrays were also based on biomimetic ideas borrowed from the cricket's cerci. A spatial arrangement of MEMS hairs with a large range of angles relative to flow direction on a dedicated platform would increase the sensitivity of such sensors by a large margin. Such design could represent a major advance to the actual mounting, on a horizontal plate, of MEMS hairs restricted to measuring longitudinal flows. This is however not a trivial task in MEMS fabrication.

List of symbols

d	hair diameter
D	cylinder diameter
f_{acq}	PIV sampling frequency
f_{flow}	oscillating air flow frequency
$F_D(y,t)$	drag per hair unit length acting at height y
$F_{VM}(y,t)$	added mass force per hair unit length acting at height y
H_n	Hankel function of the first kind
I	moment of inertia
I_h	hair moment of inertia
I_{VM}	moment of inertia of the added mass stagnating around and moving with the hair
L	cylinder length
$L(t)$	angular momentum
L_{hair}	hair length
N	number of sampling points
R	damping factor including frictional terms at the hair base
R_{VM}	damping factor due to the friction between added mass of fluid moving with the hair and surrounding air
S	spring stiffness
t	time
t_{strob}	pseudo sampling time interval
T_{acq}	inverse of the PIV sampling frequency
T_D	drag torque
T_{flow}	inverse of the signal frequency
T_R	damping torque
T_S	restoring torque
T_{VM}	torque associated with the virtual mass of fluid
U_∞	far-field velocity
U_0	flow oscillation amplitude
$V_F(y,t)$	velocity acting on the hair
V_l	longitudinal component of a flow impacting the cylinder
V_r	radial component of a flow impacting the cylinder
V_θ	circumferential component of a flow impacting the cylinder
X,Y,Z,C	complex numbers
X_i,Y_i,Z_i,C_i	imaginary parts of the complex numbers X,Y,Z,C
X_r,Y_r,Z_r,C_r	real parts of the complex numbers X,Y,Z,C
y	distance to the cylinder
α	angular deflection of the hair with respect to its equilibrium orientation
β	border effect factor
δ	phase lag between V_r and V_θ
γ	Euler's constant
λ	laser wavelength
μ_{air}	dynamic viscosity of air
ν_{air}	kinematic viscosity of air
ρ_{air}	air density
ρ_{hair}	hair density
θ	angle between the cylinder and the flow
ω	angular frequency
φ	phase displacement

Appendix

Hair movement modelling

The physical behaviour of a single hair submitted to an air flow can be modelled by the equation given by Shimozawa and Kanou (Shimozawa and Kanou, 1984a) and modified by Humphrey et al. (Humphrey et al., 1993). Most of this information is also contained in Magal et al. (Magal et al., 2006). For a rigid hair oscillating relative to a fixed axis of

rotation, conservation of angular momentum, $L(t)$, states that the rate of change of angular momentum is equal to the sum of torques acting on the hair:

$$\frac{\mathrm{d}L(t)}{\mathrm{d}t} = I\frac{d^2\alpha}{\mathrm{d}t^2} = T_\mathrm{D}(t) + T_\mathrm{VM}(t) - T_\mathrm{R}(t) - T_\mathrm{S}(t)\ , \quad \text{(A1)}$$

where I is the moment of inertia of the hair relative to the axis of rotation and α is the angular deflection of the hair with respect to its equilibrium orientation. The drag torque, T_D, arises due to frictional drag acting along the hair shaft. The torque T_VM is associated with the virtual mass of fluid, which at any instant must be also accelerated along with the hair. The damping torque, T_R, arises at the rotation point of the hair and results from frictions between the hair base and the surrounding cuticle. The restoring torque, T_S, is equivalent to spring stiffness, expressing the elasticity of the socket membrane, and arises at the rotation point of the hair. The velocity profiles are integrated in the first two torques, which drive hair motion, whereas the last two torques are always opposed to hair deflection.

Hair's moment of inertia

According to Humphrey et al. (Humphrey et al., 1993) and Kumagai et al. (Kumagai et al., 1998), the total inertial moment of a filiform hair, I (Nm s^{-2} rad^{-1}), is given by:

$$I = I_\mathrm{h} + I_\mathrm{VM}\ , \quad \text{(A2)}$$

where I_h is the hair moment of inertia:

$$I_\mathrm{h} = \frac{\pi\rho_\mathrm{hair}d^2}{48}\left[L_\mathrm{hair}\left(4{L_\mathrm{hair}}^2 + \frac{3d^2}{4}\right)\right], \quad \text{(A3)}$$

where d is hair diameter (m), L_hair is hair length (m), and ρ_hair is hair density (kg m^{-3}). I_VM represents the moment of inertia of the added mass of the fluid stagnating around and moving with the hair of constant diameter and is given by Humphrey et al. (Humphrey et al., 1993) as:

$$I_\mathrm{VM} = \frac{-\pi\mu G{L_\mathrm{hair}}^3}{6gf_\mathrm{flow}} + \frac{\pi\rho d^2{L_\mathrm{hair}}^3}{12}\ . \quad \text{(A4)}$$

Stokes (Stokes, 1851) shows that for values of the dimensionless parameter:

$$s = \frac{d}{4}\left(\frac{2\pi f_\mathrm{flow}}{\nu_\mathrm{air}}\right)^{\frac{1}{2}}\ , \quad \text{(A5)}$$

such that $s \ll 1$:

$$G = \frac{-g}{g^2 + \left(\frac{\pi}{4}\right)^2}\ , \quad \text{(A6)}$$

with:

$$g = y + \ln(s)\ , \quad \text{(A7)}$$

where γ (dimensionless) is Euler's constant, d is hair diameter (m) at height y above the cercus, f is the oscillating air flow frequency (Hz), and ν_air is the air kinematic viscosity (m^2 s^{-1}).

Fluid-induced drag and added mass torques

The fluid-induced instantaneous drag and added mass torques are obtained by integrating the fluid-induced drag and added mass forces per unit length acting along the total length of the hair, L_hair (m):

$$T_\mathrm{D}(t) = \int_0^L F_\mathrm{D}(y,t)y\ dy\ , \quad \text{(A8)}$$

$$T_\mathrm{VM}(t) = \int_0^L F_\mathrm{VM}(y,t)y\ dy\ , \quad \text{(A9}$$

where y is the position along the hair (m), and F_D(y,t) and F_VM(y,t) are the drag and added mass forces per hair unit length, acting at height y, respectively. Eqns A8 and A9 state that the total torque that acts to deflect the hair from its resting position is given by the integrated sum of all torques over the arm length of rotation y. Each of the torques is generated on an infinitesimally thin disc of the hair shaft. Theoretical expressions for F_D and F_VM, applicable to a fluid oscillating perpendicular to a hair, have been derived by Stokes (Stokes, 1851) and previously used in filiform hair modelling studies (Humphrey et al., 1993; Shimozawa et al., 1998).

Drag and added mass forces per unit length

For a fluid oscillating perpendicular to a cylindrical hair segment, the drag force acting on the cylinder at height y above the cercus surface is:

$$F_\mathrm{D}(y,t) = 4\pi\mu G V_\mathrm{F}(y,t)\ , \quad \text{(A10)}$$

where μ is the fluid dynamic viscosity (kg m^{-1} s^{-1}), G is given by Eqn A6 and $V_\mathrm{F}(y,t)$ is the velocity acting on the hair.

The added mass force per unit length is given by:

$$F_\mathrm{VM}(y,t) = \frac{-\pi\mu G\frac{\mathrm{d}V_\mathrm{F}(y,t)}{\mathrm{d}t}}{2gf_\mathrm{flow}} + \pi\rho\left(\frac{d}{2}\right)^2\frac{\mathrm{d}V_\mathrm{F}(y,t)}{\mathrm{d}t}\ , \quad \text{(A11)}$$

where G is given by Eqn A6 and g is given by Eqn A7.

Damping torque

This torque results in part from the friction between the hair base and the surrounding cuticle (Shimozawa and Kanou, 1984a; Shimozawa et al., 1998). The damping factor (Nm s^{-1} rad^{-1}) includes frictional terms at the hair base (R) as well as friction between added mass of fluid moving with the hair and surrounding air (R_VM). Both sources of torque always act so as to oppose hair motion. The total damping torque, T_R (N m^{-1}), is given by:

$$T_\mathrm{R}(t) = (R + R_\mathrm{VM})\frac{d\alpha(t)}{\mathrm{d}t}\ , \quad \text{(A12)}$$

where R (Nm s^{-1} rad^{-1}), is a constant damping factor which is allometrically related to L_hair (μm) (Shimozawa et al., 1998):

$$R = 2.88\times10^{-14}\ (L_\mathrm{hair}/1000)^{2.77}\ , \quad \text{(A13)}$$

and R_{VM} is the damping factor due to the friction between added mass of fluid moving with the hair and surrounding air:

$$R_{VM} = 4\pi\mu G\,(L_{hair}^3/3)\,. \quad \text{(A14)}$$

Restoring torque

The socket joint membrane acts as a spring, causing a restoring torque that always acts to oppose hair motion:

$$T_S(t) = S\alpha(t)\,, \quad \text{(A15)}$$

where S (Nm rad^{-1}) is the spring stiffness, which is allometrically related to L_{hair} (μm) (Shimozawa et al., 1998):

$$S = 1.9\times10^{-11}\,(L_{hair}/1000)^{1.67}\,. \quad \text{(A16)}$$

This work is part of the research conducted within the Cricket Inspired perCeption and Autonomous Decision Automata (CICADA) project (IST-2001-34718) and within the Customized Intelligent Life Inspired Arrays (CILIA) project (FP6-IST-016039). These projects are both funded by the European Community under the 'Information Society Technologies-IST' Program, Future and Emergent Technologies (FET), Lifelike Perception Systems action.

References

Abramowitz, M. and Stegun, I. A. (ed.) (1965). *Handbook of Mathematical Functions* (*National Bureau of Standards*, *Applied Mathematics Series No. 55*). Washington: Dover Publications.

Anderson, E. J., McGillis, W. R. and Grosenbaugh, M. A. (2001). The boundary layer of swimming fish. *J. Exp. Biol.* **204**, 81-102.

Barth, F. G., Wastl, U., Humphrey, J. A. C. and Devarakonda, R. (1993). Dynamics of arthropod filiform hairs. II. Mechanical properties of spider trichobothria (Cupiennius salei Keys.). *Philos. Trans. R. Soc. Lond. B Biol. Sci.* **340**, 445-461.

Bertelsen, A., Svardal, A. and Tjøtta, S. (1973). Nonlinear streaming effects associated with oscillating cylinders. *J. Fluid Mech.* **59**, 493-511.

Campbell, M., Cosgrove, J.-A., Greated, C.-A., Jack, S. and Rockliff, D. (2000). Review of LDA and PIV applied to the measurement of sound and acoustic streaming. *Opt. Laser Tech.* **32**, 629-639.

Castrejón-Pita, J. R., Castrejón-Pita, A. A., Huelsz, G. and Tovar, R. (2006). Experimental demonstration of the Rayleigh acoustic viscous boundary layer theory. *Phys. Rev. E* **73**, 036601.

Devarakonda, R., Barth, F. and Humphrey, J. A. C. (1996). Dynamics of arthropod filiform hairs. IV: Hair motion in air and water. *Philos. Trans. R. Soc. Lond. B Biol. Sci.* **351**, 933-946.

Dijkstra, M., van Baar, J. J., Wiegerink, R. J., Lammerink, T. S. J., de Boer, J. H. and Krijnen, G. J. M. (2005). Artificial sensory hairs based on the flow sensitive receptor hairs of crickets. *J. Micromech. Microeng.* **15**, 132-138.

Fletcher, N. H. (1978). Acoustical response of hair receptors in insects. *J. Comp. Physiol.* **127**, 185-189.

Gnatzy, W. and Heusslein, R. (1986). Digger wasp against crickets. I. Receptors involved in the antipredator strategies of the prey. *Naturwissenschaften* **73**, 212-215.

Holtsmark, J., Johnsen, I., Sikkeland, T. and Skavlem, S. (1954). Boundary layer flow near a cylindrical obstacle in oscillating incompressible fluid. *J. Acoust. Soc. Am.* **26**, 26-39.

Humphrey, J. A. C. and Devarakonda, R. (1993). Dynamics of arthropod filiform hairs. I. Mathematical modelling of the hair and air motions. *Philos. Trans. R. Soc. Lond. B Biol. Sci.* **340**, 423-444.

Humphrey, J. A. C., Devarakonda, R., Iglesias, I. and Barth, F. G. (1993). Dynamics of arthropod filiform hairs. I. Mathematical modelling of the hair and air motions. *Philos. Trans. R. Soc. Lond. B Biol. Sci.* **340**, 423-440.

Humphrey, J. A. C., Barth, F. G. and Voss, K. (2003a). The motion-sensing hairs of arthropods: using physics to understand sensory ecology and adaptive evolution. In *Ecology of Sensing* (ed. F. G. Barth and A. Schmid), pp. 105-115. Berlin, Heidelberg, New York: Springer-Verlag.

Humphrey, J. A. C., Barth, F. G., Reed, M. and Spak, A. (2003b). The physics of arthropod medium-flow sensitive hairs: biological models for artificial sensors. In *Sensors and Sensing in Biology and Engineering* (ed. F. G. Barth, J. A. C. Humphrey and T. Secomb), pp. 129-144. Berlin, Heidelberg, New York: Springer Verlag.

Justesen, P. (1991). A numerical study of oscillating flow around a circular cylinder. *J. Fluid Mech.* **222**, 157-196.

Koehl, M. A. R., Koseff, J. R., Crimaldi, J. P., Cooper, T., McCay, M., Wiley, M. B. and Moore, P. A. (2001). Lobster sniffing filters the spatio-temporal information in a turbulent odour plume. *Science* **294**, 1948-1951.

Kumagai, T., Shimozawa, T. and Baba, Y. (1998). The shape of windreceptor hairs of cricket and cockroach. *J. Comp. Physiol. A* **183**, 187-192.

Magal, C., Dangles, O., Caparroy, P. and Casas, J. (2006). Hair canopy of cricket sensory system tuned to predator signals. *J. Theor. Biol.* **241**, 459-466.

Mayinger, F. and Feldman, O. (2001). *Optical Measurements: Techniques and Applications* (2nd edn.). Berlin, Heidelberg, New York: Springer-Verlag.

Obasaju, E. D., Bearman, P. W. and Graham, J. M. R. (1988). A study on forces, circulation and vortex patterns around a circular cylinder in oscillatory flow. *J. Fluid Mech.* **196**, 467-494.

Raney, W. P., Corelli, J. C. and Westervelt, P. J. (1954). Acoustic streaming in the vicinity of a cylinder. *J. Acoust. Soc. Am.* **26**, 1006-1014.

Schram, C. and Riethmuller, M. L. (2001b). Evolution of vortex ring characteristics during pairing in an acoustically excited jet using stroboscopic particle image velocimetry. *4th International Symposium on Particle Image Velocimetry (PIV'01)*, Göttingen, 17–19 September, paper 1157.

Seur, J., Tuck, L. and Robert, D. (2005). Sound radiation around a flying fly. *J. Acoust. Sci. Amer.* **118**, 530-538.

Shimozawa, T. and Kanou, M. (1984). The aerodynamics and sensory physiology of range fractionation in the cercal filiform sensilla of the cricket Gryllus bimaculatus. *J. Comp. Physiol. A* **155**, 495-505.

Shimozawa, T., Kumagai, T. and Baba, Y. (1998). Structural scaling and functional design of the cercal wind-receptor hairs of cricket. *J. Comp. Physiol. A* **183**, 171-186.

Shimozawa, T., Murakami, J. and Kumagai, T. (2003). Cricket wind receptors: thermal noise for the highest sensitivity known. In *Sensors and Sensing in Biology and Engineering* (ed. F. G. Barth, J. A. C. Humphrey and T. Secomb), pp. 145-157. Berlin, Heidelberg, New York: Springer Verlag.

Stacey, M. T., Mead, K. S. and Koehl, M. A. R. (2002). Molecule capture by olfactory antennules: mantis shrimp. *J. Math. Biol.* **44**, 1-30.

Stokes, G. G. (1851). On the effect of the internal friction of fluids non the motion of pendulums. *Math. Phys. Pap.* **3**, 1-141.

Tatsuno, M. and Bearman, P. W. (1990). A visual study of the flow around an oscillating cylinder at low Keulegan-Carpenter number and low Stokes numbers. *J. Fluid Mech.* **211**, 157-182.

Tautz, J. and Markl, H. (1979). Caterpillars detect flying wasps by hairs sensitive to airborne vibration. *Behav. Ecol. Sociobiol.* **4**, 101-110.

Wang, C. (1968). On high-frequency oscillatory viscous flows. *J. Fluid Mech.* **32**, 55-68.

Williamson, C. H. K. (1985). Sinusoidal flow relative to circular cylinders. *J. Fluid Mech.* **155**, 141-174.

Chapitre 4

Couplage hydrodynamique visqueux entre les poils

Casas, J., **Steinmann, T.** & Krijnen, G. 2010 Why do insects have such a high density of flow-sensing hairs ? Insights from the hydromechanics of biomimetic MEMS sensors. *Journal of The Royal Society Interface* 7, 148795. (doi :10.1098/rsif.2010.0093)

Résumé du chapitre

Ce chapitre discute du rôle fonctionnel de la forte densité de poils présents sur les cerques de grillons. Des études antérieures ont en effet prédit un fort couplage hydrodynamique entre des poils sensoriels si densément implentés. Cependant, la perturbation de l'écoulement autour des poils n'a jamais été mesurée expérimentalement.

Résultats

Ce chapitre vise à quantifier à l'aide de la PIV l'ampleur de la perturbation de l'écoulement par des poils seuls et en tandem, en utilisant pour cela des senseurs biomimétiques MEMS (Micro-Electronical-Mechanical-System) à la place des poils filiformes de grillons. Nous testons l'influence de l'espacement interpoils sur la perturbation dans des écoulements oscillatoires de fréquence variable. Nous montrons que la diminution de l'espacement dans un réseau réduit nettement l'amplitude de la vitesse d'écoulement et augmente considérablement le déphasage entre l'écoulement principal et celui mesuré entre les senseurs. Ces effets sont d'autant plus marqués que la fréquence d'oscillation de l'écoulement est faible.

Discussion

Ces mesures nous incitent à prédire un fort couplage hydrodynamique dans les réseaux de senseurs naturels exposés à des stimuli naturels. Nous concluons enfin que la grande densité de poils des cerques de grillons fonctionne comme un ensemble de résonnateurs hydrodynamiquement couplés.

JOURNAL OF THE ROYAL SOCIETY Interface

J. R. Soc. Interface (2010) **7**, 1487–1495
doi:10.1098/rsif.2010.0093
Published online 28 April 2010

Why do insects have such a high density of flow-sensing hairs? Insights from the hydromechanics of biomimetic MEMS sensors

Jérôme Casas[1,2,*], Thomas Steinmann[1] and Gijs Krijnen[3]

[1]*Faculté des Sciences et Techniques, Institut de Recherche sur la Biologie de l'Insecte—UMR CNRS 6035, Université François Rabelais, Parc de Grandmont, Avenue Monge, 37200 Tours, France*
[2]*INRA, UR 633 Zoologie Forestière, 2163 Avenue de la Pomme de Pin, 45075 Orléans Cedex 2, France*
[3]*Faculty of Electrical Engineering, MESA+ Research Institute, Transducers Science and Technology group, University of Twente, PO Box 217, 7500 AE Enschede, The Netherlands*

Insects and arachnids are often quite hairy. The reasons for this high density of sensory hairs are unknown. Previous studies have predicted strong hydrodynamic coupling between densely packed airflow-sensitive hairs. Flow perturbation owing to single hairs and between tandem hairs, however, has never been experimentally measured. This paper aims to quantify the extent of flow perturbation by single and tandem hairs directly, using biomimetic microelectromechanical system (MEMS) hairs as physical models and particle image velocimetry (PIV) for flow visualization. Single and tandem MEMS hairs of varying interhair distances were subjected to oscillatory flows of varying frequency. Decreasing hair-to-hair distance markedly reduced flow velocity amplitude and increased the phase shift between the far-field flow and the flow between hairs. These effects were stronger for lower flow frequencies. We predict strong hydrodynamic coupling within whole natural hair canopies exposed to natural stimuli, depending on arthropod and hair sizes, and hair density. Thus, rather than asking why arthropods have so many hairs, it may be useful to address why hairs are packed together at such high densities, particularly given the exquisite sensitivity of a single hair.

Keywords: sensory ecology; physical ecology; biomimetics; hair canopy; mechanosensors; boundary layer

1. INTRODUCTION

Most arthropods have many hairs, often packed together at an unusually high density. Functional explanations for this high density depend on the type of hair. Indeed, the high density of small setae in the foot of many insects results in increased adherence (Federle 2006), whereas a countless number of aquatic and terrestrial arthropods also use hairs for particle capture, flying or swimming (Cheer & Koehl 1987). In wood crickets, the density of airflow-sensing hairs can reach values higher than 400 hairs mm^{-2} (Dangles *et al.* 2006). The reasons for such a high number and density of sensors are unclear, in particular since several studies have shown that the early instars of cockroaches and crickets, which suffer the highest mortality, have much fewer hairs, down to two in the first cockroach instars (Camhi 1984). Furthermore, the relationship between number and density changes over the course of ontogeny in a complex nonlinear manner, the highest hair density corresponding to the smallest number of hairs in wood crickets (Dangles *et al.* 2006). Using an analogy with neuronal population coding, one may assume that a high density of sensors, often each of extreme sensitivity (Shimozawa *et al.* 2003), increases the ability to characterize spatio-temporal patterns of stimuli at very small spatial scales. Such high densities imply, however, that there are hydrodynamic interactions between hairs, and thus that hairs do not act independently. The extent of the influence of a hair on its neighbours through flow perturbation has recently been addressed using experimental, theoretical and computational approaches. The aim of this work is to present experimental data on the flow field between two biomimetic microelectromechanical system (MEMS) hairs using a systematic set of stimulus velocities, frequencies and interhair spacings, and to provide a quantitative test of the theory and mathematical models derived in earlier studies.

Using spider legs exposed to oscillatory flows, Bathellier *et al.* (2005) determined the deflection

*Author for correspondence (jerome.casas@univ-tours.fr).

Received 17 February 2010
Accepted 8 April 2010

angle of tandem airflow-sensing hairs using optical methods. They did not observe fluid-mediated interactions (called thereafter viscous coupling owing to the low Reynolds number) for two freely moving hairs of similar length. By contrast, they identified a strong viscous effect if one of the hairs was immobilized, or if the hairs were of different lengths. They developed a theoretical model of viscous coupling that fitted their data well. The model also explained why viscous coupling could not be observed for two freely movable hairs of similar length: damping and driving torques cancel each other and viscous losses dominate the other effects. These authors extended their theory to hairs of dissimilar lengths, predicting an effect of viscous coupling over a distance of 30 hair diameters or more.

Recently, Cummins *et al.* (2007) applied computational methods to the same problem. Their results largely confirmed those of Bathellier *et al.* (2005) with two exceptions. First, they observed significant coupling for hairs of similar length. Second, they extended their findings to larger distances, predicting viscous coupling over 50 hair diameters or more. This was also recently observed in another computational study by Heys *et al.* (2008). Furthermore, Cummins *et al.* (2007) computed interactions for a group of several hairs and predicted (i) large phase shifts between hairs and (ii) the presence of 'dead zones' within the hair canopy, caused by strong coupling between hairs. More recently, Lewin & Hallam (in press) showed, again using computational fluid dynamics models, that viscous coupling can be negative when hairs are arranged perpendicular to the flow, implying an *increased* sensitivity of a hair owing to the inhibitory effects of its neighbour (see also Cheer & Koehl (1987), for an earlier study on variable interactions depending on the flow direction relative to hair arrangement). The predictions by Bathellier *et al.* (2005), and in subsequent studies, are based on the various theories developed over the past 10 years for single hairs (reviewed in Humphrey & Barth 2008). None of these studies have measured the flow field around hairs. Rather, the flow field has been invariably inferred from observed and computed hair movement, using existing theories.

Several limitations have so far prevented the direct measurement of airflow around biological hairs. The measurement of boundary layers around real hairs using particle image velocimetry (PIV), combined with laser-based techniques, presents a number of difficulties. First, it is nearly impossible to find a hair arrangement and laser positioning that ensures that the laser light sheet is in the focal plane of both (i) the two hairs and (ii) their common plane of movement. This is important as hairs have preferential planes of movement (Landolfa & Jacobs 1995); misalignments, therefore, lead to biased estimates. Second, owing to the high density of the hairs, other nearby, but out-of-plane, hairs may disturb the flow. This would require cutting away all but two of the hairs, a tedious and delicate task. Third, the surface of the appendages bearing the hairs to be studied, such as that of the two antenna-like structures at the rear of crickets, called cerci, contains many spines and other ultrastructures, which could increase the boundary layer of the appendage itself (Steinmann *et al.* 2006; Dangles *et al.* 2008). Any of these features may have an unknown effect on the estimation of the boundary layer around the hairs. The alternative use of physical models overcomes many of these limitations. Here, we use biomimetic MEMS sensory hairs, designed partly based on cricket hairs (Krijnen *et al.* 2006). The conditions in which flow measurements are taken with MEMS can be fully controlled, allowing us to design experiments with tandem MEMS hairs of varying inter-hair distances to measure the perturbation to flow directly, using PIV. We used a so-called parallel flow system, the most widely used system for such studies, in which the flow is in the direction defined by the plane of the two hairs.

2. MATERIAL AND METHODS

2.1. Design of MEMS hairs

MEMS hairs were made of SU-8, an epoxy that can be structured by photolithography. To obtain sufficiently long hairs, two deposition/exposure cycles of about 450 μm each are used. Depending on (i) the exact SU-8 solution, (ii) the spinning conditions, as well as (iii) the temperature-dependent shrinking effects during curing, there exist wafer-scale variations in the final SU-8 layer thickness. Catering to the negative-tone resist properties of SU-8, i.e. what is illuminated will remain after exposure and development, and the limited aspect ratio of the overall photolithographic process of about 10–20, the first layer is exposed prior to the deposition of the second layer. This allows the diameters of the hairs in the first and second layer to be dissimilar. However, this is only by design: actual diameters deviate from designed values and are invariably smaller at the bottom than at the top owing to the optical intensity profile during exposure (light is absorbed and hence the intensity decreases from top to bottom). Design values for the hair diameters of the first and second layers were 50 and 25 μm, respectively. The smaller diameter of the second part of the hairs is caused by a substantial reduction in the moment of inertia (by around 65%) allowing for increased sensitivity for a given bandwidth (Krijnen *et al.* 2007) but is non-essential in this study. Owing to technical limitations in alignment (because of the large thickness of the layers) as well as curing-induced deformations, the second part of the hair is slightly eccentric over the first part (see figure 1*a*). The diameter of the second part of the hairs was tapered from top to bottom. The total length of the MEMS hairs was 825 μm. Only fixed hairs were used in this study, given that hair movement for fully functional MEMS hairs is limited and hardly measurable with PIV (displacements of the nanometre range) and that it is much simpler to construct fixed hairs. Details of the fabrication of fully functional hair sensors are described in Bruinink *et al.* (2009). The distance between hairs varied between 450 and 2800 μm, corresponding to 9–56 hair diameters.

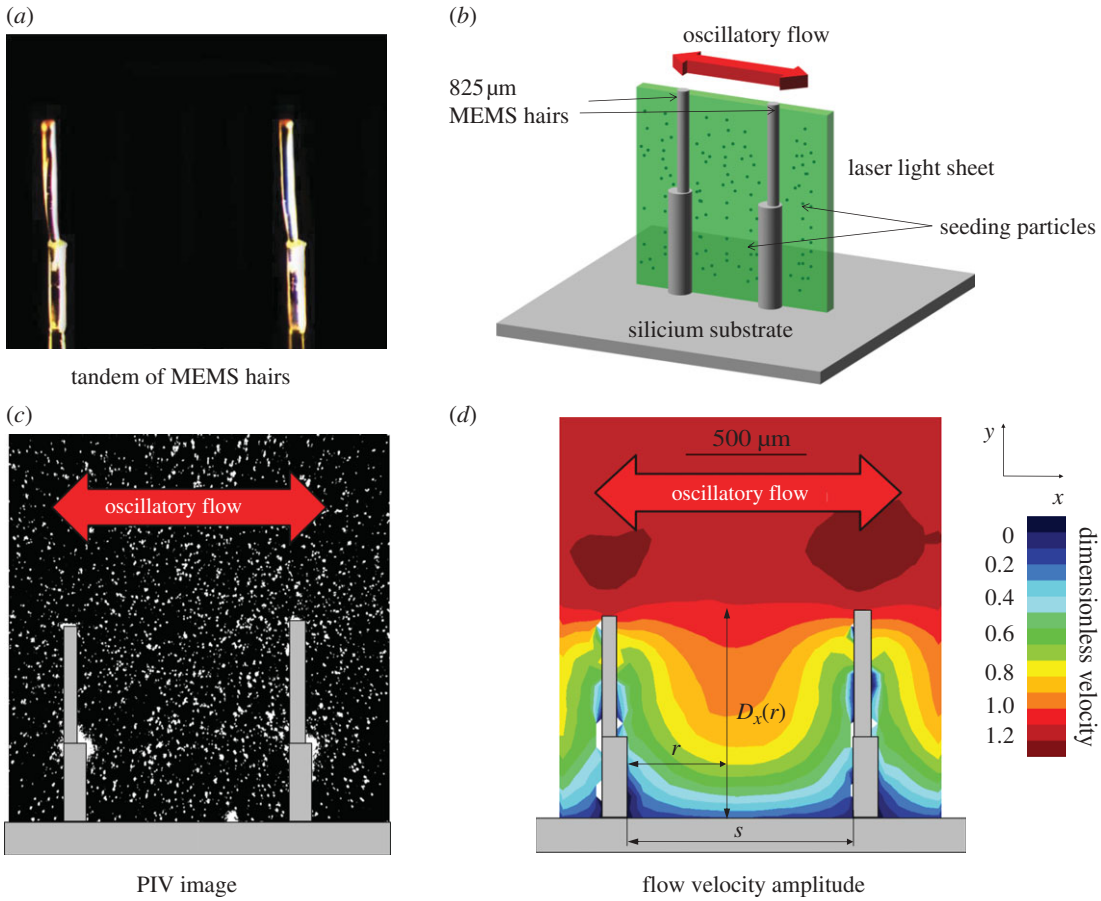

Figure 1. Set-up and definition of variables.

2.2. Experimental set-up

Single or tandem 825 μm MEMS hairs, fixed on plates of dimensions $10 \times 10\ \mathrm{mm}^2$, were placed in a glass container (dimensions: $10 \times 10 \times 10\ \mathrm{cm}^3$). One loudspeaker (40 W) was connected at one side to a sinusoidal signal generator. The air inside the sealed glass box was seeded with 0.2 μm oil particles (di-ethyl-hexyl-sebacate) using an aerosol generator. The PIV-pulsed laser (NewWave Research Solo PIV 2, 532 nm, 30 mJ, Nd:YAG, dual-pulsed; Dantec Dynamics A/S) illuminated the flow through the glass from the top. The laser sheet (width = 17 mm, thickness at focus point = 50 μm) was operated at low power (3 mJ at 532 nm wavelength) to minimize glare, and the pulse duration was 4 ± 1 ns.

A target area was imaged onto the charge-coupled device (CCD) array of a digital camera (696×512 pixels) using a stereomicroscope. The field of view was 2700×2000 μm. Particle velocities were extracted from the images by cross correlation. Owing to the information contained in the grey-level values as captured by CCD as well as the relatively large number of particles used in the cross-correlation calculations, a particle displacement precision of 0.1 pixels can be obtained. Given the entire set-up, this translates into a measurable displacement of 0.4 μm. We set the time between two pairs of images at 200 μs to provide a sufficient dynamic range of velocities, giving a velocity precision of $2\ \mathrm{mm\,s}^{-1}$. We chose a precision level larger than 1 per cent (1% of the velocity amplitude), setting the far-field flow amplitude to between 150 and 200 $\mathrm{mm\,s}^{-1}$. For a 50 μm diameter MEMS hair in air at 20°C, this corresponds to a Reynolds number of between 0.5 and 0.7, relatively close to the Reynolds number of 0.19 observed for a 10 μm diameter cricket hair. Thus, this experimental set-up provides a flow system comparable to that experienced in nature.

We used the stroboscopic principle to measure different phases of sinusoidal flow with a PIV system limited to 20 Hz. As explained in Steinmann *et al.* (2006), it consists of sampling a signal of high frequency at a frequency slightly lower than a sub-multiple of the signal frequency. This technique allows us to estimate the flow phase by inference. The flow velocity fields presented in this article are proportional to the amplitude of the flow velocity, i.e. the difference between the maximum velocity measured at $\omega t = (\pi/2)$ and the minimum velocity measured at $\omega t = -(\pi/2)$.

2.3. Theoretical approximations

Viscous coupling can be inferred by measuring the proportional change in the angle of movement of a single undisturbed hair relative to the angle of the movement of one of a pair of hairs that are coupled through flow. This change will be a function of the change in the forces acting on the hairs. These forces, in turn, are a function of the integral of the surface-normal gradient of the flow velocity over the total surface area of the hairs. Previous authors have calculated viscosity-mediated coupling

as the change in the torque acting on one of a pair of hairs, relative to the torque acting on undisturbed (single) hairs.

In this study, we are interested in the flow perturbation, rather than the hair response. Let us first describe $V_\infty(y)$, the horizontal (x-axis) component of the non-perturbed velocity on a flat plate. The infinity symbol describes the fact that this velocity does not depend on x when there is no hair, or when the velocity is measured at an infinite distance from a hair. We used the model proposed by Shimozawa & Kanou (1984) for modelling the plate boundary layer,

$$V_\infty(y) = V_0\sqrt{(1-\mathrm{e}^{-\beta y}\cos(\beta y))^2 + (\mathrm{e}^{-\beta y}\sin(\beta y))^2}, \tag{2.1}$$

where $\beta = \sqrt{2\pi f/2\nu}$.

The change D_x (in the x-direction) in near-field velocities $V_x(r,y)$ around a single hair, normalized to the far-field velocity at a height y, $V_\infty(y)$, is defined as

$$D_x(r) = \frac{V_\infty(y) - V_x(r,y)}{V_\infty(y)}, \tag{2.2}$$

with r being the distance from the hair. This perturbation thus has a value of 1 at the surface of the flow-disrupting hair. A theoretical approximation of flow perturbation D_x was initially proposed by Bathellier *et al.* (2005); see the subsequent corrections in Lewin & Hallam (in press) and by the authors (Bathellier *et al.* 2005), and we refer readers to these publications for its derivation. The proposed model assumes hairs of constant diameter and infinite hair length. As explained below, the perturbation is independent of y once the plate boundary layer has been factored out, so that we drop the dependence on y in the following. The flow perturbation is then given by the following equation:

$$D_x(r) = \left[\frac{K_2(\lambda)}{K_0(\lambda)}\frac{1}{4(r/d)^2} - \frac{K_1(2\lambda(r/d))}{\lambda(r/d)K_0(\lambda)}\right], \tag{2.3}$$

where K_0, K_1 and K_2 are modified Bessel functions of the second kind, d is the hair diameter, the dimensionless parameter $\lambda = d(1+i)/2\sqrt{2(\nu/2\pi f)}$, and ν and f are the kinematic viscosity and the fluid flow frequency, respectively.

The phase shift between the far-field flow and the flow within a hair canopy is also perturbed by the hairs. The phase shift between the far-field flow and the flow near a flat substrate without hairs, measured in the vertical y-axis, is described by the following (Shimozawa & Kanou 1984):

$$\phi(y) = \operatorname{atan}\left(\frac{\sin(\beta y)}{\exp(\beta y) - \cos(\beta y)}\right). \tag{2.4}$$

We use equation (2.4) on a comparative basis when analysing the phase shift due to the presence of hairs.

2.4. Perturbation by two hairs

Following Bathellier *et al.* (2005), the flow velocity at any location between two non-moving hairs at a distance s apart can be expressed as the sum of: (i) the unperturbed flow $V_\infty(y)$, (ii) plus the velocity perturbation $D_x(r)$ associated with hair 1, and (iii) plus the perturbation $D_x(r-s)$ for hair 2,

$$V_x(r,y) = V_\infty(y)\left(1 - \frac{D_x(r) + D_x(r-s)}{1 + D_x(s)}\right). \tag{2.5}$$

The total perturbation is

$$D_{\mathrm{tot}}(r) = \frac{D_x(r) + D_x(r-s)}{1 + D_x(s)}. \tag{2.6}$$

2.5. Perturbation measurements

PIV measurements provide two-dimensional flow velocities in the cross-section of a hair (or a pair of hairs) in the flow direction, as shown in figure 1. We first conducted measurements on a flat surface without hairs (data not shown) to obtain experimental values of $V_\infty(y)$ at the four frequencies. They were used to validate equation (2.1). The perturbation at a distance r from the hair surface, $D_x(r)$, is then determined as the average, over the entire hair height (in steps of 100 μm), of equation (2.2).

3. RESULTS

The theoretical model for the flow velocity shows a good fit for data obtained for single MEMS hairs, despite its numerous approximations (figure 2). In particular, the decrease in flow perturbation with increasing frequency, the decrease in the extent of the boundary layers and the merging of the substrate and hair boundary layers are very clear to see. A full factorial design of flow analysis using MEMS hairs arranged in tandem, with frequency and interhair distances as variables, is presented in figure 3. Data obtained for hairs spaced at an interhair distance of 2800 μm were not plotted owing to scaling difficulties. The model for tandem hairs showed a good fit for the shortest and longest distance from the hairs, with an improvement in the fit at high frequencies (figure 4). Again, the decrease of flow velocity perturbation with increasing frequency and increasing interhair distance is quite obvious. A phase shift between the flow in the far field and the flow near the substrate is expected even in the absence of hairs and their presence increases it. Reduced interhair distances lead to increased phase shifts between the far-field flow and the flow measured between two hairs (figure 5). At distances of 1.5 mm or greater, the effect of a hair on its neighbour, in terms of this phase shift, becomes negligible. The increased variability observed within the first hundred micrometres of the boundary around the substrate is due to low seeding density, a common limitation inherent to PIV.

4. DISCUSSION

Our data obtained from single and tandem MEMS hairs are consistent with the theoretical models. The form of the observed relationship at low frequencies is

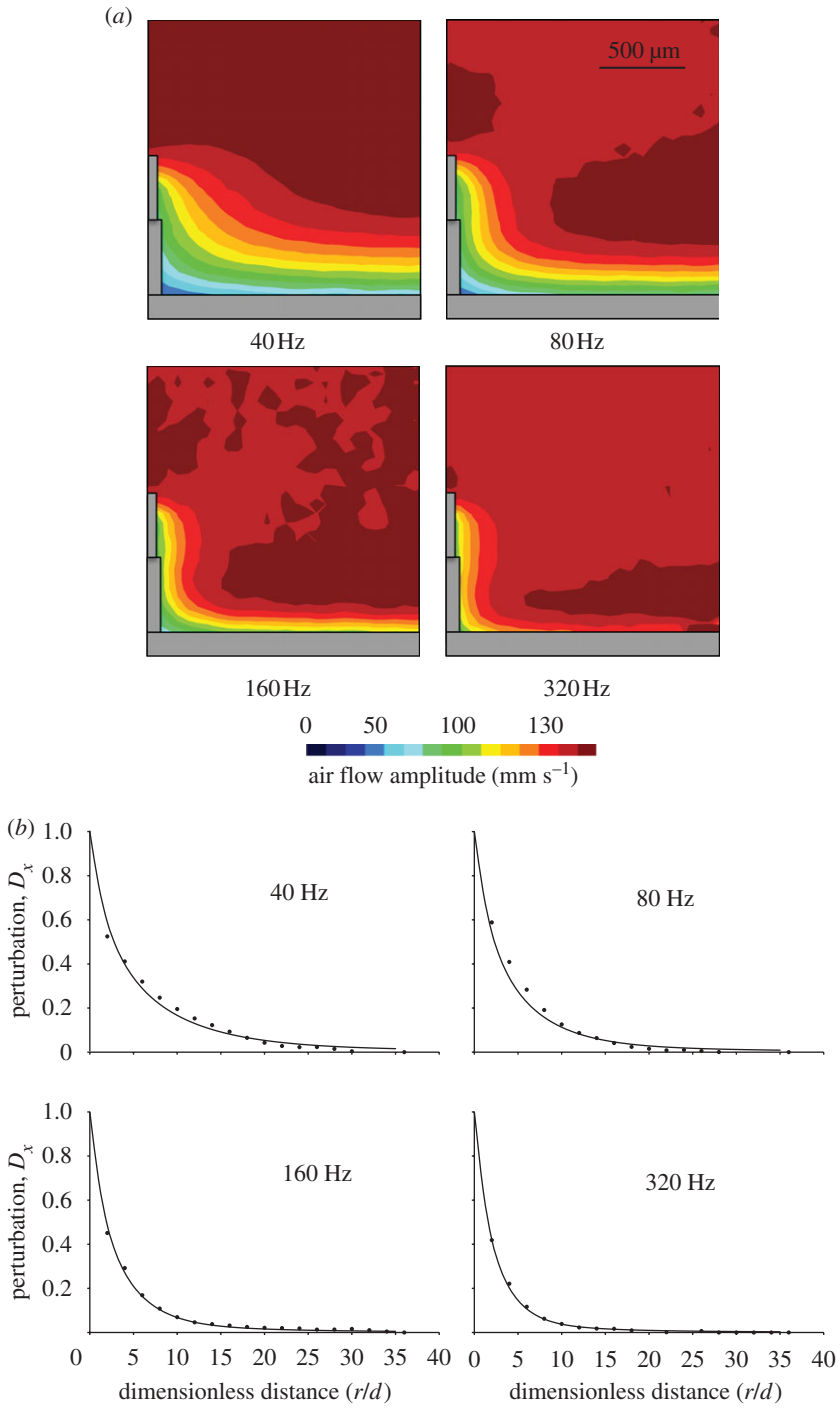

Figure 2. Perturbation of flow by a single MEMS hair at four different frequencies. (*a*) Half of the full-field image. (*b*) Dots represent observed data and lines show predictions of the analytical model (equation (2.3)). The distance from the hair is denoted by r and the hair diameter by d. (*a*) Scale bar, 500 µm.

somewhat different from the one predicted by the theoretical models, so that several assumptions are, therefore, worth discussing here. First, the finite length of a hair implies that its boundary layer is reduced near the tip, leading to an underestimation of the flow perturbation, compared with the infinite length assumption. Thus, strictly speaking, the theory is not developed for hairs of finite length and will show discrepancies with measurements, but this aspect cannot account for the reduced fit. Second, the theory assumes constant hair diameter, whereas our MEMS hairs have varying diameters. This has a negligible influence on the boundary layer at the tested frequencies, so that we used the assumption of a hair of constant diameter of 50 µm in all our computations. We observed variations at the junctions of the two parts of the hairs at frequencies higher than those analysed. Third, the theoretical models assume that the fluid inertial terms of the Navier–Stokes equation can be neglected for low values of $c = V_\infty/\sqrt{\nu 2\pi f}$, an assumption that might be valid at the highest frequency ($c = 0.3$ for 320 Hz), but less so at the lowest frequency ($c = 0.8$ at 40 Hz). There is thus a need for an improved theory of flow perturbation for such conditions. Given the overall good

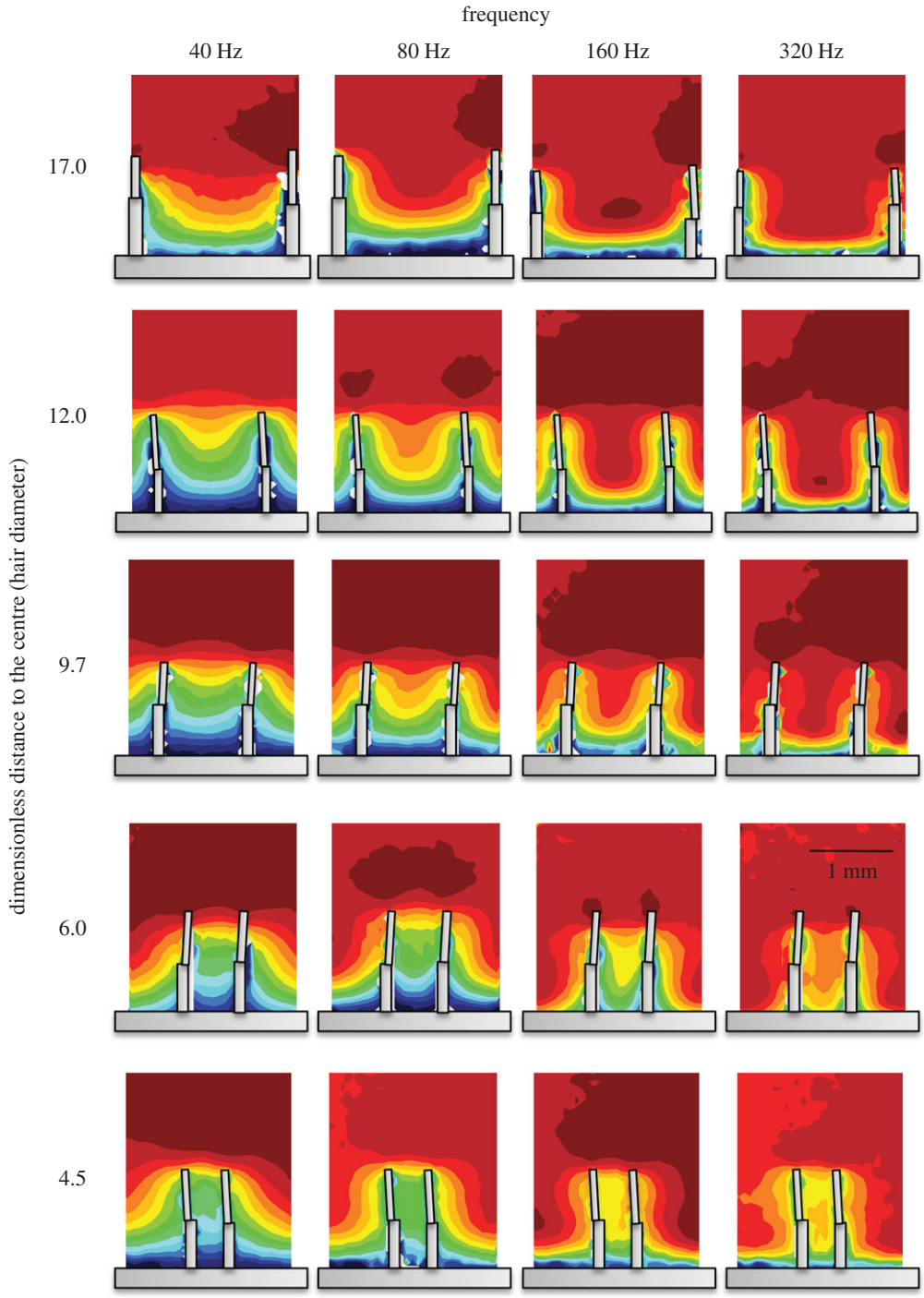

Figure 3. Full-field data for flow in the vicinity of MEMS hairs arranged in tandem, as a function of frequency and interhair distance. Data for the largest interhair distance are not shown owing to the need for different scaling.

fits, our approach using MEMS, therefore, allows us to use the predictions obtained using computational fluid dynamics models and to predict the expected effects for natural hairs, taking into account the similarities and differences between these artificial hairs and natural hairs.

The range of distances between individual MEMS hairs used in these experiments overlaps with that observed for crickets (Dangles *et al.* 2008). Indeed, for large cricket hairs ($L > 500$ um) with diameters d between 7 and 12 μm, 90 per cent of their nearest neighbouring hairs are at a distance s of between 30 and 60 μm, giving a dimensionless spacing distance of $2.5 < s/d < 8.5$. Smaller hairs, with diameters of 1–3 μm, are randomly distributed with distances between neighbouring hairs of 10–60 μm, giving a dimensionless spacing distance of $3 < s/d < 60$. The MEMS set-up covered a range of $9 < s/d < 56$. However, two major differences should be noted. First, in contrast to the negligible movements of MEMS hairs, natural hairs move. This movement, with hairs following the direction of flow, reduces the flow perturbation and hence the viscous coupling (Bathellier *et al.* 2005). Second, MEMS hairs have a much larger diameter than natural hairs. Hair diameter has a substantial effect on the extent of viscous coupling (figure 6),

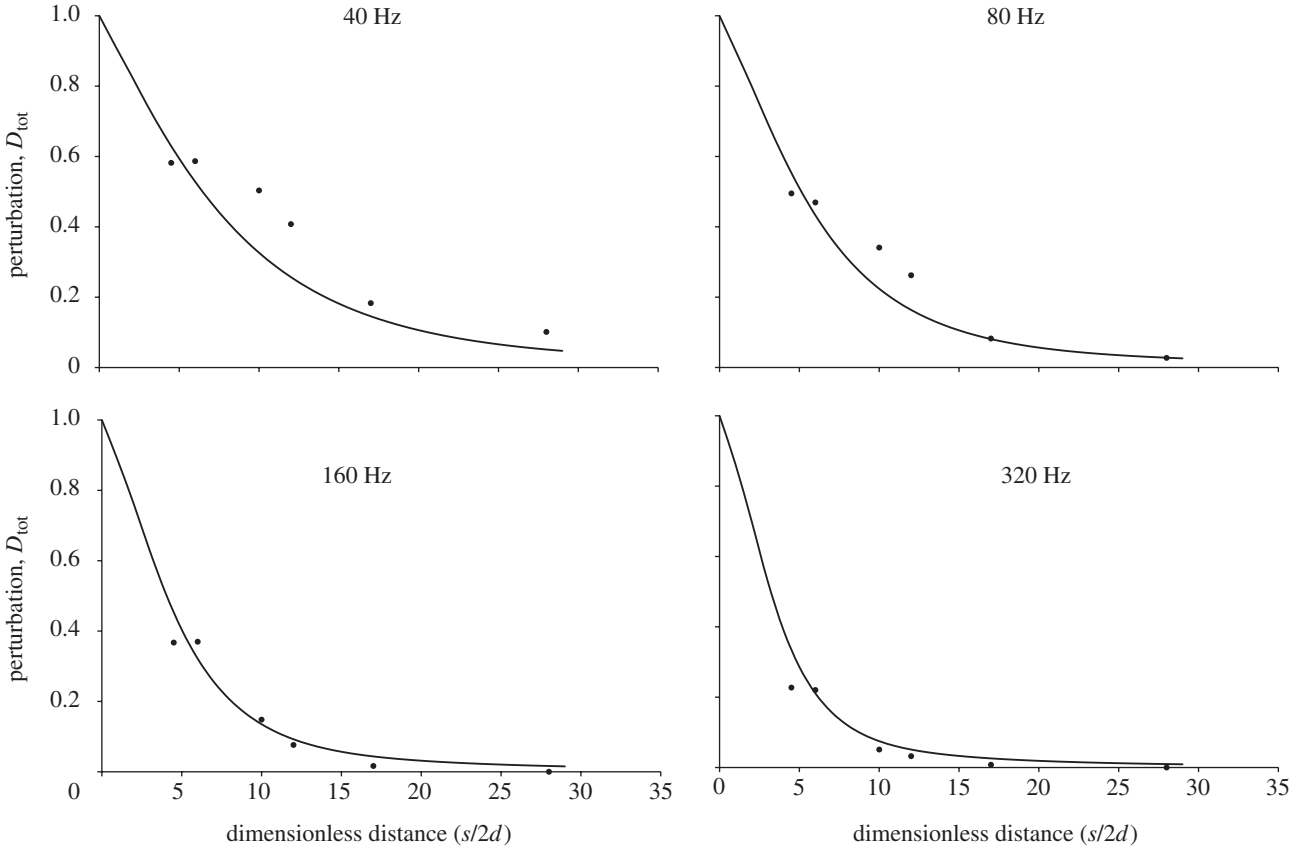

Figure 4. Flow perturbation between two MEMS hairs, as a function of interhair distance and flow frequency. Filled circles represent measurements while lines represent predicted data from the analytical model (equation (2.6)). The distance between the two hairs is denoted by s and the hair diameter by d.

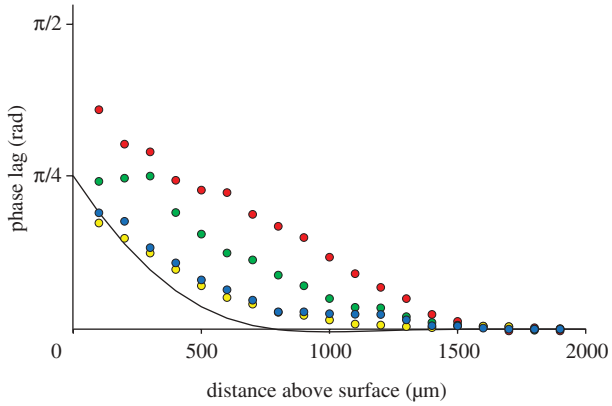

Figure 5. Observed phase lag between the far-field and local flow for two MEMS hairs as a function of interhair distance (red 600 μm, green 1000 μm, blue 1700 μm and yellow 2800 μm) at the flow frequency of 80 Hz. The solid line represents the expected phase lag on a flat plate, given in equation (2.4).

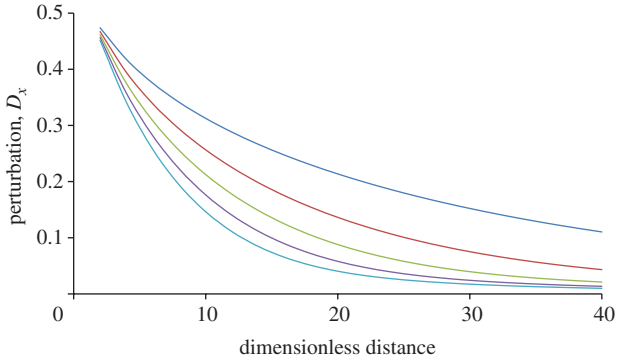

Figure 6. Effect of hair diameter on flow perturbation. Smaller hairs have a greater effect on flow perturbation when data are normalized, but a smaller effect for absolute values of flow perturbation. Blue line, 10 μm; red line, 20 μm; green line, 30 μm; violet line, 40 μm; light blue, 50 μm.

whereas the effect on flow caused by thin hairs is smaller in absolute terms, it is larger when flow perturbation is considered relative to hair diameter. Given the above caveats, our limited understanding of the effect of transverse flow on hydrodynamic interactions (Lewin & Hallam in press) and even poorer understanding for groups of hairs (Cummins *et al.* 2007), we are far from a thorough intuitive grasp of hydrodynamic interactions within hair canopies.

4.1. Implications for natural hairs

Using optical techniques to measure natural hair movement and theoretical models, Bathellier *et al.* (2005) concluded that viscous coupling can exert a strong effect over a distance of up to 30 hair diameters. Later, Cummins *et al.* (2007) and Heys *et al.* (2008), using increasingly realistic computational models, proposed that viscous coupling extends even further, up to at least 50 or more hair diameters. Strong viscous

coupling corresponds to a proportional loss of independence between hairs, reducing movement amplitude, and major alterations in the phase shifts between the far-field flow velocity and the local flow between individual hairs in the canopy. These factors together determine the likelihood and timing of action potentials being fired in the hair nerve cell. This has major effects on the function of the cercus, as shown recently by Mulder-Rosi *et al.* (in press). The relative timing of the firing of different hairs along the cercus allows the proper integration of signals, thus determining the overall signalling profile for incoming danger in the terminal abdominal ganglion. Indeed, bulk flow or flow generated in the backward direction may give weak signals or no signal at all (Mulder-Rosi *et al.* in press).

Determining the extent of viscous coupling provides further insight into the working of the cercal organ as a whole. The observed interhair distances and the short length of the cercus (0.8–4.5 mm; Dangles *et al.* 2006) suggest that strong viscous coupling is acting over the entire hair canopy, with a single hair exerting an effect on flow over nearly half of the cercus. This is reinforced by the fact that viscous coupling is particularly strong for low-frequency flows, predominantly present in the signals produced by spiders approaching their prey (Casas *et al.* 2008; Kant & Humphrey 2009). Observations by Lewin & Hallam (in press) suggesting that, depending on the spatial arrangement of its neighbours, a hair's response may be increased support the idea that the position of a hair may be as important as its individual characteristics in predicting its mechanical and physiological response (as first observed by Cummins *et al.* (2007)). Thus, further work is needed to elucidate the implications of group effects: the density of neighbouring hairs, their length and their preferred plane of movement.

In conclusion, the effect of a cricket hair on the canopy response cannot be determined by examining the contribution of a hair in isolation, despite previous attempts to do so (e.g. Magal *et al.* 2006). This conclusion contrasts with an entire body of work that has focused on the response of single hairs over many years (reviewed in Humphrey & Barth 2008; Casas & Dangles 2010). Thus, this represents a major shift of focus: with such a high density of hairs, the entire hair canopy is most likely to work as a hydrodynamically coupled set of resonators. Thus, rather than ask the question of why arthropods bear so many hairs, we need to address the issue of why hairs are packed together at such high density. How the extreme sensitivity of individual hairs is related to their loss of independence within the canopy also needs to be addressed. These phenomena may be explained by highly nonlinear ensemble reactions, the neurophysiological mechanisms of which have been only very recently tackled using appropriate geometric arrangements of hair and relevant stimuli (Mulder-Rosi *et al.* in press).

We thank Rik de Boer and Christiaan Bruinnink for building the MEMS, Greg Lewin and Brice Bathellier for discussions on the theoretical aspects and Olivier Dangles for comments on a previous version of the manuscript. This work is part of the research conducted within the Customized Intelligent Life Inspired Arrays (CILIA) project (FP6-IST-016 039), funded by the European Community under the Information Society Technologies (IST) Programme, Future and Emergent Technologies (FET), Lifelike Perception Systems action.

REFERENCES

Bathellier, B., Barth, F. G., Albert, J. T. & Humphrey, J. A. C. 2005 Viscosity-mediated motion coupling between pairs of trichobothria on the leg of the spider *Cupiennius salei*. *J. Comp. Physiol. A* **191**, 733–746. [Erratum in *J. Comp. Physiol. A* 2010 **196**, 89.] (doi:10.1007/s00359-005-0629-5)

Bruinink, C. M., Jaganatharaja, R. K., de Boer, M. J., Berenschot, E., Kolster, M. L., Lammerink, T. S. J., Wiegerink, R. J. & Krijnen, G. J. M. 2009 Advancements in technology and design of biomimetic flow-sensor arrays. In *MEMS 2009, Sorrento, Italy, 25–29 January 2009*, pp. 152–155. Piscataway, NJ: IEEE.

Camhi, J. 1984 *Neuroethology: nerve cells and the natural behavior of animals*. Sunderland, MA: Sinauer.

Casas, J. & Dangles, O. 2010 Flow sensing in arthropods: from biomechanics to ecology. *Annu. Rev. Entomol.* **55**, 505–520. (doi:10.1146/annurev-ento-112408-085342)

Casas, J., Steinmann, T. & Dangles, O. 2008 The aerodynamic signature of running spiders. *PLoS ONE* **3**, e2116. (doi:10.1371/journal.pone.0002116)

Cheer, A. Y. L. & Koehl, M. A. R. 1987 Paddles and rakes: fluid flow through bristled appendages of small organisms. *J. Theor. Biol.* **129**, 17–39. (doi:10.1016/S0022-5193(87)80201-1)

Cummins, B., Gedeon, T., Klapper, I. & Cortez, R. 2007 Interaction between arthropod filiform hairs in a fluid environment. *J. Theor. Biol.* **247**, 266–280. (doi:10.1016/j.jtbi.2007.02.003)

Dangles, O., Pierre, D., Vannier, F. & Casas, J. 2006 Ontogeny of air-motion sensing in cricket. *J. Exp. Biol.* **209**, 4363–4470. (doi:10.1242/jeb.02485)

Dangles, O., Steinmann, T., Pierre, D., Vannier, F. & Casas, J. 2008 Relative contributions of organ shape and receptor arrangement to the design of cricket's cercal system. *J. Comp. Physiol. A* **194**, 653–663. (doi:10.1007/s00359-008-0339-x)

Federle, W. 2006 Why are so many adhesive pads hairy? *J. Exp. Biol.* **209**, 2611–2621. (doi:10.1242/jeb.02323)

Heys, J., Gedeon, T., Knott, B. & Kim, Y. 2008 Modeling arthropod filiform hair motion using the penalty immersed boundary method. *J. Biomech.* **41**, 977–984. (doi:10.1016/j.jbiomech.2007.12.015)

Humphrey, J. A. & Barth, F. G. 2008 Medium flow-sensing hairs: biomechanics and models. In *Advances in insect physiology. Insect mechanics and control*, vol. 34 (eds J. Casas & S. J. Simpson), pp. 1–80. Amsterdam, The Netherlands: Elsevier.

Kant, R. & Humphrey, J. A. 2009 Response of cricket and spider motion-sensing hairs to airflow pulsations. *J. R. Soc. Interface* **6**, 1047–1064. (doi:10.1098/rsif.2008.0523)

Krijnen, G., Dijkstra, M., van Baar, J., Shankar, S., Kuipers, W., de Boer, J., Altpeter, D., Lammerink, T. & Wiegerink, R. 2006 MEMS based hair flow-sensors as model systems for acoustic perception studies. *Nanotechnology* **17**, 84–89. (doi:10.1088/0957-4484/17/4/013)

Krijnen, G. J. M., Lammerink, T. S. J., Wiegerink, R. J. & Casas, J. 2007 *Cricket inspired flow-sensor arrays*, pp. 539–546. Atlanta, GA: IEEE Sensors. (doi:10.1109/ICSENS.2007.4388455)

Landolfa, M. A. & Jacobs, G. A. 1995 Direction sensitivity of the filiform hair population of the cricket cercal system. *J. Comp. Physiol. A* **177**, 759–766.

Lewin, G. & Hallam, J. In press. A computational fluid dynamics model of viscous coupling of hairs. *J. Comp. Physiol. A*.

Magal, C., Dangles, O., Caparroy, P. & Casas, J. 2006 Hair canopy of cricket sensory system tuned to predator signals. *J. Theor. Biol.* **241**, 459–466. (doi:10.1016/j.jtbi.2005.12.009)

Mulder-Rosi, J., Cummins, G. I. & Miller, J. P. In press. The cricket cercal system implements delay-line processing. *J. Neurophysiol.* (doi:10.1152/jn.00875.2009)

Shimozawa, T. & Kanou, M. 1984 The aerodynamics and sensory physiology of range fractionation in the cercal filiform sensilla of the cricket *Gryllus bimaculatus*. *J. Comp. Physiol. A* **155**, 495–505. (doi:10.1007/BF00611914)

Shimozawa, T., Murakami, J. & Kumagai, T. 2003 Cricket wind receptors: thermal noise for the highest sensitivity known. In *Sensors and sensing in biology and engineering* (eds F. G. Barth, J. A. Humphrey & T. W. Secomb), pp. 145–159. Berlin, Germany: Springer.

Steinmann, T., Casas, J., Krijnen, G. & Dangles, O. 2006 Air-flow sensitive hairs: boundary layers in oscillatory flows around arthropod appendages. *J. Exp. Biol.* **209**, 4398–4408. (doi:10.1242/jeb.02506)

Chapitre 5

Mesures PIV de la signature aérodynamique de l'attaque de l'araignée

Casas, J., **Steinmann, T.** & Dangles, O. 2008 The aerodynamic signature of running spiders. *PLoS One* 3, e2116. (doi :10.1371/journal.pone.0002116)

Résumé du chapitre

De nombreux prédateurs présentent deux modes de recherche de nourriture, une stratégie d'embuscade et un mode d'attaque rapide. Le choix de l'une ou l'autre des deux stratégies est souvent conditionné par des critères physiologiques, biomécaniques ou encore écologiques. Cependant, rares sont les études qui tiennent compte du rôle des signaux produits par les prédateurs et perçus par les proies. Les araignées-loups sont un exemple typique ; ils chassent dans les feuilles mortes jonchant la litière des forêts, soit en utilisant une stratégie d'embuscade, soit en se déplaçant à très grande vitesse, fonçant sur leur proies surprises par la rapidité de l'attaque. L'écoulement dans l'air généré en amont de leur corps est cependant une source d'information disponible et cruciale pour les proies, comme les grillons et les cafards, afin d'anticiper l'imminence d'une attaque. Cependant, cet écoulement produit dans l'air par des arthropodes en mouvement n'avait jamais été mesuré.

Résultats

Nous présentons dans ce chapitre la mesure par PIV des écoulements générés lors des attaques d'araignées. Ces mesures ont mis en valeur des déplacements d'air importants, jusqu'à plusieurs centimètres en amont du corps de l'araignée. Ainsi, connaissant l'extrême sensibilité du système sensoriel de leur proies (les grillons) à des très faibles vitesses dans l'air, nous montrons que ces écoulements sont aérodynamiquement perceptibles plusieurs centimètres en amont du prédateur.

Discussion

Cette étude explique la distribution bimodale des stratégies d'attaques de de l'araignée. Ces résultats sont aussi compatibles avec les distances de fuites établies lors des précédentes études comportementales réalisées sur les proies. Nous concluons ce chapitre sur les implications de ces découvertes dans le contexte écologique beaucoup plus vaste et diversifié des interactions proies-prédateurs dans les litières.

OPEN ACCESS Freely available online

PLoS one

The Aerodynamic Signature of Running Spiders

Jérôme Casas[1]*, Thomas Steinmann[1], Olivier Dangles[2,3]

1 University of Tours, Institut de Recherches sur la Biologie de l'Insecte, UMR CNRS 6035, 37200 Tours, France, **2** IRD, UR 072, LEGS, UPR 9034, CNRS, 91198 Gif-sur-Yvette, France, **3** Université Paris-Sud 11, 91405 Orsay, France

Abstract

Many predators display two foraging modes, an ambush strategy and a cruising mode. These foraging strategies have been classically studied in energetic, biomechanical and ecological terms, without considering the role of signals produced by predators and perceived by prey. Wolf spiders are a typical example; they hunt in leaf litter either using an ambush strategy or by moving at high speed, taking over unwary prey. Air flow upstream of running spiders is a source of information for escaping prey, such as crickets and cockroaches. However, air displacement by running arthropods has not been previously examined. Here we show, using digital particle image velocimetry, that running spiders are highly conspicuous aerodynamically, due to substantial air displacement detectable up to several centimetres in front of them. This study explains the bimodal distribution of spider's foraging modes in terms of sensory ecology and is consistent with the escape distances and speeds of cricket prey. These findings may be relevant to the large and diverse array of arthropod prey-predator interactions in leaf litter.

Citation: Casas J, Steinmann T, Dangles O (2008) The Aerodynamic Signature of Running Spiders. PLoS ONE 3(5): e2116. doi:10.1371/journal.pone.0002116

Editor: Andrew Iwaniuk, Smithsonian Institution, United States of America

Received January 7, 2008; **Accepted** March 31, 2008; **Published** May 7, 2008

Funding: This work is part of the research conducted within the Cricket Inspired perCeption and Autonomous Decision Automata (CICADA) project (IST-2001-34718) and within the Customized Intelligent Life Inspired Arrays (CILIA) project (FP6-IST-016039). These projects are both funded by the European Community under the "Information Society Technologies-IST" Program, Future and emergent Technologies (FET).

Competing Interests: The authors have declared that no competing interests exist.

* E-mail: casas@univ-tours.fr

Introduction

Many predatory species can switch between foraging modes, usually alternating between an ambush and a cruising mode in water, soil or vegetation. Much care has been taken in evolutionary ecology to evaluate the relative advantages of foraging strategies in terms of energetics, biomechanics, success rate and impact on the ecosystem [1–7]. However, the relationship between the sensory processes involved in signal production by a predator attacking with one of both strategies and the corresponding signal perception by its escaping prey is unknown for most systems. The outcome of this relationship is likely to play an important role in defining the most appropriate predatory foraging mode. For instance, wolf spiders pursue their cricket prey on the bare soil and in leaf litter using two attack strategies [8–10]. Spiders attack prey using either an extremely slow-motion approach, corresponding almost to the ambush strategy, or by running over at relatively high speed (up to 40 cm/s, cruising strategy) [10]. Spiders attack at intermediate speeds much less frequently; biotests using a piston mimicking the attack of a spider showed that a cricket's chances of survival were highest for attacks at intermediate speed (20 cm/s) [10]. Although crickets and many other detritivorous and herbivorous arthropods are sometimes caught unaware by a spider's fast strike, they often escape with fast movements. Information contained in air signals upstream from running spiders can be used by prey in these fast escape reactions. Indeed, crickets, cockroaches and other orthropteroid insects are equipped with air-flow sensors (filiform hairs) at the rear end of their abdomen [11]. They possess many short hairs, serving as acceleration sensors, and fewer long hairs (velocity sensors) on their cerci [12]. These mechanosensors are among the most sensitive sensors in the animal kingdom, with action potentials triggered by less than one tenth the energy of a photon [13]; indeed, the orthropteroid escape system, and in particular fluid flow sensing using filiform hairs, has maintained textbook-example status over many years [14–17]. Thus, we hypothesised that spiders use the two different hunting strategies to cope with optimal air-flow detection by crickets. One strategy (ambush) substantially reduces the distance at which the prey can perceive the attack, while the other strategy (cruising) reduces the escape probability by overwhelming the prey sensory capabilities. The high speed ensures that the encounter occurs faster than the escape response.

The aims of this study were therefore: (1) to quantify the air flow in front of a running spider using digital particle imaging velocimetry (DPIV), and (2) to assess these complex flow patterns in the context of attack and escape strategies by predators and prey. Very little is known about air movements upstream from a running arthropod, limiting potential evaluation of the ecological and evolutionary importance of air-flow sensing for many predator-prey interactions. Near-field fluid movement cues are used by many invertebrate species to obtain information about potential predators, prey or mates, in both terrestrial and aquatic ecosystems. In particular, several recent studies have led to greater understanding of the physics of near-field fluid motion in animal locomotion and sensing in open enclosures. Such technological and conceptual advances have opened up the arena for similar studies on running animals [18–23].

Results

We recorded the air flow produced by wolf spiders (*Pardosa* [*lugubris*] sp., most likely P. *lugubris* (Walkenaer)) running in a small wind tunnel (Figure 1). As spiders dislike the intense laser light sheet, we obtained 14 runs from six different individuals with the

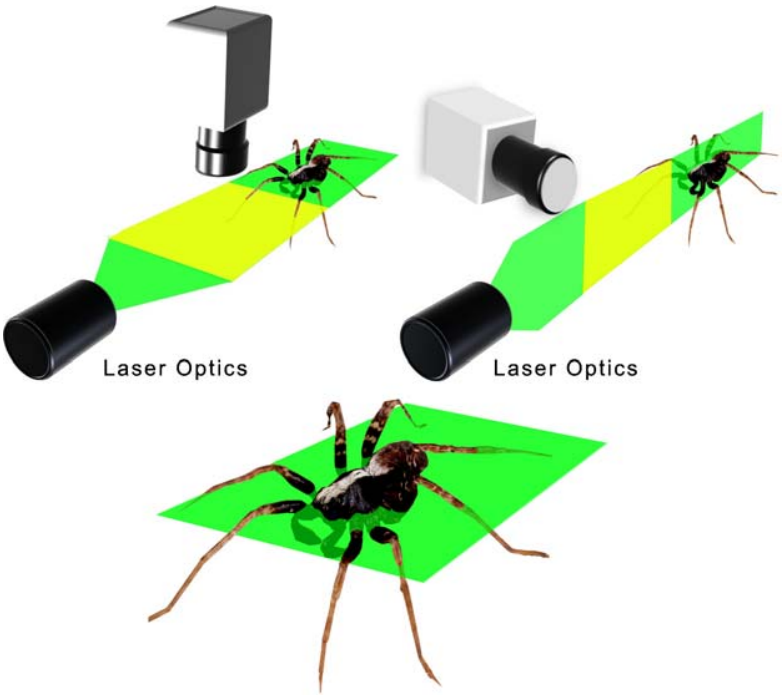

Figure 1. Digital particle image velocity (DPIV) measurements of a running spider. In the horizontal position, the laser light sheet is focussed 3 mm above the floor, at mid-height of the spider, just below the bottom eye row level. The yellow portion represents the camera's field of view. Spiders were gently triggered to run using a stick inserted through a small hole at the entrance of the wind tunnel.
doi:10.1371/journal.pone.0002116.g001

horizontal set-up, but only two runs with the vertical set-up. These were not used in the following quantitative analysis, but gave useful information on several other qualitative aspects of the flow, described below. The mean velocity of the spiders recorded in the horizontal set-up was 9.44 cm/s (SD = ±5.51; N = 14). This lies within the range of attack speeds observed under unconstrained hunting behaviour [10]. One spider ran at a high speed of 40 cm/s. This was an outlier in the velocity distribution, and so was not used to calculate the mean. Running spiders displaced air in front of and above their body trunk (Figures 2 & 3). Pockets of high velocity produced by moving legs could be distinguished and substantially extended the region of flow influenced by the spider (Figure 2). Front legs still produce a forward air movement when moving downwards, as they do not move back and forth (Figure 3B and cartoon on Figure 2). The air field within the first centimetre upstream from a spider varies considerably from run to run because it is not possible to synchronise the PIV clock with the leg kinematics. Thus, depending on the exact moment of flow field mapping, a leg may or may not have a large effect on the flow in its near vicinity (see cartoon, Figure 2). This also explains the absence of relationship observed between the air velocity at 6 mm away from the spider and the spider's body velocity, and our subsequent decision to pool individual runs for a statistical analysis. The air flow upstream from a running spider declines smoothly with distance (Figure 4); a constrained regression, using the function given in (Eq. 2) and the independently measured mean spider's velocity as a fixed parameter, lead to a good fit over the whole range of distances ($R^2 = 0.80$).

Discussion

The air field upstream from a running spider is disturbed over a large distance of several body lengths. The need for prey to perceive attacking predators from as large a distance as possible, using the minimal amount of energy, means that this information is of biological importance. Indeed, previous experimental studies on the air flow produced by attacking toads shooting out their toungs [24] and independent theoretical studies [25] suggested that cockroaches may recognise the wind signature of a predator by the low frequency components in the far field. The most sensitive hairs of crickets are the longest ones (>1000 microns), working near the thermal noise level [13]. Electrophysiological studies estimate their minimal threshold at $V_{thresh} = 30$ μm/s. Thus, using the expected flow velocity upstream from a running spider from the fitted model, this threshold should be attained at around 3 cm in front of a spider. This distance, obtained using the observed mean speed, will vary as a function of the speed of the spider. Crickets seem to make full use of this information, with their largest escape distances being 2.4 cm in front of a spider and 2.1 cm in front of a piston device mimicking the kinematics of the attack [10]. This is most impressive, given the time taken for processing information in the abdominal terminal ganglion, the insect brain, and from leg movements [26]. Thus, the cricket's entire escape system, including sensory and locomotive control, is indeed optimised to pick up the slightest air movements by the best sensors.

The implications of our results for the foraging modes of spiders are twofold. First, spiders markedly increase their likelihood of successful attacks by launching fast strikes, at the same time decreasing the potential escape time (time between danger perception by a cricket and encounter by a spider) in a non-linear fashion (Figure 5). While low speed movements imply high potential escape times, the distance at which prey can perceive predatory signals is so short that prey are nearly within reach of spiders (ambush strategy). Second, their highest speeds may correspond to the lowest potential prey escape time [26]. Such attack speeds are between 25–35 cm/s, corresponding well with

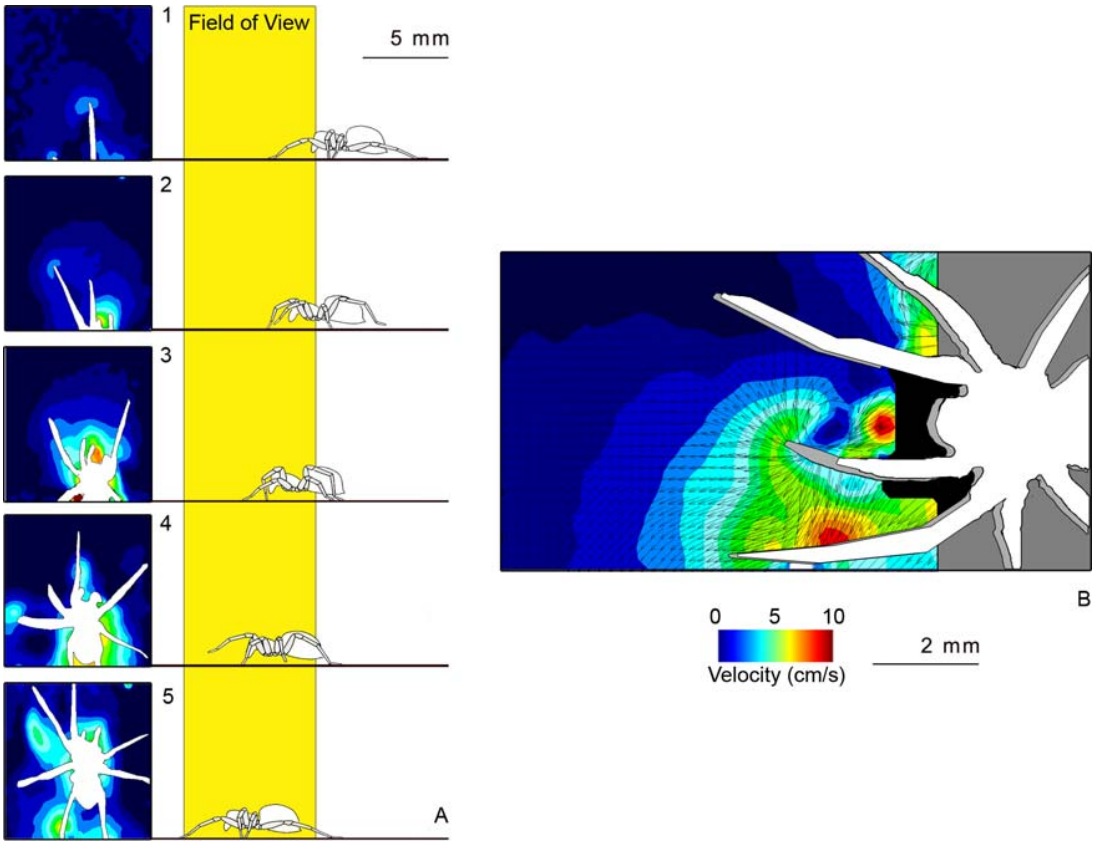

Figure 2. Horizontal flow field and close-up view of the flow around a running spider. The sequence in (A) highlights the pockets of high air-flow velocity created by leg strokes superimposed on the air movements created by the body trunk movement. Neither the tips of the spider's legs, nor their associated flow patterns, are visible as they are located below the light sheet. The time delay between two images is 500 µs; the spider was running at a speed of 5.7 cm/s. The cartoon, adapted from [9], highlights the relative position of legs to body trunk. An overlay of two images (first image in white, second image in grey) of the moving spider, separated by 500 µs, is shown in (B). The zone of flow velocities above the measurable range is in black. The running speed was 10.5 cm/s.
doi:10.1371/journal.pone.0002116.g002

the higher speeds distribution observed during spider-cricket interactions. Higher hunting speeds are seldom observed, as they do not increase the capture rate but are energetically expensive. Thus, our quantification of air flow upstream from a running predator extends the interpretation of the two foraging modes in terms of sensory processes, beyond the classical description in energetic and biomechanical terms. Future studies dedicated to body and leg kinematics should be prioritised, since our understanding of this subject is substantially poorer than that of wing and leg kinematics in insects, and their influence on the upstream flow. The role of acceleration, body posture and height over the substrate [27,28] as well as the nature of the substrate, aspects which we have neglected here, are also expected to have a major impact on the flow field upstream from the spider.

Many other invertebrate predators, including several other arachnid groups, carabid, cincidelid and staphylinid beetles, hunt prey using the same two strategies as those used by spiders. At the same time, many prey living in litter harbour well-developed cerci bearing filiform hairs triggered by slight air movements. These include primitive and modern insects such as bristletails, firebrats, springtails, cockroaches and crickets; indeed, most prey-spider interactions observed today are the same as they were some 400 million years ago [29,30]. For example, cockroaches have been extremely successful and thrive in tropical leaf litter despite strong predator pressure. Our findings demonstrate a significant role of the physical information contained in slight air currents in interspecific interactions among terrestrial arthropods and suggest a tight sensory coevolution between both opponents. Lurking predators may mostly hide and wait for their prey, but the final strike produces conspicuous signals that prey exploit for their survival.

Materials and Methods

DPIV

Our measurement set-up was composed of a sealed glass box (10×2×2 cm), seeded with 0.2 µm oil particles. Oil particles (Di-Ethyl-Hexyl-Sebacat, 0.5 L, TPAS, Dresden, Germany) were generated using an aerosol generator (ATM 230, ACIL, Chatou, France). The laser (NewWave Research Solo PIV 2, Nd:YAG, dual pulsed; Dantec Dynamics A/S, Skovlunde, Denmark) illuminated the flow produced by the spider's displacement through glass. The laser sheet (width = 17 mm, thickness at focus point = 50 µm) was operated at low power (3 mJ at 532 nm) to minimise glare. A target area (17×30 mm) was then imaged onto the CCD array of a digital camera (Photron FastCam X1280 PCI 4K) using a Macro Lens (Nikon, AF Nikkor, 60 mm, f : 2.8). The CCD captured separate image frames (1280×1024 px). Once a sequence of two light pulses was recorded, the images were divided into small subsections which were cross-correlated with each other using flow map software (Flow Manager 4.4. Dantec Dynamics A/S, Skovlunde, Denmark). The

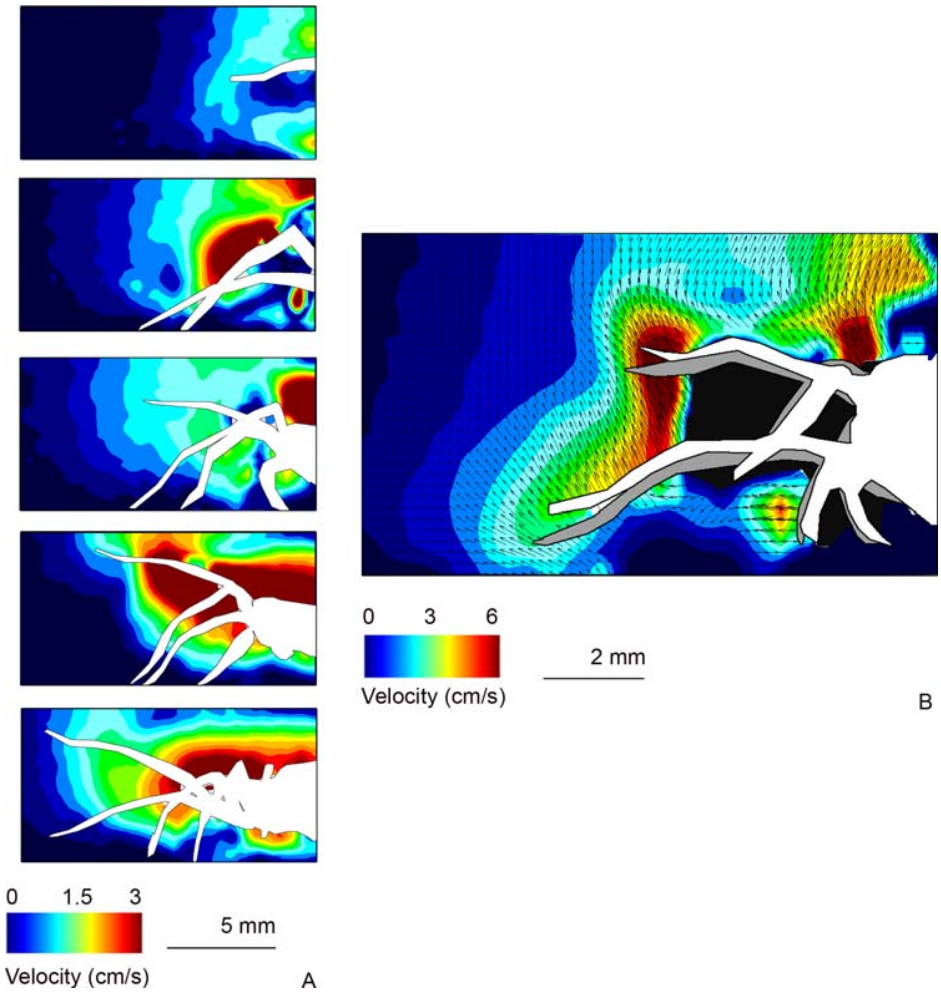

Figure 3. Vertical flow field and close-up view of the flow around a running spider. The sequence in (A) highlights the high air-flow velocity above the spider's body. The time delay between two images is 500 μs; the spider was running at a speed of 3.7 cm/s. An overlay of two images (first image in white, second image in grey) of a moving spider, separated by 500 μs, is shown in (B). The horizontal component of the air flow in the near vicinity of the legs is always directed forward, as front legs do not move back and forth (see cartoon in Figure 2). The running speed was 21 cm/s.
doi:10.1371/journal.pone.0002116.g003

correlation was achieved using an interrogation area of 32×32 pixels, allowing us to obtain valid measurements down to a particle displacement of 0.1 pixels. Using the equation,

$$\sigma_V = \frac{\sigma_{\Delta x}}{\Delta_{time}} = \frac{\sigma_{pix} d_r}{\Delta_{time}} \quad (1)$$

with $\sigma_{\Delta x}$ the minimal displacement measurable (m), $\Delta_{time} = 33$ ms, the time separating two image record and $d_r = 27$ μm the spatial resolution, one obtains the lowest detectable speed of 0.082 mm/s, and of 5.4 mm/s for a time interval of 500 μs. Conversely, with the maximal measurable particle displacement of 32 pixels, the maximal detectable speed is 2.62 cm/s for a time interval of 33 ms, and 17.3 cm/s for a time interval of 500 μs.

Estimation of spider's velocity and profile extraction

Pardosa (Koch) is the most speciose genus among Holarctic wolf spider genera. Several species groups have been recognized, based on characteristics of the copulatory organs [31]. Based upon identification of mature males from our collecting sites, *Pardosa lugubris* (Walkenaer) was the most common species. However, this species was recently shown to incorporate distinct cryptic species whose immature individuals are, to date, impossible to differentiate (Kronestedt 2007). In our experiments, we used only immature spiders because they naturally spend much of their time hunting for prey and not seeking for partners. The mean body size was 3.6 mm (S.D. = 0.2 mm, N = 6). The body size was obtained by measuring the largest width of the prothorax, to which we added the lengths of coxa and the trochanter, as these three body parts act aerodynamically as a single unit. In the studied spiders, this unit was wider than the abdomen. During a single time interval of 33 ms, a spider travelled a distance of 5 mm when moving at a speed of 15 cm/s. There are therefore no data available on flow velocity for the 5 mm space next to the body surface. The distance from the body for which no information was available was greater for greater speeds.

In the horizontal set-up, we took care that the laser light sheet is focused 3 mm above the floor, at mid-height of the spider, just below the bottom eye row level. However, we cannot ascertain that the laser light sheet, which is diverging with an angle of 24°

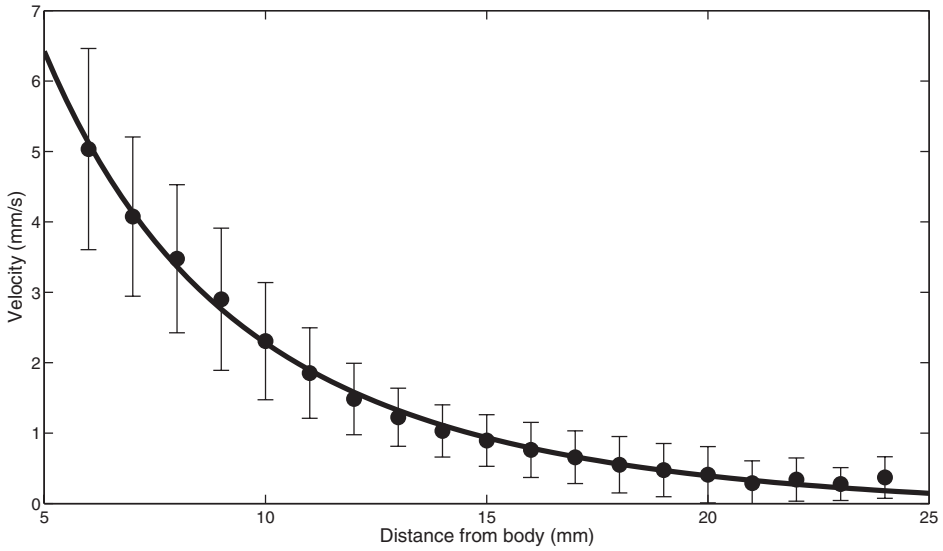

Figure 4. Flow velocity upstream of running spiders. The observed speeds (mean and standard deviation; dots and error bars, respectively), and the fit of the statistical function (Eq. 2) are represented.
doi:10.1371/journal.pone.0002116.g004

from the focal point, did not affect the spider, or during the low phase of the body oscillations. Whatever the amount of light spiders did get, it was much below the intensity of the bulk of the laser sheet, as we would otherwise see the eyes within the light sheet. We observed a tendency to avoid the laser light sheet rapidly in the vertical set-up.

We recorded 14 runs made by six *Pardosa* [*lugubris*] sp. spiders with the horizontal set-up. Measurements were only made when the spider velocity was assumed constant for several centimetres and spiders were running straight. The constant velocity assumption is derived from the measurements in [10] reporting an acceleration phase restricted to one centimetre, followed by a constant velocity. We therefore positioned the field of view of the camera at least 2–3 centimetres away from the entrance of the tunnel. The spider's velocity was determined by measuring the average velocity of the spider's body on a run. A run was restricted

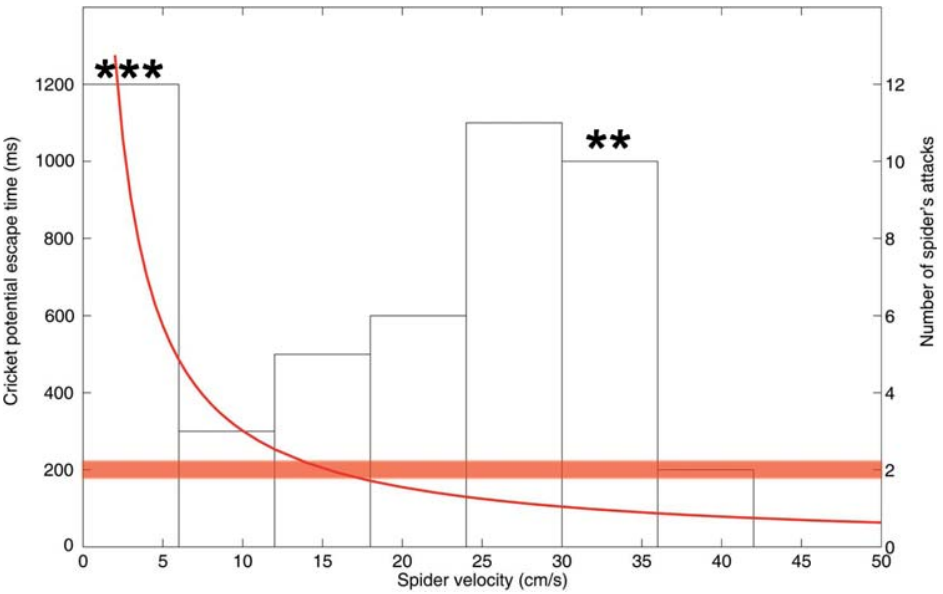

Figure 5. Spider's attack speed and cricket escape time. The potential escape time for a cricket (red line) is expressed as a function of the spider's attack speed. At slow attack speeds, the distance at which crickets can perceive spiders is limiting (ambush strategy), whereas at high hunting speeds, the escape time becomes limiting (cruising strategy). The potential escape time is defined as the time interval between predator perception by a cricket and hit by a spider running at a given speed. It is based on the distance, for a given speed, at which the threshold of 30 μm/s for danger perception is attained [13]. The minimal recorded escape time for crickets is around 0.2 ms (horizontal bar, [26]). The distribution of observed attack speeds and the five successful attacks (stars) were obtained from observations of real attacks, at constant speeds, during cricket-spider interactions [10].
doi:10.1371/journal.pone.0002116.g005

to the pairs of images (varying from one to five pairs) for which the images were of quality high enough for a faithful quantification of air flow. We extracted velocity profiles from the vector fields for each measurement. Profiles were evaluated along the upstream axis. In order to describe the flow velocity as faithfully as possible, we fitted the data with a flexible statistical function:

$$V = V_{body}\left(\frac{1}{6}\frac{A}{\frac{A}{2}+x} + \frac{1}{12}\frac{B^2}{\left(\frac{A}{2}+x\right)^2} + \frac{1}{24}\frac{C^3}{\left(\frac{C}{2}+x\right)^3}\right) \qquad (2)$$

With x being the distance to the spider's body (m), A = 0.0007, B = −0.0011 and C = 0.0179 and V_{body}, the spider's body velocity (0.0944 m/s).

Acknowledgments

We thank the consortium members of CICADA and CILIA teams for discussions, M. Greenfield, G. Krijnen, C. Lazzari, E. McCauley and J. Mogdans, and two reviewers for comments on the MS.

Author Contributions

Conceived and designed the experiments: JC TS OD. Performed the experiments: TS. Analyzed the data: JC TS. Contributed reagents/materials/analysis tools: JC TS. Wrote the paper: JC TS OD.

References

1. Schoener TW (1971) Theory of feeding strategies. Ann Rev Ecol. Sys 2: 369–404.
2. Curio E (1976) The ethology of predation. Berlin: Springer Verlag. 250 p.
3. Huey RB, Pianka ER (1981) Ecological consequences of foraging mode. Ecology 62: 991–999.
4. Kramer DL, McLaughlin RL (2001) The behavioural ecology of intermittent locomotion. Am Zool 41: 137–153.
5. Cooper WE (2005) The foraging mode controversy: both continuous variation and clustering of foraging movements occur. J Zool 267: 179–190.
6. Schmitz O (2007) Predator diversity and trophic interactions. Ecology 88: 2415–2426.
7. Schmitz OJ (2008) Effects of predator hunting mode on grassland ecosystem function. Science 319: 952–954.
8. Riechert SE (1992) Spiders as representative 'Sit and wait' predators. In: Crawley MJ, ed. Natural enemies. London: Blackwell. pp 313–328.
9. Foelix RF (1996) Biology of Spiders. Oxford: Oxford University Press. 330 p.
10. Dangles O, Ory N, Steinmann T, Christides JP, Casas J (2006) Spider's attack vs. cricket's escape: velocity modes determine success. Anim Behav 72: 603–610.
11. Edwards JS, Palka J (1974) The cerci and abdominal giant fibres of the house cricket *Acheta domesticus*. I Anatomy and physiology of normal adults. Proc R Soc Lond B 185: 83–103.
12. Shimozawa T, Kanou M (1984) Varieties of filiform hairs: range fractionation by sensory afferents and cercal interneurons of a cricket. J Comp Physiol A 155: 485–493.
13. Shimozawa T, Murakami J, Kumagai T (2003) Cricket wind receptors: thermal noise for the highest sensitivity known. In: Barth FG, Humphrey JAC, Secomb T, eds. Sensors and sensing in biology and angineering. Berlin: Springer Verlag. pp 145–157.
14. Camhi JM (1984) Neuroethology: Nerve cells and the natural behaviour of animals. Sunderland: Sinauer Associates. 432 p.
15. Tautz J (1989) Medienbewegung in der Sinneswelt der Arthropoden. Stuttgart: Gustav Fischer Verlag. 59 p.
16. Gnatzy W (1996) Digger wasp vs. cricket: neuroethology of a predator-prey interaction. Stuttgart: Gustav Fischer Verlag. 92 p.
17. Dangles O, Casas J, Coolen I (2006) Textbook cricket goes to the field: the ecological scene of the neuroethological play. J Exp Biol 209: 393–398.
18. Dickinson MH, Farely CT, Full RJ, Koehl MAR, Kram R, et al. (2000) How animals move: an integrative view. Science 288: 100–106.
19. Koehl MAR, Koseff JR, Crimaldi JP, Cooper T, McCay M, et al. (2001) Lobster sniffing filters the spatiotemporal information in a turbulent odour plume. Science 294: 1948–1951.
20. Taylor GK, Nudds RL, Thomas ALR (2003) Flying and swimming animals cruise at a strouhal number tuned for high power efficiency. Nature 425: 707–711.
21. Warrick DR, Tobalske BW, Powers DR (2005) Aerodynamics of the hovering hummingbird. Nature 435: 1094–1097.
22. Steinmann T, Casas J, Krijnen G, Dangles O (2006) Air-flow sensitive hairs: boundary layers in oscillatory flows around arthropod appendages. J Exp Biol 209: 4398–4408.
23. Lauder GV, Madden PGA (2008) Advances in comparative physiology from high-speed imaging of animal and fluid motion. Annu Review Physiol; Doi: 10.1146/annurev.physiol.70.113006.100438.
24. Plummer MR, Camhi JM (1981) Discrimination of sensory signals from noise in the escape system of the cockroach: the role of wind acceleration. J Comp Physiol A 142: 347–357.
25. Rinberg D, Davidowitz ÆH (2003) Wind spectra and the response of the cercal system in the cockroach. J Comp Physiol A 189: 867–876.
26. Tauber E, Camhi JF (1995) The wind-evoked escape behaviour of the cricket *Gryllus bimaculatus*: integration of behavioural elements. J Exp Biol 198: 1895–1907.
27. Full RF, Tu MS (1991) Mechanics of a rapid running insect: two-, four-, and six-legged locomotion. J Exp Biol 156: 215–231.
28. Nishikawa K, Biewener AA, Aerts P, Ahn AN, Chiel HJ, et al. (2007) Neuromechanics: an integrative approach for understanding motor control. Integr Comp Biol 47: 16–54.
29. Labandeira CC (2002) Paleobiology of predators, parasitoids, and parasites: death and accommodation in the fossil record of continental invertebrates. Paleo Soc Papers 8: 211–249.
30. Grimaldi D, Engel MS (2005) Evolution of the insects. Cambridge: Cambridge University Press. 755 p.
31. Kronestedt T (2007) A new species of wolf spider from the Pyrenees, with remarks on other species in the Pardosa pullata-group (Araneae, Lycosidae). Zootaxa 1650: 25–40.

Chapitre 6

Modélisations par éléments finis de la signature aérodynamique de l'attaque de l'araignée

Casas, J. & **Steinmann, T.** 2014 Predator-induced flow disturbances alert prey, from the onset of an attack. *Proceedings of The Royal Society B.* 281. (http ://dx.doi.org/10.1098/rspb.2014.1083)

Résumé du chapitre

Nombreuses sont les proies qui, à l'image du grillon des bois, perçoivent au dernier moment l'approche de leur prédateur et déclenchent une action de fuite salvatrice. Ainsi pour le prédateur, les derniers instants précédant la capture de sa proie sont tout aussi important que sa recherche. Cette étude s'inscrit dans le cadre général des études sur les trajectoires conjointes des prédateurs et proies lors de leurs interactions. Elle consiste à estimer le rapport entre les distances auxquelles le prédateur, l'araignée, lance son attaque et celles auxquelles la proie, le grillon des bois, perçoit le danger.

Résultats

Ce chapitre présente l'évaluation par résolution numérique des écoulements d'air générés en amont d'une araignée en mouvement. Les vitesses de l'écoulement, dans un volume de simulation autour d'un modèle très simplifié d'araignée, ont été évaluées en résolvant les équations de Navier & Stokes incompressibles par la méthode des éléments finis. La prise en compte de la taille de son corps, de sa vitesse et de l'effet de sol ont tous été nécessaires pour obtenir une représentation fidèle de la signature aérodynamique de l'attaque de l'araignée, mesurée dans le chapitre précédent. Nous avons en outre déterminé que le mouvement rapide de ses pattes avant ne représentait qu'une contribution mineure dans la génération de cet écoulement susceptible d'avertir la proie de sa présence. Nous avons établi que la relation entre la vitesse d'attaque et la distance maximale à laquelle le grillon pouvait percevoir le danger était parabolique.

Discussion

Cette relation parabolique, vitesse d'attaque/distance de perception, divise l'espace délimité par ces deux variables en deux régions distinctes. Pour certaines vitesses d'attaque, le rapport entre la distance de perception et la distance d'attaque est supérieure à un. Ce sont des zones dans lesquelles une attaque a de grande chance de se traduire par un succès. Cependant dans le contexte particulier de l'interaction entre le grillon et l'araignée, ce rapport ne dépasse pas un, impliquant la perception immédiate du danger dès le début de l'attaque. Cette perception très précoce se rencontre dans de nombreuses autres interactions proies prédateurs. Elle peut, dans tous ces cas, avoir de grandes conséquences sur les capacités des prédateurs à anticiper les mouvements de leurs proies respectives.

PROCEEDINGS OF THE ROYAL SOCIETY B

rspb.royalsocietypublishing.org

Research

Cite this article: Casas J, Steinmann T. 2014 Predator-induced flow disturbances alert prey, from the onset of an attack. *Proc. R. Soc. B* **281**: 20141083.
http://dx.doi.org/10.1098/rspb.2014.1083

Received: 5 May 2014
Accepted: 24 June 2014

Subject Areas:
biomechanics, biophysics, behaviour

Keywords:
sensory ecology, predator–prey interactions, flow sensing, danger perception, ground effect

Author for correspondence:
Jérôme Casas
e-mail: jerome.casas@univ-tours.fr

Electronic supplementary material is available at http://dx.doi.org/10.1098/rspb.2014.1083 or via http://rspb.royalsocietypublishing.org.

Royal Society Publishing

Predator-induced flow disturbances alert prey, from the onset of an attack

Jérôme Casas and Thomas Steinmann

Institut Universitaire de France IUF and Institut de Recherche sur la Biologie de l'Insecte, University of Tours, IRBI UMR CNRS 7261, Av. Monge, 37200 Tours, France

Many prey species, from soil arthropods to fish, perceive the approach of predators, allowing them to escape just in time. Thus, prey capture is as important to predators as prey finding. We extend an existing framework for understanding the conjoint trajectories of predator and prey after encounters, by estimating the ratio of predator attack and prey danger perception distances, and apply it to wolf spiders attacking wood crickets. Disturbances to air flow upstream from running spiders, which are sensed by crickets, were assessed by computational fluid dynamics with the finite-elements method for a much simplified spider model: body size, speed and ground effect were all required to obtain a faithful representation of the aerodynamic signature of the spider, with the legs making only a minor contribution. The relationship between attack speed and the maximal distance at which the cricket can perceive the danger is parabolic; it splits the space defined by these two variables into regions differing in their values for this ratio. For this biological interaction, the ratio is no greater than one, implying immediate perception of the danger, from the onset of attack. Particular attention should be paid to the ecomechanical aspects of interactions with such small ratio, because of the high degree of bidirectional coupling of the behaviour of the two protagonists. This conclusion applies to several other predator–prey systems with sensory ecologies based on flow sensing, in air and water.

1. Introduction

Predation involves a sequence of steps, starting with prey encounter, followed by prey detection, identification, attack and subjugation, and ending with consumption [1]. It is difficult to assess the chances of predation success for each of the steps in this sequence in natural conditions, as few studies have been carried out on entire predation sequences. One such study, a field study of over 2000 predator–prey interactions between crab spiders and their prey community, found that the probability of completing each step plummeted along the predation sequence, from over 50% for the first step after encounter (i.e. landing on an occupied flower), to much less than 10% for the final strike [2]. As these probabilities must be multiplied to give the overall probability of success, the probability of prey capture was estimated at 3.5% for prey alighting on an inflorescence harbouring a spider, consistent with the low success rates reported in other studies [3,4]. Studies on wild ranging carnivores and raptor birds have also yielded low estimates of capture success [5]. Thus, encountering a prey is only the first step; the predator must then subdue and capture the prey, and these steps are just as important as finding the prey in the first place.

For these and many other predator–prey interactions, the final steps of a close range interaction are often rapid and violent, stretching the physiological responses of both protagonists to their limits. For example, mantis shrimps exert extraordinary smashing forces on mollusc shells, to such a point that they may cause water cavitation [6]. The C-start of small fishes escaping predators is also very powerful [7,8]. It is during these final steps of behavioural interactions that ecomechanics—fluid dynamics and solid mechanics in an ecological context—connect sensing, moving and behavioural ecology, determining the final success or failure of capture [9]. A framework for understanding the conjoint trajectories of predator and prey and their ecomechanics during the final steps

of the interaction is thus required, also to understand the longer term coevolutionary forces that shape the strategies used [10–12].

Such a framework can be developed from another recently developed framework focusing on predator sensory ecology [13]. This framework relates sensory distance, the distance at which a prey is sensed, to the motor distance of a predator, the distance that the predator requires to stop before swallowing a prey, for example. What really matters is the set of locations that can be reached in a given time. We therefore refer here to distances rather than volumes (as in the original study), to simplify presentation. The ratio of sensory distance to motor distance provides considerable insights into behavioural and biomechanical control strategies, such as the minimal turning radius and other kinematic aspects relating to predator inertia. This ratio can also be used to distinguish between different types of attack mode. In the 'collision' mode, the sensory distance is smaller than the motor distance required for the predator to come to a halt: predators literally crash into their prey. The 'deliberative' mode, typical of dolphin echolocation and of visual predators, for example, is essentially the opposite situation and occurs when the ratio is high. Other examples are provided by birds of prey high in the air swooping down on a rodent on the ground and cheetahs hunting impalas over hundreds of metres [14]. This mode is typical of predators using an active 'find-and-destroy' strategy in which the predator may change course during action ('after deliberation'). The 'reactive' mode corresponds to a ratio of about one, as seen in knifefish, for example [13]. This mode of attack involves the rapid, direct coupling of sensation and action. Predators can also switch from a deliberative mode to a reactive mode at shorter distances from their target, as in echolocating porpoises [15].

This framework uses the predator as the focal point, but neglects the prey. It can be extended to pairs of predator and prey, by defining two different distances: the distance required for the predator to instigate an attack and the maximal distance at which the prey can perceive the danger. The first of these distances is observed during an interaction, whereas the second must be inferred from a combination of the conspicuousness of the predator and the sensory abilities of the prey. The reference frame for this new framework is thus shifted from the predator to the predator–prey pair. The ratio of these two distances (i.e. attack to perception) provides an appreciation of the combined ecomechanical factors influencing attack and escape strategies that no study focusing on a single participant can provide [12].

The interaction between *Pardosa* sp., wolf spiders, and *Nemobius sylvestris*, wood crickets, is amenable to such analyses based on this ratio of predator attack and prey danger perception distances. Wolf spiders and wood crickets constitute a predator–prey system for which conjoint pursuit–escape trajectories and respective strategies are unusually well understood in both controlled and natural settings ([16] and references therein). Wolf spiders have a bimodal hunting strategy combining a true 'sit-and-wait' strategy, in which crickets must be within reach to trigger spider attack, with an active 'sit-and-pursue' strategy [17–19]. Crickets have developed a very sensitive early warning system [20]. This system, based on filiform hairs, senses the faintest of air flows produced by attacking spiders. It sets the danger perception threshold, which has been estimated at 30 $\mu m\ s^{-1}$ [20], and is thus a key element determining the probability of the cricket escaping. Estimates of both spider attack distances and maximal cricket danger perception distances are required to estimate the ratio. Attack distances have already been measured in the laboratory and in the field [16]. Indeed, we previously showed that spiders attack their cricket prey at a distance of some 3 cm on leaf litter and that this distance is doubled if the predator and prey are located on a flat surface, such as a Petri dish [16]. In this study, we aimed to estimate the second, more difficult half of the ratio, the maximal danger perception distance of crickets as function of the speed of attacking spiders. This requires faithful predictions of the air disturbances upstream from an attacking spider from modelling of the relative contributions of the main body, legs and ground effect to flow amplitude as a function of the distance to a spider. Using the threshold for the perception of flow velocities by crickets cited above as a cutoff value, we can then calculate the second distance and, thus, the ratio.

We used a three-step approach. We first designed a three-sphere computational model of a running spider and estimated the deformations of air flow around it by computational fluid dynamics (CFD) with the finite-element method (FEM). This oversimplified, but classical approximation is discussed below. The CFD–FEM approach involves the efficient numerical solution of the Navier–Stokes equations describing fluid dynamics and is most suitable for complex problems for which analytical solutions do not exist [21]. These technical aspects are outlined in the electronic supplementary material, appendix. Once the computational algorithm was deemed appropriate, we then compared the computed flow disturbances of our running spider model with previously published experimental data for the flow disturbances created by spiders running at an intermediate speed of about 10 $cm\ s^{-1}$. Once the contribution of the different body parts to air flow had been estimated and the complete model had been accepted, we explored the entire range of observed values for attack speed, running the model from 0 to 40 $cm\ s^{-1}$. Each attack speed produced a different volumetric field of velocities, from which we extracted the cricket danger perception distance as a function of spider speed.

2. Material and methods

We will first describe the geometric elements used to model moving spiders. The model is highly simplified, but remains too complex for analytical calculation of the upstream flow. A CFD–FEM numerical scheme must therefore be used to solve the full Navier–Stokes equation. However, we first needed to check that our implementation of the FEM was correct. We did this by experimentally exploring the two limiting cases of very slow and fast translation of a single sphere and by testing our FEM model on these well-known cases. The observed flow disturbances and model predictions were then compared with analytical approximations of the Navier–Stokes equation available for these highly simplified situations. Once these comparisons had been carried out and we had confirmed that the FEM implementation was appropriate, we applied it to the full Navier–Stokes equations for the three-sphere model of a running spider.

(a) Spider kinematics and modelling of constitutive elements

We describe here the rationale underlying our model of a running spider and the estimation of its parameters. A running spider is modelled as an ensemble of three spheres: one for the body trunk, and the other two for the front leg tips. Schematically,

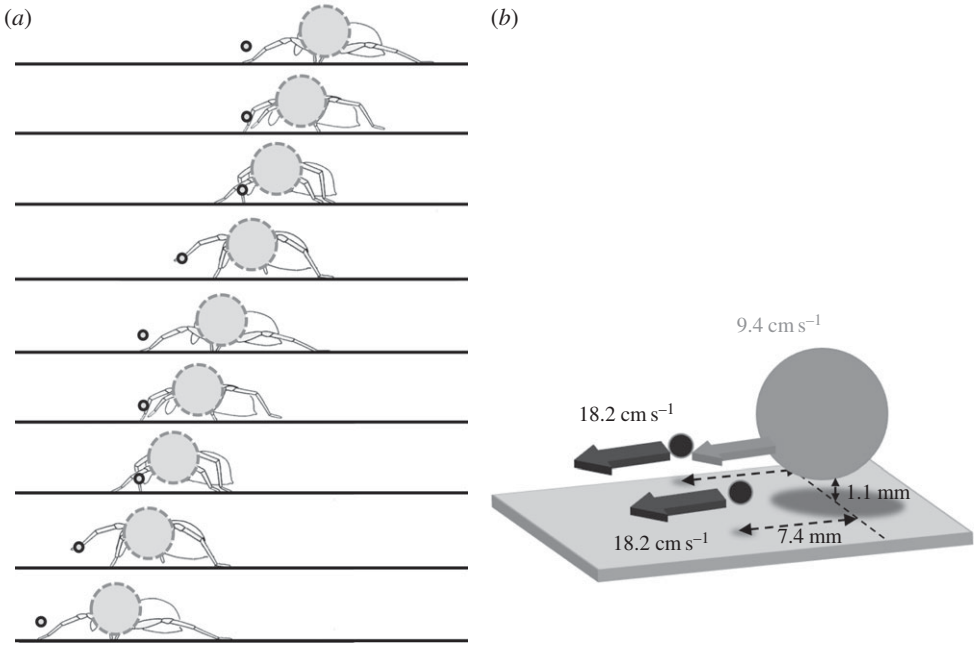

Figure 1. Establishment of the CFD model of a running spider. (*a*) A schematic of the kinematics of a running spider showing that the body trunk moves at constant speed, whereas the legs move intermittently, at a speed at most twice that of the body trunk (*b*). The body trunk is modelled by a sphere of the spider size and the leg tips are modelled as spheres with diameters identical to that of the metatarsus. Parameter values are set such that the computed flow disturbances correspond to the extreme cases defining a volume of flow velocities corresponding to the least favourable situation for spiders, i.e. the maximal danger perception distance for crickets.

spider bodies move at a constant velocity, whereas the front legs alternate between high-speed movements and periods in a stationary position (figure 1*a*,*b*). A first approximation for the body is to consider it as a sphere with diameter identical to the spider body size diameter. The flow perturbations reaching the furthest distances from the spider are generated when the moving legs are in maximal extension. We modelled only the tips of the legs, using a diameter corresponding to the diameter of the tarsus. When the legs are motionless and close to the body, they act together as a single aerodynamic unit. When they move, the legs move at the same time, in a single plane, with constant speed (figure 1*b*).

The estimation of body and leg velocities and of the geometric relationships between the different elements of the model was based on 14 recorded runs made by six spiders in a previous study by Casas *et al.* [18]. Mean body size (3.6 mm, s.d. = 0.2 mm, $n = 6$) was estimated by adding coxa and trochanter lengths to the width of the prothorax at its widest part, as these three body parts act aerodynamically as a single unit. In the spiders studied, this unit was wider than the abdomen. The diameter of the metatarsus (0.37 mm, s.d. = 0.027 mm, $n = 6$) was estimated at the point at which the laser sheet crossed a leg. The distances between the two front legs and between the front legs and the body trunk were also measured at these points. Spider velocity was determined by measuring the mean velocity of the spider body on a run long enough for the extraction of a meaningful value. Speed measurements were made only if spider velocity remained constant for several centimetres and spiders were running in a straight line. Another set of six spiders was used to estimate height above the ground in the same set-up and conditions, but with a different, side of view. The distance from the ground to the lowest point of the opisthosoma was 1.1 mm (s.d. = 0.2 mm, $n = 6$).

Mean body speed was 9.44 cm s^{-1} (s.d. = 5.5 cm s^{-1}, $n = 14$ measured on six spiders), with minimal and maximal observed values of 3 and 20 cm s^{-1}, respectively. The legs moved at twice the speed of the body trunk (mean leg speed = 18.24 cm s^{-1}, s.d. = 9.05 cm s^{-1}, $n = 18$ on six spiders). The distance between the body and the legs, measuring from their respective centres, was 7.4 mm (s.d. = 0.2 mm, $n = 11$ on six spiders) at their most distant point in the air.

(b) Finite-element computations of the Navier–Stokes equations for the three spheres spider model

Once the CFD–FEM implementation of a single translating sphere had been validated (see the electronic supplementary material, appendix), we used this implementation to solve the full three-dimensional incompressible Navier–Stokes equation for a three-sphere spider model immersed in an immobile fluid (air: $\eta_{air} = 1.56 \times 10^{-5}$ m^2 s^{-1} and $\rho_{air} = 1.1774$ kg m^{-3}). The distance to the walls in the spider direction was set to 20 cm (corresponding to over 50 body lengths), as no change in velocity was observed with further expansions of the simulation volume. The distance between the centres of the three spheres and the ground was 2.9 mm. The simulations were run in a volume of $20 \times 7 \times 2$ cm, subdivided into 6000 triangular elements by automatic recursive and adaptive meshing with the Delaunay algorithm. The Navier–Stokes equation was solved with a stationary solver (GMRES linear system solver) in the COMSOL Multiphysics package (COMSOL Multiphysics 3.3, COMSOL AB., 2006).

(c) Comparing model output between models and with observations

The output of the model is a volumetric field of velocities filling the entire simulation domain. Using an air velocity perception threshold for crickets of 30 μm s^{-1}, we were able to define another volumetric field of velocities within the original simulation volume, the surface of which corresponded to this threshold value. The flow velocities contained within this new volume, itself smaller than the simulation volume and irregular in shape, are, by definition, all above the cricket's perception threshold. The maximal extent of this volume in the direction of the cricket is the maximal danger perception distance. It can be extracted by the definition of two additional planes crossing the volume. One of these planes is vertical, located between the legs of the spider and spanning the distance between the spider and the cricket. The other plane is horizontal and crosses

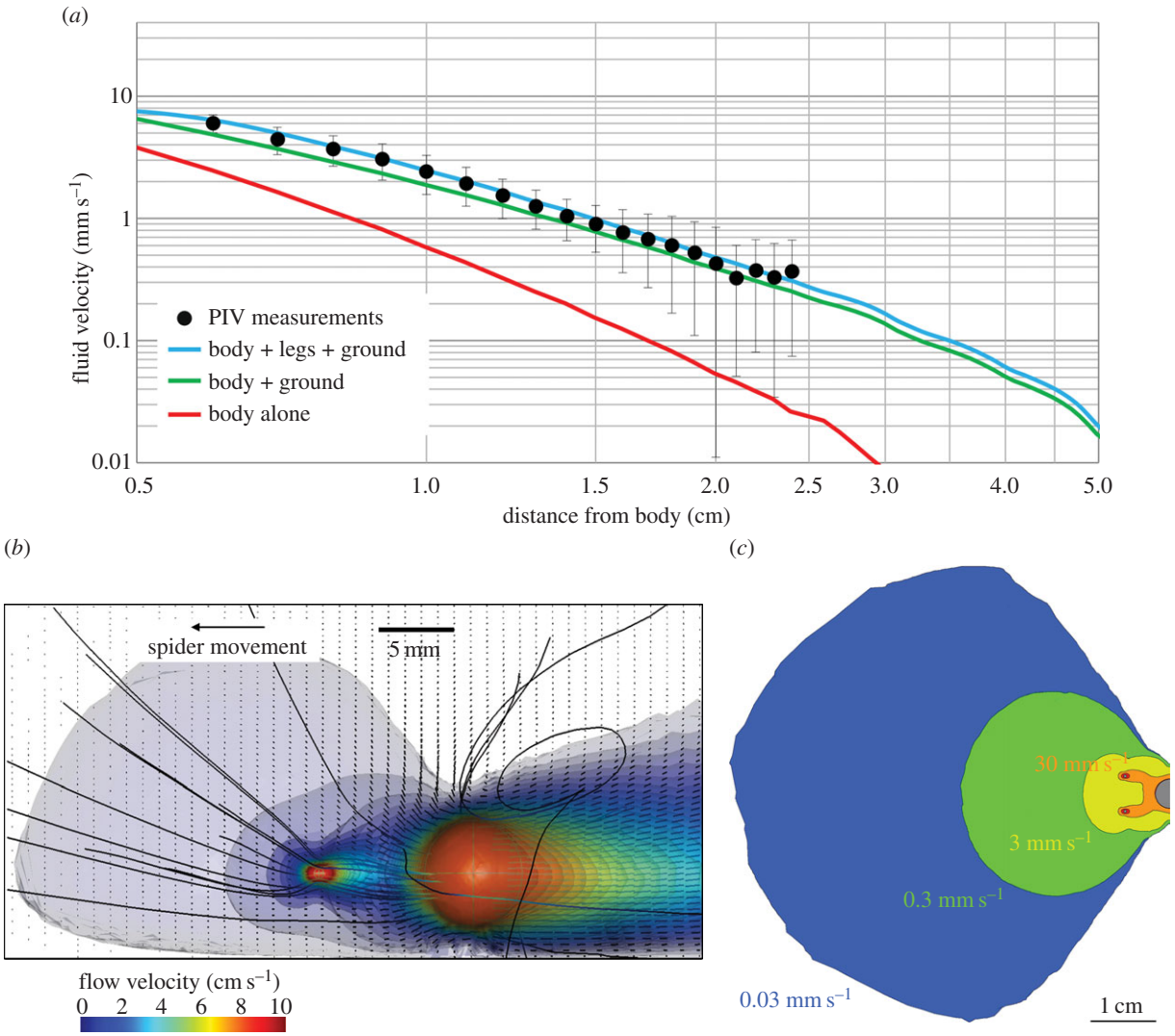

Figure 2. Maximal flow disturbances upstream from an attacking spider moving at a speed of 9.5 cm s^{-1}. (*a*) Contributions of the body trunk, legs and ground effect to flow speed at spider mid-height, as calculated from the CFD model. The red line is the flow computed for the body alone, the green line corresponds to the body plus the ground effect and the blue line corresponds to the body plus the ground effect and the legs. The measurement points and their confidence intervals, in black, are taken from Casas *et al*. [18]. (*b*) The isosurfaces on the side view represent the external surface of a volume of velocities over a given velocity threshold level. The lowest level, in light blue, corresponds to velocities over 2.1 mm s^{-1}. The vector field represents the direction and speed of flow. The asymmetry of the streamlines and the contours of the velocity volumes indicates the large impact of the ground effect. (*c*) Five isosurfaces of different flow velocities in the horizontal plane at leg height. Each isosurface, from dark blue to orange, represents a surface with internal velocities greater than 30 µm s^{-1}, 300 µm s^{-1}, 3 mm s^{-1}, 3 cm s^{-1} and 9 cm s^{-1}, respectively. All parameters were set as in figure 1*b*.

the centre of the leg tips at the instant at which they are extended furthest from the body and moving (figure 1*b*). The maximal danger perception distance thus provides a snapshot within a cycle of continuous leg movements. From the spider's point of view, larger danger perception distances are the least advantageous. Our approach, in which leg kinematics are modelled by computing only the largest volume of velocities, and hence maximum perception distance, is analogous to the study of analytically unsolvable differential equations in applied mathematics: super- and sub-solutions are obtained to yield encompassing solutions without taking into account the complex dynamics between them [22]. We did not use statistical approaches, such as AIC and allied summaries of goodness-of-fit, to compare models, because our approach was clearly not statistical in nature [23].

3. Results

The spider is at the greatest disadvantage with respect to its prey when the legs are maximally extended, as this maximal extension and the high speed of the legs increase flow disturbances. Flow velocities therefore peak at this point in the leg movement cycle, maximizing the information available to the cricket prey.

The Reynolds number of attacking spiders can be estimated from spider size (3.6 mm) and velocity (from 1 to 40 cm s^{-1}). The Reynolds number of attacking spiders is therefore approximately 2–90, for the highest speeds.

Our CFD–FEM computational solution of the full Navier–Stokes equation for a simplified three-sphere spider model reproduced flow velocities similar to those observed for spiders running at the mean speed (figure 2*a*). However, it was not sufficient to take only the body into account. The ground effect had to be incorporated to achieve a good fit. The further addition of the front legs improved the fit, albeit to a much lesser degree. The strong ground effect was best assessed by extracting the flow disturbances perpendicular to the ground and considering the asymmetry of both the streamlines and the isosurfaces (figure 2*b*). At the observed mean

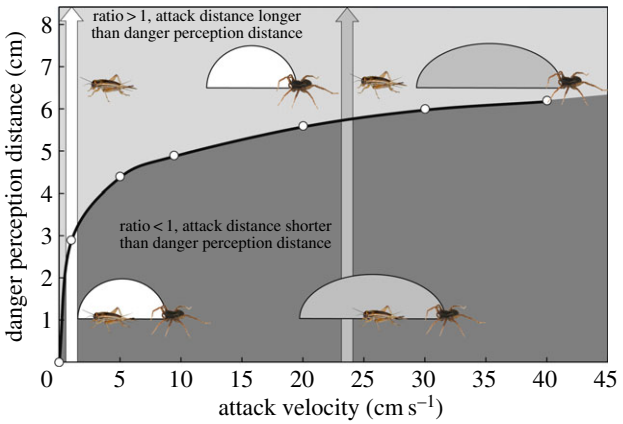

Figure 3. Maximal danger perception distances in crickets, as a function of spider attack velocity. These distances depend on the aerodynamic conspicuousness of spiders and the sensory abilities of crickets. The maximal flow velocities created by the three-sphere spider model were first extracted from the volume of flow velocities according to a procedure described in the main text. A cutoff value of 30 $\mu m\ s^{-1}$, corresponding to the cricket flow perception threshold, was applied, to define the maximal danger perception distance. The relationship between the attack speed and the maximal danger perception distance splits the space defined by these two variables into two regions differing in their values for the ratio of attack to danger perception distances. For a given attack speed, spiders launching their attack from a distance below the curve will be sensed from onset of the attack. By contrast, the spider has a head-start over its prey if it launches its attack from further away. This is illustrated for a low and a high attack speed. (Online version in colour.)

speed, the threshold velocity of 30 $\mu m\ s^{-1}$ for air flow disturbances was reached at a distance of up to 5 cm from the spider (figure 2*c*). Furthermore, thresholds two orders of magnitude above the nominal threshold are reached at a distance equivalent to about one body length of the predator. Such distances are still relatively large and allow escape.

The monotonous increase in the maximal distance at which spiders are perceived by crickets as a function of spider speed is a consequence of increasing spider attack velocity, resulting in greater flow disturbances (figure 3). The speed of the spider is considered to be constant during the attack, but differs between attacks.

4. Discussion

Spiders attack crickets at intermediate flow regimes, characterized by Reynolds numbers of approximately 2–90. This implies that both inertial and viscous forces must be taken into account when modelling upstream flow disturbances and that analytical approximations break down. CFD–FEM is the tool of choice for calculating flow disturbances for such intermediate regimes. This numerical method is also routinely used to compute the flow disturbances of copepods, which swim at similar Reynolds numbers [24].

Our computational results demonstrate that the upstream flow generated by running spiders can be faithfully represented with a small number of factors—body size, speed and height above ground—providing information about the role of all body parts in generating flow disturbances. Our findings are consistent with previous studies of swimming copepods, which also identified body shape, body speed and orientation as the principal factors determining the flow field around the body [25–29]. By contrast, the complex motion patterns of beating appendages are of major importance in copepods, whereas the legs of spiders make only a minor contribution to upstream air velocity. Spider legs have marked influence only when fully extended, resulting in an increase in effective body size. This difference in the importance of the contribution of appendages to flow disturbances between spiders and copepods cannot be explained by Reynolds numbers, which are similar for both species. Instead, it may reflect differences in the number of appendages (greater in copepods), their plane of motion with respect to that of the body and the absence of a ground effect in a water column. Indeed, the relatively large ground effect may decrease the relative importance of leg movements in the production of air flow disturbances by spiders. The precise and complete tracking of leg kinematics and more sophisticated models are required to improve our understanding of the role of legs in generating disturbances to air flow in front of moving animals.

The parabolic relationship between spider speed and flow perception explains the benefits of the bimodal—'sit-and-wait' and 'sit-and-pursue'—attack strategy of the spider [17,19]. Moving at very low speed results in the generation of a negligible signal. Running at high speed enables the spider to overcome the warning and escape system of the prey even if highly conspicuous. Running at low and intermediate speeds does not render the spider less conspicuous to its prey and may be highly disadvantageous, allowing the prey more time to escape. These implications are consistent with previous findings [17], despite the erroneous assumption used in this previous study, and by Kant & Humphrey [30]. The lack of estimation and simulation of leg and ground effects in these two papers, two elements magnifying flow disturbances, resulted in a need to double the body size with respect to observations to achieve an appropriate fit. Both papers tended to overestimate the rate of decrease in flow velocity disturbance in front of the spider due to the explicit [30] or implicit [17] assumption that the flow was a potential flow, whatever the spider attack velocities. As a result, these two papers underestimated both the maximal distance at which crickets were able to sense attacking spiders of realistic sizes and the continuous increase in this distance with increasing speed.

Expanding the framework of predator sensory and control distances to predator–prey pairs highlights differences in the degree of overlap between predator attack and prey escape distances [17,31]. In terms of the dichotomous classification of attack modes described in the Introduction, the 'sit-and-wait' mode may be considered to be an extreme case in which the attack distance is almost zero, as the prey approaches a stationary predator. As a corollary, the attack speed is also almost zero, implying that there is no danger perception distance. By contrast, the 'active search' mode can generate a whole range of ratios of attack to danger perception distances, as a function of the speed of the spider. We previously showed that spiders attack their cricket prey at a distance of 3–6 cm, depending on the substrate [16]. We show here that the cricket is able to perceive the danger over distances of approximately 3 cm for low attack speeds and up to 6 cm for the highest running speeds. For a given spider running speed, the ratio is thus usually about or slightly below one. Ratios greater than one are typical of situations in which the spider launches a targeted attack from a large distance on an as yet unwary prey. Such ratios are not

common in our biological system for two reasons. First, the densities of wood crickets and wolf spiders are often high (up to 400 and 50 individuals per square metre, respectively, [32]), so the mean distance between the predator and its prey is often no more than a few centimetres. Furthermore, the architectural complexity of the leaf litter makes long-range attacks almost impossible: leaf fragments in the leaf litter are only about 3 cm long [16]. Thus, even at low cricket densities, the architecture of the leaf litter habitat makes it very difficult for the spider to launch a long-distance attack. In another study in a different system, in grassland vegetation, ranging spiders and their grasshopper prey were often found at short distances from each other, only a few centimetres apart [19]. We therefore conclude that the ratio of predator attack distance to prey danger perception distance is often about one or lower, in both systems. This conclusion may also apply to the myriad of other predator–prey systems within the soil and in highly structured habitats, such as vegetation.

The implications of these findings are twofold. First, there are ecomechanical implications concerning a large range of unrelated characteristics pertaining to the manoeuverability and capture capabilities of spiders in the final instants of the interaction, the subjugation of the prey. Very little is known about these aspects, and the kinematics of spider leg movements during prey capture are almost entirely unknown. This contrasts strongly with the situation for similar studies on mouth movements in suction feeding fishes during close-range prey capture [33]. For prey crickets, our findings suggest that future studies should focus on the hitherto neglected aspects of danger identification and motor control during escape, echoing recent neurophysiological studies on the cercal response to stimuli with various spatial and temporal patterns [34,35]. These aspects have been little studied in most invertebrate predator–prey systems. Second, our findings have ecological implications concerning the importance of the post-encounter steps within a predation sequence in predator–prey interactions. Indeed, for ratios greater than one, attention should be focused on the foraging predator, with the prey considered to be non-interacting. The probability of prey capture may then be considered to be either constant, depending on some phenotypic characteristic of the prey [36,37], or dependent purely on the state of the predator, with satiated predators often less successful [38]. By contrast, a strong bidirectional coupling of the behaviour of the two antagonists would be expected, from the start of the attack, for ratios close to and below one. Another example of this is provided by the attacks of plankton-feeding fish on evasive copepods [39]. These fish, which detect their prey visually, launch attacks at distances of a couple of millimetres from the prey. The danger perception distances of the prey are much larger, owing to the bow wave generated by the moving fish. However, these fish mostly succeed in capturing their prey by generating 'compensatory suction'. They suck water into their mouths, thereby decreasing the unintentional signal emitted in the plane of the prey: a hydrodynamic stealth mode of prey capture. In situations characterized by a ratio no greater than one, capture probability is a function of a larger number of variables. Not only are the ecomechanical properties of the two antagonists important, as in the former case, but the bidirectional coupling of the behaviour of predator and prey must also be taken into account. Wood crickets and wolf spiders on the forest floor, grasshoppers and spiders in grassland vegetation and plankton-feeding fishes and copepods in water constitute predator–prey systems in which sensory ecology during attack is heavily based on flow sensing. They are also characterized by the unintentional production of aero- and hydrodynamic signals by the predator from the onset of an attack. A systematic survey of other predator–prey interactions based on different sensory ecologies would give insight into their positioning in terms of the degree of coupling during attack.

Acknowledgements. We thank A. Landres, O. Dangles, S. Pincebourde and S. Sane for their numerous comments on a previous version of the manuscript and the subject matter editor and the referees for their incisive comments.

References

1. Endler JA. 1991 Interactions between predators and prey. In *Behavioural ecology: an evolutionary approach* (eds JR Krebs, NB Davies), pp. 169–196. Oxford, UK: Blackwell Scientific.
2. Brechbühl R, Casas J, Bacher S. 2011 Diet choice of a predator in the wild: missed opportunities along the prey capture sequence. *Ecosphere* **2**, art 133. (doi:10.1890/ES11-00323.1)
3. Reader T, Higginson AD, Barnard CJ, Gilbert FS, and The Behavioral Ecology Field Course. 2006 The effects of predation risk from crab spiders on bee foraging behavior. *Behav. Ecol.* **17**, 933–939. (doi:10.1093/beheco/arl027)
4. Morse DH. 1979 Prey capture by the crab spider *Misumena calycina* (Araneae: Thomisidae). *Oecologia* **39**, 309–319. (doi:10.1007/BF00345442)
5. Curio E. 1976 *The ethology of predation*. Berlin, Germany: Springer.
6. Patek SN, Korff WL, Caldwell RL. 2004 Biomechanics: deadly strike mechanism of a mantis shrimp. *Nature* **428**, 819–820. (doi:10.1038/428819a)
7. Stewart WJ, Cardenas GS, McHenry MJ. 2013 Zebrafish larvae evade predators by sensing water flow. *J. Exp. Biol.* **216**, 388–398. (doi:10.1242/jeb.072751)
8. Domenici P, Blagburn JM, Bacon JP. 2011 Animal escapology I: theoretical issues and emerging trends in escape trajectories. *J. Exp. Biol.* **214**, 2463–2473. (doi:10.1242/jeb.029652)
9. Denny M, Helmuth B. 2009 Confronting the physiological bottleneck: a challenge from ecomechanics. *Integr. Comp. Biol.* **49**, 197–201. (doi:10.1093/icb/icp070)
10. Abrams PA. 2000 The evolution of predator–prey interactions: theory and evidence. *Annu. Rev. Ecol. Evol. Syst.* **31**, 79–105. (doi:10.2307/221726)
11. Lima SL. 2002 Putting predators back into behavioral predator–prey interactions. *Trends Ecol. Evol.* **17**, 70–75. (doi:10.1016/S0169-5347(01)02393-X)
12. Combes SA, Rundle DE, Iwasaki JM, Crall JD. 2012 Linking biomechanics and ecology through predator–prey interactions: flight performance of dragonflies and their prey. *J. Exp. Biol.* **215**, 903–913. (doi:10.1242/jeb.059394)
13. Snyder JB, Nelson ME, Burdick JW, MacIver MA. 2007 Omnidirectional sensory and motor volumes in electric fish. *PLoS Biol.* **5**, e301. (doi:10.1371/journal.pbio.0050301)
14. Wilson AM, Lowe JC, Roskilly K, Hudson PE, Golabek JKA, McNutt JW. 2013 Locomotion dynamics of hunting in wild cheetahs. *Nature* **498**, 185–189. (doi:10.1038/nature12295)
15. Wisniewska DM, Johnson M, Beedholm K, Wahlberg M, Madsen PT. 2012 Acoustic gaze adjustments during active target selection in echolocating porpoises. *J. Exp. Biol.* **215**, 4358–4373. (doi:10.1242/jeb.074013)
16. Morice S, Pincebourde S, Darboux F, Kaiser W, Casas J. 2013 Predator–prey pursuit–evasion games in

structurally complex environments. *Integr. Comp. Biol.* **53**, 767–779. (doi:10.1093/icb/ict061)

17. Dangles O, Ory N, Steinmann T, Christides J-P, Casas J. 2006 Spider's attack versus cricket's escape: velocity modes determine success. *Anim. Behav.* **72**, 603–610. (doi:10.1016/j.anbehav.2005.11.018)
18. Casas J, Steinmann T, Dangles O. 2008 The aerodynamic signature of running spiders. *PLoS ONE* **3**, e2116. (doi:10.1371/journal.pone.0002116)
19. Miller JRB, Ament JM, Schmitz OJ. 2014 Fear on the move: predator hunting mode predicts variation in prey mortality and plasticity in prey spatial response. *J. Anim. Ecol.* **83**, 214–222. (doi:10.1111/1365-2656.12111)
20. Shimozawa T, Murakami J, Kumagai T. 2003 Cricket wind receptors: thermal noise for the highest sensitivity known. In *Sensors and sensing in biology and engineering* (eds F Barth, JC Humphrey, T Secomb), pp. 145–157. Berlin, Germany: Springer.
21. Löhner R. 2008 *Applied computational fluid dynamics techniques: an introduction based on finite element methods*. New York, NY: Wiley.
22. Cantrell RS, Cosner C. 2003 *Spatial ecology via reaction–diffusion equations*. New York, NY: Wiley.
23. White JW, Rassweiler A, Samhouri JF, Stier AC, White C. 2014 Ecologists should not use statistical significance tests to interpret simulation model results. *Oikos* **123**, 385–388. (doi:10.1111/j.1600-0706.2013.01073.x)
24. Visser A. 2001 Hydromechanical signals in the plankton. *Mar. Ecol. Prog.* **222**, 1–24. (doi:10.3354/meps222001)
25. Jiang H, Kiørboe T. 2011 The fluid dynamics of swimming by jumping in copepods. *J. R. Soc. Interface* **8**, 1090–1103. (doi:10.1098/rsif.2010.0481)
26. van Duren LA, Stamhuis EJ, Videler JJ. 2003 Copepod feeding currents: flow patterns, filtration rates and energetics. *J. Exp. Biol.* **206**, 255–267. (doi:10.1242/jeb.00078)
27. Jiang H, Osborn TR, Meneveau C. 2002 The flow field around a freely swimming copepod in steady motion. Part I: theoretical analysis. *J. Plankt. Res.* **24**, 167–189. (doi:10.1093/plankt/24.3.167)
28. Malkiel E, Sheng J, Katz J, Strickler JR. 2003 The three-dimensional flow field generated by a feeding calanoid copepod measured using digital holography. *J. Exp. Biol.* **206**, 3657–3666. (doi:10.1242/jeb.00586)
29. Catton KB, Webster DR, Brown J, Yen J. 2007 Quantitative analysis of tethered and free-swimming copepodid flow fields. *J. Exp. Biol.* **210**, 299–310. (doi:10.1242/jeb.02633)
30. Kant R, Humphrey JAC. 2009 Response of cricket and spider motion-sensing hairs to airflow pulsations. *J. R. Soc. Interface* **6**, 1047–1064. (doi:10.1098/rsif.2008.0523)
31. Riechert SE. 2009 Spiders as representative 'sit-and-wait' predators. In *Natural enemies* (ed. M Crawlay), pp. 313–328. Oxford, UK: Blackwell Scientific Publications.
32. Gabbutt PD. 1959 The bionomics of the wood cricket, *Nemobius sylvestris* (Orthoptera: Gryllidae). *J. Anim. Ecol.* **28**, 15–42. (doi:10.2307/2011)
33. Skorczewski T, Cheer A, Cheung S, Wainwright PC. 2014 Use of computational fluid dynamics to study forces exerted on prey by aquatic suction feeders. *J. R. Soc. Interface* **44**, 475–484.
34. Mulder-Rosi J, Cummins GI, Miller JP. 2010 The cricket cercal system implements delay-line processing. *J. Neurophys.* **103**, 1823–1832. (doi:10.1152/jn.00875.2009)
35. Dupuy F, Steinmann T, Pierre D, Christidès J-P, Cummins G, Lazzari C, Miller J, Casas J. 2012 Responses of cricket cercal interneurons to realistic naturalistic stimuli in the field. *J. Exp. Biol.* **215**, 2382–2389. (doi:10.1242/jeb.067405)
36. Jeschke JM, Kopp M, Tollrian R. 2002 Predator functional responses: discriminating between handling and digesting prey. *Ecol. Monogr.* **72**, 95–112. (doi:10.1890/0012-9615(2002)072[0095:PFRDBH]2.0.CO;2)
37. Metz JAJ, van Batenburg FHD. 1985 Holling's 'hungry mantid' model for the invertebrate functional response considered as a Markov process. Part I. The full model and some of its limits. *J. Math. Biol.* **22**, 209–223. (doi:10.1007/BF00275716)
38. Van Rijn PC, Bakker FM, Van der Hoeven WA, Sabelis MW. 2005 Is arthropod predation exclusively satiation-driven? *Oikos* **109**, 101–116. (doi:10.1111/j.0030-1299.2005.12987.x)
39. Gemmell BJ, Adhikari D, Longmire EK. 2014 Volumetric quantification of fluid flow reveals fish's use of hydrodynamic stealth to capture evasive prey. *J. R. Soc. Interface* **11**, 20130880. (doi:10.1098/rsif.2013.0880)

Appendix. Validation des modélisations par éléments finis

A. Particle image velocimetry (PIV) measurements

PIV is the laser-based non-invasive technique of choice for visualizing and quantifying the full field of fluid movements around moving objects of various sizes and speeds. We used the PIV measurement system described by Casas *et al.* (2008). Our experimental setup consisted of two sealed glass boxes (10x6.2x6.2 cm) for the experiments on spheres of 1 mm and 8 mm and a larger box (34x25x17 cm) for experiments on spheres of 30 mm, both seeded with 0.2 ?m oil particles. Oil particles (Di-Ethyl-Hexyl-Sebacat, 0.5 L, TPAS, Dresden, Germany) were generated with an aerosol generator (ATM 230, ACIL, Chatou, France). The laser (NewWave Research Solo PIV 2, Nd :YAG, dual-pulsed ; Dantec Dynamics A/S, Skovlunde, Denmark) illuminated the flow produced by sphere displacement through the glass box. A laser sheet (width=17 mm, thickness at focus point=50 m) was operated at low power (3 mJ at 532 nm) to minimize glare. A target area of various sizes (10x8 mm for small spheres of 1 mm and 50x40 mm for larger spheres of 8 mm and 30 mm) was then imaged onto the CCD array of a digital camera (Photron FastCam X1280 PCI 4K) with a macro lens (Nikon, AF Nikkor, 60 mm, f : 2.8). The CCD captured separate image frames (30 fps, 1280x1024 pixels). Once a sequence of two light pulses was recorded, the images were divided into small interrogation areas of 32x32 pixels, which were cross-correlated with flow map software (Flow Manager 4.4. Dantec Dynamics A/S, Skovlunde, Denmark). The inter-frame time was set to 500 s and the correlation algorithm used yielded valid measurements for particle displacements of down to 0.1 pixels. Observed speeds, and the lowest measurable speed were estimated as described by Casas *et al.* (2008) and Dangles *et al.* (2006b).

B. Testing our implementation of the CFD-FEM numerical scheme for a single translating sphere

CFD-FEM is a very powerful technique, but not without risks and pitfalls. We therefore thoroughly checked our algorithm by (i) experimentally estimating the flow disturbances around a single translating sphere in flow visualization experiments, carried out by PIV, followed by (ii) analytical approximations of the results and (iii) CFD-FEM computations. We used a single translating sphere of various diameters and velocities to cover the whole range of Reynolds numbers corresponding to different flow regimes, as experienced by a running spider.

We experimentally explored five flow regimes (Re=1, 4.2, 16, 154, 577), using combinations of spheres of different diameters (D=1 mm, 8 mm and 30 mm) with various sphere velocities (V=1.7 cm/s, 6.5 cm/s, 25.8 cm/s, 30 cm/s and 31.8 cm/s). These Re numbers correspond to spider speeds of 0.4, 1.8, 6.9, 67 and 250 cm/s. The sphere was mounted on a small rod, which was fixed on a moving controllable piston. The sphere diameter and velocity were constrained to specific values by the availability of sphere diameters and by the way the piston was programmed. Sphere experiments were conducted far from the wall of the measurement box, to avoid ground and wall effects. We used PIV to determine the flow velocities in a plane crossing the center of the moving spheres. The velocity profiles were extracted in the direction of sphere displacement

(See Figure in the electronic appendix).

We fitted two analytical approximations of the Navier-Stokes equation, representing two extreme cases of flow regimes, to the data. For the lowest flow regime, the analytical approximation of the full Navier-Stokes equation is known as the Stokes approximation. The flow velocity components according to Stokes are :

$$u_r = Ucos\theta \left(\frac{3}{2}\frac{a}{r} - \frac{1}{2}\frac{a^3}{r^3} \right)$$

$$u_\theta = Usin\theta \left(\frac{3}{4}\frac{a}{r} + \frac{1}{4}\frac{a^3}{r^3} \right)$$

where U is the sphere velocity, θ is the angle with respect to the direction of movement of the sphere, a is the radius of the sphere and r is the distance from the sphere center. In the direction of sphere displacement (where θ =0, cos θ=1 and sin θ=0), these components become :

$$u_r = U \left(\frac{3}{2}\frac{a}{r} - \frac{1}{2}\frac{a^3}{r^3} \right)$$

$$u_\theta = 0$$

For the high-flow regime, the analytical approximation of the full Navier-Stokes equation is known as the potential flow approximation. The flow velocity components in the direction of sphere displacement (at θ =0, cosθ=1 and sinθ=0) are, according to potential flow theory :

$$u_r = U \left(\frac{a^3}{r^3} \right)$$

$$u_\theta = 0$$

The Stokes approximation to experimental PIV measurements was found to be valid only for *Re* numbers of one or below (Figure 6.1). The potential flow approximation was valid at high *Re* numbers but remained unsatisfactory, even at the highest observed speed of spider locomotion (40 cm/s). Both analytical models were found to be poor approximations of the flow for the whole range of speeds used by attacking spiders.

We then compared the CFD-FEM implementation of a translating sphere, using the same parameters as described in the main text, with the experimental data and analytical solutions. The figure in the electronic appendix shows that the CFD-FEM implementation fitted the experimental data very well, and this was confirmed by analytical approximations, where valid. We used the same computational parameters as for simulations of three translating spheres for a running spider, as explained in the main text, except for the distance to the ground and the simulation volume (reflecting the dimensions of the PIV measurement boxes). We modeled flow disturbances around a quarter of the sphere only, because there was no ground effect in these CFD simulations. We assumed horizontal and vertical flow symmetry, by defining an axis centered on the sphere and oriented in the direction of its displacement. The boundary conditions of the simulation volume were chosen so as to stay as close as possible to the PIV measurements. The velocity at the surface of the sphere was therefore set to the inlet velocity, whereas the upstream and downstream boundaries of the simulation volume were defined as open boundaries with normal stress.

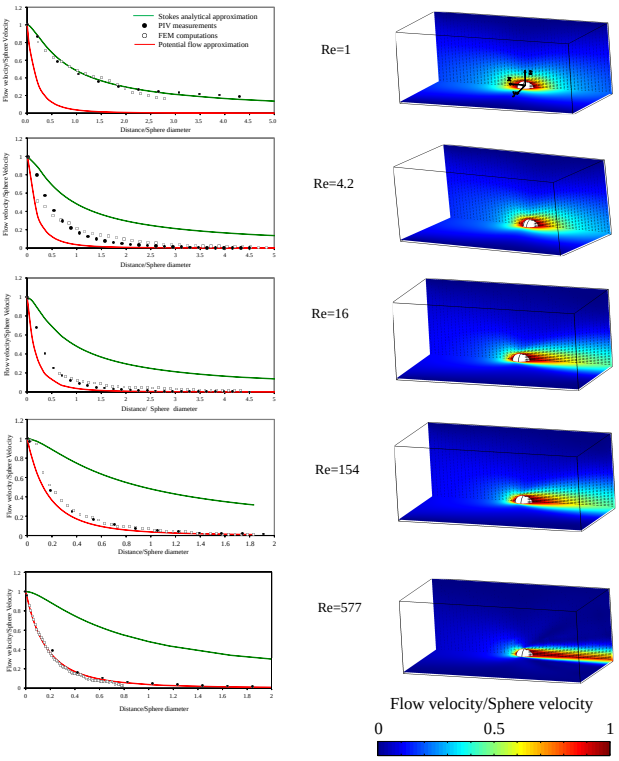

FIGURE 6.1. **Flow velocities upstream from a translating sphere as function of the speed of translation for various *Re* numbers (left) and a full-field 3D view of the finite element model (right)**. Single-point measurements of flow velocities were obtained by PIV (empty circles). In each panel, we also present the velocities obtained from CFD-FEM computations (full dots), predicted according to the Stokes (upper green line) and potential flow (lower red line) analytical approximations. Flow velocities and distances from the sphere are normalized, to harmonize data obtained for different sphere diameters and speeds. In the 3D representation, the flow amplitudes are shown in color and the vectors represent the amplitude and direction of flow.

Chapitre 7

Performances comparées des poils biomimétiques et naturels

Droogendijk, H., Casas, J., **Steinmann, T.**, and Krijnen, G. J. M. (2014). Performance assessment of bio-inspired systems : flow sensing MEMS hairs. *Bioinspiration & Biomimetics*, 10(1) :16001.

Résumé du chapitre

Ce chapitre présente, pour la première fois, une étude comparée des performances des senseurs de flux biomimétiques et de leurs homologues naturels, les poils filiformes des grillons. Cette étude théorique est basée sur l'adaptation d'un modèle mécanique classique de déflexion d'un poil. Bien que très utilisé en ingénierie pour caractériser l'utilité relative de certains dispositifs, le concept de facteur de mérite est très peu répandu en biomimétique. Nous définissons ce facteur de mérite comme étant inversement proportionnel au produit du seuil de détection et du temps de réponse. Ainsi un poil qui a un faible seuil de détection et un faible de temps de réponse sera considéré comme très performant. Nous déterminons aussi les performances des senseurs biomimétiques et naturels à l'aide de différents critères : la sensibilité, l'efficacité énergétique, le seuil de détection et le temps de réponse.

Résultats

Il apparaît à la lumière de cette comparaison que le système sensoriel du grillon surpasse grandement et sur tous les critères son homologue biomimétique. Cette approche comparative nous a permis de cibler les éléments essentiels et nécessaires à l'optimisation des senseurs biomimétiques de flux. Les deux paramètres clefs d'optimisation des poils naturels sont (i) leur très grande efficacité énergétique, assurée par l'adéquation entre la résistance à la rotation de leur chaussette et la résistance visqueuse que leur oppose l'air et (ii) leur rapidité de réponse, assurée par leur régime d'amortissement critique.

Discussion

L'étude des relations allométriques entre la géométrie du poil et ses propriétés mécaniques nous indique que l'effet d'une variation de longueur du poil est beaucoup plus importante sur sa trainée visqueuse et son moment d'inertie que sur sa fréquence propre. Cette faible dépendance entre la fréquence de résonance et la longueur du poil nous indique ainsi que la fréquence de résonance ne semble pas être la cible principale de la sélection naturelle, mais un trait secondaire. Il apparait donc important que les biologistes, qui focalisaient depuis des années leur attention sur cette fréquence de résonnance, se recentrent à présent sur l'étude des autres propriétés mécaniques des poils et notamment sur l'étude des propriètées de la membrane de la chaussette, beaucoup moins étudiée.

Bioinspiration & Biomimetics

RECEIVED
16 May 2014

ACCEPTED FOR PUBLICATION
23 October 2014

PUBLISHED
19 December 2014

PAPER

Performance assessment of bio-inspired systems: flow sensing MEMS hairs

H Droogendijk[1], **J Casas**[2], **T Steinmann**[2] **and G J M Krijnen**[1]

[1] MESA+ Institute for Nanotechnology, University of Twente, Enschede, The Netherlands
[2] Institut Universitaire de France-IUF, Institut de Recherche sur la Biologie de l'Insecte, IRBI-UMR CNRS 7261, Université François, Tours, France

E-mail: h.droogendijk@utwente.nl

Keywords: biomimetics, figure of merit, metrics, hair, flow sensor, MEMS

Abstract

Despite vigorous growth in biomimetic design, the performance of man-made devices relative to their natural templates is still seldom quantified, a procedure which would however significantly increase the rigour of the biomimetic approach. We applied the ubiquitous engineering concept of a figure of merit (FoM) to MEMS flow sensors inspired by cricket filiform hairs. A well known mechanical model of a hair is refined and tailored to this task. Five criteria of varying importance in the biological and engineering fields are computed: responsivity, power transfer, power efficiency, response time and detection threshold. We selected the metrics response time and detection threshold for building the FoM to capture the performance in a single number. Crickets outperform actual MEMS on all criteria for a large range of flow frequencies. Our approach enables us to propose several improvements for MEMS hair-sensor design.

1. Introduction

The engineering concept of a figure of merit (FoM) is hardly used in the biomimetic field: a recent survey using web of science found a maximum of a dozen of papers making quantitative comparisons between biomimetic devices and their biological templates using such metrics. When done, the results are somewhat disappointing at first. For example, such comparison between biomimetic flapping wing systems and birds or insects showed that animals have generally lower values of FoM [1]. In that study, as well as in a theoretical study on osmotic actuation inspired by plants [2], the choice of the criteria used for building the FoM was a key step because the evolutionary pressures at play in the real biological system are usually unknown.

Despite these caveats, the concept of a FoM is a tool of choice in the biomimetic design toolbox because it forces us to declare unambiguously (i) the criteria to use and their functional relationship, (ii) the way to measure them both in the artefact and on the organism (iii) the targeted performance, (iv) the achieved gap between the organism and the artefact, (v) the level of improvement and (vi) the trade-off between metrics. Thus, the results of comparison between nature and technology contain important and valuable lessons. While more theoretical work on such issues is certainly warranted, the engineering world has its own technical conditions in terms of material properties, energy consumption, signal analysis etc so that the number of possible scenarios for computing FoMs is very large, if not endless. Thus, an alternative experimental route, based on real measurements of built devices of varying properties and real organisms, consists in defining an FoM made of several criteria spanning a wide range of possible variables of importance in the biological system. In this paper, such a procedure is presented, and applied to bio-inspired flow sensors, inspired by the cricket's capability of sensing airflows using long, tiny hairs.

1.1. Bio-inspired flow sensors

To obtain information about the environment, and e.g. avoid predator attacks, crickets are capable of sensing low-frequency flows by mechanoreceptive sensory hairs. These so-called filiform hairs, which are situated on the back of the cricket's body on two appendices called cerci, are each lodged in a socket, mechanically guiding the hair to move in a preferred

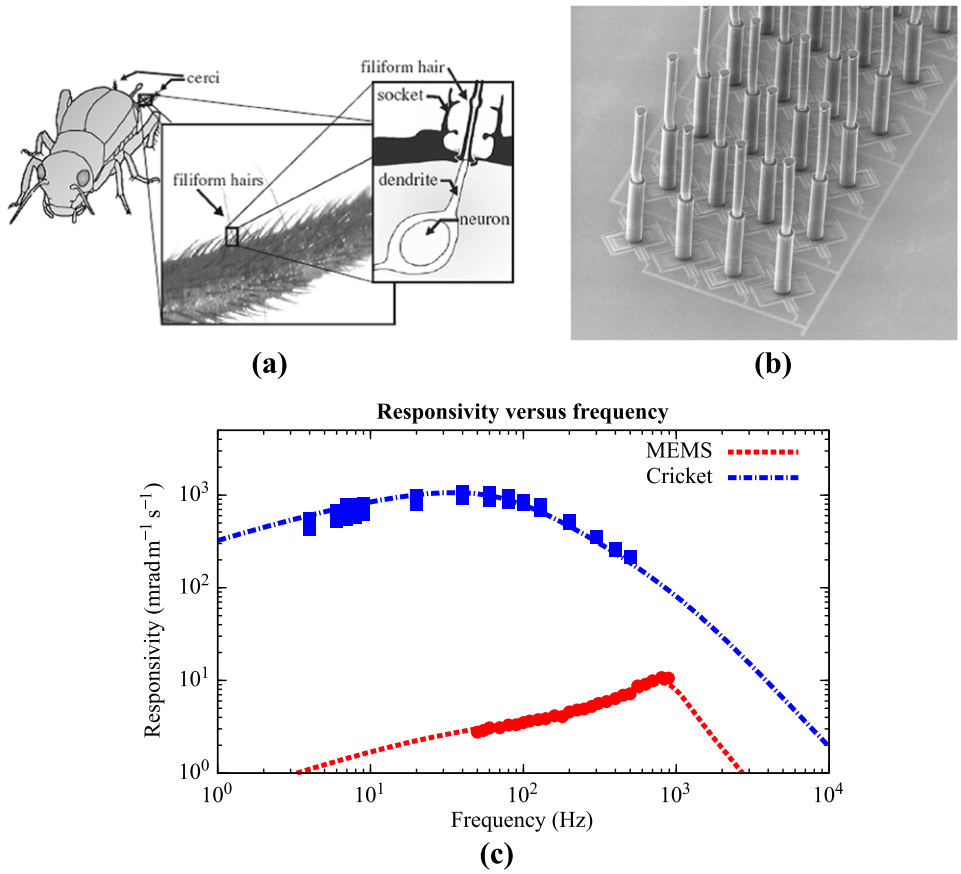

Figure 1. Flow perception by crickets using mechanoreceptor filiform hairs [10, 12] (a) and an SEM image of biomimetic hair flow sensors fabricated using MEMS technology [13] (b). Responsivity as function of frequency for the natural and man-made hairs (c). Crickets hairs (blue) are 800–900 μm, MEMS hairs (red) are 800 μm long. Points represent experimental values extracted from [4] and [13], while the fitted curves are based on equation (6).

direction. When subjected to airflow, upon rotation of the hair base, a dendrite is mechanically excited causing its associated neuron to generate action potentials (figure 1(a)). This sensory system responds to very low energy-levels down to the hair's thermo-mechanical noise, i.e. on the order of $k_B T$ [3], with corresponding velocity amplitudes down to about 30 μm s^{-1} [4]. The associated rotational amplitudes required to trigger a neural response are of the order of range 10^{-5}–10^{-4} rad [3]. The measurement of such tiny energies, which is an impressive performance throughout the entire animal kingdom, is the main reason why engineers and biologists have marvelled at these filiform hairs for so long.

Taking the cricket cercal hair sensors as a source of inspiration, several research groups have worked on the development of artificial counterparts for airflow measurements by exploiting MEMS technology [5–9]. In our work, hair-sensor inspired flow-sensors for measurement of (tiny) ac-airflows have been designed and fabricated [10]. Evolved fabrication methods and designs (figure 1(b)) have led to electronic-noise limited performance, enabling the detection and measurement of flow velocities in the range of sub-mm s^{-1} while retaining a bandwidth on the order of 1 kHz [11].

From all existing MEMS cricket-inspired flow sensory systems developed up to now, none shows equal or better performance than that of the cricket. To illustrate this, we consider the experimentally determined sensor responsivity, which is the normalized angular amplitude versus frequency, for both crickets and MEMS hair flow sensors, as shown in figure 1(c). Here, we use the term *responsivity* (the ratio of the output quantity to the input physical quantity) instead of the term *sensitivity* (the stimulus level required to produce a threshold response). We observe in figure 1(c) that the cricket clearly shows a much larger angular amplitude for a given airflow velocity amplitude and for a broad range of frequencies. Though, a better performance compared to the cricket's flow sensory system has been in fact attained by human technology some time ago: the MEMS microflown devices are able to measure speeds as low as 1 μm s^{-1} (in 1 kHz bandwidth) [14] and laser Doppler anemometry and allied optical means are in fact outperforming the animal. The cost of such technological performance is however high: the technology is bulky, requires a lot of energy and a handling care that is much more delicate

than the insect shows for its sensory hairs. They live in rough environments and do not seem to care much about chocks, mud or dust, and occasionally loose one or two hairs. Thus, it is the seemingly incompatibility between the frugality in the design of the sensors and their fantastic performance that is exciting the minds of the engineers and biologists. Here, we do not address the robustness of natural and biomimetic sensors. Would we do so, the natural system would certainly perform better in this respect. We just assume that both systems have a reason for being, i.e. they both are useful in their own environments and within their operational constraints.

Quantifying the performance of hair flow sensors based on the normalized angular amplitude is just one metric. Other metrics for quantifying performance can be defined, and from a judiciously chosen combination of metrics an FoM can be composed and evaluated. In this paper, five of such metrics to quantify the performance of hair flow sensors, as well as a FoM, are presented. These are all numerically evaluated for both the cricket and the MEMS sensors, and important insights are gained from the results.

2. Hair mechanical model

The natural and MEMS hairs can be considered as a flow-driven inverted pendulum (figure 2(a)). Understanding this system requires us to both understand the flow-hair interaction as well as the mechanical response to the flow-induced torque on the hairs. This analysis has been successfully and thoroughly described by e.g. Shimozawa *et al* [4], Humphrey and Barth [15] and Bathellier *et al* [16]. For completeness, we primarily reiterate these models (see appendix) and cast them in a formalism suitable to our analyses, while adding an original contribution considering mechanical impedance at the end of the section.

In the mechanical model, S is the torsional stiffness, R and D are damping terms, J and C/ω are contributions to the moment of inertia, and $T(t)$ is the torque acting on the hair by the viscous forces due to the airflow. The various parts constitute a second order mechanical system and exhibit corresponding behaviour with resonance and a mechanical roll-off proportional to $1/\omega^2$ beyond resonance (figure 1(c)), in which ω is the flow frequency.

The system's rotational angle amplitude Θ_m is determined by both the mechanical parameters (S, R and J) and the airflow related parameters (D and C/ω), as shown in appendix. Since the hair flow sensor is considered to be subjected to harmonic airflows with frequency ω, the hair itself will exhibit harmonic motion with angular velocity $\dot{\theta}(t)$, which can be calculated by taking the derivative of $\Theta_\mathrm{m} e^{j(\omega t+\phi_\mathrm{m})}$ with respect to time:

$$\frac{\mathrm{d}\theta(t)}{\mathrm{d}t} = \Omega_\mathrm{m} e^{j(\omega t+\phi_\mathrm{m})}, \qquad \Omega_\mathrm{m} = j\omega\Theta_\mathrm{m}. \quad (1)$$

As a consequence, the system may alternatively be described as a dynamical system in terms of state variables (θ and T), their time-derivatives ($\dot{\theta}$, $\dot{T}$) and their constitutive relations given by compliances, inductances and resistances [17]. In this description, the time-derivative of the extensive variable, in this case the angular velocity, is called the 'flow' (not to be confused with the airflow) and the intensive variable, here the drag torque, the 'effort'. The compliances (S), inductances (J and C/ω) and resistances (R and D) can be considered as impedances. Using the definition for $\dot{\theta}(t)$ for harmonic motion, (A.19) can be rewritten to:

$$T_\mathrm{h}(t) = \left[(R+D) + j\left(J\omega - \frac{S}{\omega} + C\right)\right]\frac{\mathrm{d}\theta(t)}{\mathrm{d}t}, \quad (2)$$

where $T_\mathrm{h}(t)$ equals the hair torque as a result of the contributors to the flow-induced drag torque A and B:

$$T_\mathrm{h}(t) = V_0 e^{j\omega t}(A + jB), \quad (3)$$

in which V_0 is the far field airflow amplitude. From (2) follows that the torque $T_\mathrm{h}(t)$ consists of impedances by the airflow related parameters (due to Stokes's mechanical impedance) and the mechanical hair parameters. A schematic view of these impedances is given in figure 2(b), which is an abstracted version of figure 2(a). Generally, the hair with moment of inertia J is suspended by a torsional spring S and has a torsional resistance R. The air itself also contributes to the total torque balance, where C can be considered as 'air virtual mass' and D as added air viscous damping. Now, the hair flow sensor system can be described for harmonic airflows simply by

$$V_0(A + jB) = \left(Z_\mathrm{a} + Z_\mathrm{m}\right)\Omega_\mathrm{m} e^{j\phi_\mathrm{m}}, \quad (4)$$

where the airflow and mechanical contributions in terms of impedances Z_a and Z_m are separated (see also figure 2(c)). Consequently, the airflow impedance Z_a and the hair mechanical impedance Z_m are defined as:

$$Z_\mathrm{a} = D + jC, \qquad Z_\mathrm{m} = R + j\left(J\omega - \frac{S}{\omega}\right). \quad (5)$$

3. Performance metrics

In general, the performance of a sensory system can be described by either independent metrics or a judiciously chosen combination of metrics by the definition of a so-called FoM. In this section, five independent metrics are defined to quantify the performance of the described hair flow sensory system: responsivity, power transfer, power efficiency, response time and detection threshold. Additionally, a sixth metric is defined, which is a FoM based on three of the listed independent metrics. These metrics are described one by one below.

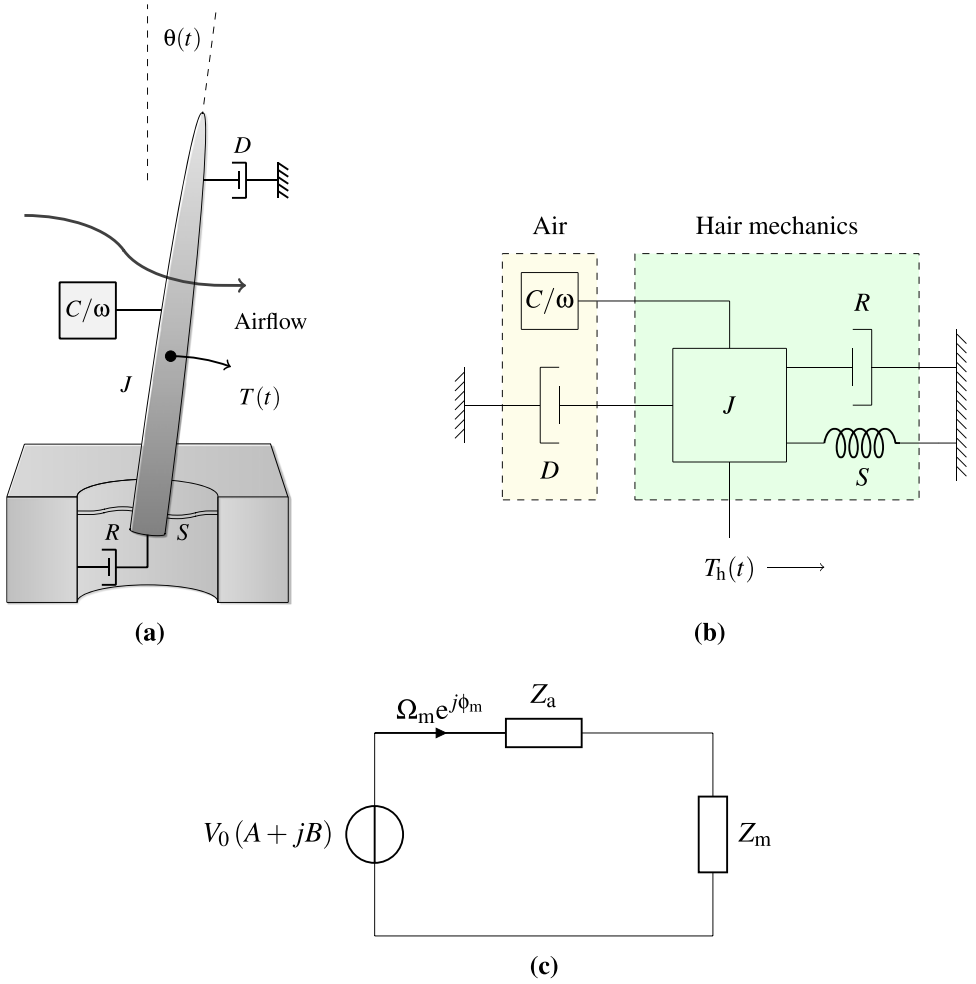

Figure 2. Second order mechanical system of the natural hair (a) and the corresponding mechanical impedance implementation (b). Simple circuit representation of the impedances in the airflow-hair-sensor interaction (c). See text for the definition of the variables.

3.1. Responsivity

A characteristic of a sensory system is its responsivity. In engineering, systems are often designed to have a high responsivity. We define the responsivity of the hair flow sensory system as the resulting rotational angle amplitude per flow velocity amplitude:

$$\frac{\Theta_m}{V_0} = \frac{\sqrt{A^2 + B^2}}{\sqrt{\left[S - J\omega^2 - C\omega\right]^2 + \left[(R + D)\omega\right]^2}}, \quad (6)$$

where the first equality is due to the linear response of the hair-sensors with respect to airflow in accordance with the analysis of section 2. Following the approach by Bathellier *et al* [16], an upper limit for the responsivity can be defined. Under the conditions that the system operates at its resonance frequency ($S - J\omega^2 = 0$), the absence of socket damping ($R = 0$), negligible air virtual mass ($C \ll D$) and the fact that $A^2 \gg B^2$ [4], the limit of responsivity will be

$$\left.\frac{\Theta_m}{V_0}\right|_{\text{limit}} = \frac{A}{D\omega}, \quad (7)$$

where the system is dimensioned to have its maximum at frequency ω. The limit of responsivity is fully determined by the flow-torque interaction on the hair and the airflow frequency. The drag-torque contributor A can be directly related to D [4]:

$$A = \frac{3D}{2L}\left|K(\omega, L)\right|, \quad (8)$$

where the unitless parameter $|K(\omega, L)|$ captures the influence of the substrate on the incoming flow [16]. In our case, the values for $|K(\omega, L)|$ are found between 0 and 1. Therefore, the maximum achievable responsivity for the hair flow sensory system becomes

$$\left.\frac{\Theta_m}{V_0}\right|_{\text{limit}} = \frac{3}{2}\frac{1}{L\omega}, \quad (9)$$

which simply contains the hair length L and the airflow frequency ω.

3.2. Power transfer

The second metric for characterization of the performance of hair flow sensors is how much power is

transferred to the mechanical part of the hair sensory system compared to the total power in the system (see also figure 2(b)). The time-averaged power P_t dissipated by the resistive part of the mechanical impedance Z_m is given by

$$P_t = \Omega_{rms}^2 \Re\left(Z_m\right) = \frac{1}{2}\Omega_m^2 \Re\left(Z_m\right), \quad (10)$$

where Ω_m is the hair rotational angular velocity amplitude:

$$\Omega_m = \frac{|T_h|}{|Z_a + Z_m|}, \qquad |T_h| = V_0\sqrt{A^2 + B^2}, \quad (11)$$

with $|T_h|$ is the flow-induced torque amplitude. The transferred power P_t is maximum when the impedances Z_m and Z_a are matched, according to the maximum power transfer theorem [18], which requires:

$$\Re\left(Z_m\right) = \Re\left(Z_a\right), \qquad \Im\left(Z_m\right) = -\Im\left(Z_a\right), \quad (12)$$

which implies

$$R = D, \qquad \omega^2 = \frac{S}{J + C/\omega}. \quad (13)$$

In case the impedances are matched, the maximum transferable power P_{max} can be calculated and is given by

$$P_{max} = \frac{|T_h|^2}{8D}. \quad (14)$$

Now, we define the transferred power ratio λ as the ratio between the power P_t present in the resistive part of the mechanical impedance (R) and the power present in the total system in case of matched impedances P_{max}:

$$\lambda = \frac{P_t}{P_{max}} = \frac{4RD}{\left|Z_a + Z_m\right|^2}, \quad (15)$$

where the limit for maximum power transfer is simply

$$\lambda\,|_{limit} = 1. \quad (16)$$

3.3. Power efficiency

Thirdly, power efficiency can be considered as a metric for sensor performance. The power efficiency η can be defined as the ratio between the power dissipated by the resistance R of the mechanical system to the power developed by the incoming airflow in the hair-system. The power dissipated in the resistance R is given by (10) and the total power P_{tot} input into the system is simply

$$P_{tot} = \frac{1}{2}\left|T_h\right|\Omega_m. \quad (17)$$

Using the previously defined impedances and (4), the power efficiency η is defined as

$$\eta = \frac{P_t}{P_{tot}} = \frac{R}{\left|Z_a + Z_m\right|}. \quad (18)$$

Also here, the limit for maximum power efficiency is simply

$$\eta\,|_{limit} = 1. \quad (19)$$

3.4. Response time

The performance of wind receptor hairs can also be determined against the metric of response time. Besides a power-efficient and sensitive sensory system, also the ability to quickly respond to a change in flow contributes to the performance of the system. The corresponding response time τ_{95}—a measure for agility—is calculated from the second order differential equation, describing the mechanical behaviour of the system in response to a torque step function. Our definition of response time is also known as settling time, which is the time required to reach and stay within a range of a certain percentage of the final value. The general solution of a damped mass-spring system is

$$\theta(t) = \Theta_1 e^{-r_1 t} + \Theta_2 e^{-r_2 t}, \quad (20)$$

where Θ_1 and Θ_2 need to be derived from initial conditions and r_1 and r_2 are found from

$$r_{1,2} = \frac{\Gamma}{2} \pm \sqrt{\left(\frac{\Gamma}{2}\right)^2 - \omega_n^2} = \frac{\Gamma}{2} \pm \omega_n\sqrt{\zeta^2 - 1}, \quad (21)$$

with Γ and ω_n constants which can be expressed using the damping ratio ζ as

$$\Gamma = \frac{R_t}{J_t} = 2\zeta\omega_n, \qquad \omega_n^2 = \frac{S}{J_t}. \quad (22)$$

Considering the presence of the air impedance in the total model, the total damping R_t and total moment of inertia J_t are given by

$$R_t = R + D, \qquad J_t = J + \frac{C}{\omega}. \quad (23)$$

Further, note that the damping ratio ζ can also be expressed as:

$$\zeta = \frac{1}{2}\left[\frac{H(0)}{H(\omega_n)}\right] = \frac{1}{2}\left[\frac{R_t\omega_n}{S}\right], \quad (24)$$

where $H(\omega)$ is the mechanical transfer function $H(\omega)$ of the system:

$$H(\omega) = \frac{1}{\left(S - J_t\omega^2\right) + jR_t\omega}. \quad (25)$$

Since the quantities C, D and J_t contain a frequency-dependency, these parameters are evaluated at resonance ($\omega = \sqrt{S/J}$) in this work. The general solution of (20) is either real or complex. When the damping ratio ζ is equal or greater than one, the solution is real and the hair moves without oscillations towards the point of torque equilibrium, dominated by the mathematically slow moving term. When the damping ratio ζ becomes smaller than one, the square root term becomes imaginary and the hair shows overshoot towards its equilibrium, leading to a longer stabilization time. The response time τ_{95}, indicated as the time

to get stable within 95% of the end value, is approximated as:

$$\tau_{95} \approx \begin{cases} \dfrac{3}{\zeta\omega_n} & \text{if } \zeta < 0.5, \\ \dfrac{6\zeta}{\omega_n} & \text{if } \zeta > 1. \end{cases} \quad (26)$$

A precise mathematical solution for the response time τ_{95} is rather involved. A spline interpolation is used for connecting the two asymptotes smoothly and obtaining a good approximation, which is not shown here. The best response time is obtained when ζ corresponds to a slightly underdamped system [19]. Consequently, the lower limit for the response time is found when:

$$\zeta\,|_{\text{limit}} = \frac{1}{2}\sqrt{2}. \quad (27)$$

3.5. Detection threshold

Another metric of performance for a sensory system is its signal-to-noise ratio (SNR). Generally, when the SNR is equal or higher than one, the system is able to detect the input signal. As a result, when the responsivity is given, the noise level of the system determines its detection threshold. To find the fundamental detection threshold of the flow susceptible hairs, the mechanical-thermal noise due to Brownian motion of molecules in the hair structure needs to be addressed [20]. The associated power spectral density of this (white) noise is given by

$$\bar{T}_n^2 = 4k_B T_0 R_t, \quad (28)$$

where $\bar{T}_n^2$ is the squared equivalent noise torque, k_B is the Boltzmann's constant, T_0 is the ambient temperature and R_t is the total resistance given by (23). The noise equivalent angle Θ_n is found by integrating the noise power over the full spectrum and taking the square root:

$$\Theta_n = \sqrt{\int_0^\infty \bar{T}_n^2 |H(\omega)|^2 d\omega}. \quad (29)$$

The detection threshold amplitude V_{th}, in m s^{-1}, is found by dividing the sensor's equivalent noise angle Θ_n by the amplitude of the rotational angle Θ_m at a far field flow amplitude V_0 of 1 m s^{-1}, where the latter is required for normalization of (6):

$$V_{th}(\omega) = \frac{\Theta_n}{\Theta_m(\omega)\big|_{V_0=1\text{ m s}^{-1}}}. \quad (30)$$

The minimum achievable detection threshold is determined by both the torsional resistance R and the responsivity of the hair sensory system. Namely, by reducing the noise and increasing the responsivity a better SNR is obtained. The lowest thermal noise values occur when the hair thermal-mechanical motion is fully determined by the added damping by air D, since this constant depends on the hair geometry. Thus, letting $R = 0$. Also, the best responsivity is achieved when the limit of (9) is fulfilled. Therefore, the threshold for the lowest measurable flow amplitude is defined as:

$$V_{th}(\omega)\big|_{\text{threshold}} = \frac{2}{3}\Theta_n L\omega, \quad (31)$$

with Θ_n the equivalent noise angle ($R = 0$):

$$\Theta_n = \sqrt{4k_B T_0 \int_0^\infty \frac{D}{\left(S - J_t\omega^2\right)^2 + D^2\omega^2} d\omega}. \quad (32)$$

3.6. FoM

In engineering, figures of merit are frequently defined for particular materials or devices in order to determine their relative utility for an application. In our case, responsivity is of high importance in a sensory system, but also the time it takes for the system to respond to a change in airflow and a low detection threshold. Because the responsivity is by itself already covered in our definition of the detection threshold by (30), we eventually defined the FoM for a hair flow sensory system as:

$$\text{FoM} = \frac{1}{\text{Detection threshold} \times \text{Response time}}, \quad (33)$$

for which the response time and detection threshold have been defined previously, together with their physical limits. As a consequence of this FoM, the flow sensory system performs well by having a low detection threshold (able to measure tiny flows) and a short response time (fast system). There are numerous ways to define an FoM and we decided to leave out power metrics, for reasons given in section 5.1.

4. Evaluation of metrics

Based on the described metrics, both the cricket cercal hair and the MEMS hair flow sensors are evaluated for varying values of the parameters listed in table 1. Since most mechanical parameters (e.g. C and D) have a slight frequency-dependency, an airflow is considered with a frequency of 200 Hz, which is a frequency within the cricket's sensing bandwidth, near its maximal responsivity (see figure 1(c)) thus allowing for a fair comparison.

Also the differences between the cricket and the MEMS hair flow sensor system are listed by means of a so-called lead factor for the cricket. That is, how many times better the cricket performs on the respective metric with respect to the MEMS sensor system. The detection threshold of the MEMS hair flow sensor is based here on thermal-mechanical noise only and does not represent the current state of performance, for which the detection threshold is 1.11 mm s^{-1} at 200 Hz due to limitations by electronic noise [21]. In practice, the current MEMS sensors perform worse when taking into account this measured detection

Table 1. Characteristics of a cricket cercal hair (non-metrics data from [4]) and a MEMS hair (non-metrics data from [13]) for a flow frequency of 200 Hz. The lead factor indicates the rational difference between the cricket and the MEMS sensor system.

Quantity	Symbol	Cricket	MEMS	Lead factor
Hair parameters				
Hair length	L	800 μm	800 μm	n/a
Base diameter	d	7.01 μm	44 μm	0.16×
Density	ρ	1100 kg m^{-3}	1200 kg m^{-3}	0.92×
Mechanical parameters				
Torsional stiffness	S	1.31×10^{-11} N m rad^{-1}	9.5×10^{-9} N m rad^{-1}	0.001×
Torsional resistance	R	1.55×10^{-14} N m s rad^{-1}	1.20×10^{-12} N m s rad^{-1}	0.013×
Added virtual damping	D	1.01×10^{-14} N m s rad^{-1}	1.83×10^{-14} N m s rad^{-1}	0.55×
Moment of inertia	J	2.44×10^{-18}kg m^3	3.12×10^{-16} kg m^3	0.008×
Added virtual mass	C/ω	1.81×10^{-18} kg m^3	7.20×10^{-18} kg m^3	0.25×
Metrics				
Responsivity	Θ_m/V_0	0.592 rad m^{-1} s^{-1}	0.004 rad m^{-1} s^{-1}	148×
Power transfer	λ	0.92	0.0014	657×
Power efficiency	η	0.59	0.149	4.0×
Response time	τ_{95}	5.87 ms	1.59 ms	0.27×
Detection threshold	V_{th}	73.7 μm s^{-1}	352 μm s^{-1}	4.8×
Figure of merit	FoM	2.312×10^6 m^{-1}	1.787×10^6 m^{-1}	1.29×

threshold, which results in a current FoM-score that is about four times lower than the cricket's.

The length of natural hairs varies in crickets from 100–1500 μm [22, 23]. Hair length is furthermore a key variable in determining the hair's mechanical response and also one of the easiest parameters to vary when building MEMS. We therefore explored the performance of natural and MEMS hairs as function of their length.

Taking the allometric scaling property for cricket hairs by Shimozawa *et al* [4] into account (i.e. the quantities S, R and d all depend directly on the hair length L), the graphs from figure 3 (leftside) result upon varying the cricket hair length L: 400 μm, 800 μm and 1600 μm. Further, in the same figure (right side) the impact of variations in hair length for the MEMS hair sensory system is shown (with the parameters S, R and d fixed, since allometric scaling does not apply for MEMS), and a comparison with the cricket's performance can be made. For both hair types, the physical limits for the various metrics are indicated by a horizontal dotted line. Since the response time is a frequency-independent quantity, it is shown with respect to the hair length L in figure 4, together with its physical limit. Evaluation of the FoM for both cricket and MEMS is shown in figure 5, for which also the maximum physically achievable limit is indicated by a horizontal dotted line.

5. Discussion

The entire work, including the FoM, is focussed on single sensors. Sensors in nature often come in high numbers, and may interfere with each other. For example, the interaction between hairs can be described by the viscosity-mediated coupling between hairs [24, 25]). Another example of exploiting multiple hairs is the measurement of spatial-temporal flow patterns using artificial hair flow sensors to arrive at so-called 'flow cameras' [26]. Changing the focus to the optimality of a whole sensing system made of many sensors would require a very different approach in which emergent properties are the expected outcome. This aim is however further down the road, as it implies having a better grasp at the nonlinear interactions between individual sensors than what is available today.

Our model of the hair mechanics is based on the analysis by Shimozawa *et al* [4]. We made substantial advance on the computation of impedances with both real and imaginary parts. The concept of impedance matching by equalling the real parts of the impedances ($R = D$) had been mentioned earlier by Shimozawa *et al* [4] and Bathellier *et al* [16], but the imaginary parts ($\omega^2 = S/[J + C/\omega]$) were not addressed in either of both. As a result, a complete definition of the power metrics for both transfer and efficiency can now be made. The SNR, and hence the sensitivity (expressions (28)–(32)), is also new and is valuable when comparing artificial and natural hairs. Our performance analysis is applicable to hair flow sensors in general, and hence it can also be used to e.g. flow sensors for sensing in water [15].

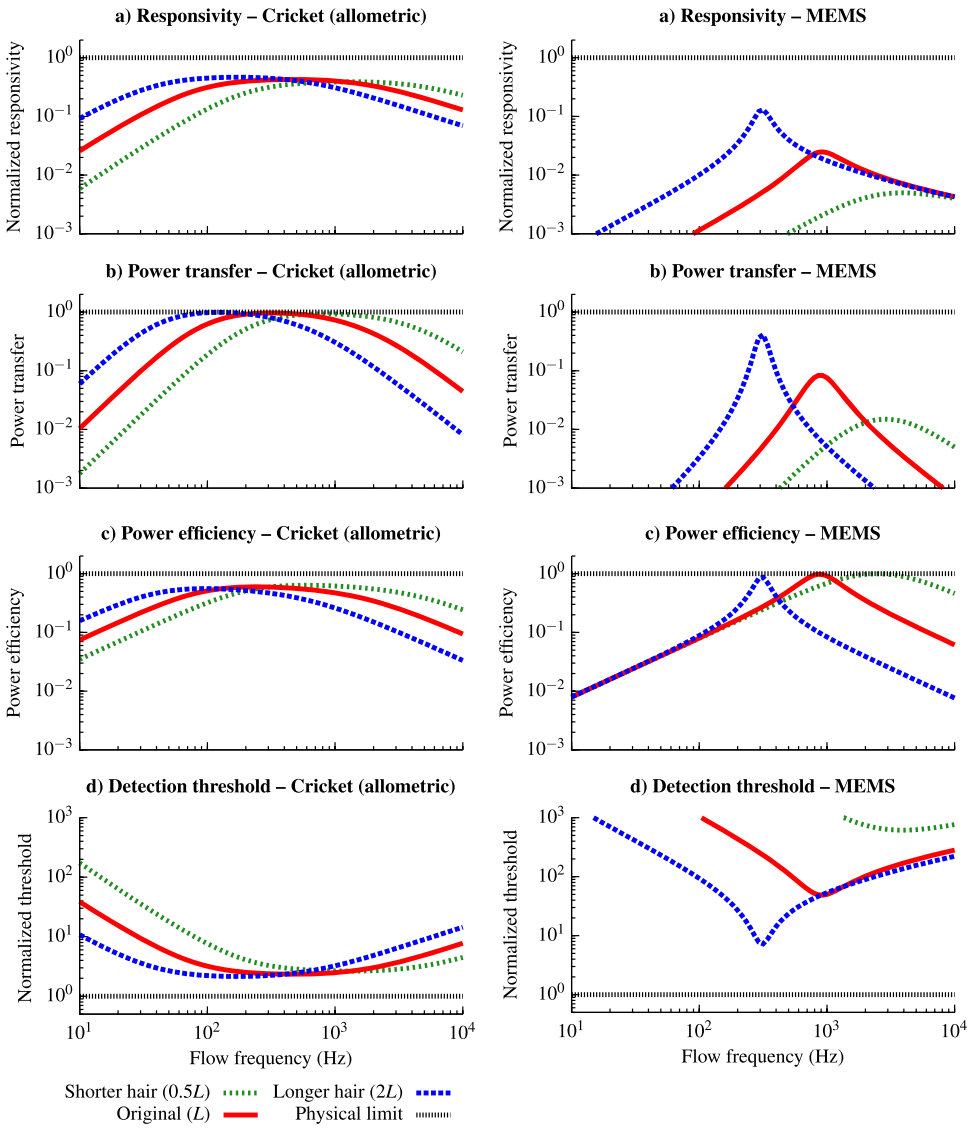

Figure 3. Performance metrics of natural and MEMS hairs of varying lengths as function of flow frequency. Both hairs are 800 μm long. Metrics are normalized when possible. Allometric scaling among the hair's variables is applied to the cricket hair. Values are given in the text.

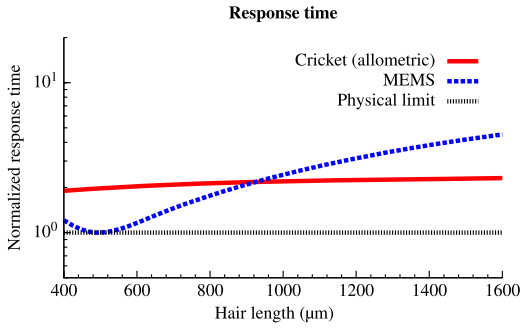

Figure 4. Response time as function of hair length for natural (red) and MEMS hairs (blue), normalized by the optimal response time ($\zeta = \frac{1}{2}\sqrt{2}$). Allometric scaling is used for the cricket.

5.1. Model evaluation and choice of performance metrics

The considered linear second order mechanical model yields analytical solutions to all six metrics, a convenient and handy outcome. However, it is possible that our linear mechanical model is incomplete and consequently needs to be adapted for a more accurate description of the real mechanical behaviour. For example, Shimozawa *et al* [4] propose to describe the torsional stiffness S as a viscoelastic (Maxwell) element. A similar finding was reported by McConney *et al* [27] where it was determined that at low angular velocity the motion of the hair is most accurately captured by a three-parameter viscoelastic model. Research for the Drosophila by Göpfert and Robert [28] indicates that the torsional stiffness S shows nonlinearity, indicating that a similar nonlinearity in the torsional stiffness S for the natural wind receptor hairs described here cannot be excluded. Nevertheless, the modelling of Humphrey *et al* [29], Shimozawa *et al* [4] and Bathellier *et al* [16] produced results which were largely in line with experimental findings over a

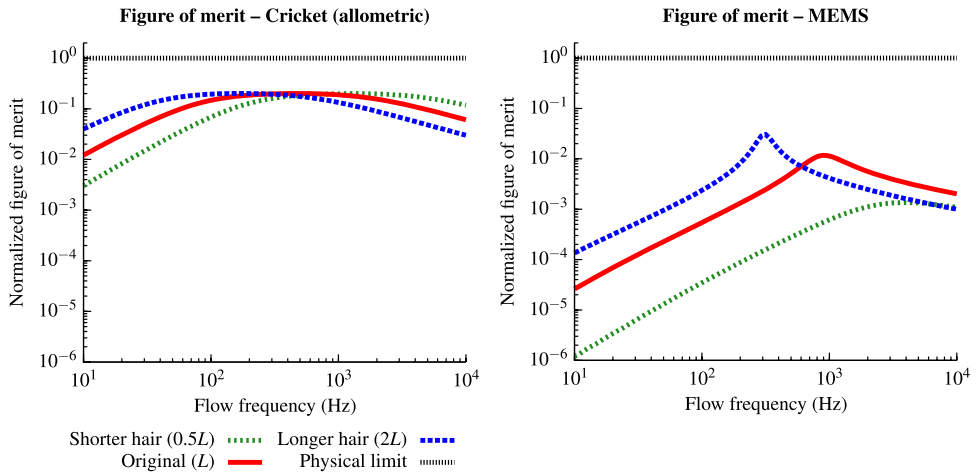

Figure 5. Figure of merit of natural and MEMS hairs of varying lengths as function of flow frequency, normalized by the physical limit. Allometric scaling among the hair's variables is applied to the cricket hair.

reasonable large bandwidth (see figure 1(c) as well), yielding credibility to the models used in this paper.

The exact definitions of several metrics might impact the final outcome and need to be discussed. First, the role of power transfer is not evident, hence our avoidance in using it in the definition of the FoM. Considering the power available to the system a distinction can be made between power transfer λ and power efficiency η. Maximum power efficiency occurs when the source impedance Z_a is minimized, transferring maximum power to the mechanical impedance Z_m. However, the torque T_h contributors parameters A and B both depend on the hair geometry as well, and in a comparable fashion as parameters C/ω and D (see model building). This means that minimizing D leads to a significant decrease of T_h, thus even less power transfer. Therefore, we think that maximum power transfer might be more important than maximum power efficiency. As for the cricket's hairs, it is possible that impedance matching plays a role in the cricket sensory system. For example, Keil [30] implies that a good power transfer by impedance matching is desired for effective flow measurement. By contrast, it is questionable whether a high power efficiency is present at all in crickets. As for our MEMS hair flow sensors, improving power transfer can only be obtained by reducing the sensor's mechanical damping R, as $R \gg D$. This would lead to a strongly underdamped system when S and J remain unchanged and we have to conclude that improving power transfer would be at the cost of increased response time.

The response time is another metric which might be defined in varying ways. We defined it as the fastest possible stable output in response to a step function, which generally implies having a critically damped mechanical system as being the best performing system. As for the cricket, it has been found that their cercal hairs are indeed close to critically damped systems [4, 16]. Thus, our definition of the response time seems consistent with this observation. As for the MEMS hair flow sensor system, the angular amplitude is measured directly. Therefore, we defined the response time as being the ability to measure the airflow velocity both in a fast and non-ringing way.

The FoM, hardly used in biomimetic and nature-inspired technology, is a composite single number. A high degree of subjectivity exists in the way such an index is built, the choice of functional relationship between its constituents, being linear, quadratic or else. Nevertheless, a single number gives the engineer a handy estimate of overall performance of a system or device, in particular in relative terms. The performances of cricket and MEMS-based hair flow sensory systems, as based upon our FoM, indicate that the cricket's flow sensors are performing over four times better than the current MEMS hair flow sensors. In contrast to the MEMS sensors, the cricket's flow sensors approach the physical limit for all metrics, leaving substantial room for improvement of the MEMS hairs.

5.2. Cross-talk between sensory modalities and multifunctional sensory systems

So far in all published literature, the hair structures have been considered to be primarily responsive towards airflows. However, by the very nature of the hair mechanical system the sensory system will also respond to inertial effects due to external accelerations. Therefore the sensor system can suffer from cross-talk when it is not only subjected to airflow, but also to accelerations. This might be well the case during the chase-escape bouts between prey crickets and predator spiders in nature [31]. This inertial responsivity affects the measurement of airflows and can potentially lead to distortion of the flow-induced signal. Since both cricket and MEMS hair flow sensors are affected by inertial effects, a comparison between

them can also be made for the undesired inertial responsivity.

We considered the torques acting on the hair due to airflow and due to inertial effects by external accelerations. To calculate the acceleration-induced torque acting on the hair, the analysis laid out in [32] is used. Since the hair diameter plays a much stronger role in the acceleration induced torque ($\propto d^2$) compared to the flow-induced torque ($\propto d^{1/3}$) [32, 33], the exact hair geometry is additionally taken into account for both cricket hairs [34] and MEMS hairs [13]. The ratio between flow-induced torque and acceleration-induced torque is taken as a measure. The calculated ratio of the normalized flow responsivity (torque per m s^{-1}) versus the normalized acceleration responsivity (torque per m s^{-2}) is generally about 40 times larger for a cricket 800 μm hair compared to a MEMS hair of the same length [32]. The hair diameter d plays therefore a pivotal role and the MEMS hair flow sensor performs notably worse due to its relative thickness. As a result, to minimize the inertial responsivity for a hair flow sensor, the system clearly benefits from having a hair with a small diameter. By contrast, changing the hair length L has negligible impact on the ratio of responsivities, since both flow-induced torque and acceleration-induced torque scale with L^2 [32, 33].

It is unknown at this stage if crickets might use these hairs as inertial sensing devices, as they also possess other sensors, assumed to be dedicated to that purpose, the clavate sensillae [35–37]. What is described here as a nuisance might be turned into an advantage if the sensor array is multifunctional. However, the bias induced by such cross-talk remains to be taken into account at the cost of increased neural processing. These considerations about cross-talk between sensory modalities, stemming from the engineering and device characterization point of view, are totally new to the field of hair based flow sensing, both in man-made and in natural systems. More general cross-talk between sensory modalities is hardly studied in natural systems (it is for example totally absent in [38]).

5.3. Improving MEMS flow sensors: learning from nature

Evidently, when comparing MEMS and cricket's hair-flow sensors, the latter is superior to the former on all metrics evaluated. Any or a combination of the metrics may hold the key to directions for optimization of hair-based flow sensors in general. From an engineering point of few the parameters that allow for variations are the hair geometry (d, L, J), the rotational stiffness (S) and rotational damping (R). For a given hair-geometry and frequency the torque (through A and B) and the additional mass (C) and damping (D) effects are determined. What we like to investigate is whether the FoM, as a proxy for overall performance, can be improved markedly by changing some of the hair-sensor parameters.

We first explore the potential for optimization that stems from a hair-geometry centric engineering approach: changing the hair length and diameter. Altering hair length is among the most obvious possibilities to improve at least some of the metrics. Since the flow-drag torque interaction constants A and B strongly depend on L and the constants C/ω and D are relatively small for a MEMS hair flow sensor, increasing its hair length will also give a much higher responsivity and lower detection threshold. The lower threshold is caused by the fact that A and B are much more affected than the hair mechanical system $H(\omega)$ and thus a slight change in thermal mechanical noise. However, for both cricket and MEMS, a disadvantage of increasing L is the increased response time, which makes the system responding slower to changes in flow. Kant and Humphrey [39] investigated the responsivity of cricket hairs towards airflow pulsations and indeed found that short hairs are significantly more responsive to rapid changes in airflow than long hairs. Cummins and Gedeon [40] derived similar conclusions for hairs with different lengths by modelling and estimating their response towards airflow pulsations. Changing the hair geometry in order to minimize the added virtual damping D is complex, since this will also affect the flow-induced drag torque and generally leads to a smaller rotational angular amplitude. In conclusion, increasing the hair length L of the MEMS sensors will help to bring their performance closer to their limits, but the resonance frequency of the system reduces and the resonance peak sharpens. Thus, what we seem to gain in performance through selected aspects is lost through others, and the overall gain in FoM is small (see for example figure 5, right).

We then explore other venues by considering the outcome of the metric evaluation (figures 3 and 5). We observe that the cricket's hairs—in contrast to the MEMS hairs—operate close to their physical limit over a broad range of frequencies, in agreement with the observations by Bathellier *et al* [16]. To increase the normalized MEMS sensor's performance for a broad range of frequencies, similar to the cricket, the limit definitions shown in (9), (27) and (32) hold the key. We formulate a strategy based on two observations; in cricket hair-sensors

(i) impedance matching allows for maximum power transfer, and

(ii) critical damping ascertains the shortest possible response time.

Consequently, for an optimized MEMS hair-sensor, our strategy stipulates that one can start from an arbitrary hair geometry (d, L, J) and chose the remaining parameters (R, S) such that conditions (i) and (ii) are fulfilled. We will show in the next paragraph that this is a feasible approach since for a given hair geometry the torque related parameters A

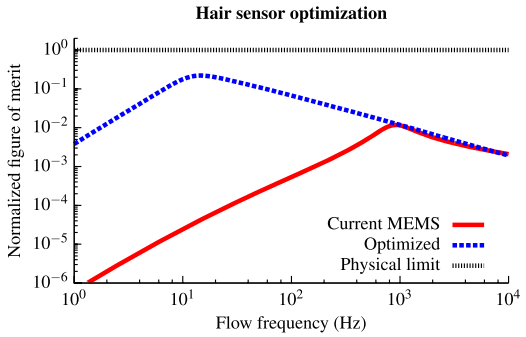

Figure 6. Optimization of the MEMS hair flow sensor.

and B as well as the added mass C and damping D parameters are determined, and the freedom to chose S and R allows to fulfil conditions (i) and (ii).

We start our optimization procedure by inspection of (6). To realize impedance matching given by (13), R should be chosen such that $R = D$, in accordance with the experimental findings of Shimozawa *et al* [4]. For an optimally damped structure, with minimum response time, ζ should equal $\frac{1}{2}\sqrt{2}$. As a result, the following design rules for a flow sensor operating close to the physical limit are obtained:

$$R = D, \qquad S = \frac{2D^2}{J_t}. \tag{34}$$

Inspection of $C(\omega)$ and $D(\omega)$ shows that they are weak functions of frequency; $C = O(\omega^{0.33})$ and $D = O(\omega^{0.22})$ for relevant hair diameters. Hence, (34) can be evaluated without exact knowledge of ω_n. Note that an iterative approach may be used to strictly conform to conditions given by (34) with arbitrary precision. Adherence to (34) helps to fulfil conditions (i) and (ii) for any given hair. However, it leaves no freedom to determine the natural frequency at the same time. Hence, we have to conclude that for an optimal performing hair-sensor the best-frequency is implicitly determined by the characteristics of the hair only. Adherence to (34) then results in:

$$\omega_n = \sqrt{\frac{S}{J_t}} = \sqrt{2}\left(\frac{D}{J_t}\right), \tag{35}$$

implying that high natural frequencies are primarily obtained through thin hairs (since C, D, J, and therefore also J_t, are expected to be $O(L^3)$ at given d value). For MEMS hair-sensors this results in $\omega_n = O(d^{-2})$.

To illustrate the proposed optimization scheme, we applied it to our current MEMS flow sensor model and evaluated the FoM, as shown in figure 6. We observe that the current MEMS hair flow sensor can be greatly improved, much closer approaching its physical limit, by adapting R and S. Despite the fact that the optimization route illustrated in figure 6 requires a reduction of the torsional stiffness by more than 10 000 times relative to the current value, coinciding with an almost 100 times reduction in natural frequency, the FoM improves nearly over the entire frequency range. Such optimization may practically be limited due to constraints by the exploited MEMS technology.

While the above considerations pertain mainly to the man-made artefacts and possible ways to improve their performance, they have also consequences for our understanding of the bauplan of natural hairs. The converging of the allometric scaling we obtained through pure deduction of our physical model with the observed scaling laws obtained on cricket by Shimozawa *et al* [4] is indeed a strong support to the idea that the model captures some basic principles valid for both natural and man-made hairs. Indeed, the observed allometric scaling results for the hair diameter and moment of inertia are $D = O(L^3)$ and $J = O(L^{4.32})$. Our design strategy predicts $S = O(L^{1.68})$, very close to the experimentally determined $S = O(L^{1.67})$. One would furthermore expect $\omega_n = O(L^{-1.34})$, again very close to the $O(L^{-1.32})$ experimentally observed. Given the strong convergence of theoretically expected and experimentally measured scaling laws, we might hypothesize that the tuning of a hair resonant frequency might be not the main target of natural selection, but a secondly derived trait, as it is in our design strategy. This implies focussing the biologist's attention away from the hair frequency response, which was a major focus of decades long work [22] towards the mechanical properties of the socket membrane determining the hair responsivity and power transfer, which has been much less studied (see e.g. [41]). While the FoM and the physically based model developed for its computation functions mainly as a bridge between biology and technology in this work, its uses can reach much further, into the scientific disciplines themselves.

Acknowledgments

The authors would like to thank STW/NWO and Institut Universitaire de France for supporting this research.

Appendix. Oscillating airflow and Stokes' drag coefficient

The flow susceptible hair is subjected to an oscillatory flow $v(t)$ with a given far field amplitude V_0 and angular frequency ω. Assuming that the flow $v(t)$ is oscillating over a flat surface the no-slip boundary condition gives rise to the height y-dependent velocity profile [42, 43]:

$$v(y, t) = V_0 e^{j\omega t}\left(1 - e^{-\beta y}e^{-j\beta y}\right), \tag{A.1}$$

where β is proportional to the reciprocal of the boundary layer thickness δ_b, with ν the kinematic

viscosity:

$$\beta = \sqrt{\frac{\omega}{2\nu}}. \tag{A.2}$$

Note that we use complex notation and take the observable quantities implicitly to be the respective real parts. The expression for $v(y, t)$ is written as a phasor with an amplitude V_y and phase shift ζ_y:

$$v_y(t) = V_y e^{j\left(\omega t+\zeta_y\right)}, \tag{A.3}$$

where

$$\begin{aligned} V_y &= V_0 \kappa(y), \\ \kappa(y) &= \sqrt{1 + e^{-2\beta y} - 2e^{-\beta y}\cos(\beta y)}, \end{aligned} \tag{A.4}$$

and

$$\zeta_y = \arctan\left(\frac{e^{-\beta y}\sin(\beta y)}{1 - e^{-\beta y}\cos(\beta y)}\right). \tag{A.5}$$

With the velocity profile known, the forces exerted on the hair are calculated by Stokes' mechanical impedance Z_S as derived for a cylinder subject to oscillatory movement [44]. The relationship between the flow velocity V and the drag force F per unit length can be expressed as [45, 46]:

$$Z_S = \frac{F}{V} = \pi\rho\left(\frac{d}{2}\right)^2 \omega\Gamma(\omega), \tag{A.6}$$

in which $\Gamma(\omega)$ is called the hydrodynamic function and given by

$$\Gamma(\omega) = j\left[1 + \frac{4K_1\left(\sqrt{j\psi}\right)}{\sqrt{j\psi}K_0\left(\sqrt{j\psi}\right)}\right], \tag{A.7}$$

where K_0 and K_1 are modified Bessel functions of the second kind and ψ is the Stokes parameter:

$$\psi = \frac{\omega}{\nu}\left(\frac{d}{2}\right)^2. \tag{A.8}$$

For $\psi \ll 1$ the mechanical impedance Z_S given in (A.6) can be approximated by a series expansion leading to the expression used by Shimozawa *et al* [4] and Humphrey *et al* [29]:

$$Z_S \approx 4\pi\mu G + j\left[\pi\rho\left(\frac{d}{2}\right)^2\omega - \frac{\pi^2\mu G}{g}\right], \tag{A.9}$$

with μ and ρ the dynamic viscosity and density of air respectively and d the hair diameter. In these equations G, g and s are dimensionless parameters:

$$\begin{aligned} G &= \frac{-g}{g^2 + (\pi/4)^2}, \\ g &= \gamma + \ln(s), \\ s &= \frac{d}{4}\sqrt{\frac{\omega}{\nu}} = \frac{\sqrt{\psi}}{2}. \end{aligned} \tag{A.10}$$

Note that for cricket hairs (A.9) suffices over the entire frequency range of interest. However, for MEMS hairs, owing to their larger diameters as well as larger bandwidth (A.7) needs to be used at higher frequencies. Next, the dynamic drag force per unit length $F(t)$ can be expressed as

$$F(t) = V_0 |Z_S| e^{j\left(\omega t+\eta_S\right)}, \quad \eta_S = \arg\left(Z_S\right). \tag{A.11}$$

The velocity profile of the oscillatory flow is given by (A.3), but to calculate the drag forces on the hair using Stokes's mechanical impedance, the relative velocity of the hair V_{ry} is required, where y is the position along the hair. Assuming the resulting hair movement to be harmonic the relative velocity is given by

$$V_{ry}(t) = V_y e^{j\left(\omega t+\zeta_y\right)} - jy\Theta_m\omega e^{j\left(\omega t+\phi_m\right)}, \tag{A.12}$$

where Θ_m is the hair angular deflection amplitude and ϕ_m its phase. Using Stokes's mechanical impedance, the resulting force per unit length on the flow susceptible hair is found:

$$F_y(t) = |Z_S|\left[V_y e^{j\left(\omega t+\zeta_y+\eta_S\right)} - jy\Theta_m\omega e^{j\left(\omega t+\phi_m+\eta_S\right)}\right]. \tag{A.13}$$

The torque $T(t)$ on the hair is calculated from the force per unit length $F(t)$ acting on the hair:

$$T(t) = \int_0^L F_y(t, y) y \mathrm{d}y. \tag{A.14}$$

As a result, the torque $T(t)$ can be written as

$$\begin{aligned} T(t) = V_0 e^{j\omega t}&\left[\int_0^L \kappa(y) y |Z_S| e^{j\left(\zeta_y+\eta_S\right)}\mathrm{d}y\right] \\ &- j\omega\Theta_m e^{j\left(\omega t+\phi_m\right)}\left[\int_0^L |Z_S| y^2 e^{jy\eta_S}\mathrm{d}y\right], \end{aligned} \tag{A.15}$$

or in a simplified form as

$$T(t) = V_0 e^{j\omega t}[A + jB] - j\omega\Theta_m e^{j\left(\omega t+\phi_m\right)}[D + jC], \tag{A.16}$$

where

$$\begin{aligned} A &= \int_0^L \kappa(y)|Z_S| y \cos\left(\zeta_y + \eta_S\right)\mathrm{d}y, \\ B &= \int_0^L \kappa(y)|Z_S| y \sin\left(\zeta_y + \eta_S\right)\mathrm{d}y, \\ C &= \int_0^L |Z_S| y^2 \sin(\eta_S)\mathrm{d}y, \\ D &= \int_0^L |Z_S| y^2 \cos(\eta_S)\mathrm{d}y. \end{aligned} \tag{A.17}$$

Following Shimozawa *et al* [4], the total torque (A.16) must be inserted in the right-hand side of the second order differential equation for the hair-rotation:

$$J\frac{\mathrm{d}^2\theta(t)}{\mathrm{d}t^2} + R\frac{\mathrm{d}\theta(t)}{\mathrm{d}t} + S\theta(t) = T(t), \tag{A.18}$$

with S is the torsional stiffness, R the torsional resistance and J the moment of inertia. It is assumed that the hair is harmonically driven with frequency ω, giving:

$$-\omega^2 J\Theta_m e^{j(\omega t+\phi_m)} + j\omega R\Theta_m e^{j(\omega t+\phi_m)} + S\Theta_m e^{j(\omega t+\phi_m)} = V_0 e^{j\omega t}[A + jB] + \omega\Theta_m e^{j(\omega t+\phi_m)}[C - jD]. \quad (A.19)$$

This expression can be simplified to

$$\Theta_m e^{j\phi_m}\left[S - J\omega^2 - C\omega + j\omega(R + D)\right] = V_0[A + jB]. \quad (A.20)$$

Consequently, the hair angular deflection amplitude Θ_m and phase ϕ_m are found to be:

$$\Theta_m = \frac{V_0\sqrt{A^2 + B^2}}{\sqrt{\left[S - J\omega^2 - C\omega\right]^2 + [(R + D)\omega]^2}}, \quad (A.21)$$

and

$$\phi_m = \arctan\left(\frac{B\left[S - J\omega^2 - C\omega\right] - A[(R + D)\omega]}{A\left[S - J\omega^2 - C\omega\right] + B[(R + D)\omega]}\right). \quad (A.22)$$

In these expressions, A and B are contributions to the flow-induced drag torque $T(t)$, D is the virtual added damping and C/ω is the virtual added air mass (see also figure 2(a)) [4, 29].

References

[1] Mayo D B and Leishman J G 2010 Comparison of the hovering efficiency of rotating wing and flapping wing micro air vehicles *J. Am. Helicopter Soc.* **55** 25001

[2] Sinibaldi E, Puleo G L, Mattioli F, Mattoli V, Di Michele F, Beccai L, Tramacere F, Mancuso S and Mazzolai B 2013 Osmotic actuation modelling for innovative biorobotic solutions inspired by the plant kingdom *Bioinsp. Biomim.* **8** 025002

[3] Shimozawa T, Murakami J and Kumagai T 2003 Cricket wind receptors: thermal noise for the highest sensitivity known *Sensors and Sensing in Biology and Engineering* (Vienna: Springer) pp 145–57

[4] Shimozawa T, Kumagai T and Baba Y 1998 Structural scaling and functional design of the cercal wind-receptor hairs of cricket *J. Comp. Physiol.* A **183** 171–86

[5] Ozaki Y, Ohyama T, Yasuda T and Shimoyama I 2000 An air flow sensor modeled on wind receptor hairs of insects *Proc. MEMS 2000 (Miyazaki, Japan)* pp 531–6

[6] Chen N, Tucker C, Engel J, Yang Y, Pandya S and Liu C 2007 Design and characterization of artificial haircell sensor for flow sensing with ultrahigh velocity and angular sensitivity *J. Microelectromech. Syst.* **16** 999–1014

[7] Wang Y-H, Lee C-Y and Chiang C-M 2007 A mems-based air flow sensor with a free-standing microcantilever structure *Sensors* **7** 2389–401

[8] Sadeghi M, Peterson R and Najafi K 2011 Micro-hydraulic structure for high performance biomimetic air flow sensor arrays *Technical Digest—IEDM (December 2011, Washington DC)* p 29

[9] Tao J and Yu X 2012 Hair flow sensors: from bio-inspiration to bio-mimicking—a review *Smart Mater. Struct.* **21** 113001

[10] Dijkstra M, van Baar J J J, Wiegerink R J, Lammerink T S J, de Boer J H and Krijnen G J M 2005 Artificial sensory hairs based on the flow sensitive receptor hairs of crickets *J. Micromech. Microeng.* **15** 132–8

[11] Bruinink C M, Jaganatharaja R K, de Boer M J, Berenschot J W, Kolster M L, Lammerink T S J, Wiegerink R J and Krijnen G J M 2009 Advancements in technology and design of biomimetic flow-sensor arrays *Proc. MEMS 2009 (Sorrento, Italy)* pp 152–5

[12] Dangles O, Magal C, Pierre D, Olivier A and Casas J 2005 Variation in morphology and performance of predator-sensing system in wild cricket populations *J. Exp. Biol.* **208** 461–8

[13] Droogendijk H, Bruinink C M, Sanders R G P, Dagamseh A M K, Wiegerink R J and Krijnen G J M 2012 Improving the performance of biomimetic hair-flow sensors by electrostatic spring softening *J. Micromech. Microeng.* **22** 065026

[14] de Bree H-E 2003 An overview of microflown technologies *Acta Acust. United Acust.* **89** 163–72

[15] Humphrey J A C and Barth F 2008 Medium flow-sensing hairs: biomechanics and models *Adv. Insect Physiol.* **34** 1–80

[16] Bathellier B, Steinmann T, Barth F G and Casas J 2012 Air motion sensing hairs of arthropods detect high frequencies at near-maximal mechanical efficiency *J. R. Soc. Interface* **9** 1131–43

[17] Olson H F 1943 *Dynamical Analogies* (New York: D Van Nostrand)

[18] Cartwright K V 2008 Non-calculus derivation of the maximum power transfer theorem *Tech. Interface*

[19] Shinners S M 1998 *Modern Control System Theory and Design* 2nd edn (New York: Wiley)

[20] Gabrielson T B 1993 Mechanical thermal noise in micro-machined acoustic and vibration sensors *IEEE Trans. Electron Devices* **40** 903–9

[21] Dagamseh A M K, Bruinink C M, Wiegerink R J, Lammerink T S J, Droogendijk H and Krijnen G J M 2013 Interfacing of differential-capacitive biomimetic hair flow-sensors for optimal sensitivity *J. Micromech. Microeng.* **23** 035010

[22] Dangles O, Steinmann T, Pierre D, Vannier F and Casas J 2008 Relative contributions of organ shape and receptor arrangement to the design of cricket's cercal system *J. Comp. Physiol.* A **194** 653–63

[23] Miller J P, Krueger S, Heys J J and Gedeon T 2011 Quantitative characterization of the filiform mechanosensory hair array on the cricket cercus *PLoS One* **6** e27873

[24] Bathellier B, Barth F, Albert J and Humphrey J 2005 Viscosity-mediated motion coupling between pairs of trichobothria on the leg of the spider cupiennius salei *J. Comp. Physiol.* A **191** 733746

[25] Casas J, Steinmann T and Krijnen G 2010 Why do insects have such a high density of flow sensing hairs? Insights from the hydromechanics of biomimetic mems sensors *J. R. Soc. Interface* **7** 1487–95

[26] Dagamseh A M K, Wiegerink R J, Lammerink T S J and Krijnen G J M 2012 Towards a high-resolution flow camera using artificial hair sensor arrays for flow pattern observations *Bioinsp. Biomim.* **7** 046009

[27] McConney M E, Schaber C F, Julian M D, Eberhardt W C, Humphrey J A, Barth F G and Tsukruk V V 2009 Surface force spectroscopic point load measurements and viscoelastic modelling of the micromechanical properties of air flow sensitive hairs of a spider (cupiennius salei) *J. R. Soc. Interface* **6** 681–94

[28] Göpfert M C and Robert D 2002 The mechanical basis of drosophila audition *J. Exp. Biol.* **205** 1199–208

[29] Humphrey J, Devarakonda R, Iglesias I and Barth F 1993 Dynamics of arthropod filiform hairs: I. Mathematical modeling of the hair and air motions *Phil. Trans.: Biol. Sci.* **340** 423–44

[30] Keil T A 1997 Functional morphology of insect mechanoreceptors *Microsc. Res. Tech.* **39** 506–31

[31] Morice S, Pincebourde S, Darboux F, Kaiser W and Casas J 2013 Predator-prey pursuit-evasion games in structurally complex environments *Integr. Comp. Biol.* **ict061** 1–13

[32] Droogendijk H, de Boer M J, Sanders R G P and Krijnen G J M 2013 Design, fabrication and characterization of a biomimetic accelerometer inspired by the cricket's clavate hair *Proc. IEEE Sensors (Baltimore, MD, USA, 3-6 November 2013)* pp 167–70

[33] Krijnen G, Floris A, Dijkstra M, Lammerink T and Wiegerink R 2007 Biomimetic micromechanical adaptive flow-sensor arrays *Proc. SPIE* **6592** 65920F

[34] Kumagai T, Shimozawa T and Baba Y 1998 The shape of wind-receptor hairs of cricket and cockroach *J. Comp. Physiol.* A **183** 187–92
[35] Murphey R K 1981 The structure and development of a somatotopic map in crickets: the cereal afferent projection *Dev. Biol.* **88** 236–46
[36] Sakaguchi D S and Murphey R K 1983 The equilibrium detecting system of the cricket: physiology and morphology of an identified interneuron *J. Comp. Physiol.* A **150** 141–52
[37] Horn E and Bischof H-J 1983 Gravity reception in crickets: the influence of cereal and antennal afferences on the head position *J. Comp. Physiol.* A **150** 93–98
[38] Smith C U M 2008 *Biology of Sensory Systems* 2nd edn (New York: Wiley)
[39] Kant R and Humphrey J A C 2009 Response of cricket and spider motion-sensing hairs to air flow pulsations *J. R. Soc. Interface* **6** 1047–64
[40] Cummins B and Gedeon T 2012 Assessing the mechanical response of groups of arthropod filiform flow sensors *Frontiers in Sensing* (Vienna: Springer)
[41] Schaber C F, Gorb S N and Barth F G 2011 Force transformation in spider strain sensors: white light interferometry *J. R. Soc. Interface* **9** 1254–64
[42] Panton R L 1996 *Incompressible Flow* (New York: Wiley)
[43] Steinmann T, Casas J, Krijnen G and Dangles O 2006 Air-flow sensitive hairs: boundary layers in oscillatory flows around arthropod appendages *J. Exp. Biol.* **209** 4398–408
[44] Stokes G G 1851 On the effect of the internal friction of fluids on the motion of pendulums *Trans. Camb. Phil. Soc.* **9** 1–141
[45] Williams R E and Hussey R G 1972 Oscillating cylinders and stokes' paradox *Phys. Fluids* **15** 2083–8
[46] Shi Y and Sader J E 2010 Lattice boltzmann method for oscillatory stokes flow with applications to micro- and nanodevices *Phys. Rev.* E **81** 036706

Chapitre 8

Optimalité des soies filiformes

Steinmann, T. & Casas, J. 2016 The heterogeneity of cricket flow sensing hairs conveys the complex flow signature of predator attack. (*soumis*)

Résumé du chapitre

Les longueurs des poils filiformes des arthropodes terrestres s'étalent sur plus d'un ordre de grandeur, de 100 μm à 5 mm. Les travaux antérieurs sur la biomécanique des poils ont identifié à plusieurs reprises les poils les plus longs comme étant les plus sensibles. Deux études théoriques récentes prétendent cependant que les poils les plus courts seraient aussi les plus sensibles. Ce chapitre expose les raisons de cette divergence et explique ainsi la présence du continuum de longueurs de poils observé dans les canopées de poils de grillons. Ce chapitre se découpe en quatre parties. Tout d'abord, nous résolvons le conflit décrit ci-dessus de manière théorique, en proposant un nouveau modèle de déflexion du poil. Nous considérons la déflexion complète d'un poil dans le flux généré par son prédateur en prennant en compte à la fois les aspects initiaux de son démarrage et l'écoulement réel à long terme auquel sera soumis le poil. Afin de tester le modèle, nous avons estimé dans une seconde étape les paramètres mécaniques des poils et dans une troisième étape le flux produit par un piston imitant l'attaque d'un prédateur, à l'aide de l'anémométrie laser doppler (LDA). La quatrième étape a consisté à comparer les valeurs prédites et observées de plusieurs déplacements de poils soumis à l'écoulement généré par ce piston.

Résultats

Il apparaît que le conflit provenait essentiellement de l'utilisation de différents modèles de flux par les différents auteurs. Alors que presque tous les auteurs ont utilisé un flux oscillatoire mono-fréquentiel, d'autres ont utilisé un flux impulsif imitant le début d'une attaque. Notre solution de l'équation générale de la déflexion d'un poil contient la partie homogène de la solution, expliquant la déflexion du poil dans l'écoulement lors des instants précoces de l'attaque, quand sa réponse naturelle est la plus importante. A cette solution homogène s'ajoute la solution particulière, importante à plus long terme, quand le prédateur approche de la proie et quand la réponse forcée du poil domine. L'ajustement de ce nouveau modèle est excellent pour les longs poils et bon pour les poils plus courts.

Discussion

Nous montrons que les poils courts et longs sont aussi sensibles les uns que les autres, mais à différentes échelles temporelles au cours d'une attaque. Le fait de posséder une canopée de poils, dont les longueurs montrent un tel continuum, permet ainsi de répondre avec efficacité à n'importe quel moment et pour n'importe quelle dynamique d'attaque. Alors que les poils courts sont plus agiles, leur capacité à extraire de l'énergie dans l'air est plus limitée, de sorte que les poils plus longs pourraient éventuellement réagir plus tôt, une fois que leur angle minimal de déclenchement est atteint, en dépit du fait d'être plus lent que les petits. Cependant, cette interaction complexe entre la souplesse des poils et leur sensibilité est en outre modulée par la taille du prédateur, ainsi que par la distance et la vitesse à laquelle il lance son attaque, caractéristiques qui définissent les propriétés de l'écoulement. Il semble ainsi que l'hétérogénéité de la canopée de poils filiformes des grillons reflète la complexité de l'écoulement d'une attaque, depuis son lancement jusqu'à sa conclusion.

The heterogeneity of cricket flow sensing hairs conveys the complex flow signature of predator attack

Thomas Steinmann[1*] and Jérôme Casas[1]
[1] *Institut de Recherche sur la Biologie de l'Insecte*
UMR CNRS 7261 - Université François Rabelais
37200 Tours, France

[*] Author for correspondence (thomas.steinmann@univ-tours.fr)

September 27, 2016

Abstract

Arthropod flow sensing hair length ranges over more than an order of magnitude, from 0.1 to 5 mm. Previous studies repeatedly identified the longest hairs as the most sensitive, but recent studies identified the shortest hairs as the most responsive. We resolved this apparent conflict by proposing a new model taking into account both the initial and long-term aspects of the flow pattern produced by a lunging predator. We estimated the mechanical parameters of the hairs and the flow produced by predators mimics and compared the predicted and observed values of hair displacements. Short and long hairs respond over different time scales during the course of an attack. By harboring a canopy of hairs of different lengths, forming a continuum, the insect can fractionize these moments. Short hairs are more agile, but are less able to harvest energy from the air. This may result in longer hairs firing their neurons earlier, despite their slower deflection. The complex interplay between hair agility and sensitivity is also modulated by predator distance and the attack speed, characteristics defining flow properties. The heterogeneity of the hair canopy mirrors the flow complexity of an entire attack, from launch to grasp.

Keywords : predator-prey interaction, biomechanics, sensory ecology, filiform hairs, 'matched filters'

Contents

1 Introduction

The ability of animals to sense biotic and abiotic changes in their environment depends greatly on the performance of their sensors. The peripheral sensory structures and their associated sensory neural circuits have evolved to deal with complex sensory information, by matching their properties to the characteristics of the most crucial sensory stimulus they need to detect (Wehner (1987), von der Emde and Warrant (2015)). Arthropods can detect the movement of the surrounding fluid, usually through the deflection of long filiform hairs from their resting position (Casas and Dangles (2010)). Crickets live on forest litter. Their survival is at least partly dependent on their ability to detect their predators with hundreds of these filiform hairs, each of which is lodged into a socket and connected to a single neuron (Gnatzy and Tautz (1980)). When a hair moves up to a given angle from its resting position, it transfers enough energy to the attached neuron to trigger an action potential. The disturbances of air flow upstream from running spiders have been assessed by particle image velocimetry and computational fluid dynamics with finite-element method (Casas et al. (2008), Casas and Steinmann (2014)). The relationship between attack speed and the maximal distance at which the cricket can perceive the danger is parabolic. This implies an immediate perception of the danger, from the onset predator attack, at the distances and speeds observed in nature (Casas and Steinmann (2014)). The cricket cercal system is known to be one of the most sensitive sensory systems in existence, and it is widely assumed that increasing hair length is associated with greater individual hair sensitivity (Shimozawa and Kanou (1984a), Humphrey et al. (1993)). However, longer hairs are heavier and more inert, and would therefore be expected to be less responsive. These conflicting views may result from the use of different criteria for optimality, but they may also be due to differences in the nature of the stimuli used in experimental studies. In most studies, the filiform hairs were considered to respond to highly controlled oscillating flows (Shimozawa and Kanou (1984a), Kumagai et al. (1998) Humphrey et al. (1993)) or to generic impulse flows (Cummins and Gedeon (2012)). Historically, the cricket mechanosensor has been described as an inverted pendulum, a second-order mechanical system, and studied through engineering approaches, through the determination of its harmonic response. However, studies of biologically relevant stimuli focusing on the flow generated by running spiders have shown that the flow is neither a simple sinusoidal nor an impulse flow, instead being a hybrid between the two (Casas et al. (2008), Casas and Steinmann (2014)).

Elucidating the response of sensors to this complex stimulus will provide us with information about their specific functionality. Hair responses to biologically relevant stimuli have been studied by Kant and Humphrey (2009) and, more recently, by Cummins and Gedeon (2012). In earlier models, preceding that of Kant & Humphrey, the hair was considered as a harmonic oscillator, oscillating in a harmonic flow, without taking into account its initial motion. Kant & Humphrey showed that early movements were of key importance and could not be neglected. They predicted the deflection of hairs of various lengths subjected to a flow generated by an accelerating sphere. They modeled the flow as an accelerating pulsation that decreased in magnitude over time and with increasing distance from the source. This temporal decay was approximated by a Gaussian function, itself the function of a binary rectangular switch. The authors were interested in both the increase and decay of the flow perturbation. The use of this approximation enabled them to model the flow boundary layer and, thus, the drag forces promoting hair deflection. Based on the results they obtained with this novel approach, they claimed that shorter hairs could respond more sharply and with a greater amplitude than longer hairs. Cummins and Gedeon (2012) calculated the impulse response function (IRF) of the hairs, their response to a rapid change, as a Dirac pulse. They did not convolve this IRF with different air velocities to predict the hair response to relevant signals but restricted their analysis to the

impulse response functions of different arrangements of hairs. Their prediction of an earlier and stronger reaction of shorter hairs is consistent with the findings of Kant & Humphrey, but completely opposed to previous thinking. Unfortunately, the temporal changes in flow velocity and acceleration generated by an approaching predator and the deflection of the stimulated hairs were not quantified in any of these studies, leaving these more realistic situations untested. In this study, we considered the entire temporal history of the flow field generated by a predator, rather than focusing exclusively on a sudden flow generated by an accelerated cylinder, as in the study by Kant & Humphrey. We aimed to find an explanation for the presence of a continuum of hair lengths in real hair canopies, as observed in crickets. The resolution of the discrepancy between short-hair responsiveness and long-hair sensitivity required the deconstruction of a long-held analogy in which the cricket cercus is compared with the hardware implementation of a spectrum analyzer. This deconstruction is described in our general theory of hair moving in impulsive transient flow. This model was validated on experimental data on large deflections and extrapolated to smaller deflections, to resolve the conflict and demonstrate that both short and long hairs are optimal, but in response to different inputs. However, the resolution of this conflict is possible only with the use of new and comprehensive optimality criteria based upon both sensitivity and reponsiveness.

2 A general theory of hair moving in impulsive transient flows

Both this study and that of Kant and Humphrey (2009) involve the development of a physical–mathematical model simulating the response of a filiform hair to an airflow pulsation $V_f(t)$ generated by the sudden attack of a predator running at a velocity V_p. Our model of hair deflection is based on that of Kant & Humphrey. The main difference between the two approaches concerns the choice of temporal history of predator approach, and, thus, flow conditions. In the Kant and Humphrey model, the predator stops immediately after making a very rapid movement, producing an instantaneous flow impulse that attenuates in a Gaussian fashion (Figure 1.a). By contrast, we chose to model the entire time history of the flow produced by the predator, from its start until eventual prey capture (Figure 1.b).

We provide below a detailed description of the differences between the two approaches. We first explain the equation for the motion of a hair, linking the hair deflection angle θ to the total torque T due to drag force, added mass force and pressure gradient force (Figure 2.a). The total torque T acting on a hair depends on the deflection of the hair itself, as the forces applied to the hair depend on its motion relative to the surrounding fluid V_f : $V_r = V_f - y\theta$ (Figure 2.a). We separated all components relating to hair deflection from those relating to flow velocity in the expression of torque. This made it possible to express the forcing function Q_{SC}, related only to fluid velocity V_f and independent of hair deflection angle θ. We describe (i) the analytical expression of pulse fluid velocity ${V_f}^{KH}$ used in the K & H model and its corresponding Fourier series V_0^{mKH} and (ii) the numerical temporal flow generated by a simulated predator attack V_f^{SC} and its corresponding Fourier series V_0^{mSC}, the input of our model. In section 2.3, we focus on our choices for the boundary layer effect, describing the modification of flow velocity V_f by the hair substrate (Figure 2.b). Finally, section 2.4 provides a resolution of the equation of motion and the development of a general analytical solution. After defining the boundary conditions for hair deflection, we obtained a general solution superimposing (i) the homogeneous solution of the equation of motion, i.e. the natural response of the system, and (ii) the particular solution of the equation of motion, i.e the forced response of the system.

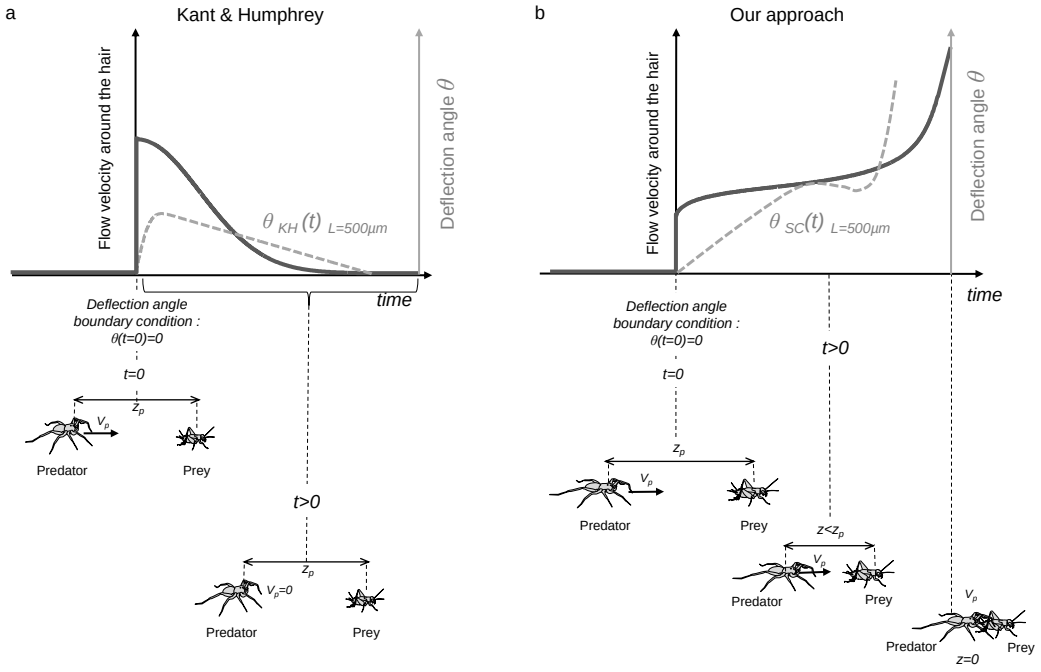

Figure 1: Differences between Kant & Humphrey's model (a) and our approach (b). (a) On the left panel, the flow velocity produced by a predator around a hair jumps from 0 to its initial and maximal value at $t = 0$, decreasing thereafter. The distance between predator and prey z_p is constant. (b) On the right panel, the flow velocity around a hair also jumps from 0 to its initial value at $t = 0$, but it is initially minimal and subsequently increases. The distance between predator and prey z_p decreases with time.

2.1 Modeling the intrinsic response of a hair

A hair is represented as a straight cylinder of length L and diameter d, standing vertically on a flat plate and rotating around its base (Figure 2.a). The conservation of angular momentum for the motion of a filiform hair, approximated as a forced, damped harmonic oscillator, is given by :

$$I_h\ddot{\theta} + R_h\dot{\theta} + S_h\theta = T \tag{1}$$

where, θ (rad), $\dot{\theta}$ (rad s^{-1}) and $\ddot{\theta}$ (rad s^{-2}) are the angular displacement, velocity and acceleration of the hair about its pivot point. I_h (N m $s^2 rad^{-1}$) is the moment of inertia of the hair; S_h (N m rad^{-1}) and R_h (N m s rad^{-1}) are the hair torsional restoring constant and damping constant, respectively, and T (N m) is the total torque acting on the hair. This model was introduced by Humphrey et al. (1993).

The joint linking the hair to the cuticle is modeled as a linear viscoelastic element that resists hair deflection θ with a torque $-S_h\theta$ and also experiences a frictional torque $R_h\dot{\theta}$, reflecting the rotational energy dissipated by the hair at the joint. In the Kant & Humphrey approach, the total torque acting on the hair is determined from geometry and is given by:

$$T_{KH} = \int_0^L (F_D + F_{AM} + F_{PG})ydy \tag{2}$$

where (i) F_D (N m^{-1}), (ii) F_{AM} (N m^{-1})and (iii) F_{PG} (N m^{-1}) are forces per unit length acting on the hair, due to (i) the viscous drag, (ii) the added mass of air around the hair and (iii) a pressure gradient force, respectively. The Reynolds number is low, $Re = \frac{V_r d}{\nu} < 0.1$, with d the

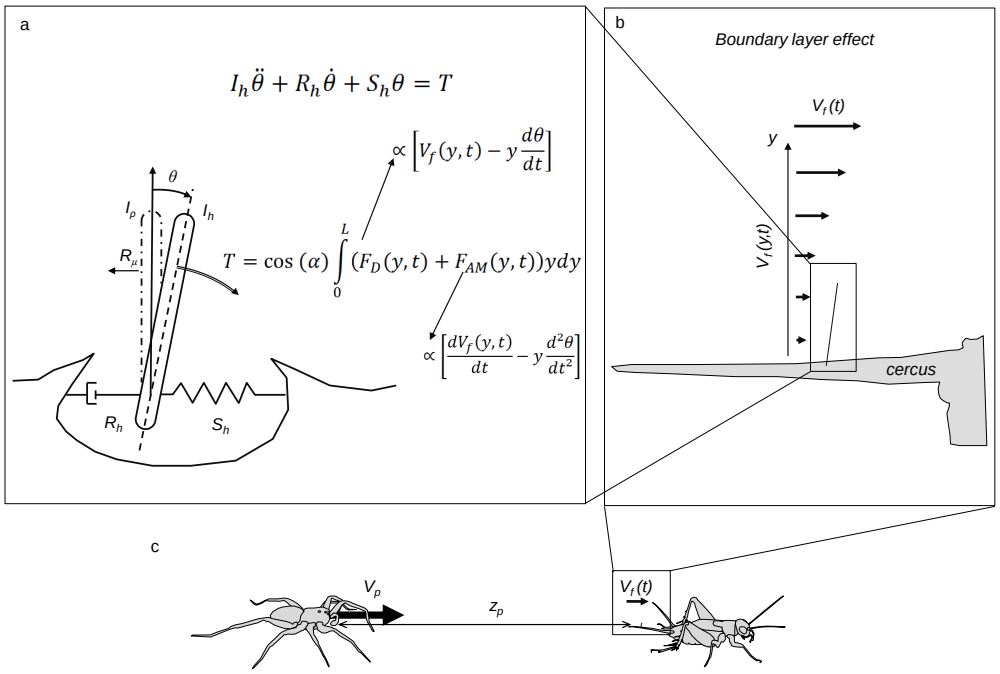

Figure 2: Main components of models of the response of the hair to a flow pulsation produced by a running predator. The spider runs at a velocity V_p towards the cricket initially placed at a distance z_p from the spider. The movement of the predator in the incompressible fluid produces a flow displacement up to several centimeters in front of its body. (a) Summary of the mathematical formalism used to model the dynamics of the filiform hairs. The total torque acting on hair T is a function of (i) the drag force F_D, proportional to the flow velocity V_f and (ii) the added mass force F_{AM}, proportional to the time derivative of V_f. (b) At distance z_p, the flow velocity $V_f(t)$ produced by predator displacement is modified in the vicinity of the cricket cercus supporting the filiform hairs. Flow velocity in this boundary layer is $V_f(y,t)$, with the boundary conditions $V_f(\infty,t) = V_f(t)$ and $V_f(0,t) = 0$.(c) Diagramatic representation of predator/prey interaction.

filiform hair diameter (ranging from 5 to 10 μm) and $\nu = 1.56 \times 10^{-5} m^2 s^{-1}$ the kinematic viscosity of air. The viscous forces thus dominate, and the drag force is given by the classical Oseen (White (1991)) equation. F_D simplifies to:

$$F_D = \frac{\pi \mu V_r}{2} \tag{3}$$

With $\mu = 1.81 \times 10^{-5} kg/(ms)$ being the dynamic viscosity of air. The added mass force F_{AM} is due to the added mass of air accelerated with the hair it surrounds and is given by:

$$F_{AM} = \pi \left(\frac{d}{2}\right)^2 \rho \dot{V}_r \tag{4}$$

The pressure gradient force F_{PG} is the force required to accelerate the air that would occupy the volume of the length of the hair if it were absent and is equal to:

$$F_{PG} = \pi \left(\frac{d}{2}\right)^2 \rho \dot{V}_f \tag{5}$$

where $V_r = V_f - V_h$ (m.s^{-1}) is the relative velocity of the air (V_f) with respect to that of the hair (V_h). The velocity of the hair depends on its distance y (m) from the substrate and is given by $V_h = y\dot{\theta}$. Replacing this value in the integral of total torque T_{KH} gives:

$$T_{KH} = \int_0^L \left(\frac{\pi\mu}{2} \left(V_f - y\dot{\theta} \right) + \pi \left(\frac{d}{2} \right)^2 \rho \left(\dot{V}_f - y\ddot{\theta} \right) + \pi \left(\frac{d}{2} \right)^2 \dot{V}_f \right) y dy \tag{6}$$

$$T_{KH} = \int_0^L \left(\frac{\pi\mu}{2} V_f + \pi \left(\frac{d}{2} \right)^2 \rho \dot{V}_f \right) y dy - \pi \left(\frac{d}{2} \right)^2 \frac{\rho L^3}{3} \ddot{\theta} - \frac{\pi\mu L^3}{6} \dot{\theta} \tag{7}$$

Substituting equation (9) in the equation of motion (1) gives:

$$\left(I_h + I_\rho \right) \ddot{\theta} + \left(R_h + R_\mu \right) \dot{\theta} + S_h \theta = Q_{KH} \tag{8}$$

with

$$I_\rho = \pi \left(\frac{d}{2} \right)^2 \frac{\rho L^3}{3} \tag{9}$$

and

$$R_\mu = \frac{\pi\mu L^3}{6} \tag{10}$$

being additional inertia and damping contributions due to the air medium, respectively. The quantity Q_{KH} is the forcing function used by Kant & Humphrey:

$$Q_{KH} = \int_0^L \left(\frac{\pi\mu}{2} V_f + \pi \frac{d^2}{2} \rho \dot{V}_f \right) y dy \tag{11}$$

In our approach, previously described for harmonic flows in the study by Bathellier et al. (2012) and generalized here to impulse flows, the total torque acting on the hair is defined as:

$$T_{SC} = \int_0^L cos(\alpha) \left(F_{AM} + F_D \right) y dy \tag{12}$$

with

$$F_{AM} = \rho\pi \frac{d^2}{4} \frac{\partial \left(V_f - V_h \right)}{\partial t} \tag{13}$$

$$F_D = \frac{\pi\mu}{2} \left(V_f - V_h \right) \tag{14}$$

and $\cos(\alpha)$ reflecting the effect of the preferential directionality of the hair and α (rad) being the angle between the direction of flow and the preferential orientation of the hair.

Replacing equations (15) and (16) in equation (14) gives:

$$T_{SC} = cos(\alpha) \int_0^L \left(\frac{\pi\mu}{2} V_{_f} \rho + \pi \frac{d^2}{4} \dot{V}_f \right) y dy - \frac{\pi\mu L^3}{6} \dot{\theta} - \pi \left(\frac{d}{2} \right)^2 \frac{\rho L^3}{3} \ddot{\theta} \tag{15}$$

Substituting equation (15) in equation of motion (1) gives :

$$\left(I_h + I_\rho \right) \ddot{\theta} + \left(R_h + R_\mu \right) \dot{\theta} + S_h \theta = Q_{SC} \tag{16}$$

The quantity Q_{SC} is our forcing function:

$$Q_{SC} = cos(\alpha) \int_0^L \left(\frac{\pi\mu}{2} V_f + \pi \frac{d^2}{4} \rho \dot{V}_f \right) y dy \tag{17}$$

Thus, in our model, equation (16) is equivalent to equation 8 in the Kant & Humphrey model. In summary, a first difference between the two models is the smaller contribution of the time derivative of flow velocity to the forcing function of equation (17) in our model. We do not explicitly include the pressure gradient force F_{PG} in the balance of forces acting on an element of hair length *dy*, as it is already contained in F_{AM}.

2.2 Modeling forcing flows away from the hair

In the forcing function of Kant & Humphrey, Q_{KH}, the velocity of the flow V_f is the analytical solution of a flow field parallel to the longitudinal axis of an infinitely long cylinder representing the cercus. The authors assume that the velocity distribution due to a flow produced by a predator lunging towards its prey will consist of linearly superposed harmonic sinusoids with arbitrary frequencies, $\omega_m = 2\pi m \Delta f$, with Δf the frequency step of the discrete Fourier transform of V_f. The summation of these harmonic sinusoids results in the following expression of the velocity flow:

$$V_f^{KH}(t) = \sum_{m=0}^{\infty} {V_0}^m{}_{KH} e^{-i\omega_m t} \tag{18}$$

Where ${V_0}^m{}_{KH}$ is the amplitude of the sinusoidal wave associated with frequency ω_m. In the Kant & Humphrey model, the flow results from the sudden movement of a predator in the vicinity of its prey, represented by a pulsation velocity function with a rich frequency content. They chose to use a temporal Gaussian pulsation that was a function of a binary rectangular switch, as they were interested in both the development of this perturbation and its decay. They thus modeled the movement of a hair due to a infinitely quick acceleration of an incoming predator at a distance z_p from its prey, moving at a velocity V_p and stopping immediately after the start of the movement. The distance from the prey thus remains *de facto* unaltered in their model. In their model, the frequency content of the stimulus flow is not a function of the velocity of the attack, but is instead determining by the characteristic duration of the pulsation $\sigma = (2\beta)^{-1/2}$. This duration varies between 7 and 220 ms. The impulse flow can thus be described as follows:

$$V_f^{KH}(t) = V_p \Big(1 + \frac{z_p}{D}\Big)^{-3} e^{-\beta |t|^2} \tag{19}$$

This equation of impulse flow can be expressed in terms of a Fourier series, in the same spirit as equation (20). ${V_f}^{KH}$ can also be expressed as:

$$V_f^{KH}(t) = \sum_{m=0}^{\infty} {V_0}^m{}_{KH}(z_p, \beta) e^{-i\omega_m t} \tag{20}$$

with the amplitude of the sinusoidal waves associated with the frequency ω_m:

$${V_0}^m{}_{KH}(z_p, \beta) = V_p \Big(1 + \frac{z_p}{D}\Big)^{-3} \frac{1}{\pi} \int_{-\pi}^{\pi} e^{-\beta t^2} e^{-i\omega_m t} dt \tag{21}$$

We chose to use the discrete Fourier series of more biologically relevant flows directly, rather than using a forcing function to represent the Gaussian decay of the flow. These flows correspond to the entire temporal flow produced by a piston mimicking the predator, measured as described in Appendix A.

2.3 Modeling forcing flows in the vicinity of the hair and cercus

The flow velocity $V_f(t)$ is modified in the vicinity of the hair substrate (figure 2.b). We describe here the Kant & Humphrey expression for the boundary layer, and the boundary layer effect in their model. At this scale, V_f is not merely a function of time t, it also depends on the distance to the substrate y. The velocity of flow in this boundary layer is expressed as $V_f(y,t)$, with the boundary conditions $V_f(\infty,t) = V_f(t)$ and $V_f(0,t) = 0$.

Kant & Humphrey solved their equation of motion (8) by determining an explicit analytical form of the velocity ${V_f}^{KH}$ that was a function of the boundary layer effect dependent on the distance y from the surface of cercus. They used the Fourier decomposition of ${V_f}^{KH}(t)$ and

estimated the boundary layer affecting each harmonic component of the Fourier series. The equation for a boundary layer in a harmonic oscillatory flow past a longitudinal cylinder (i.e. the cercus) was given by Humphrey et al. (1993). The shape of this boundary layer depends mainly on flow frequency and cercus diameter. Assuming that ${V_f}^{KH}(t)$ is the sum of sinusoidal flows of amplitude ${V_0}^m{}_{KH}$ and frequency ω_m, Kant & Humphrey expressed the velocity profile along component y as:

$$V_f^{KH}(y,t) = \sum_{m=0}^{\infty} {V_0}^m{}_{KH} e^{-i\omega_m t} \left(1 - \frac{K_0(\lambda_m R)}{K_0(\lambda_m)}\right) \tag{22}$$

where $\lambda_m = \frac{D}{2}\left(\frac{i\omega_m}{\nu}\right)^{1/2}$, the flow oscillation $\omega_m = m\,(2\pi f)$, $R = 1 + y/(\frac{D}{2})$, D is the cercus diameter, ${V_0}^m{}_{KH}$ is the amplitude of the sinusoidal wave associated with the frequency ω_m, ν is the kinematic viscosity of the air and $K_0()$is the modified Bessel function operator of the second kind. Equation (22) reflects the fact that non-harmonic flow in the boundary layer over a substrate is the sum of the boundary layers of each of its frequency-dependent components (Larson (1996)). Taking equations (11), (18) and (22), and using ${V_f}^{KH}(y,t)$ and its time derivative, Kant & Humphrey defined the forcing function Q_{KH} as:

$$Q_{KH} = \sum_{m=0}^{\infty} \left(\frac{\pi\mu}{2} - i\omega_m \pi \frac{d^2}{4}\rho\right) {V_0}^m{}_{KH} K_{KH}\left(\omega_m, L\right) e^{-i\omega_m t} \tag{23}$$

The integral in equation (23) encompasses the boundary layer effect and was explicitly calculated by Kant & Humphrey as:

$$K_{KH}\left(\omega_m, L\right) = \int_0^L \left(1 - \frac{K_0(\lambda_m R)}{K_0(\lambda_m)}\right) y dy = \frac{R_L^2 - 1}{2} - \frac{R_L K_1\left(R_L \lambda_m\right) - K_1\left(\lambda_m\right)}{\lambda_m K_0\left(\lambda_m\right)} \tag{24}$$

with $R_L = 1 + L/(\frac{D}{2})$.

In our model, we chose to use another expression of the velocity V_f (according to Steinmann et al. (2006)):

$$V_f^{SC}(y,t) = \sum_{m=0}^{\infty} {V_0}^m{}_{SC} e^{-i\omega_m t} \left(1 - \frac{e^{-(1+i)\sqrt{\frac{\omega_m}{2\nu}}y}}{\sqrt{1 + \frac{2y}{D}}}\right) \tag{25}$$

so that our forcing function becomes :

$$Q_{SC} = \cos(\alpha) \sum_{m=0}^{\infty} \left(\frac{\pi\mu}{2} - i\omega_m \pi \frac{d^2}{4}\rho\right) {V_0}^m{}_{SC} K_{SC}\left(\omega_m, L\right) e^{-i\omega_m t} \tag{26}$$

with the boundary layer effect factor being :

$$K_{sc}\left(\omega_m, L\right) = \int_0^L \left(1 - \frac{e^{-(1+i)\sqrt{\frac{\omega_m}{2\nu}}y}}{\sqrt{1 + \frac{2y}{D}}}\right) y dy \tag{27}$$

While the formulations are different between Kant & Humphrey and ours, the underlying physics is identical, as confirmed by the very similar numerical outputs of equation (24) and equation (27).

2.4 Synthesis: hairs moving under impulsive transient flows

The final steps for solving the equation of a hair movement consist in solving the second order inhomogeneous differential equation (16). Here we do not describe the resolution of Kant & Humphrey equation (2.33), but rather focus on the resolution of our model. We however followed the method of Kant & Humphrey. Some of the following steps are well known and kept here only for comprehensiveness. The general solution ($\theta(t)$)of equation (16) consists of the homogeneous ($\theta_h(t)$) and particular ($\theta_p(t)$) solutions (Greendberg M. D. (1988)). The classical steps of solving such equation (see appendix B) lead to:

$$\theta_{SC}(t) = \sum_{m=0}^{\infty} \frac{cos(\alpha)\left(\frac{\pi\mu}{2} - i\omega_m \pi \frac{d^2}{4}\rho\right) {V_0^m}_{SC} K_{SC}(\omega_m, L)}{-I_T {\omega_m}^2 - (R_h + R_\mu)\omega_m + S_h} \left[\frac{\omega_m i + \gamma_2}{\gamma_1 - \gamma_2} e^{-\gamma_1 t} - \frac{\omega_m i + \gamma_1}{\gamma_1 - \gamma_2} e^{-\gamma_2 t} + e^{-i\omega_m t}\right] \tag{28}$$

This expression is similar to the solution of Kant & Humphrey, except that the quotient in the sum factor of our equation (28), that we will name the mechanical transfer function F_{mec} :

$$F_{mec}^{SC} = \frac{1}{-I_T {\omega_m}^2 - i(R_h + R_\mu)\omega_m + S_h} \tag{29}$$

is different from the one appearing in Kant & Humphrey equations (2.29), (2.31), (2.32) and (2.33) :

$$F_{mec}^{KH} = \frac{1}{O^2 - {\omega_m}^2 - 2iO\zeta\omega_m} = \frac{1}{\frac{S_h}{I_T} - {\omega_m}^2 - i\left(\frac{R_h + R_\mu}{I_T}\right)\omega_m} \tag{30}$$

$$= \frac{1}{\frac{1}{I_T}\left(S_h - I_T {\omega_m}^2 - (R_h + R_\mu)\omega_m\right)} = I_T . F_{mec}^{SC} \tag{31}$$

We were unable to retrace the results of Kant & Humphrey and the use of their equation of F_{mec}^{KH} leads to inconsistent results.

In order to get an intuitive feeling of the internal working of equation (28), we work through an example to determine the deflection of a 500 μm hair, using a single mono-frequency impulse. To achieve this, we first set the discrete frequency step (frequency sampling interval) to $\Delta f = 20\ Hz$ and $V_0^m = 0$ for all values of m, except for $m{=}1$ where $V_0^1 = 1$. It results that the equation:

$$V_f(t) = \sum_{m=0}^{\infty} V_0^m e^{-i\omega_m t} \tag{32}$$

becomes

$$V_f(t) = real(V_0^1 e^{-i2\pi\Delta f t}) = \cos(2\pi\Delta f t) \tag{33}$$

This temporal expression of velocity corresponds to a sinusoidal wave flow of amplitude 1 m/s and frequency 20 Hz. At time t=0, the velocity is set to $V_f(t{=}0^+){=}1$ m/s. Using equation (28), we can derive the expression of the change in hair deflection over time:

$$\theta(t) = \cos(\alpha) T F_{mec}^{SC} \left(\frac{\pi\mu}{2} - i2\pi\Delta f \pi \frac{d^2}{4}\rho\right) {V_0^m}_{SC} K_{SC}(\omega_m, L) \left[\frac{2\pi\Delta f i + \gamma_2}{\gamma_1 - \gamma_2} e^{\gamma_1 t} - \frac{2\pi\Delta f i + \gamma_1}{\gamma_1 - \gamma_2} e^{\gamma_2 t} + e^{-i2\pi\Delta f t}\right] \tag{34}$$

equivalent to $\theta(t) = \Gamma_1 e^{\gamma_1 t} + \Gamma_2 e^{\gamma_2 t} + \Gamma_3\ e^{-i2\pi\Delta f t}$, with the boundary conditions $\theta(0) = 0$ and $\dot{\theta}(0) = 0$. For short times $t \ll \frac{1}{2\pi f}$, the homogeneous part ($\Gamma_1 e^{\gamma_1 t} + \Gamma_2 e^{\gamma_2 t}$) is much larger than the particular part $\Gamma_3\ e^{-i2\pi\Delta f t}$. The movement of the hair is constrained by the boundary conditions at $t{=}0$ and is determined principally by the homogeneous coefficients. This means that the natural response of the hair drives its behavior at early time points, as shown in figure 3, in which the general solution follows its homogeneous component for times below 1 ms. For times exceeding 2.5 ms, the general solution much more closely resembles the particular solution, indicating that the movement of the hair is dependent principally on its forced response.

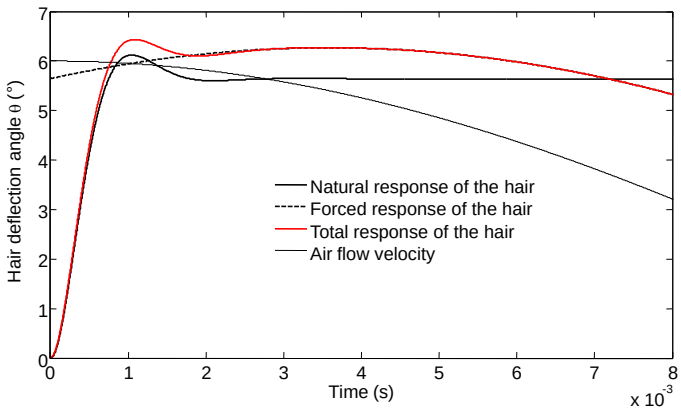

Figure 3: Comparison of the natural and forced response components of the total response (red) of a 500 μm -long hair to a 20 Hz single-frequency air flow impulse. The natural response of the hair is described by the homogeneous solution of the equation of motion (34), whereas the forced response is described by the particular solution of equation (34). The total response of a hair is determined as the sum of its natural and forced responses.

3 Experimental validation of the new model

We validated our model by comparing the model output $\theta_{SC}(t)$ (equation (28)) with measurements of hair deflection under the flow produced by an approaching piston. As explained in section 2.4, the deflection of the hair is dependent principally on its mechanical parameters I_T, R_h, R_μ, S_h, γ_2 and γ_1 and on the flow produced by the piston $V_{0_{SC}}^m$. The methodology used to estimate the mechanical parameters is described in detail in Appendix C. Appendix A introduces the techniques used to determine the flow produced by the piston and explains the influence of piston movement velocity on the spectral component of flow velocity in the vicinity of the hair.

3.1 Methods

Adult male and female crickets (*Acheta domesticus*) were anesthetized by chilling, and the legs, wings and female ovipositor were removed. The crickets were fixed on a micromanipulator placed in a sealed glass box. The moving piston, also placed in the box, was positioned to move in the anterio-posterior axis of the body of the cricket (Figure (4)). Hair deflection was monitored with a high-speed video camera, at 1000 frames per second (Vision Research Phantom V9.1), with a binocular lens. We had to work at high magnification (10x) to obtain an accurate estimate of hair deflection. The time origin ($t = 0$) was estimated as the time at which the piston started moving.

The velocity of hair deflection was extracted from 1000 Hz video recordings, by comparing subpixel displacement in successive images, using a correlation algorithm on an area of 32 pixels^2 (*Dantec Dynamic Studio 2.30 2009*). With this subpixel interpolation correlation algorithm, a 2-Megapixel camera for imaging and a field of view of 2 $\times$ 2 mm^2, we expected to obtain a theoretical displacement resolution of 0.1 μm. This represents a theoretical minimal deflection angle of 0.01° for a hair with a length of 500 μm. The deflection measurements were restricted to larger attack velocities (30 cm/s and 58 cms/s), due to background noise from unwanted residual low-amplitude air displacements and piston vibrations transmitted through the cricket cerci. We measured the deflection of six isolated hairs (L=382, 386, 632, 795, 870 and 1063 μm)

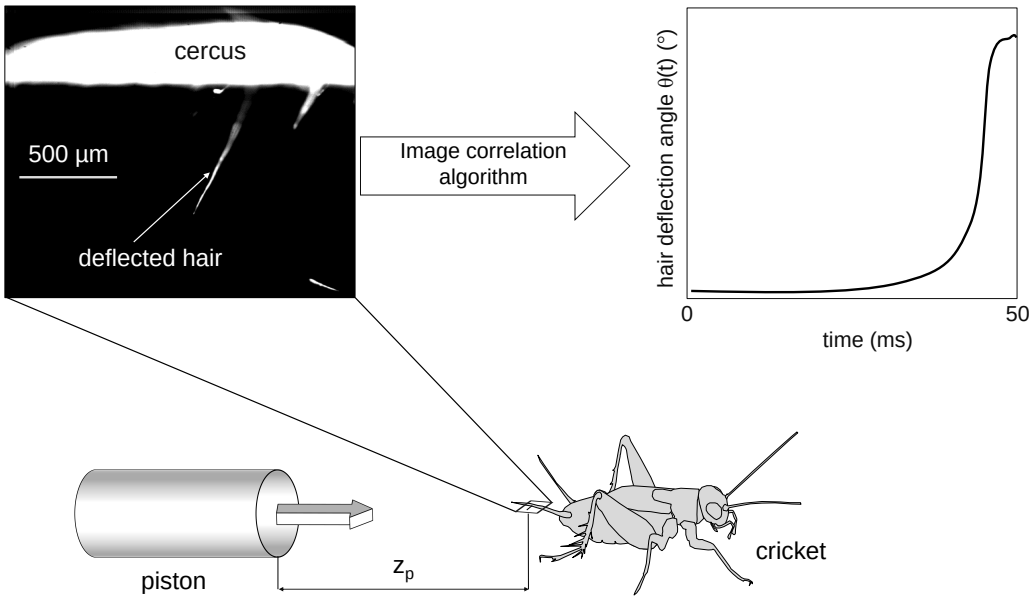

Figure 4: Experimental setup used to measure hair by the piston flow. In a sealed glass box, the 8 mm-diameter moving piston was placed at a distance of $z_p = 5$ cm in front of the test specimen. The piston was moved in the anterio-posterior axis of the cricket body. A 1000 fps high-speed camera mounted on a 10x binocular lens was used to monitor hair deflection.

during the approach of the piston at these velocities.

One key element taken into account when fitting our model (equation (28)) was the preferential plane of deflection of the hair. This factor greatly affects the amount of flow available for hair deflection (Miller et al. (2011), Heys et al. (2012)). Unlike its length, the directionality α of the hair was not known and had to be estimated by regression. We first fitted equation (28), using the ${V_0}^m{}_{SC}$ estimated for the piston approaching at 58 cm/s, with directionality α as the sole fit parameter, from measurements on hairs of six lengths, for a velocity of 58 cm/s. This made it possible to estimate the directionality of the hair. We then cross-validated our model by estimating the deflection of the hair subjected to air flow from the piston approaching at 30 cm/s, using α as a fixed parameter in equation (28), with ${V_0}^m{}_{SC}$ estimated at that speed. At 30 cm/s, we were able to record deflection for only four hairs. The deflections of the 386 and 870 μm hairs under the flow produced by the piston moving at 30 cm/s were too small to be detected.

3.2 Results

The results are summarized in Figure (5). In each of the six panels of the figure, the gray and red solid curves represent the deflection as modeled with equation (28). In this equation, parameters I_T, R_h, R_μ, S_h, γ_2 and γ_1 are predetermined as they are constrained by hair length, as shown in Appendix C. ${V_0}^m{}_{SC}$ is a complex parameter determined by flow and estimated in Appendix A. The model predictions are reasonably good, at least for the three longest hairs. For the smallest hair (382 μm), we recorded a large mean deflection at intermediate times that the model was unable to predict.

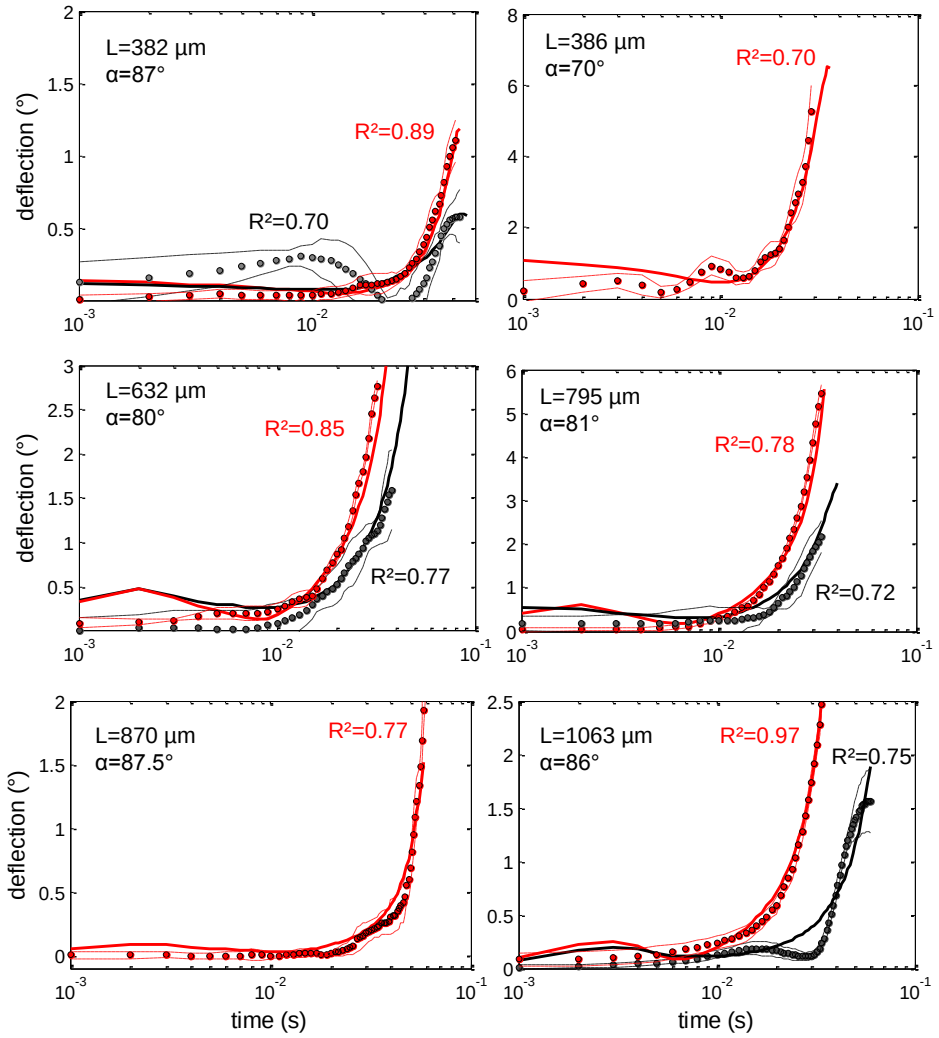

Figure 5: Comparing hair deflection measurement and model prediction. The points represent the measurements of deflection for six isolated hairs (L=382, 386, 632, 795, 870 and 1063 μm). The gray points represent the average deflection time for a hair of the given length in response to the flow produced by the piston approaching at 30 cm/s. The thin black lines represent the standard deviation. The red points and red thin lines represent the mean deflection and standard deviation for the same hair subjected to the flow produced by a piston approaching at 58 cm/s.

4 Discussion

4.1 Limitations of our experimental and theoretical approaches

We will discuss here the field of relevance of our experimental and theoretical study.

Fourier series decomposition is classically used to model the impulsive transient boundary layer $V_f^{SC}(y,t)$ in descriptions of the theoretical evolution of turbulent boundary layers (Larson (1996)). The implicit superimposition should, however, be validated by means of further PIV experiments on the changes in the boundary layer over a cricket cercus during the increase in impulsive flow generated by the approach of a piston. Alternatively, computational fluid dynamics (CFD) can be used for the numerical validation of this approach.

The disparity of formalism between the equations of Kant and Humphrey (2009) (equation (2.33) in their manuscript) and Bathellier et al. (2012) (equation 3.1 in their manuscript) blurs the fact that the formalism used by Bathellier et al. (2012) is actually just the particular part of the general Kant & Humphrey solution. Appendix D highlights the analogies between the model of Kant & Humphrey and our model.

Our model assumes that the hairs are independent, and does not, therefore, take into account the viscous medium coupling effect between hairs. Despite the absence of this effect from the model, and previous demonstrations of its importance (Bathellier et al. (2005), Casas et al. (2008)), we can predict its qualitative impact on the response of hairs to impulsive flows. We already know that viscous coupling between hairs is maximized at low frequency and for small hairs (Casas et al. (2008)). We would thus expect the difference in sensitivity between small and long hairs in response to low velocity attacks to be increased by viscous coupling. Furthermore, the sensitivity of small hairs to higher attack velocities is likely to be less strongly affected by the viscous coupling effect.

4.2 Resolution of conflict: short and long hairs are both optimal, but to different inputs

The major result arising from the Kant & Humphrey model is that short hairs are more responsive than long hairs to their particular flow pulsation, due to a lower total inertia, torsional restoring constant and total damping constant. This is at odds with previous results, which identified long hairs as the most sensitive ones. This discrepancy results from the use of different definitions of hair reactions, and the focus exclusively on steady sinusoidal flows in previous studies (Shimozawa and Kanou (1984b), Humphrey et al. (1993), Shimozawa et al. (1998)). Our model resolves this discrepancy by providing the general solution, a superimposition of natural and forced responses. We provide an intuitive illustration of the various parts of the solution of our model, by working through an example of a solution to a simpler "harmonic impulsion": single-frequency sinusoidal flow. Real flows are, of course, multi-frequential and our model also deals with this more complicated case. Let us first consider four different hairs, of 500, 1000, 2000 and 3000 μm in length, all subjected to attacks at a speed of 10 cm/s and a distance of 2.5 cm, corresponding to a frequency of 2 Hz (half-period 125 ms). The natural responses of the hairs drive their behavior at early time points (i.e. before 40 ms), at which the general solution follows the homogeneous solution (Figure 6.a). After 40 ms, the general solution closely follows the particular solution, indicating that the movement of the hairs is dependent mostly on their forced responses. Short hairs react quickly, but they cannot harvest much energy from the fluid, and may, therefore, not reach their threshold angle (the methods for determining the agility and threshold angle of hairs are given in Appendix E). Long hairs pick up the flow velocity later, but they deflect to a much greater extent, due to the combination of a larger surface area, projection into a region further away from the body and a lower spring stiffness. Long hairs are optimal for picking up such "slow" flows. Let us now consider a faster attack at 40 cm/s and a distance of 1 cm, corresponding to a signal of 20Hz (half-period 12.5 ms). Short hairs again react quickly, resulting in large hair deflections as the input provides sufficient energy (Figure 6.b). The neurons attached to these hairs are therefore likely to fire first. Long hairs cannot follow the first phase of the signal due to their inertia, and they attain their threshold angles much later. Thus, the neurons connected to long hairs cannot fire sufficiently quickly for the detection of fast flows, a task to which short hairs are much better suited.

The threshold angle for detection is the key to determine which hair neuron fire first. Thus, the sensitivity of a given hair relative to another hair depends not only on its ability to reach a given triggering angle rapidly, but also its capacity to extract energy from the fluid medium and translate it into mechanical energy dissipated at the basal joint. Shimozawa et al. (2003)

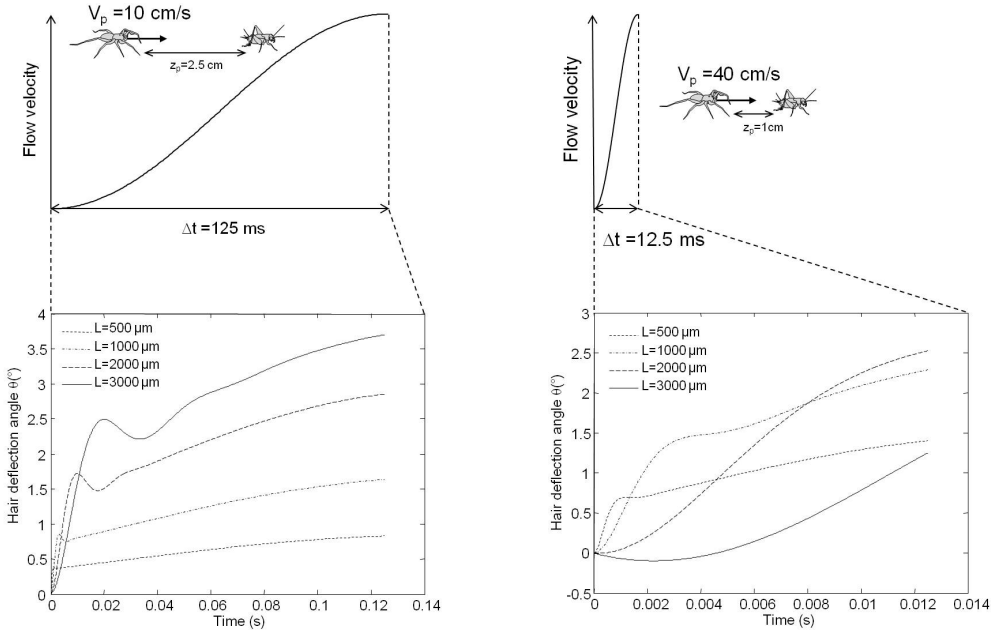

Figure 6: Comparison of the deflections of hairs of different lengths, ranging from 500 μm to 3000 μm, subjected to two different flows produced during an attack. (a) Slow increasing flow velocity, lasting 125 ms, produced by a predator launching its attack at a distance of 2.5 cm and a velocity of 10 cm/s. (b) Rapidly increasing flow velocity, lasting 12.5 ms, produced by a predator launching its attack at a distance of 1 cm and a velocity of 40 cm/s.

and Barth and Höller (1999) reported threshold angles of 0.001° to 0.1° and they showed that physiologically, and regardless of their length, the trichobothria of spiders are all broadly tuned to a frequency range of about 50 to 100 Hz. Shimozawa et al. (2003) discovered a monotonic decline in the threshold angle as a function of hair length, with the neurons of the longest hairs firing at the smallest angles. A theoretical approach based on background noise level (appendix E) confirmed these experimental results.

Thus, the tradeoff between mechanical agility, which declines with increasing hair length, and sensitivity, which increases with increasing hair length, defines the time required to reach the firing threshold. Furthermore, this trade-off keeps hair lengths and firing times in a bounded region. Prey animals make full use of an array of hairs of all lengths to cope with interactions as complex and crucial as the launch of a predator attack, pursuit and final assault. The heterogeneity of the hair canopy mirrors the flow complexity of an entire attack, from launch to grasp, and thus provides another example of a dynamic matched filter (Wehner (1987), von der Emde and Warrant (2015)).

Authors' contributions

Conceived and designed the experiments: J.C. T.S. Performed the experiments and the model derivation: T.S. Analyzed the data: J.C. T.S. Wrote the paper: J.C. T.S. This work is part of the PhD thesis of T.S. under the supervision of J.C.

References

Barth, F. G. and Höller, A. (1999). Dynamics of arthropod filiform hairs . V . The response of spider trichobothria to natural stimuli. Philosophical Transactions of the Royal Society B: Biological Sciences, (June 1997):183–192.

Bathellier, B., Barth, F. G., Albert, J. T., and Humphrey, J. a. C. (2005). Viscosity-mediated motion coupling between pairs of trichobothria on the leg of the spider Cupiennius salei. Journal of comparative physiology. A, Neuroethology, sensory, neural, and behavioral physiology, 191(8):733–46.

Bathellier, B., Steinmann, T., Barth, F. G., and Casas, J. (2012). Air motion sensing hairs of arthropods detect high frequencies at near-maximal mechanical efficiency. Journal of the Royal Society, Interface / the Royal Society, 9(71):1131–43.

Casas, J. and Dangles, O. (2010). Physical ecology of fluid flow sensing in arthropods. Annual review of entomology, 55:505–20.

Casas, J. and Steinmann, T. (2014). Predator-induced flow disturbances alert prey, from the onset of an attack. Proceedings of the Royal Society B: Biological Sciences, 281(1790).

Casas, J., Steinmann, T., and Dangles, O. (2008). The aerodynamic signature of running spiders. PloS one, 3(5):e2116.

Cummins, B. and Gedeon, T. (2012). groups of arthropod fi liform fl ow sensors. In F. G. Barth et al., editor, Frontiers in sensing, pages 239–250. Springer-Verlag.

Gnatzy, W. and Tautz, J. (1980). Ultrastructure and Mechanical Properties of an Insect Mechanoreceptor : Stimulus-transmitting Structures and Sensory Apparatus of the Cercal Filiform Hairs of Gryllus. Cell Tissue Research, 463:441–463.

Greendberg M. D. (1988). Advanced Engineering Mathematics. Prentice Hall.

Heys, J. J., Rajaraman, P. K., Gedeon, T., and Miller, J. P. (2012). A model of filiform hair distribution on the cricket cercus. PloS one, 7(10):e46588.

Humphrey, J. A. C., Devarakonda, R., Iglesias, I., Barth, F. G., Trans, P., and Lond, R. S. (1993). Dynamics of Arthropod Filiform Hairs . I . Mathematical Modelling of the Hair and Air Motions. Philosophical Transactions of the Royal Society B: Biological Sciences, pages 423–444.

Kant, R. and Humphrey, J. a. C. (2009). Response of cricket and spider motion-sensing hairs to airflow pulsations. Journal of the Royal Society, Interface / the Royal Society, 6(40):1047–64.

Kumagai, T., Shimozawa, T., and Baba, Y. (1998). Mobilities of the cercal wind-receptor hairs of the cricket, Gryllus bimaculatus. Journal of Comparative Physiology A: Sensory, Neural, and Behavioral Physiology, 183(1):7–21.

Larson, M. (1996). A closed form solution for turbulent wave boundary layers. In Costal Engineering Proceedings, pages 3244–3256. International Conference on Coastal Engineering (ICCE).

Miller, J. P., Krueger, S., Heys, J. J., and Gedeon, T. (2011). Quantitative characterization of the filiform mechanosensory hair array on the cricket cercus. PloS one, 6(11):e27873.

Shimozawa, T. and Kanou, M. (1984a). The aerodynamics and sensory physiology of range fractionation in the cereal filiform sensilla of the cricket Gryllus bimaculatus. Journal of comparative physiology A, 155:495–505.

Shimozawa, T. and Kanou, M. (1984b). Varieties of filiform hairs : range fractionation by sensory afferents and cercal interneurons of a cricket. Journal of comparative physiology A, 155:485–493.

Shimozawa, T., Kumagai, T., and Baba, Y. (1998). Structural scaling and functional design of the cercal wind-receptor hairs of cricket. Journal of Comparative Physiology A: Sensory, Neural, and Behavioral Physiology, 183(2):171–186.

Shimozawa, T., Murakami, J., and Kumagai, T. (2003). Cricket Wind Receptors: Thermal Noise for the Highest Sensitivity Known. In Barth, F., Humphrey, J., and Secomb, T., editors, Sensors and Sensing in Biology and Engineering SE - 10, pages 145–157 LA – English. Springer Vienna.

Steinmann, T., Casas, J., Krijnen, G., and Dangles, O. (2006). Air-flow sensitive hairs: boundary layers in oscillatory flows around arthropod appendages. The Journal of experimental biology, 209(Pt 21):4398–408.

von der Emde, G. and Warrant, E. (2015). The Ecology of Animal Senses. Springer.

Wehner, R. (1987). 'Matched filters'-neural models of the external world. Journal of comparative physiology. A,, 161:511–531.

White, F. M. (1991). Viscous Fluid Flow. McGraw-Hill.

Appendix A. Flow velocity measurements

I. Material and Methods

The forcing velocity $V_f^{SC}(t)$ was derived from the LDA measurements made for a piston mimicking attack by a spider. The flow disturbance was produced with a moving piston (LAL35 actuator/LACI controller, Cedrat Technologies, Meylan, France) that had already been used and tested in previous studies (Dangles et al. (2006), Dupuy et al. (2012)). The displacement of the 8 mm-diameter piston was controlled precisely, with macro commands, via hyperterminal software and the RS 232 port of a laptop, and was monitored with a high-speed camera (Photron fastcam, operating at 1000 fps). Below, we define the time origin (t=0) as the instant at which the piston starts to move, at a distance of 5 cm from the LDA measurement point. A laser Doppler anemometry (Dantec Dynamics FlowLite LDA System) system was used to measure the flow produced by the piston moving at five different velocities. Figure A1 shows the LDA measurement setup of the flow produced in front of the piston moving at a constant velocity. The piston was placed at a distance of 5 mm from the ground in a glass sealed box seeded with oil droplets (see details of the measurement and setup in Dangles et al. (2006) and Casas et al. (2008)).

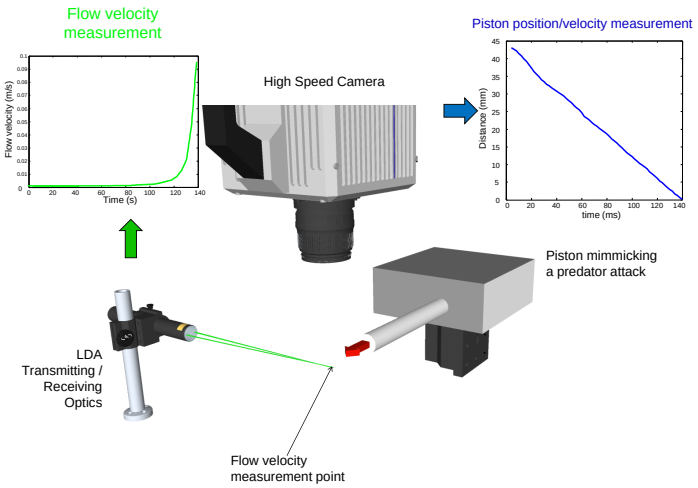

Figure A1. Piston flow velocity measurement by laser Doppler anemometry and high-speed imaging.

Measurement involved filming the displacement of the piston to determine its velocity while measuring the flow velocity by means of LDA at a fixed point. This fixed position represents the virtual position of the cricket cercal hair. We computed the flow velocity produced by the piston movement $V_f^{SC}(t)$ for speeds of (i) 5, (ii) 11, (iii) 30 and (iv) 58 cm/s. The above flow velocities were input into the model. The time required for the piston to reach the measurement point was (i) 1000, (ii) 454, (iii) 167 and (iv) 86 ms, respectively for these velocities. The sampling frequencies of both the high-speed camera and the LDA were set at f_s =1000 Hz and the measurement length was $N = 500$. We thus obtained a complex spectral amplitude $|{V_0}^m{}_{SC}(\omega_m)|$ and phase $\phi_{V_0^m}(\omega)$ for $\frac{2\pi f_s}{N} < \omega_m < \frac{2\pi f_s}{2}$.

II. Results

The LDA measurements of the velocity of the flow produced in front of a piston moving at the

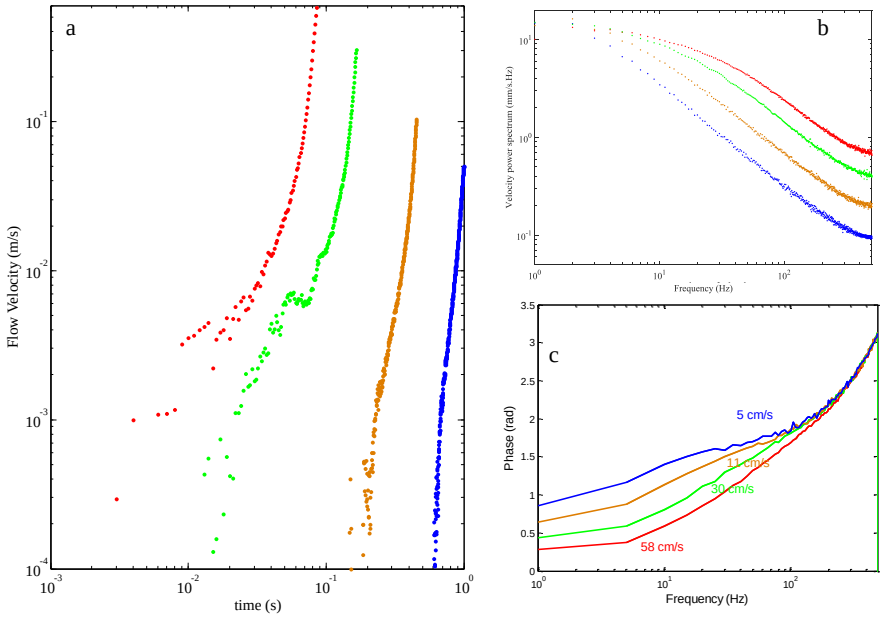

Figure A2. Flow velocity produced by a moving piston, as measured by LDA. (a) The dots represent the four attack velocities, (b) the power spectrum and (c) the phase spectrum of the flow velocities (58, 30, 11 and 5 cm/s, from red to blue).

four constant velocities are presented in Figure A2. For all velocities, the piston starts moving at t=0 and a distance of z_p=5 cm from the measurement point. A piston moving at V_p=58 cm/s (red points) reaches the LDA measurement point early, at a time $t_p = \frac{z_p}{V_p}$ =86 ms, whereas a piston moving at V_p=5 cm/s (blue points) reaches the measurement point later, at t_p=1000 ms. Our measurement setup and averaging over 10 reproducible measurements resulted in a flow velocity sensitivity of 10^{-4} m/s. For a piston moving at 5 cm/s, this minimal detectable velocity is reached 180 ms after the piston starts moving, whereas, for a piston moving at 58 cm/s, this velocity is reached 3 ms after the piston starts moving. For each measurement, we derived an average flow acceleration $a_p = \frac{V_p}{t_p}$, which is proportional to the maximal velocity reached V_p and inversely proportional to the time required to reach this maximal velocity, $t_p = \frac{z_p}{V_p}$. Thus $a_p = \frac{(V_p)^2}{z_p}$ is proportional to the square of piston velocity, and inversely proportional to the distance at which the piston started moving.

For a given distance z_p, there is a parabolic increase in flow velocity acceleration with increasing piston velocity. This increase in the slope of the curve of flow velocity with increasing piston velocity translates into a shift of the frequency distribution in the power spectrum (Figure A2.b). The spectral analysis of the air flow generated provides information about the energy and temporal content available to the sensory system of a prey. For all velocities, the power spectrum is large at low frequencies and smaller at higher frequencies. The high frequency components are very weak. The spectral analysis showed that, at all frequencies, low piston velocities produced less energy in the flow than high piston velocities (Figure A2.b). The phase representation showed that an increase in piston velocity translated into a decrease in phase lag for all frequency components of the signal (Figure A2.c), as shown in the temporal representation. Low-piston velocity flows are delayed, whereas the phase is advanced for high-attack velocity flows (Figure A2.c). Thus, an increase in attack velocity translates into a stronger signal that is available earlier for detection by the prey.

Appendix B. Solving the equation of motion

The aim of this appendix B is to lay out the different steps leading to the solution (equation (28)) of equation (16), which gives the deflection of the hair as a function of time.

The homogeneous form of the equation (16) is :

$$I_T\ddot{\theta}_h + (R_h + R_\mu)\,\dot{\theta}_h + S_h\theta_h = 0 \tag{B1}$$

with $I_T = I_h + I_\rho$. As the determinant $\triangle = (R_h + R_\mu)^2 - 4S_hI_T$ is always positive, the homogeneous solution of equation (16) is a linearly independent superposition of two solutions $C_1e^{\gamma_1 t}$and $C_2e^{\gamma_2 t}$:

$$\theta_h(t) = C_1e^{\gamma_1 t} + C_2e^{\gamma_2 t} \tag{B2}$$

with the two time constants $\gamma_1 = \frac{-(R_h+R_\mu)+\sqrt{\Delta}}{2I_T}$ and $\gamma_2 = \frac{-(R_h+R_\mu)-\sqrt{\Delta}}{2I_T}$, and the constants C_1 and C_2 satisfying the boundary conditions of the general solution $\theta(0) = 0$ and $\dot{\theta}(0) = 0$.

The particular solution satisfying equation (16) is :

$$I_T\ddot{\theta}_p + (R_h + R_\mu)\,\dot{\theta}_p + S_h\theta_p = \cos(\alpha)\ \sum_{m=0}^{\infty}\left(\frac{\pi\mu}{2} - i\omega_m\pi\frac{d^2}{4}\rho\right){V_0^m}_{SC}K_{SC}(\omega_m, L)\ e^{-i\omega_m t} \tag{B3}$$

We can solve this equation for a given value of m, leading to $\theta_p^m(t)$. The complete particular solution $\theta_p(t)$ will be the sum of these solutions, for each m, from *m=0 to* ∞ *:*

$$\theta_p(t) = \sum_{m=0}^{\infty}\theta_p^m(t) \tag{B4}$$

For a given m, the left term of equation (B3) is proportional to $e^{-i\omega_m t}$over time. We would therefore expect θ_p^m to take the form: $\theta_p^m(t) = Ae^{-i\omega_m t}$, such that $\dot{\theta}_p^m(t) = -\omega_m Ae^{-i\omega_m t}$ and $\ddot{\theta}_p^m(t) = -\omega_m^2 Ae^{-i\omega_m t}$.

For a given value of m, replacing these expressions of angle, angular velocity and angular acceleration in equation (B3), therefore gives:

$$\left(-I_T{\omega_m}^2A - i(R_h + R_\mu)\,\omega_m A + S_hA\right)e^{-i\omega_m t} = \cos(\alpha)\ \left(\frac{\pi\mu}{2} - i\omega_m\pi\frac{d^2}{4}\rho\right){V_0^m}_{SC}K_{SC}(\omega_m, L)\,e^{-i\omega_m t} \tag{B5}$$

$$\theta_p^m(t) = \frac{\left(\frac{\pi\mu}{2} - i\omega_m\pi\frac{d^2}{4}\rho\right){V_0^m}_{SC}K_{SC}(\omega_m, L)\,e^{-i\omega_m t}}{-I_T{\omega_m}^2 - i(R_h + R_\mu)\,\omega_m + S_h} \tag{B6}$$

and

$$\theta_p(t) = \sum_{m=0}^{\infty}\frac{\left(\frac{\pi\mu}{2} - i\omega_m\pi\frac{d^2}{4}\rho\right){V_0^m}_{SC}K_{SC}(\omega_m, L)\,e^{-i\omega_m t}}{-I_T{\omega_m}^2 - i(R_h + R_\mu)\,\omega_m + S_h} \tag{B7}$$

The general solution of equation (16), representing generic hair movement is:

$$\theta(t) = \theta_h(t) + \theta_p(t) = C_1e^{\gamma_1 t} + C_2e^{\gamma_2 t} + \cos(\alpha)\ \sum_{m=0}^{\infty}\frac{\left(\frac{\pi\mu}{2} - i\omega_m\pi\frac{d^2}{4}\rho\right){V_0^m}_{SC}K_{SC}(\omega_m, L)\,e^{-i\omega_m t}}{-I_T{\omega_m}^2 - i(R_h + R_\mu)\,\omega_m + S_h} \tag{B7}$$

The boundary conditions of the general solution $\theta(0) = 0$ and $\dot{\theta}(0) = 0$ give the two linear sets of equations for the determination of C_1 and C_2. We then obtain the following expression of the general solution:

$$C_1 = \cos(\alpha) \sum_{m=0}^{\infty} \frac{\omega_m i + \gamma_2}{\gamma_1 - \gamma_2} \frac{\left(\frac{\pi\mu}{2} - i\omega_m \pi \frac{d^2}{4}\rho\right) {V_0^m}_{SC} K_{SC}(\omega_m, L)}{-I_T {\omega_m}^2 - (R_h + R_\mu)\omega_m + S_h} \tag{B8}$$

$$C_2 = \cos(\alpha) \sum_{m=0}^{\infty} \frac{\omega_m i + \gamma_1}{\gamma_1 - \gamma_2} \frac{\left(\frac{\pi\mu}{2} - i\omega_m \pi \frac{d^2}{4}\rho\right) {V_0^m}_{SC} K_{SC}(\omega_m, L)}{-I_T {\omega_m}^2 - (R_h + R_\mu)\omega_m + S_h} \tag{B9}$$

Appendix C. Estimation of hair mechanical parameters

The harmonic deflection measurements for the cercal hairs of adult female crickets (*Nemobius sylvestris*) analyzed here were previously presented by Bathellier et al. (2012). Here, we re-analyze the data, to extract not only the amplitude of the intrinsic mechanical response, but also the phase of the response.

I. Materials and Methods

In equation (D3), the reduced mechanical constants are $\omega_s = S/R_\mu$, $\omega_i = R_\mu/I$ and $r = R/R_\mu$. R is the resistance in the hair socket, I is the moment of inertia of the hair, S is the spring stiffness and R_μ is the air damping resistance. V_0^m is the amplitude of the harmonic oscillation (m/s), and $K_B(\omega, L)$ is the boundary layer effect factor, which reflects the change in flow velocity profile acting on the hair length. The phase shift between the far field flow velocity and the angular displacement of the hair is:

$$\triangle\phi_{hair}(\omega, L) = \phi_K(\omega, L) - \phi_F(\omega, r, \omega_s, \omega_i) + \frac{\pi}{2} \tag{C1}$$

with $\phi_K(\omega, L)$, the phase shift in the boundary layer and $\phi_F(\omega, r, \omega_s, \omega_i) = arctan\left(\frac{\frac{\omega_s}{\omega} - \frac{\omega}{\omega_i}}{1+r}\right)$ the phase shift associated with the intrinsic response of the hair.

We fitted equations (D3) and (C1) to measurements of hair amplitude and phase shift for seven hairs of various lengths (410, 440, 490, 700, 870 and 1000 μm), for frequencies $30Hz < f < 300Hz$ (using the procedure lsqcurvefit.m in MATLAB 7(R14), The Mathworks). To ensure a convergence of the fits, we were forced to constrain the parameters to the following ranges: $0 < r < 1.1$, $1 < \omega_s < 2000$, $1 < \omega_i < 17000$. These fits of phase shift and amplitude enabled us to obtain structural scaling fits of r, ω_i and ω_s : $\omega_s = A\left(\frac{L}{1000}\right)^B$, $\omega_i = C\left(\frac{L}{1000}\right)^D$ and $r = E\left(\frac{L}{1000}\right)^F$ where A, B, C, D, E and F are the fitting parameters of the structural scaling.

II. Results

Figure C1.a shows the fit of the expression of $\theta_{max}(\omega_m)$ for seven isolated cricket cercal hairs and for frequencies ranging from 30 Hz to 300 Hz. The phase response of these hairs is shown in Figure C1.b for the same harmonic flows. The curves represent equation (D3) of $\theta_{max}(\omega_m)$ in Figure C1.a and the associated phase shifts $\Delta\phi_{hair}(\omega, L)$ (equation (C1)) in Figure C1.b, both fitted with the reduced mechanical constants r,ω_i and ω_s. The boundary layer effect $|K|(\omega, L)$ is obtained from the equation (2.28) for flow parallel to a cylinder.

The fit of structural scaling equations for r,ω_i and ω_s linking mechanical parameters to hair length L is shown in Figure C1.c. It is clear that ω_i and ω_s are highly dependent on hair length as ω_s scales with $468\left(\frac{L}{1000}\right)^{-1.4}$ and ω_i scales with $2950\left(\frac{L}{1000}\right)^{-2}$. There is no scaling law for the reduced torsional resistance r. From our measurements and fits, the reduced resistance in the hair socket seems to be independent of hair length and is estimated at $r = 0.4$. By contrast, the reduced constants ω_s and ω_i decrease with hair length, implying that spring stiffness is lower for longer hairs and that the inertia is higher for longer hairs.

We chose to use $R_\mu = \frac{\pi\mu L^3}{6}$, following Bathellier et al. (2012). Our choice of Oseen theory to define the drag coefficient acting on filiform hairs was based on the accuracy with which it fit the results presented by Bathellier et al. (2012). Our allometric scaling function for the reduced parameter r suggests that resistance is not dependent on hair length. We did not find an invariance of torsional resistance with length. Instead, we found that the ratio of torsional

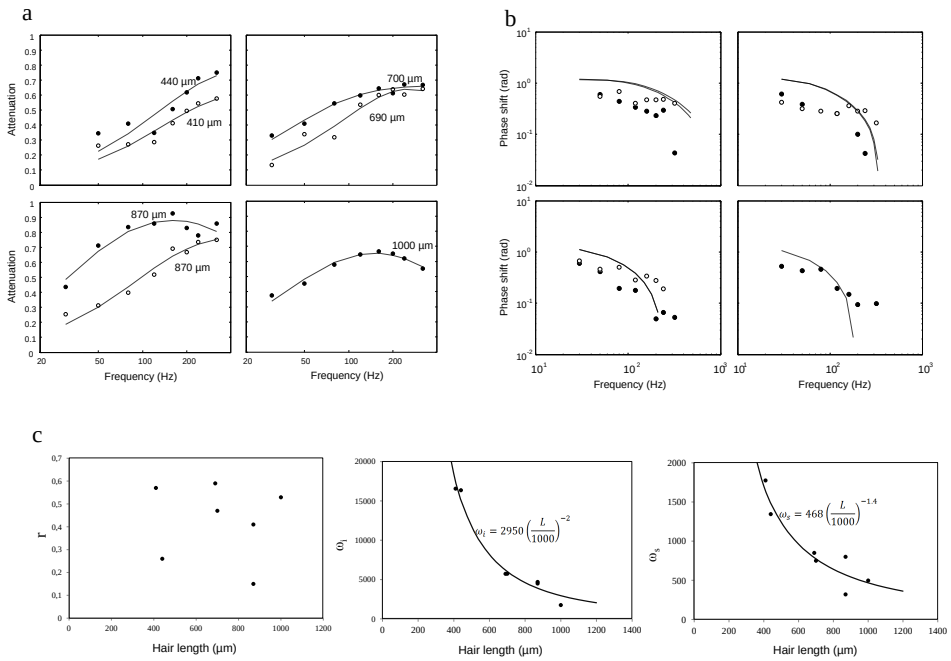

Figure C1. Fit of peak angular displacements, phase shifts and structural scaling of reduced mechanical parameters. (a) The dots represent the deviation from the physical limit, calculated by dividing the tip velocity of the hair measured by PIV by its physical limit $\frac{3|V_0{}^m{}_{SC}(\omega)|}{2L\omega}$, for seven isolated cricket cercal hairs. Solid lines represent the best fit of $|F(\omega, r, \omega_s, \omega_i)|\, K(\omega, L)$. (b) The dots represent the phase lags of the seven isolated hairs with the surrounding flow (outside the boundary layer) and the lines represent the fit of $\phi_F(\omega, r, \omega_s, \omega_i)$. (c) The three graphs represent r, ω_i, ω_s , respectively. They were obtained by fitting deviation from the physical limit $|F(\omega, r, \omega_s, \omega_i)|\, K(\omega, L)$ and phase lag $\phi_F(\omega, r, \omega_s, \omega_i)$ for the same seven isolated hairs. The lines represent the structural fits between parameters ω_s, ω_i and hair length.

	Shimozawa et al (1998)	*Kant & Humphrey (2010)*	*Cummins & Gedeon (2012)*	*Our data*
Species	*Gryllus bimaculatus*	*Gryllus bimaculatus*	*Gryllus bimaculatus*	*Acheta Domesticus*
ω_s=S/R_μ (s)	$752(L/1000)^{-1.3}$	$1530(L/1000)^{-1.33}$	$752(L/1000)^{-1.3}$	$468(L/1000)^{-1.4}$
ω_i=R_μ/I (Hz)	$6600(L/1000)^{-1.1}$	$1498(L/1000)^{-1.34}$	$6600(L/1000)^{-1.1}$	$2950(L/1000)^{-2}$
r=R/R_μ	$0.23(L/1000)^{-0.5}$	$2.32(L/1000)^{-0.23}$	$0.23(L/1000)^{-0.5}$	$0.4(L/1000)^{0}$

Table C2. Comparison of the structural scaling function determined this and previous studies. This function represents the allometric relationship between hair length and the mechanical parameters of the hair: spring stiffness $S(N.m)$, torsional resistance $R(N.m.s)$ and moment of inertia $I(N.m.s^2)$.

resistance to drag resistance was constant. This independence of the reduced parameter is an expression of impedance matching between the resistance in the air and the resistance in the basal joint of the socket. The torsional resistance in the socket is highly proportional to the drag resistance in air R_μ, the value for this torsional resistance being 40% the drag resistance in air. It is, therefore, highly dependent on hair length.

We report our results in Table C2, alongside those of Shimozawa et al. (1998),Kant and Humphrey (2009) and Cummins and Gedeon (2012). Figure C3 compares the mechanical parameters — spring stiffness $S = R_\mu/\omega_s$, the moment of inertia $I = R_\mu/\omega_i$ and torsional resistance $R = R_\mu r$ — for these papers. The parameters presented in table C2 are reduced parameters. Our parameters are very close to those chosen by these other authors, despite the use of different species for the measurements.

Appendix D. Analogies between our model and that of Kant & Humprey

The aim of this appendix D is to highlight the analogies between our model and that of Kant & Humprey. We expressed a general solution of the motion of a hair subjected to any driving flow under equation (28). The harmonic solution can easily be derived from this solution, by setting the homogeneous solution to zero, choosing $\cos(\alpha) = 1$ and asserting that the harmonic solution is the mono-frequency particular solution, with ω_m constant and $V_f^{SC}(t) = V_0^m e^{-i\omega_m t}$. The harmonic solution is then:

$$\theta_h(t) = \frac{\left(\frac{\pi\mu}{2} - i\omega_m \pi \frac{d^2}{4}\rho\right) K_{SC}(\omega_m, L)}{-I_T {\omega_m}^2 - i\left(R_h + R_\mu\right)\omega_m + S_h} V_0^m e^{-i\omega_m t} \tag{D1}$$

$$= \left(\frac{\left(\frac{\pi\mu}{2} - i\omega_m \pi \frac{d^2}{4}\rho\right)}{\frac{\pi\mu}{6} L^3 {\omega_m}}\right)\left(\frac{1}{-\frac{\omega_m}{\omega_i} + \frac{\omega_s}{\omega_m} - i(r+1)}\right) K_{SC}(\omega_m, L)\ V_0^m e^{-i\omega_m t}$$

In this expression, we recognize three different contributions influencing the response of a hair: (i) the physical limit $\left(\frac{\left(\frac{\pi\mu}{2} - i\omega_m \pi \frac{d^2}{4}\rho\right)}{\frac{\pi\mu}{6} L^3 \omega_m}\right)$, (ii) the mechanical filter $\left(\frac{1}{-\frac{\omega_m}{\omega_i} + \frac{\omega_s}{\omega_m} - i(r+1)}\right)$ and (iii) the boundary layer effect $K_{SC}(\omega_m, L)$ as described by Bathellier et al. (2012). The first contribution is an expression of the maximal harvestable forces in the fluid. It is a complex expression, implying that the hair experiences a change of phase due to the balanced contributions of the drag force and the added mass force. The added mass force depends on the velocity and acceleration of the flow. The balance between the drag and added mass forces depends mainly on flow frequency. By calculating the ratio of these two forces, we showed that, even at frequencies as high as 10 kHz, the drag force is an order of magnitude higher than the added mass force. We therefore simplified the expression to $\frac{3}{L^3 \omega_m}$. We can rewrite the expression of the mechanical filter in the amplitude of the harmonic solution $\theta_{max}(\omega_m)$ to reveal the formalism of Bathellier et al. (2012):

$$\theta_{max}(\omega_m) = \frac{3}{L^3 \omega_m} \frac{L^2 K_B(\omega_m, L)/2\ V_0^m}{\sqrt{\left(\frac{\omega_s}{\omega_m} - \frac{\omega_m}{\omega_i}\right)^2 + (r+1)^2}} \tag{D2}$$

$$\theta_{max}(\omega_m) = \frac{3}{2L\omega_m} \frac{|K_B(\omega_m, L)|\ V_0^m}{\sqrt{\left(\frac{\omega_s}{\omega_m} - \frac{\omega_m}{\omega_i}\right)^2 + (r+1)^2}} \tag{D3}$$

This corresponds exactly to the expression of the analytical solution for the peak angular displacement of the equation 3.1 of Bathellier et al. (2012), demonstrating that this expression really is the mono-frequential particular part of the Kant & Humphrey solution for generic hair movement.

Appendix E. Hair agility and threshold angle for firing

The aim of this appendix E is to describe the estimation of two angles of a moving hair: the maximal angle of deflection and the angle at which the nerve connected to the hair fires, the threshold angle for perception. By definition, the threshold angle for firing is smaller than the maximal angle of deflection.

I. Hair agility

The two key factors conditioning the ability of a hair to reach its minimal threshold angle are its impulse response time τ_{95} and the energy available in the fluid medium (i.e. the flow velocity) between t=0 and t= τ_{95}. The impulse response time of the hair, τ_{95}, provides an estimate of the agility of the hair. It should be noted that the impulse response time (τ_{95}) is not necessarily equal to the reaction time. τ_{95} is the time required for the hair to reach 95% of its maximal achievable angle when subjected to a velocity step function. The maximal achievable angle is dependent on the mechanical parameters of the hair, but it is also a function of velocity step function amplitude. If this maximal achievable angle is smaller than the threshold angle, the hair will never reach its threshold angle. By contrast, if the maximal achievable angle is larger than the threshold angle, the deflection of the hair will eventually reach the threshold angle.

The impulse response time is equal to :

$$\tau_{95} = \left|\frac{1}{\gamma_1}\right| = \left|\frac{1}{\gamma_2}\right| = \left|\frac{2I_T}{-\left(R_h + R_\mu\right) + \sqrt{\triangle}}\right| \tag{E1}$$

The computation of τ_{95} for different hair lengths shows that short hairs of 100 μm have very small reaction times, of the order of 100 μs, whereas long hairs reaction time last up to 2 or 5 ms (Figure E1).

II. Threshold angle of reaction

The good fit of our model to measurements of hair deflections (Figure 5) makes it possible to predict small transient hair deflections. The model can also be used to predict the time elapsed between the start of predator movement and the instant at which the hair reaches its minimal threshold angle. Knowledge of the threshold angle for deflection makes it possible to evaluate hair reaction times for different velocities. This reaction time is the time elapsed between the instant the impulsion starts (i.e. the start of the predator attack), and the instant at which the hair reaches its threshold angle. This is the threshold angle that must be reached to compress the tubular body sufficiently for the sensory neuron at the base of the hair to deliver an action potential (Gnatzy and Tautz (1980)).

The deflection angle of the mechanosensor triggering an action potential was estimated by Shimozawa et al. (2003) at 0.001° to 0.1°. Moreover, Barth and Höller (1999) showed that, physiologically and regardless of their length, the trichobothria of spiders are all broadly tuned to a frequency range between about 50 and 100 Hz, with threshold deflection angles of about 0.1°, but as small as 0.01°in some cases (Barth and Höller (1999)). This triggering angle represents the minimal angle at which the movement of a hair may be considered not to be due to Brownian thermal noise anymore, but to result from a biotic or abiotic change in the surrounding air flow. Rather than choosing an arbitrary fixed threshold angle, we choose to define the threshold angle for deflection as proposed by Droogendijk et al. (2014). These authors defined a Brownian noise equivalent angle θ_n by integrating the mechanical-thermal noise due to the Brownian motion

of molecules in air over the full frequency spectrum. The noise due to Brownian motion is estimated as the product of the spectral density of white noise $4k_BT_0R$ and the mechanical transfer function $|F(\omega, r, \omega_s, \omega_i)|$.

$$\theta_n = \sqrt{\int_0^\infty 4k_BT_0 \frac{|F(\omega, r, \omega_s, \omega_i)|^2}{R_\mu \omega^2} d\omega} \tag{E2}$$

Figure E2 represents the deflection threshold angle estimated by equation (E2) and shows that the equation (E2) leads to an overestimation of the sensory threshold compared to the measurements of Shimozawa et al. (2003). For long hairs, the qualitative trend of decline of the deflection sensory threshold is however appropriate.

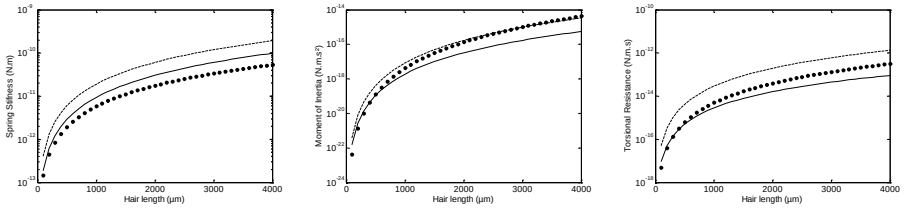

Figure C3. Comparison of spring stiffness S, moment of inertia I and torsional resistance R, estimated with the allometric equations in Figure 7. Data from Shimozawa et al. (1998) (solid line), Kant and Humphrey (2009) (dashed line) and our data (black dots).

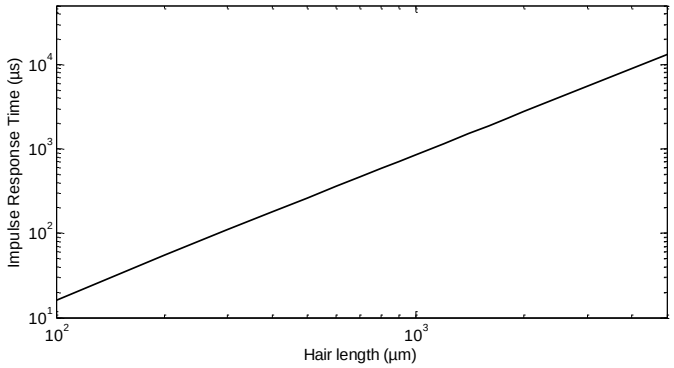

Figure E1. Impulse response time τ_{95} for hair lengths ranging from 100 μm to 5000 μm.

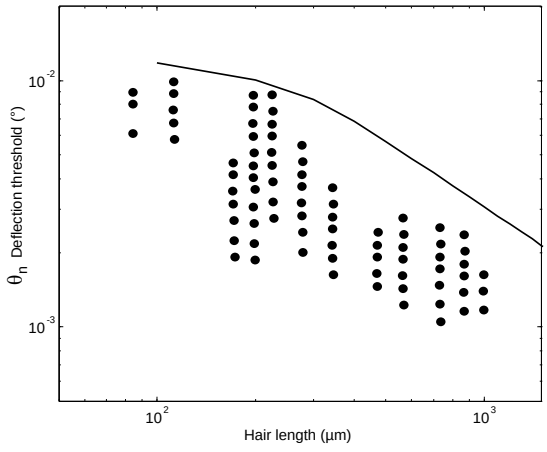

Figure E2. Deflection angle threshold against hair length. (black line) Numerical estimation of the deflection threshold due to Brownian noise from equation (E2) (Droogendijk et al. (2014)). (dots) Measurements of the detection threshold of filiform hairs of *Grillus Bimaculatus* for sinusoidal flows of various frequencies, ranging from 5 Hz to 100Hz, taken from Shimozawa et al. (2003).

References

Barth, F. G. and Höller, A. (1999). Dynamics of arthropod filiform hairs . V . The response of spider trichobothria to natural stimuli. Philosophical Transactions of the Royal Society B: Biological Sciences, (June 1997):183–192.

Bathellier, B., Steinmann, T., Barth, F. G., and Casas, J. (2012). Air motion sensing hairs of arthropods detect high frequencies at near-maximal mechanical efficiency. Journal of the Royal Society, Interface / the Royal Society, 9(71):1131–43.

Casas, J., Steinmann, T., and Dangles, O. (2008). The aerodynamic signature of running spiders. PloS one, 3(5):e2116.

Cummins, B. and Gedeon, T. (2012). groups of arthropod fi liform fl ow sensors. In F. G. Barth et al., editor, Frontiers in sensing, pages 239–250. Springer-Verlag.

Dangles, O., Ory, N., Steinmann, T., Christides, J.-P., and Casas, J. (2006). Spider's attack versus cricket's escape: velocity modes determine success. Animal Behaviour, 72(3):603–610.

Droogendijk, H., Casas, J., Steinmann, T., and Krijnen, G. J. M. (2014). Performance assessment of bio-inspired systems : fl ow sensing MEMS hairs. Bioinspiration & Biomimetics, 10(1):16001.

Dupuy, F., Steinmann, T., Pierre, D., Christidès, J.-P., Cummins, G., Lazzari, C., Miller, J., and Casas, J. (2012). Responses of cricket cercal interneurons to realistic naturalistic stimuli in the field. The Journal of experimental biology, 215(Pt 14):2382–9.

Gnatzy, W. and Tautz, J. (1980). Ultrastructure and Mechanical Properties of an Insect Mechanoreceptor : Stimulus-transmitting Structures and Sensory Apparatus of the Cercal Filiform Hairs of Gryllus. Cell Tissue Research, 463:441–463.

Kant, R. and Humphrey, J. a. C. (2009). Response of cricket and spider motion-sensing hairs to airflow pulsations. Journal of the Royal Society, Interface / the Royal Society, 6(40):1047–64.

Shimozawa, T., Kumagai, T., and Baba, Y. (1998). Structural scaling and functional design of the cercal wind-receptor hairs of cricket. Journal of Comparative Physiology A: Sensory, Neural, and Behavioral Physiology, 183(2):171–186.

Shimozawa, T., Murakami, J., and Kumagai, T. (2003). Cricket Wind Receptors: Thermal Noise for the Highest Sensitivity Known. In Barth, F., Humphrey, J., and Secomb, T., editors, Sensors and Sensing in Biology and Engineering SE - 10, pages 145–157 LA – English. Springer Vienna.

Chapitre 9

Discussion Générale

Résumé du chapitre

Je discuterai dans ce dernier chapitre les implications et limites des modèles décrits dans les différentes parties qui constituent ce mémoire. Cette discussion sera composée de trois parties. Dans une première partie, je proposerai une application du modèle impulsionnel de mouvement du poil décrit dans le chapitre 8, qui pourrait nous permettre de comprendre le codage, par un réseau de senseurs, des diffèrents paramètres d'une attaque du prédateur. Je conclurai cette partie sur un éventuel codage de l'écoulement généré par l'approche d'un prédateur par l'activation successive des neurones sensoriels de poils de différentes directionalitées. Dans une seconde partie, je discuterai nos choix concernant le modèle mécanique viscoélastique de mouvement du poil, je décrirai un modèle alternatif un peu plus complexe que le modèle classique et j'expliquerai comment des expériences de microscopie à force atomique (AFM) nous permettraient de valider ce nouveau modèle. Nous nous focaliserons dans la dernière partie sur les méthodes et techniques utilisées pour caractériser théoriquement et expérimentalement les écoulements autour des organes sensoriels. Après avoir décrit une nouvelle méthode de simulation de l'écoulement instationnaire autour d'une structure et l'avoir comparée aux résultats utilisés dans le chapitre 8, nous décrirons les techniques expérimentales qui nous permettront, dans le futur, de mesurer ces écoulements instationnaires. Nous détaillerons ensuite nos choix de futures techniques expérimentales envisagées pour caractériser les écoulements tridimensionnels autour de structures sensorielles complexes. Je conclurai cette discussion sur le rôle primordial des aspects tridimensionnels instationnaires sur le fonctionnement de réseaux de senseurs, biologiques ou artificiels.

9.1 Réponse d'un réseau de senseurs

Pour la survie des grillons, il est primordial que les caractéristiques morphologiques et neuronales de leur système cercal aient évolué au fil du temps pour conférer aux individus la capacité de coder plusieurs informations sur la nature de la prédation. La fuite de la proie doit être, entre autre, conditionnée par (i) la vitesse du prédateur, (ii) la distance à laquelle ce dernier a lancé son attaque, (iii) la direction d'oú provient cette attaque et (iv) l'environnement physique (Dangles *et al.* (2006c), Dupuy *et al.* (2011), Morice *et al.* (2013)). La pertinence de la réaction de fuite du grillon dépend de la façon dont ce réseau, composé de centaines de senseurs individuels, va traduire les divers facteurs transmis dans le fluide lors de l'arrivée d'un prédateur (Dangles *et al.* (2006b), Dupuy *et al.* (2012)). On peut légitimement s'attendre à ce que la réaction individuelle d'un poil filiforme à un stimulus particulier dépende de (i) sa longueur, (ii) sa position sur le cerque, (iii) sa directionnalité et (iv) soit de plus, conditionnée par le couplage visqueux entre les poils. Or, dans la plupart des études sur la morphologie du système cercal, les chercheurs ont prouvé que les variabilités inter-individuelles et inter-spécifiques de placement, directionnalité et taille des poils, étaient très faibles (Landolfa et Jacobs (1995), Landolfa et Miller (1995), Jacobs *et al.* (2008), Dangles *et al.* (2008)). Cette faible variabilité inter-spécifique semble ainsi nous indiquer que les attributs structurels du système sensoriels des grillons ont été soumis à une importante pression de sélection. De nombreuses métriques ont ainsi été définies au fil des ans pour caractériser leur performance (Chapitre 7 de ce mémoire (Droogendijk *et al.* (2014)), Chapitre 8) : le temps de réponse, la sensibilité et le seuil de déclenchement. Nous allons essayer de comprendre dans cette discussion, comment le réseau de senseurs pourrait coder des informations importantes, et dans quelle mesure certains caractères structurels conservés et peu variables inter-individuellement, comme la directionnalité des soies, pourraient avoir un rôle important dans le codage de différents critères de l'attaque d'un prédateur. Pour ce faire, nous devons déterminer la réponse des soies sensorielles de diverses tailles, diverses localisations sur le cerque ou encore diverses directionnalités, à des stimuli réalistes. Nous modifierons les caractéristiques des stimuli telles que la vitesse, la distance et la direction de la prédation en utilisant les résultats des simulations FEM (Finite Elements Method) des flux générés par des araignées en mouvement (Chapitre 6, Casas et Steinmann (2014)).

9.1.1 Stimuli extraits des simulations en éléments finis

Nous avons modélisé la vitesse de flux d'air fléchissant le poil, en utilisant les résultats des simulations en éléments finis (FEM) de l'écoulement généré en amont d'une araignée en mouvement. Ces résultats et la méthodologie utilisée pour faire ces simulations sont présentés dans le chapitre 6 de ce mémoire (Casas et Steinmann (2014)). Nous avons estimé le flux généré en amont d'un modèle simplifié d'araignée pour des vitesses de courses variant entre 5 cm/s et 60 cm/s. La figure 9.1 illustre la façon dont nous avons extrait l'écoulement autour d'un poil filiforme de la proie à partir des résultats des simulations FEM. Les profils de vitesse $V_f^{SC}(z)$ ont été extraits le long d'un axe médian dans la section du corps de l'araignée, représentée par

la plus grosse sphère (sous l'isosurface rouge) sur la figure 9.1.b. $V_f^{SC}(z)$ dépend principalement de la distance z le long de l'axe médian et de la vitesse de la sphère V_p. On définit qu'au temps $t = 0$, la distance entre la sphère et le point où l'on décrit la vitesse, c'est à dire la distance séparant la proie et le prédateur, est $z = z_p$ et qu'au temps $t = t_0$, cette distance est nulle. Ceci implique que si la vitesse de l'araignée est constante,t_0 et z_p sont reliés par l'expression $t_0 = \frac{z_p}{V_p}$. On obtient ensuite la variation temporelle de la vitesse $V_f^{SC}(t)$ en procédant au changement de variable $\mathrm{t} = \frac{\mathrm{z_p - z}}{\mathrm{V_p}}$. C'est à partir de cette variation temporelle que l'on va déterminer la série de Fourier complexe correspondante V_0^{mSC}, en utilisant un algorithme de transformée de Fourier discrète rapide (FFT). Son module $\left|V_0^{mSC}\right|$ correspond à l'amplitude du contenu fréquentiel de l'écoulement transitoire autour du poil et son argument $\phi_{V_0^m}$ représente la phase des différentes oscillations de différentes fréquences. La somme de la série de Fourier converge vers l'expression temporelle $V_f^{SC}(t)$ et on peut écrire :

$$V_f^{SC}(t) = \sum_{m=0}^{\infty} {V_0^m}_{SC}\, e^{-i\omega_m t} = \sum_{m=0}^{\infty} |{V_0^m}_{SC}|_{SC}\, e^{-i\omega_m t + \phi_{V_0^m}} \tag{9.1}$$

9.1.2 Analyse de sensibilité du modèle

Effet de la vitesse d'attaque

Le premier paramètre qu'un réseau de senseurs de tailles différentes pourrait traduire est la vitesse d'approche du prédateur. Pour comprendre comment cette vitesse module la réaction de l'ensemble des senseurs, nous allons dans une première partie déterminer l'influence de la vitesse d'attaque sur les temps de réaction de poils de différentes longueurs. La figure 9.2 représente les résultats de notre modèle de déflexion des poils lors de l'approche d'un prédateur. Dans la partie gauche, le prédateur attaque à 40 cm/s et démarre à 8 cm de la proie, distance qu'il parcourt en 200 ms. Les poils les plus courts se déclenchent en premier, $t_{200\mu m}$=40μs après le lancement de l'attaque, tandis que les poils les plus longs réagiront $t_{2000\mu m}$=1 ms après le début de l'attaque. Donc pour une vitesse d'attaque de 40 cm/s, on peut estimer le rapport entre le temps de réaction des petits et des longs poils comme $\frac{t_{2000\mu m}}{t_{200\mu m}} = 25$. Dans la partie droite de la figure, le prédateur attaque à 10 cm/s en partant d'une distance de 15 cm, qu'il pourra parcourir en 1500 ms. Le plus petit poil réagit au bout de $\mathrm{t}_{200\mu m}$=200 μs tandis que le plus long régira au bout de $t_{2000\mu m}$ =2ms. A cette vitesse d'attaque, le rapport entre le temps de réaction des petits et des longs poils est donc réduit à $\frac{t_{2000\mu m}}{t_{200\mu m}} = 10$. A de faibles vitesses d'attaque les petits poils ne vont réagir que 10 fois plus vite que les longs poils, tandis qu'à de plus fortes vitesses d'attaque les petits poils vont réagir 25 fois plus vite. Notre modèle nous indique donc que le changement de la vitesse d'attaque du prédateur se traduit par une modification de l'amplitude d'étalement temporel des réactions des poils de différentes longueurs.

Cette étude a consisté à déterminer la réaction des poils, non plus dans des écoulements oscillatoires, mais dans des écoulements transitoires réalistes. C'est cette approche qui nous a permis de revisiter la question du large spectre de tailles de poils sur le cerque. Nous avons prédit que les neurones sensoriels des petits poils se déclenchent donc en premier, et que les longs

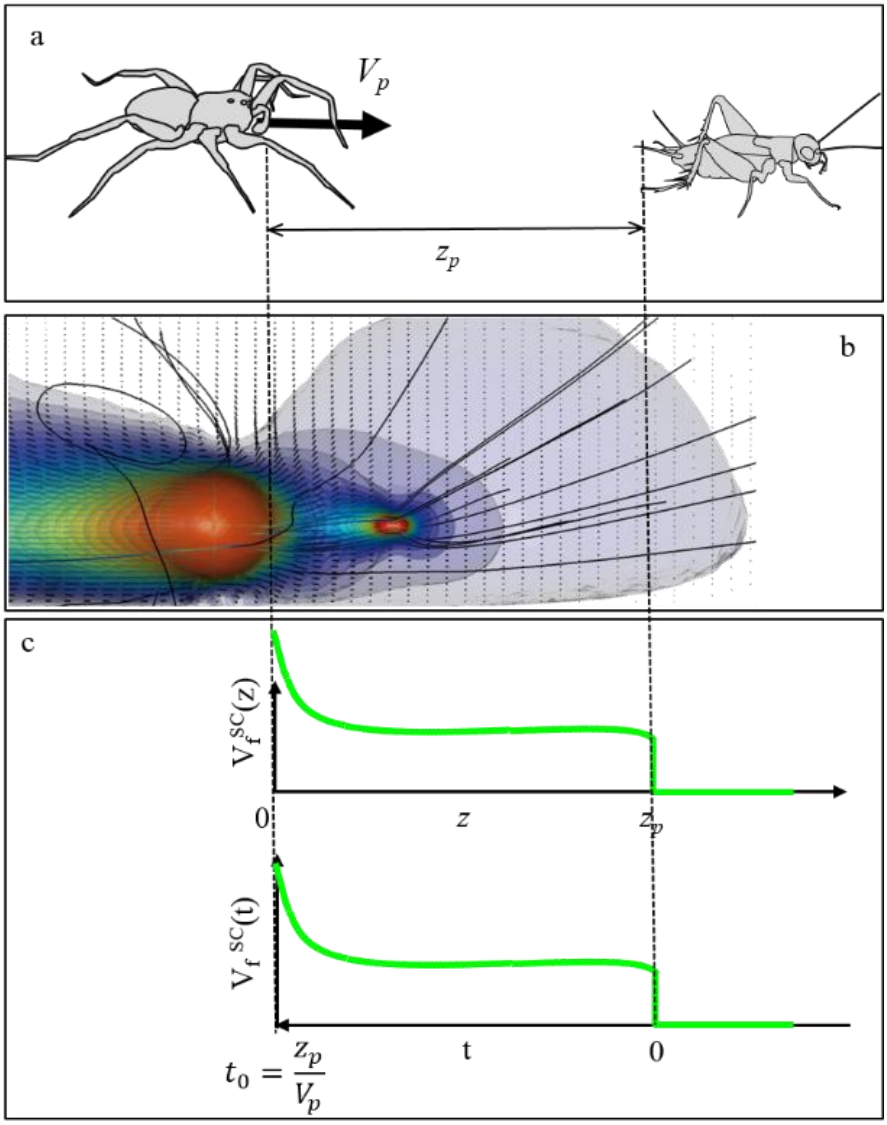

FIGURE 9.1: **Méthodologie utilisée pour déterminer l'évolution temporelle de l'écoulement $V_f^{SC}(t)$ autour des poils filiformes, à partir des simulations FEM du flux généré en amont d'un modèle simplifié d'araignée en mouvement.** (a) Représentation schématique de l'interaction proie prédateur. L'araignée, se dirige vers sa proie, initialement située à la distance z_p, à une vitesse V_p. (b) Vue de coté des résultats de la simulation FEM. Les isosurfaces représentent les surfaces externes des volumes d'écoulements où les vitesses sont supérieures à un seuil défini. Le niveau le plus faible, en bleu clair, correspond à des vitesses de 2.1 mm/s. Le niveau le plus élevé en rouge correspond à des vitesses supérieures de 10 cm/s. Les sphères symbolisant le corps et les pattes postèrieures de l'araignée sont situées sous les isosurfaces de couleur rouge. Le champ de vecteurs représente la direction et la vitesse de l'écoulement. L'assymétrie des lignes d'écoulement et des volumes iso-surfaciques met en valeur le très fort impact de la présence du sol sur les vitesses. (c) Le profil de vitesse $V_f^{SC}(z)$ est extrait le long d'un axe médian dans la section du corps de l'araignée. A chaque distance z correspond un temps $t = \frac{z_p - z}{V_p}$ et on définit que l'araignée atteint le grillon à $t_0 = \frac{z_p}{V_p}$. La détermination de l'évolution temporelle de la vitesse $V_f^{SC}(t)$ consiste schématiquement à déterminer $V_f^{SC}(t = 0)$ comme étant la vitesse à la distance $z = z_p$, puis à se rapprocher de l'araignée pour l'atteindre à $z = 0$, correspondant au temps $t = t_0$.

poils sont recrutés plus tard. La dynamique de ce recrutement de poils de longueurs différentes, semblant refléter la vitesse de l'attaque, pourrait être la première étape du codage du signal complexe émis par le prédateur lors de son approche. L'étude de ces réponses met en lumière une adaptation de la structuration du réseau de senseurs aux motifs fréquentiels des signaux des prédateurs. Il se pourrait qu'une large gamme de longueurs de poils confère au niveau primaire du système cercal, la capacité de traduire la complexité du flux généré par le prédateur en un motif particulier d'impulsions.

Sur la figure 9.2, nous avons intentionnellement utilisé une représentation logarithmique des temps, pour mettre en valeur la forte croissance des angles de déflexion au démarrage des poils, traduisant leurs réponses transitoires. On remarque que durant 10 μs et 1000 μs, en fonction de sa longueur, le poil va rapidement fléchir jusqu'à des petits angles situés entre 0.01 et 0.1 degrés. Ces angles, bien que très faibles en comparaison de l'échelle totale de déflexion des poils, sont suffisants pour provoquer l'émission d'un potentiel d'action dans le neurone à la base du poil (Shimozawa *et al.* (2003)).

On remarque aussi que pour toutes les longueurs de poils, l'angle de déflexion, qui croît extrêmement vite au début de la simulation, va ensuite stagner jusqu'à des temps situés entre 10 et 50 ms, où l'augmentation devient à nouveau très forte. Cette étrange réaction du poil, qui peut être partiellement expliquée par la représentation logarithmique des temps, est principalement dûe à la superposition des solutions homogènes et particulières de l'équation du moment angulaire, décrite dans le chapitre 8. La solution homogène est composée de deux exponentielles dont les constantes de temps sont $1/\gamma_1$ et $1/\gamma_2$. Les parties réelles de γ_1 et γ_2 étant négatives, cette solution homogène décroit naturellement exponentiellement vers zéro avec le temps. Cette décroissance se superpose cependant à la lente augmentation de la solution particulière durant les quelques premières dizaines de millisecondes, temps à partir duquel la solution particulière montre une augmentation rapide, jusqu'aux temps plus grands. C'est la superposition de ces deux solutions qui provoque l'existence d'une zone de stagnation apparente de déflexion après une croissance aux temps courts.

Effet de la distance d'attaque

Le second paramètre de l'attaque qui pourrait être codé par le réseau de poil est la distance à laquelle le prédateur lance son attaque. Nous avons simulé, comme montré dans la figure 9.3, l'effet de la distance à laquelle est lancée l'attaque sur la rapidité de déflexion des poils pour une vitesse d'attaque de 40 cm/s et pour des distances d'attaque comprises entre 1 et 8 cm, ce qui correspond à des temps de trajet du prédateur compris entre 25 et 200 ms. Plus l'attaque démarre près de la proie et plus la réaction des poils est rapide. Les petits poils (200 μm) réagissent entre 10 et 50 μs après le démarrage tandis que les long poils de 1000 μm réagissent entre 50 et 150 μs après le démarrage de l'attaque. Les différences dans les temporalités d'activations des petits et longs poils sont donc très faibles. Il semble qu'elles varient très peu avec la distance d'attaque du prédateur

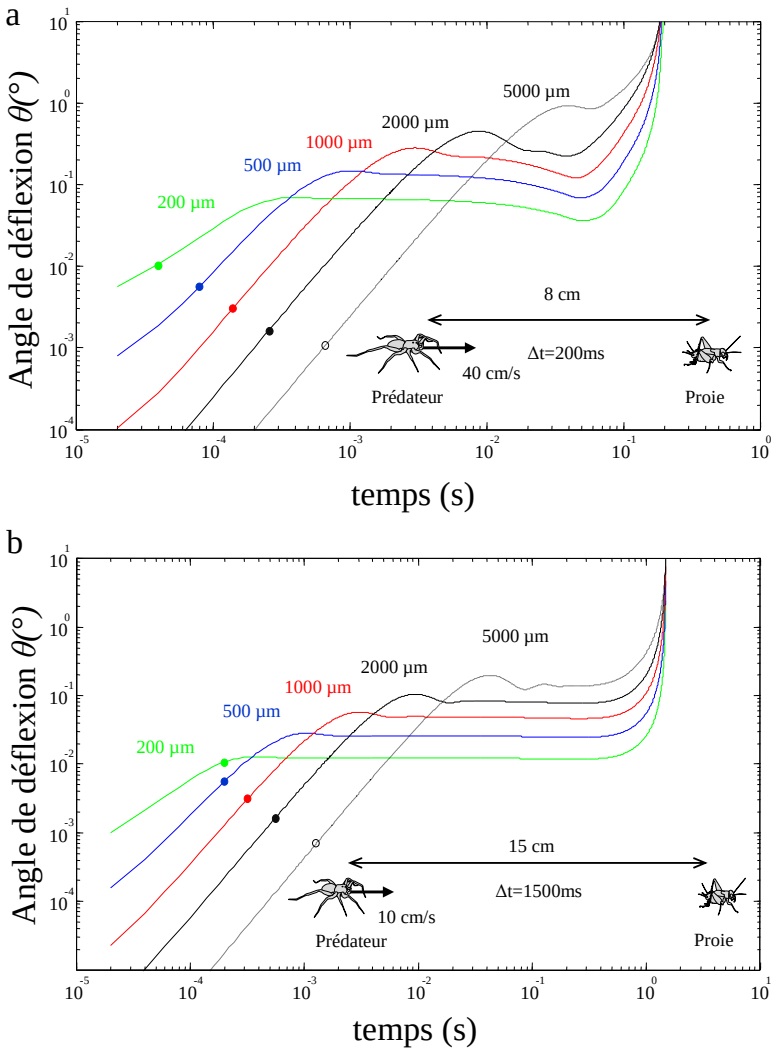

FIGURE 9.2: **Influence de la vitesse d'attaque sur la déflexion de poils de différentes longueurs** (L=200, 500, 1000, 2000 and 5000 μm). Le flux d'air utilisé comme entrée du modèle de déflexion est déterminé à partir des simulations FEM du flux généré en amont d'un modèle simplifié d'araignée en mouvement. (a) La distance d'attaque est de 8cm et la vitesse d'attaque est de 40 cm/s. (b) La distance d'attaque est de 15 cm et la vitesse d'attaque est de 10 cm/s. Les points sur les courbes de déflexion indiquent les instants où les poils atteignent l'angle minimal permettant la génération d'un potentiel d'action.

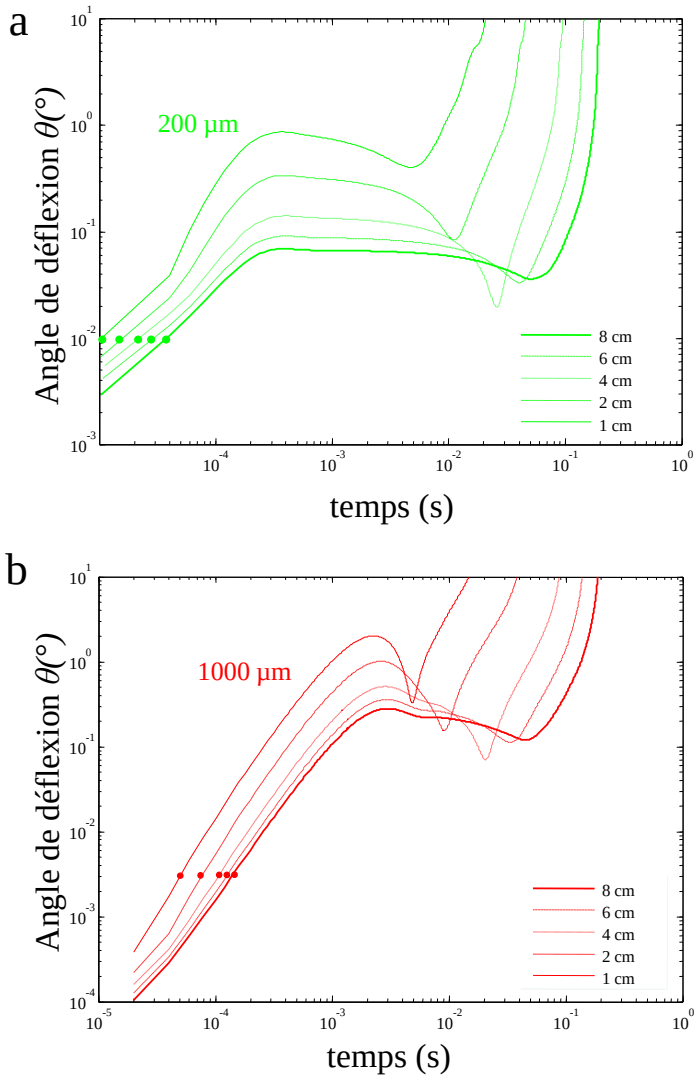

FIGURE 9.3: **Influence de la distance d'attaque sur la déflexion de poils de différentes longueurs** (L=200 et 1000 μm). Le flux d'air utilisé comme entrée du modèle de déflexion est déterminé à partir des simulations FEM du flux généré en amont d'un modèle simplifié d'araignée en mouvement à 40cm/s et commençant sa course à diverses distances de la proie (zp=1, 2, 4, 6 et 8 cm). (a) Déflexion temporelle d'un poil de 200 μm. (b) Déflexion temporelle d'un poil de 1000 μm. Les points sur les courbes de déflexion indiquent les instants où les poils atteignent l'angle minimal permettant la génération d'un potentiel d'action.

Effet de la position sur le cerque et delay line

Outre la longueur des poils, leurs positions respectives sur le cerque pourraient être un facteur permettant de coder divers paramètres de l'attaque. Nous avons simulé l'effet de la position d'un poil sur son temps de réaction. La figure 9.4 représente la réaction de 2 poils de 200 et 1000 μm situés dans la partie distale (trait continu pointe du cerque) ou proximale (trait pointillé - base du cerque - soit à 8 mm de l'apex du cerque) et ceci pour deux vitesses d'attaque, 10 et 40 cm/s, d'un prédateur démarrant à 4 cm de sa proie. Pour un même poil à la base et à la pointe du cerque, l'évolution temporelle de la déflexion est différente et les poils situés à la pointe semblent atteindre plus rapidement de très grands angles de déflexion. Cependant, la vitesse de réaction d'un poil est mesurée par sa rapidité à atteindre son angle de déflexion minimal. Or ce temps est équivalent à la base et à la pointe pour des petits et des grands poils, quelque soit la vitesse d'attaque (Figure 9.4). Aux temps élevés, la vitesse de l'écoulement, qui va faire fléchir le poil, est plus élevée dans la partie distale du cerque que dans sa partie proximale. Cependant cette différence de vitesse dans l'écoulement entre les deux zones du cerque est très faible aux temps courts. Or, nous avons précédemment constaté que c'était la vitesse de démarrage du poil, c'est à dire sa réponse transitoire, décrite par la solution homogène de l'équation du moment angulaire, qui conditionnait principalement l'instant où un potentiel d'action était émis. D'après notre modèle, la spatialité de la répartition des poils n'a donc que très peu d'influence sur la capacité à traduire la vitesse ou la distance d'une attaque.

En 2010, Mulder-Rosi *et al.* (2010) avaient déjà déterminé le rôle fonctionnel de la dimension physique du cerque dans son fonctionnement global. Après avoir déterminé que les vitesses caractéristiques de conduction des potentiels d'action dans les axones des neurones sensoriels étaient les mêmes dans tout le cerque (V=1.9 mm/ms), ces auteurs ont mis en évidence l'existence d'une différence de temps de propagation des signaux provenant de différents récepteurs le long du cerque. Ils stimulèrent ensuite successivement les poils positionnés dans différentes zones du cerque, de la pointe à la base et inversement, à l'aide d'un astucieux générateur de flux à becs multiples. Ils découvrirent que la réponse des afférents sensoriels était maximisée quand le stimulus était dirigé de la pointe à la base du cerque. Ils suggérèrent ainsi que le système cercal du grillon fonctionnait en quelque sorte comme une *ligne de retard* (*delay line*), les poils les plus proches de la sources de stimulus réagissant avant les poils les plus éloignés. Il est intéressant de mettre nos résultats sur l'influence de la position des poils en perspective avec leurs travaux. Notre modèle nous indique que quelque soit la vitesse d'attaque d'un prédateur, les poils situés n'importe où sur la structure vont réagir en même temps. Cette instantanéité des déflexions des poils de même taille quelque soit leur distance par rapport à la base du cerque, s'oppose donc aux résultats de Mulder-Rosi *et al.* (2010). Leur étude supposait implicitement une déflexion successive des poils le long du cerque. La différence provient de la différence de stimulus imposé entre les deux études. Dans la leur étude, Mulder-Rosi *et al.* (2010) fléchissaient successivement les poils à l'aide d'une variation gaussienne de la vitesse d'écoulement, d'une amplitude de 3 cm/s, à la pointe du cerque. Cette amplitude maximale d'écoulement diminuant fortement en s'approchant de la base du cerque. Le choix de stimulus conditionne les conclusions sur le rôle fonctionnel des caractéristiques morphologiques du cerque que tirent les différents auteurs.

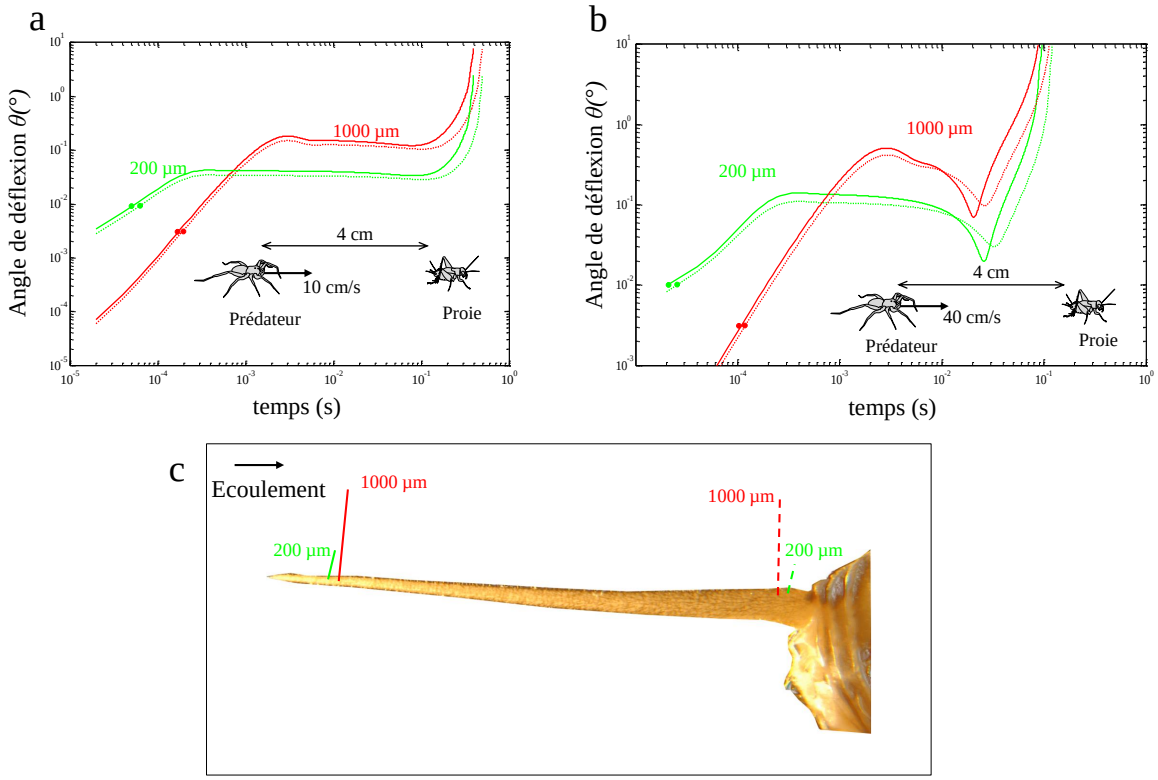

FIGURE 9.4: **Influence de la position sur le cerque sur la déflexion de poils de différentes longueurs** (L=200 et 1000 μm). Le flux d'air utilisé comme entrée du modèle de déflexion est déterminé à partir des simulations FEM du flux généré en amont d'un modèle simplifié d'araignée en mouvement et commençant sa course à une distance de la proie z_p=4 cm. (a) Déflexion temporelle de deux poils de longueurs égales à 200 μm et 1000 μm pour une vitesse d'attaque de 10 cm/s. (b) Déflexion temporelle de deux poils de longueurs égales à 200 μm et 1000 μm pour une vitesse d'attaque de 40 cm/s. Les points sur les courbes de déflexion indiquent les instants où les poils atteignent l'angle minimal permettant la génération d'un potentiel d'action.(c) Schéma représentant les deux positions à la pointe et à la base du cerque, séparées de 8 mm.

Effet de la directionnalité

La direction préférentielle de flexion d'un poil filiforme est aussi un facteur qui va fortement influencer sa susceptibilité à atteindre rapidement son angle minimal de déclenchement dans le courant généré par l'approche du prédateur. Nous avons pris en compte cet effet en modulant les forces de traînées agissant sur un poil par le cosinus de l'angle préférentiel de ce dernier. Cet angle préférentiel est défini par rapport à l'axe du flux généré par le prédateur. La figure 9.5 représente les déflexions de trois poils (250, 500 et 1000 μm) dans un flux généré par un prédateur allant à une vitesse de 40 cm/s démarrant à 8 cm. Bien évidemment, les poils alignés avec le flux vont fléchir plus fortement que les poils perpendiculaires au flux qui, eux ne subiront aucune trainée visqueuse.

Si on se focalise sur la simulation de déflexion d'un poil de 250 μm (Figure 9.5.b), on voit que, si ce petit poil est orienté dans le sens du flux (α=0°), il va atteindre son angle de déflexion minimal de 0.01° très tôt, vers 40 μs. Si il est orienté à 80° avec le flux, il réagira un peu plus tard, au bout de 400 μs. En revanche, on constate que pour des orientations préférentielles de 85 à 88°, ce poil ne réagira que bien plus tard, au bout de 100 ms. Il existe ainsi, pour les courts poils, une orientation critique au delà de laquelle le temps de déclenchement va être fortement affecté. Si on se concentre à présent sur la réaction d'un poil de 1000 μm (Figure 9.5.d), on constate qu'il atteindra son angle de déclenchement à 200 μs lorsqu'il est orienté dans le flux, et à 1 ms lorsque son angle préférentiel est de 88 ° avec le flux. Il semble ainsi que les longs poils subissent, dans une moindre mesure, l'effet délétère d'une mauvaise orientation sur leur temps de déclenchement. Cette différence d'effet de la directionnalité sur le déclenchement des petits et longs poils s'explique par l'interaction de trois phénomènes, (i) les différences dans la réponse transitoire des petits et des longs poils, (ii) leurs différentes capacités à extraire de l'énergie dans le flux et (iii) la différence de seuil de déclenchement du neurone sensoriel à leur base. Bien que les petits poils réagissent très vite et très tôt, ils ne vont pas atteindre des angles très élevés après leur phase transitoire de démarrage. Le poil de 250 μm orienté dans le flux atteindra par exemple un plateau à 0.1° entre 500 μs et 50 ms. C'est sa petite taille qui lui confère une grande réactivité, mais sa faible surface en contact avec le flux, et le fait qu'il soit plongé dans la couche limite, minimise grandement sa traînée visqueuse. L'effet de cette traînée sera d'autant plus petit que l'angle de direction préférentielle avec le flux sera grand. Ainsi, un poil de même longueur dont l'axe de directionnalité préférentielle serait de 85°, verrait lui aussi son angle de déflexion atteindre rapidement un plateau entre 500 μs et 50 ms. Cependant, ce plateau de 0.007 ° sera inférieur à son angle de déclenchement, qui est aussi assez élevé ($\theta_{thesh}\,(L = 250\ \mu m) = 0.01°$ voir Chapitre 8). Le long poil de 1000 μm a, en revanche, un seuil de déclenchement beaucoup plus faible ($\theta_{thesh}(L = 1000\ \mu m) = 0.003°$). Il réagira beaucoup moins rapidement que le petit poil mais sa capacité à extraire beaucoup d'énergie dans le fluide, de part sa plus grande surface, lui permettra de fléchir jusqu'à atteindre un peu plus tard un plateau à 0.4°, entre 2 ms et 50 ms, pour une orientation de 0° avec le flux. La réduction de l'effet de la traînée visqueuse est pour lui aussi proportionnelle à son orientation dans le flux. Même pour une orientation de 88°, la traînée visqueuse sur ce long poil sera cependant suffisante pour lui faire atteindre un angle supérieur à son seuil de déclenchement de 0.003° dans ce plateau

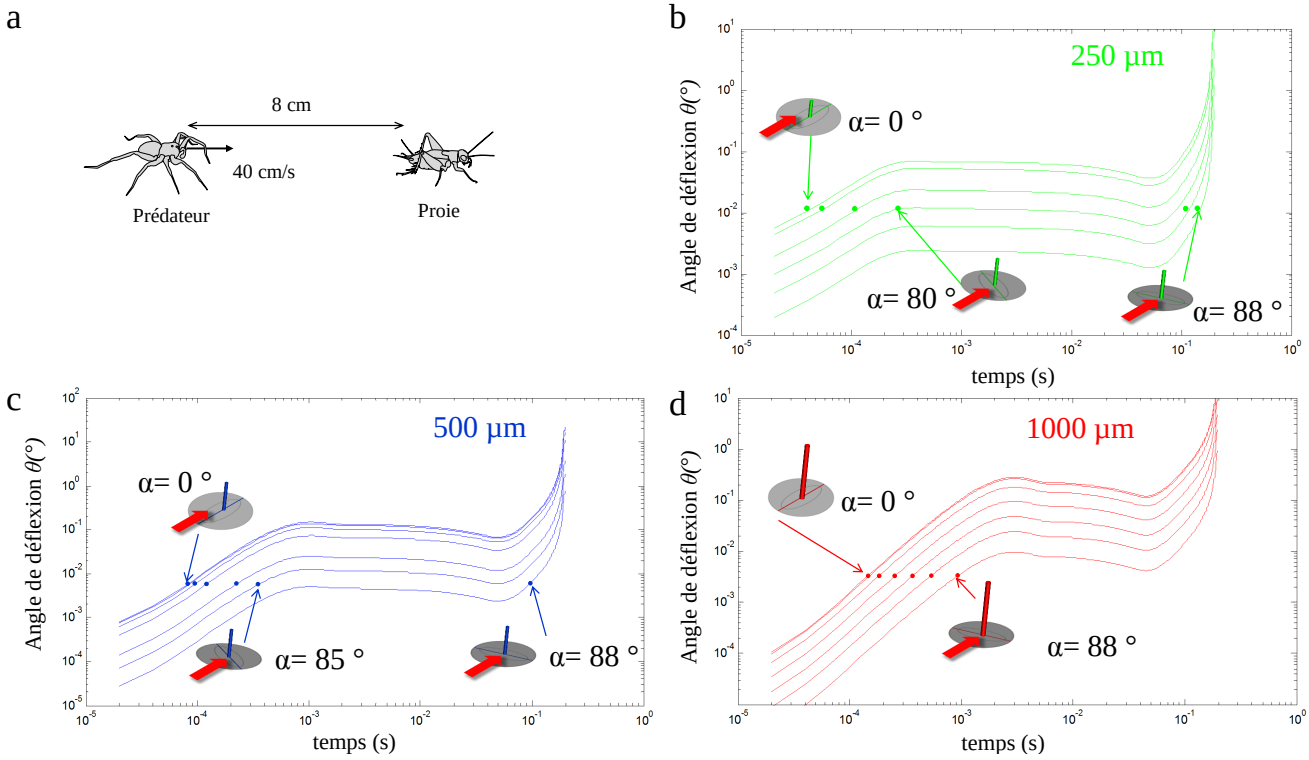

FIGURE 9.5: **Influence de la direction préférentielle du poil sur sa déflexion pour trois longueurs de poils différentes et pour six directionnalités** (α= 0 , 50, 70, 80, 85 et 88°). (a) Le flux d'air utilisé comme entrée du modèle de déflexion est déterminé à partir des simulations FEM du flux généré en amont d'un modèle simplifié d'araignée en mouvement à 40cm/s et commençant sa course à une distance de la proie de z_p=8 cm. (b) Effet de l'orientation pour un poil de 250 μm. (c) Effet de l'orientation pour un poil de 500 μm. (d) Effet de l'orientation pour un poil de 1000 μm. Les points sur les courbes de déflexion indiquent les instants où les poils atteignent l'angle minimal permettant la génération d'un potentiel d'action.

entre 2ms et 50 ms. Les réactivités des petits et des longs poils sont donc fortement affectées par l'orientation de leurs plans préférentiels. Le prochain paragraphe discutera d'un éventuel codage de la vitesse de l'écoulement, généré par l'approche d'un prédateur par l'activation successive des neurones sensoriels de poils de différentes directionalités.

9.1.3 La directionnalité et le codage de l'approche d'un prédateur

L'étude de l'effet de la directionnalité de la chaussette, dans laquelle est positionné le poil, nous indique que cette directionnalité est aussi un facteur structurel déterminant, qui discriminera les temps de réactivité des différents poils. Si on s'intéresse à un des facteurs clefs de la réactivité d'un poil, à savoir l'instant où le neurone sensoriel situé sous le poil va pouvoir déclencher un potentiel d'action, on réalise que cette direction préférentielle a un effet beaucoup plus important que la taille du poil ou sa position sur le cerque. On constate en outre que, quel que soit les modalités de l'attaque (vitesse, distance de démarrage du prédateur), les longs poils vont réagir assez rapidement même si ils sont orientés quasiment perpendiculairement au flux. On sait grâce aux études de Jacobs et Theunissen (1996) et Miller *et al.* (2011) que la direction

préférentielle de flexion des poils est projetée à travers des connexions synaptiques, depuis les neurones sensoriels à leur base, et ce jusqu'au ganglion abdominal terminal. C'est sur cette carte de projection en forme de spirale que vont s'organiser les arborisations des neurones sensoriels (l'illustration de cette carte neuronale est visible dans les figures 10 & 11 du manuscrit Jacobs et Theunissen (1996)). Les différentes directionnalités sont représentées de manière continue le long de la spirale. Ce sont ensuite les arborisations dendritiques des inter-neurones géants qui vont extraire la direction du courant en venant se connecter aux régions correspondants aux différentes directionnalités de la carte. La figure 9.5.d nous indique par des points rouges les instants où vont réagir des poils de 1000 μm, de différentes directionnalités allant de 0° à 88°. Notre modèle montre que pour un même stimulus, des poils d'orientations différentes vont être activés successivement : les poils orientés dans le flux en premier, et les poils dont la directionnalité est perpendiculaire au flux, bien plus tard. Lors de l'approche d'un prédateur, on peut donc s'attendre à ce que le déclenchement successif de leurs neurones sensoriels active les différentes zones de directionnalité de la carte neuronale dans le ganglion abdominal terminal, et ceci à tour de rôle. Une activation, à tour de rôle, de différentes directionnalités peut cependant tout aussi bien être attribuée, après analyse par le système du grillon, au fait qu'un prédateur modifie sa direction de provenance au cours de l'attaque. Mais dans le cas présent, le plus probable serait que les neurones sensoriels sous les poils envoient des potentiels d'actions quand les poils de différentes directionnalités ont tour à tour atteint leur angle de déclenchement. La rapidité d'activation de différentes zones anatomiques du ganglion abdominal terminal pourrait ainsi être une caractéristique importante dans le codage de la vitesse d'approche du prédateur. En 2011, Miller *et al.* (2011) ont caractérisé quantitativement les réseaux de poils sur des cerques de différents grillons *Acheta domesticus*, déterminant leurs longueurs, positions et orientations, rappelant que la variation inter-individuelle des schémas d'organisation structurelle était très faible. La même équipe a aussi proposé encore plus récemment un modèle prédictif de distribution des orientations préférentielles des poils (Heys *et al.* (2012)). On pourrait ainsi envisager, à la lumière de ces études et à l'aide de nos conclusions, la mise au point d'un modèle de réponse globale du système sensoriel du grillon. La comparaison des résultats d'un tel modèle, avec des données neurophysiologiques multipoints simultanées dans différentes zones du ganglion abdominal terminal, pourrait ensuite nous permettre de vérifier le cas échéant les hypothèses d'activations successives de régions spécifiques.

9.1.4 Utilité de l'hypersensibilité des neurones sensoriels ?

La sensibilité d'un poil filiforme est définie comme étant l'angle minimal de déflexion qu'il doit atteindre pour que le neurone sensoriel situé à sa base déclenche un potentiel d'action. Il a été estimé que l'énergie nécessaire, pour atteindre ces angles de déclenchement, était extrêmement faible et équivalait à celle du bruit thermique ambiant, faisant des poils filiformes des grillons les senseurs les plus sensibles du monde animal (Shimozawa *et al.* (2003), Chapitre 8). Leur réponse revêt ainsi un caractère non linéaire, le neurone sensoriel ayant besoin de cette énergie minimale pour déclencher l'émission d'un potentiel d'action (Shimozawa *et al.* (2003)), il ne répond pas en dessous de ce seuil énergétique. Cette hypersensibilité, couplée au caractère

non linéaire de leur réponse, permet ainsi aux poils d'extraire de l'information dans du bruit de fond, par un effet de résonance stochastique (Levin et Miller (1996)).

Les conclusions sur le fonctionnement du réseau cercal sont souvent basées sur des mesures électro-physiologiques. Celles-ci sont, la plupart du temps, réalisées de manière extracellulaire dans diverses régions d'interconnexions neuronales du ganglion abdominal terminal du grillon et ne prennent pas en compte le bruit de fond. Il a ainsi été montré qu'une loi d'échelle pouvait prédire que le nombre cumulé de potentiels d'action était fonction de la vitesse de l'écoulement du fluide autour des cerques (Dupuy *et al.* (2012)). Ces mesures de l'activité électrique intègrent en général des réponses aussi bien phasiques que toniques de divers neurones sensoriels situés sur tout le cerque. Cette vision "statistique" du fonctionnement du système sensoriel du grillon consiste à considérer le système cercal comme un intégrateur qui acquière un signal sur une relativement longue période de quelques dizaines de millisecondes pour en extraire une information pertinente. Ces études permettent, en diminuant les amplitudes de stimulation oscillatoire, de déterminer la sensibilité de divers poils à diverses fréquences en mesurant souvent leur réponse à plusieurs oscillations successives.

Bien que nous n'adoptions pas un point de vue orthogonal à cette vision statistique, notre démarche dynamique est cependant assez différente. Nous n'émettons dans notre modèle aucune supposition sur le caractère phasique ou tonique des neurones sensoriels. De plus, lors de la simulation de la réponse d'un poil à un stimulus réaliste, nous nous sommes particulièrement intéressés au démarrage de sa déflexion. C'est lors de cet instant primordial que l'hypersensibilité du poil prend une autre signification que nous appelons "dynamique" : elle permet alors au poil de réagir très tôt en atteignant très vite son petit angle de déclenchement.

9.2 Vers un nouveau modèle viscoélastique du poil

La plupart des études biomécaniques des soies sensorielles du grillon ainsi que les résultats présentés dans ce mémoire de thèse sont basés sur la représentation de la suspension du poil par un modèle viscoélastique 'spring & dashpot' à deux paramètres (un ressort et une résistance). C'est l'utilisation de ce modèle simple qui permet de simuler la réponse mécanique d'un poil de grillon. Ce choix, qui peut paraître arbitraire au premier abord, a été validé à maintes reprises (Humphrey *et al.* (1993), Shimozawa et Kanou (1984b), Bathellier *et al.* (2012), Chapitre 8). Cependant, les études concernant la morphogénèse du poil lui même et de la suspension situées dans la chaussette indiquent que ces deux éléments primordiaux sont secrétés par deux types de cellules épithéliales différentes, aux caractéristiques mécaniques et élastiques différentes (Shimozawa *et al.* (1998), Shimozawa et Kanou (1984b)). De plus, Barth et Höller (1999) ont aussi supposé que les propriétés viscoélastiques particulières des dendrites elles-mêmes pouvaient expliquer les motifs de réponses phasiques des cellules sensorielles. Elles répondent préférentiellement à des mouvements mais pas du tout à des déformations/compressions statiques. Shimozawa *et al.* (1998) supposent même une différenciation entre les modèles viscoélastiques des longs et des petits poils. Dans une récente étude, Joshi et Miller (2016) rappellent que la structure de la chaussette n'a été que rudimentairement caractérisée d'un point de vue mécanique. Leurs modélisations à base d'éléments finis confirment que cette structure agit bien

comme un ressort. Cependant, ces auteurs évoquent eux aussi l'existence de deux constantes de raideur qui sont toutes les deux déterminées lors du mouvement de flexion du poil. La première constante de raideur a été déterminée avant le contact de la base du poil avec la protubérance cuticulaire. La seconde constante de raideur a été déterminée après le contact et a été éstimée comme étant quatre fois plus élevée que la première.

Il s'avère que les propriétés mécaniques de la suspension du poil dans la chaussette, à savoir sa (ou ses) constante(s) de raideur et sa (ou ses) constante(s) d'amortissement, n'ont jamais été directement mesurées. Les valeurs numériques de ces constantes sont généralement inférées via la réponse harmonique des poils dans des écoulements oscillatoires. Il est ainsi légitime de remettre en question les valeurs numériques estimées, et ceci pour deux raisons. La première est que toutes ces études supposent implicitement la validité d'un modèle viscoélastique à deux éléments. La seconde est liée à la difficulté d'estimer correctement les forces appliquées aux poils. Elles sont tout au plus succinctement déterminées d'après les valeurs des vitesses de flux en champ lointain, en estimant la trainée visqueuse sur les poils situés dans des couches limites. Nous proposons ici une méthode permettant de mesurer directement ces propriétés mécaniques, et ceci en estimant directement les forces appliquées sur les poils filiformes de grillons. Des méthodes alternatives d'estimation des propriétés mécaniques des soies filiformes ont déjà été proposées, notamment par Barth *et al.* (2004). La méthode employée par ces auteurs consistait à estimer les forces (ou moments) impliquées lors du retour de poils tactiles à leur position d'origine en les stimulant à l'aide de capillaires en verre qui se déformaient sous la résistance des poils. Les forces impliquées dans ces déformations de capillaires en verres étaient préalablement et indépendamment estimées. Schaber et Barth (2015) ont aussi utilisé cette technique dans une récente étude pour mesurer les constantes de raideur des poils tactiles de la jonction tibia-metatarse chez les araignées *Cupeniennius salei*.
La microscopie à force atomique (AFM) peut être utilisée en mode contact pour venir directement 'pousser' les poils filiformes, nous permettant de déterminer simultanément leur déflexion et la force qu'on leur applique. McConney *et al.* (2009) ont utilisé l'AFM pour étudier les propriétés mécaniques des suspensions des poils sensoriels d'araignées *Cupiennius salei*. Ils ont notamment décrit le fonctionnement de la suspension à l'aide d'un nouveau modèle viscoélastique comportant trois éléments. L'application de cette démarche expérimentale au grillon pourrait être forte utile à la compréhension plus précise du fonctionnement de ses poils filiformes et des rôles spécifiques des petits et des long poils. Nous présentons dans une première partie la définition de ce nouveau modèle et ses différences avec le modèle viscoélastique standard. Dans une seconde partie, nous proposons un plan expérimental de la mesure mécanique directe des propriétés viscoélastiques de la suspension des poils par microscopie à force atomique.

9.2.1 Paramètres des modèles viscoélastiques

Lors de l'étude des propriétés élastiques et résistives (ou visqueuses) des matériaux, il est coutumier de chercher à décrire comment un matériaux se déforme lorsqu'il est soumis à une contrainte. On définit dans notre analyse les déformations comme étant la déflexion de la soie filiforme, supposée rigide, et les contraintes comme étant les forces appliquées à une certaine

distance de l'axe de rotation du poil. On peut définir deux équations de la conservation du moment angulaire du poil filiforme, basées sur deux modèles viscoélastiques différents décrit dans la figure 9.6 (Salençon (2009)). Une première équation décrit la suspension supportant le poil comme un modèle de Kelvin-Voigt à deux paramètres. Ce modèle est composé d'une partie élastique, un ressort de constante de raideur S_{2p} (N.m.rad^{-1}) capable d'emmagasiner de l'énergie pour la restituer. Ce ressort se trouve en parallèle avec une résistance de constante d'amortissement R_{2p} (N.m.s.rad^{-1}) qui elle dissipera l'énergie (Figure 9.6.a). Le poil est ainsi considéré comme un oscillateur harmonique amorti et forcé. L'équation de conservation du moment angulaire caractérisant le système est la suivante :

$$I\ddot{\theta} + R_{2p}\dot{\theta} + S_{2p}\theta = T \tag{9.2}$$

où I (N.m.s.rad^{-1}) est le moment d'inertie du poil, T est le moment appliqué sur le poil et θ (rad), $\dot{\theta}$ (rad.s^{-1}) et $\ddot{\theta}$ (rad.s^{-2}) sont respectivement, l'angle de déflexion, la vitesse angulaire et l'accélération angulaire du poil. Si la vitesse de rotation du poil est constante, son accélération est nulle ($\ddot{\theta} = 0$), l'équation (9.2) peut se simplifier :

$$R_{2p}\frac{d\theta(t)}{dt} + S_{2p}\theta(t) = T(t) \tag{9.3}$$

Le second modèle, dit linéaire standard, est plus complexe et consiste cette fois-ci à décrire la suspension du poil par un modèle viscoélastique composé d'un ressort de constante de raideur S_{3p} (N.m.rad^{-1}) en parallèle avec une résistance de constante d'amortissement R_{3p} (N.m.s.rad^{-1}), elle même en série avec un ressort S'_{3p} (N.m.rad^{-1}) (Figure 9.6.b). L'équation de conservation du moment angulaire caractérisant le système est la suivante :

$$I\ddot{\theta} + R_{3p}\left(1 + \frac{S_{3p}}{S'_{3p}}\right)\dot{\theta} + S_{3p}\theta = T + \frac{R_{3p}}{S'_{3p}}\dot{T} \tag{9.4}$$

Ici $\dot{T} = dT/dt$ (N.m.s^{-1}) est la dérivée temporelle du moment imposé au poil. On peut simplifier l'équation (9.4) en considérant que la vitesse de rotation du poil est constante :

$$R_{3p}\left(1 + \frac{S_{3p}}{S'_{3p}}\right)\frac{d\theta(t)}{dt} + S_{3p}\theta(t) = T(t) + \frac{R_{3p}}{S'_{3p}}\frac{dT(t)}{dt} \tag{9.5}$$

9.2.2 Mesures de contrainte/déformation par AFM

Différentes étapes de la mesure

Pour déterminer les propriétés viscoélastiques de la suspension du poil, il faut mesurer sa déformation par l'intermédiaire de sa déflexion θ, lors de l'application d'une contrainte T à l'aide d'une pointe nanométrique habituellement utilisée en microscopie à force atomique (AFM). L'AFM peut être ainsi utilisée en mode contact et la mesure consiste à venir toucher la soie filiforme à l'aide d'une pointe supportée par un levier, comme décrit dans les différentes étapes de la figure 9.7. Dans un premier temps, il faut s'assurer d'approcher très précisément le

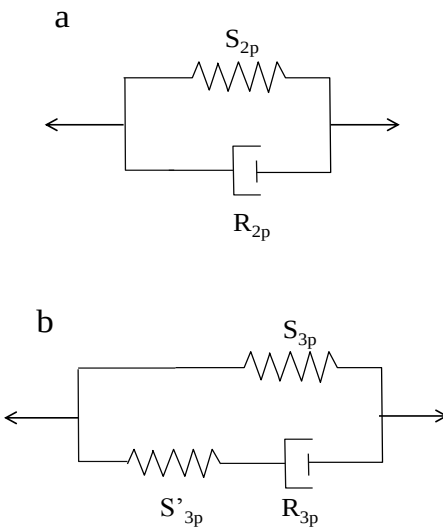

FIGURE 9.6: **Représentation schématique de la suspension de poils filiformes par deux types de modèles viscoélastiques**. (a) Modèle de Kelvin-Voigt à deux éléments. (b) Modèle solide linéaire standard à trois éléments.

poil (phase 1 de la figure 9.7) avec la pointe. Dans cette étape, le levier qui supporte la pointe n'est pas défléchie. Quand la pointe est assez proche du poil, les forces de van der Walls vont attirer la pointe vers le poil et le contact va s'établir à la distance d_c de son axe de rotation (phase 2).

Le levier continue ensuite sa course et fléchit le poil (phase 3). C'est durant cette phase que la suspension à la base du poil va s'opposer au moment imposé par la pointe. La rétroaction du poil, face à la force de contrainte imposée par le levier via la pointe, va faire fléchir le levier. Cette flexion du levier sera mesurée par la déflexion d'un rayon laser. Cette réflexion est ensuite projetée sur un réseau de photodiodes, dont l'intensité de sortie I (nA) sera proportionnelle à la déflexion du levier, et donc à la contrainte F (N) imposée à la soie filiforme. Enfin, quand le poil sera rentré en contact avec la protubérance cuticulaire située à sa base et qu'il aura atteint son angle de déflexion maximal (phase 4), la force imposée par la pointe va le faire se courber. A partir de ce moment là, on ne mesurera plus la résistance de la suspension du poil mais directement les paramètres viscoélastiques de la soie filiforme elle même, bien plus rigide. La mesure dynamique nous permet de déterminer la vitesse d'approche de la pointe, la vitesse de déflexion du poil et l'évolution temporelle de la contrainte imposée au poil.

Choix de la pointe AFM

Il faudra choisir un levier soutenant la pointe AFM dont la constante de raideur permette à la fois d'appliquer les forces/couples pour lesquels le poil est toujours dans sa phase de déflexion linéaire tout en assurant une déflexion mesurable de ce levier à ces faibles forces. La contrainte $F\,(N)$ imposée par une pointe AFM peut être déterminée par la loi de Hooke qui la relie à la déformation du levier (cantilever) Δz (m) par l'intermédiaire de la constante de raideur :

$$F = -k.\Delta z \tag{9.6}$$

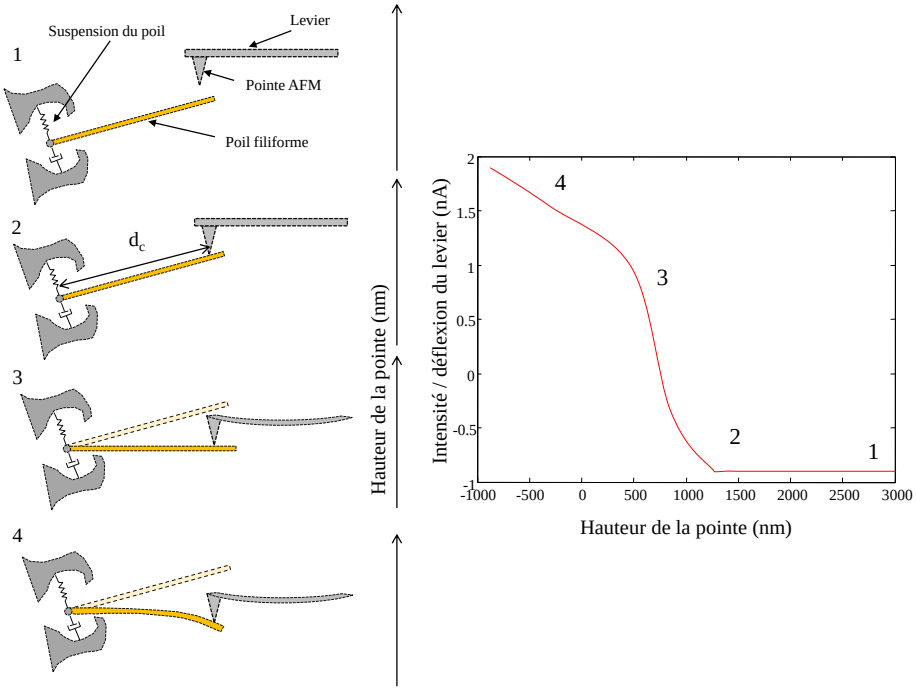

FIGURE 9.7: **Différentes étapes de la mesure à l'aide de la microscopie à force atomique par contact sur une soie filiforme de *Acheta domesticus***. La mesure, qui consiste à venir toucher le poil filiforme à l'aide d'une pointe supportée par un levier, pemettra de déterminer les propriétés viscoélastiques de la suspension du poil. Les diffèrentes étapes sont décrites dans le texte.

où $k = 2\pi^3 l^3 w \sqrt{\frac{\rho^3}{E}} {f_0}^3$est la constante de raideur, l (m) la longueur du levier, w (m) sa largeur, ρ (kg/m^3) sa densité, E (N/m) le module de Young du levier et f_0 (Hz) sa fréquence de résonance. Les forces de traînée communément appliquées aux poils filiformes ont été estimées comme comprises entre 10^{-13} et 10^{-12} N.m pour des oscillations d'amplitudes comprises entre 0.1 et 10° (Shimozawa et Kanou (1984b), Humphrey *et al.* (1993)). Ce qui veut dire que pour faire fléchir 'linéairement' un poil de 1000 μm entre 0.1° et 10°, il faudra être capable de le pousser à sa pointe (c'est à dire le plus loin possible de son axe de rotation, afin de lui appliquer le couple le plus grand possible) en lui appliquant une contrainte comprise entre $\frac{10^{-13}\ N.m}{1000\ \mu m} = 100$ pN et $\frac{10^{-12}\ N.m}{1000\ \mu m} = 1000$ pN. Il existe une large gamme de sondes AFM aux constantes de raideur k adaptées à la détermination des propriétés mécaniques locales de matériaux biologiques. Les sondes les plus souples sont notamment utilisées pour sonder les propriétés élastiques de la surface d'échantillons biologiques, et possèdent une constante de raideur de l'ordre de 0.01 N/m pour une longueur de 125 μm (uniqprob^{TM} - soft contact mode). Ces pointes génèrent des contraintes aussi faibles que 10 pN (Sirghi *et al.* (2008)). Cette sensibilité est amplement suffisante pour rester dans la zone de linéarité de déflexion des poils.

9.2.3 Ajustement des modèles viscoélastiques

Une fois la mesure déformation/contrainte du poil enregistrée, il conviendra d'y ajuster l'un ou l'autre des modèles viscoélastiques. La figure 9.8 représente la mesure AFM attendue sur un poil de (1000 μm) dont la réponse mécanique correspondrait à celle d'un modèle de Kelvin-Voigt

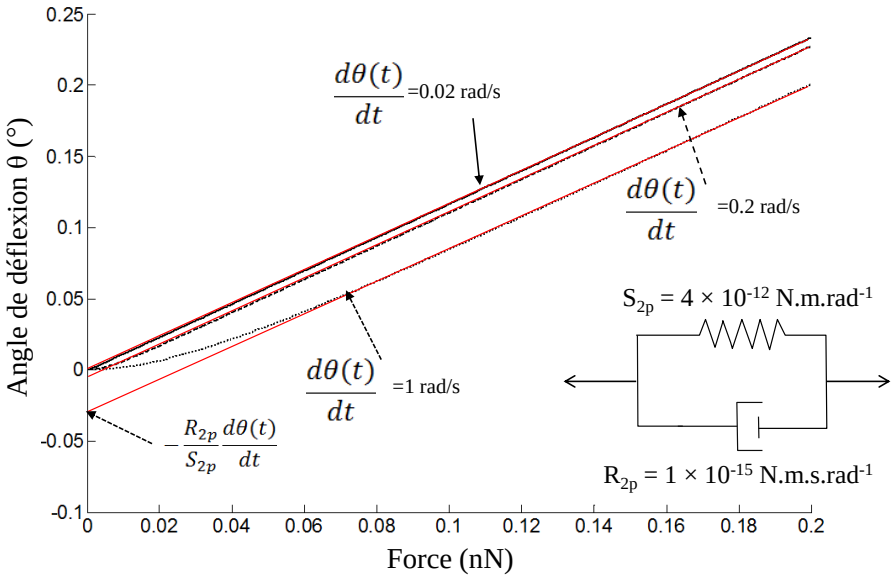

FIGURE 9.8: **Estimation de la variation attendue de l'angle de flexion θ d'un poil filiforme de longueur 1000 μm en fonction de la force F (nN) appliquée par la pointe AFM**, à l'aide du modèle viscoélastique de Kelvin Voigt à deux éléments. Cette courbe déformation/contrainte est tracée pour trois dynamique de déformations correspondant à 3 vitesses de déflexion 0.02 rad/s (trait plein), 0.2 rad/s (trait interrompu) et 1rad/s (trait pointillé).

à deux paramètres ($R_{2p} = 1 \times 10^{-15}$ N.m.s.rad^{-1} et $S_{2p} = 4 \times 10^{-12}$ N.m.rad^{-1}) , (Humphrey *et al.* (1993)). On a représenté sur ce graphe l'angle de déflexion du poil en fonction de la force appliquée sur la pointe de ce dernier. L'équation (9.3) a été résolue numériquement par une méthode de Euler du premier ordre pour obtenir la variation de $\theta(t)$ en fonction de la variation de $T(t)$ (Greendberg M. D. (1988)). En faisant varier la vitesse d'augmentation de la contrainte $\frac{dT(t)}{dt}$, on modifie la vitesse de déflexion $\frac{d\theta(t)}{dt}$ (entre 0.02 rad/s et 1 rad/s) et on constate que l'on ne fait varier que très peu le coefficient directeur de la partie linéaire de la relation entre θ et T qui est égale à $\frac{1}{S_{2p}}$. Cependant ce changement de vitesse de contrainte va modifier l'ordonnée à l'origine de cette relation linéaire, qui n'est autre que $-\frac{R_{2p}}{S_{2p}}\frac{d\theta(t)}{dt}$.

Nous avons également résolu l'équation (9.5), décrivant la réponse d'un système linéaire standard à trois éléments ($R_{3p} = 1.5 \times 10^{-12}$ N.m.s.rad^{-1}, $S_{3p} = 2.9 \times 10^{-11}$ N.m.rad^{-1}et $S'_{3p} = 2.8 \times 10^{-11}$ N.m.rad^{-1}), par la méthode de Euler du premier ordre pour représenter la variation de $\theta(t)$ en fonction de la variation de $T(t)$ et ceci pour diverses dynamiques de déformations (Figure 9.9).

Il apparaît, à la comparaison des figures 9.8 et 9.9, que l'évolution de la relation entre la déformation et la contrainte dépend fortement du type de modèle viscoélastique choisi. Cependant, pour une vitesse de dèflexion donnée, les modèles de Kelvin Voigt et linéaire standard pourront prédire pratiquement la même évolution de l'angle de déflexion en fonction de la contrainte, bien que les valeurs numériques des coefficients de frottement soient très différentes. La figure 9.10 illustre ce phénomène : si l'on fléchit le poil à une vitesse de 0.08 rad/s, on peut estimer que l'angle de déflexion attendu sera exactement le même pour la même force exercée et ceci pour les deux modèles à deux et trois paramètres. Ceci s'explique par le fait que

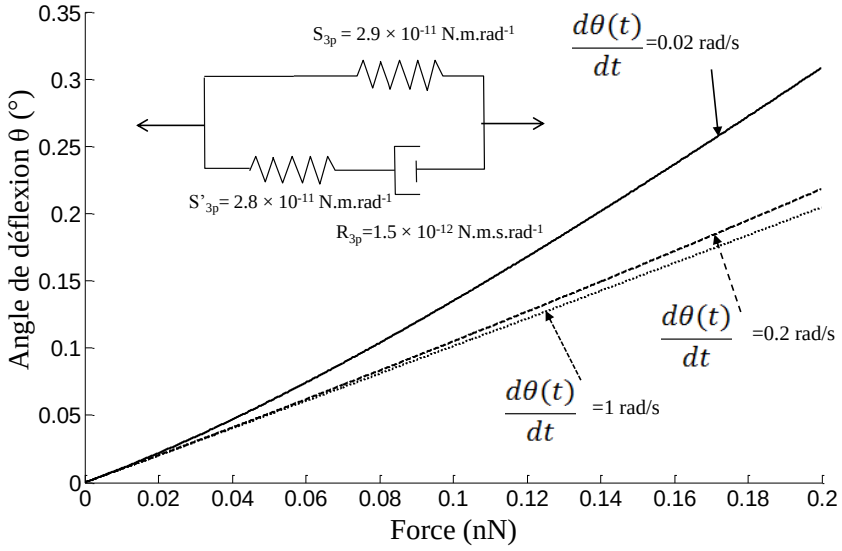

FIGURE 9.9: **Éstimation de la variation de l'angle de flexion θ d'un poil filiforme de longueur 1000 μm en fonction de la force F(nN) appliquée par la pointe AFM**, à l'aide du modèle viscoélastique standard linéaire à trois éléments. Cette courbe déformation/contrainte est tracée pour trois dynamique de déformations correspondant à 3 vitesses de déflexion 0.02 rad/s (trait plein), 0.2 rad/s (trait interrompu) et 1rad/s (trait pointillé).

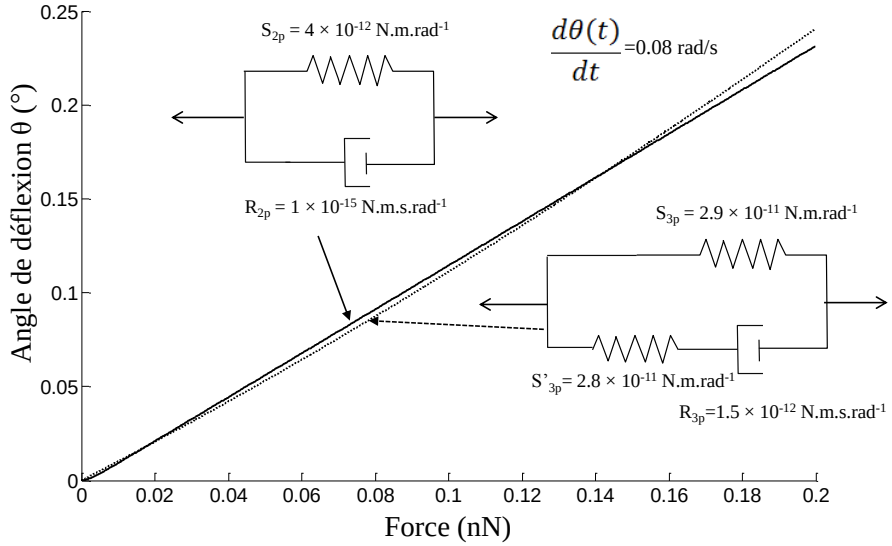

FIGURE 9.10: **Éstimation de la variation de l'angle de flexion θ d'un poil filiforme de longueur 1000 μm en fonction de la force F(nN) appliquée par la pointe AFM,** à l'aide des deux modèles viscoélastiques, celui de Kelvin Voigt (trait plein) et le modèle standard linéaire à trois éléments (trait pointillé). Cette courbe déformation/contrainte est estimée pour une vitesse de déflexion de 0.08 rad/s.

cette suspension est un système dynamique. La seul façon de départager ces deux modèles, qui pourraient s'ajuster aussi bien l'un que l'autre à une mesure de contraintes/déformations AFM, serait donc de répéter cette mesure à diverses dynamiques.

9.3 Les couches limites instationnaires tridimensionnelles

Bien que modélisé depuis de nombreuses années comme des récepteurs placés sur des structures bidimensionnelles dans des flux oscillatoires, le fonctionnement des poils filiformes est en réalité conditionné par la réponse à des écoulements surement beaucoup plus complexes. Nous nous focaliserons dans cette dernière partie sur les méthodes et techniques utilisées pour caractériser théoriquement et expérimentalement ces écoulements. Après avoir décrit une nouvelle méthode de simulation de l'écoulement instationnaire autour d'une structure et l'avoir comparé aux résultats utilisés dans le chapitre 8, nous décrirons les techniques expérimentales qui nous permettront de mesurer ces écoulements instationnaires. Nous détaillerons ensuite nos choix des futures techniques expérimentales envisagées pour mesurer les écoulements tridimensionnels autour de structures sensorielles complexes. Nous conclurons cette discussion sur le rôle primordial de ces aspects tridimensionnels instationnaires sur le fonctionnement de réseau de senseurs, biologiques ou artificiels.

9.3.1 Couches limites transitoires et décomposition de Fourier

Le modèle de Kant et Humphrey (2009) et le nôtre (Chapitre 8) supposent implicitement que le flux transitoire généré par l'approche du prédateur peut être décomposé en une somme de flux oscillatoires. Ces deux modèles supposent ainsi que, la couche limite de cet écoulement transitoire à proximité de la structure qui supporte les poils, peut être décomposée en une série de Fourier de couches limites oscillatoires stationnaires de différentes fréquences. Connaissant les structures des couches limites dans des flux oscillatoires (Holtsmark *et al.* (1954), Humphrey *et al.* (1993), Steinmann *et al.* (2006) (Chapitre 3)), on en déduit alors la couche limite. Cette supposition implicite mérite cependant d'être validée (i) par la résolution numérique des équations de Navier et Stokes incompressibles et (ii) expérimentalement par une mesure du flux transitoire autour d'un cylindre. Dans un soucis didactique, il nous apparaissait plus simple de présenter dans une première partie les profils de vitesse dans les couches limites d'un flux transitoire obtenus par résolution numérique des équations de Navier et Stokes incompressibles par la méthode des éléments finis. Nous présenterons ensuite notre méthode de détermination des profils de vitesse dans les couches limites par décomposition de l'écoulement transitoire en série de Fourier. Dans une troisième partie, nous déterminerons dans un premier temps les différences entre les profils estimés par la résolution numérique et ceux obtenus par la décomposition de Fourier puis nous estimerons, dans un second temps, l'impact de ces différences sur les forces de traînées visqueuses auxquelles sont soumis les poils filiformes. Nous en tirerons des conséquences sur les tailles de poils avant de conclure par la présentation d'une expérience permettant d'estimer ces couches limites transitoires.

Détermination des profils de vitesses dans les couches limites d'un flux transitoire par résolution numérique des équations de Navier et Stokes incompressibles par la méthode des éléments finis

Afin de valider numériquement l'utilisation de la sommation de série de Fourier, nous avons utilisé un solveur commercial de dynamique des fluides computationnelle par éléments finis (COMSOL Multiphysics 3.4) pour déterminer l'évolution des champs de vitesse $\boldsymbol{u} = \begin{bmatrix} u \\ v \end{bmatrix}$ autour d'un cylindre de 1 mm placé transversalement dans un flux transitoire bidimensionnel. Nous avons ainsi résolu numériquement les équations de Navier - Stokes incompressibles 2D autour d'un cylindre immobile dans un fluide (de viscosité cinématique η_{air}=1.56 $\times$ 10^{-5} m^2s^{-1} et de densité ρ_{air}=1.1774 $kg.m^{-3}$). Les équations de continuité et de quantité de mouvement sont, respectivement, les suivantes :

$$\frac{\partial u}{\partial x} + \frac{\partial v}{\partial y} = 0$$

$$\rho \frac{\partial \boldsymbol{u}}{\partial t} + \rho \boldsymbol{u} \nabla . \boldsymbol{u} = \nabla . \left[-p\boldsymbol{I} + \eta \left(\nabla . \boldsymbol{u} + (\nabla . \boldsymbol{u})^{\boldsymbol{T}} \right) \right] \tag{9.7}$$

Nous avons simplifié le problème hydrodynamique à l'étude de l'écoulement transversal autour d'une section du cerque, elle aussi transversale . Nous avons estimé que le flux d'air généré en amont d'une araignée $\mathbf{u}(t)$ qui s'approche de sa proie pouvait être décrit par l'expression de l'évolution temporelle du flux généré devant une sphère de rayon R se déplaçant à une vitesse V_0 (Casas et Steinmann (2014), Chapitre 7). Ce flux a pu être simulé pendant un temps t_{tot} et on peut exprimer $\mathbf{u}(t)$ comme :

$$\begin{aligned} \boldsymbol{u}\,(t) &= \frac{V_0 (R)^3}{\left((t_{tot} - t)\, V_0 + R \right)^3} \\ \boldsymbol{u}\,(t) &= \frac{V_0 (\tau)^3}{\left((t_{tot} - t) + \tau \right)^3} \end{aligned} \tag{9.8}$$

avec le temps caractéristique de l'attaque $\tau = \frac{R}{V_0}$. Ce temps, correspondant au rapport de la taille du prédateur sur sa vitesse, a un rôle important dans la dynamique du flux autour de la proie. Cet écoulement, que l'on peut supposer de manière simplifiée comme purement horizontal, sera utilisé comme première condition de bord sur les frontières du domaine de notre simulation numérique. La seconde condition de bord sera une vitesse nulle à la frontière du cylindre. La surface totale de modélisation de 4×6cm a été maillée à l'aide de 25000 éléments, comme illustré dans la figure 9.11. Le maillage a été réalisé à l'aide d'une procédure de maillage triangulaire adaptif qui consistait à accroître la densité de maille proportionnellement à la complexité de la géométrie. On a ainsi optimisé la densité du maillage dans les zones où l'on s'attendait à avoir les plus grand gradient de vitesse dans l'écoulement. La densité a ainsi été fixée à (i) 20 éléments par cm à la frontière du domaine de modélisation et à (ii) 20 éléments par mm à la frontière du cylindre.

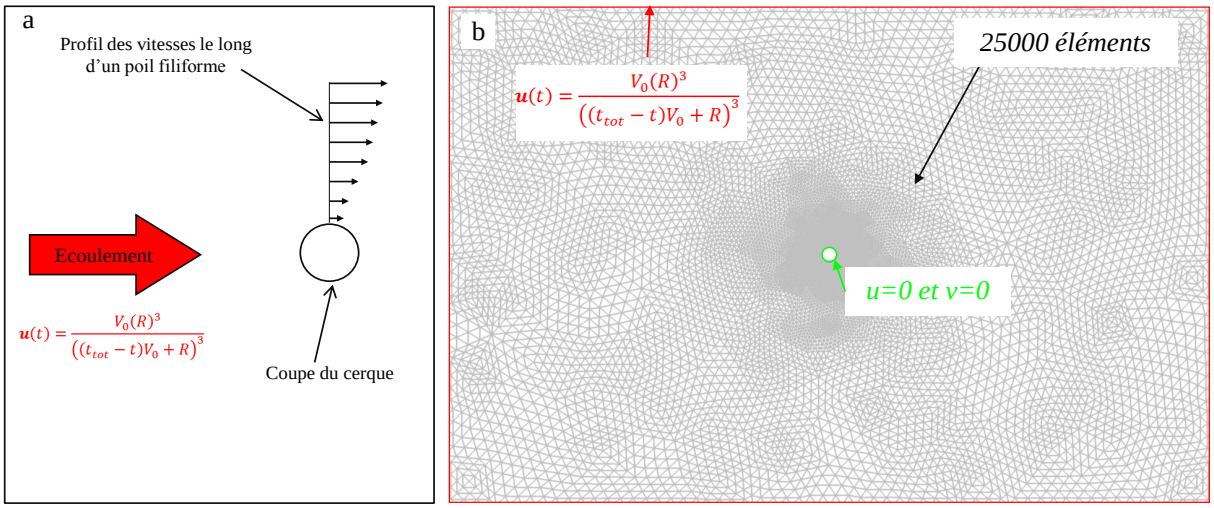

FIGURE 9.11: **Ecoulement, maillage et paramétrage de la résolution numérique par éléments finis des vitesses dans une tranche bidimensionnelle du fluide autour d'un obstacle cylindrique.** (a) Schéma de l'écoulement à résoudre. L'écoulement instationnaire est considéré comme constant spatialement aux bornes du domaine de modélisation et décrit par l'équation 9.8. (b) Le maillage est composé de 25000 éléments triangulaires. Les vitesse sont nulles le long du périmètre circulaire du cylindre.

Nous avons utilisé un solveur transitoire qui résolvait le système linéaire d'équations par généralisation de la Méthode de Minimisation du Résidu (GMRES) et ceci pour des pas de temps de 1 ms entre $t_0 = 0$ et $t_{tot} = 0.5$ ms. La vitesse V_0 et le rayon R de la sphère générant l'écoulement impulsionnel aux frontières du domaine de simulation, et spécifiant les conditions de bord du problème, ont été respectivement fixés à 30 cm/s et 4 mm. La figure 9.12 représente les vitesses horizontales extraites le long d'un profil de 1 cm, perpendiculaire au flux , au dessus du cylindre de diamètre 1 mm pour différents instants. En bleu, à 490 ms, soit 10 ms avant l'instant où la vitesse est maximale, la vitesse de champ lointain adimensionnée est égale à 0.2 m/s. On constate qu'à la fin de la simulation pour $t = t_{tot}$, les conditions de bords spécifient une vitesse maximale égale à V_0.

Les profils de vitesse, le long d'un axe perpendiculaire au cylindre, présentés dans la figure 9.12.b, nous permettent d'estimer les couches limites dans cet écoulement transitoire. On en déduit que les vitesses de l'écoulement seront impactées entre 0 et 3 mm autour du cylindre. La vitesse sera fortement réduite entre 0 et 500 μm, puis elle dépassera la vitesse de l'écoulement entre 500 et 3000 μm. Il semble en outre que l'épaisseur de la couche limite n'évolue pas fortement avec le temps. Nous constatons aussi que la simulation prédit une légère dissymétrie dans l'écoulement entre l'avant et l'arrière du cylindre, cette dissymétrie s'accentuant avec le temps. Nous avons choisi en première approximation d'imposer la même variation de vitesse sur toutes les frontières du domaine de simulation. Cependant nous avons montré que l'écoulement généré par l'arrivée d'un prédateur n'est pas homogène dans l'espace, mais décroit au cube de la distance (Chapitre 6 et 7, Casas *et al.* (2008), Casas et Steinmann (2014)). Une estimation plus

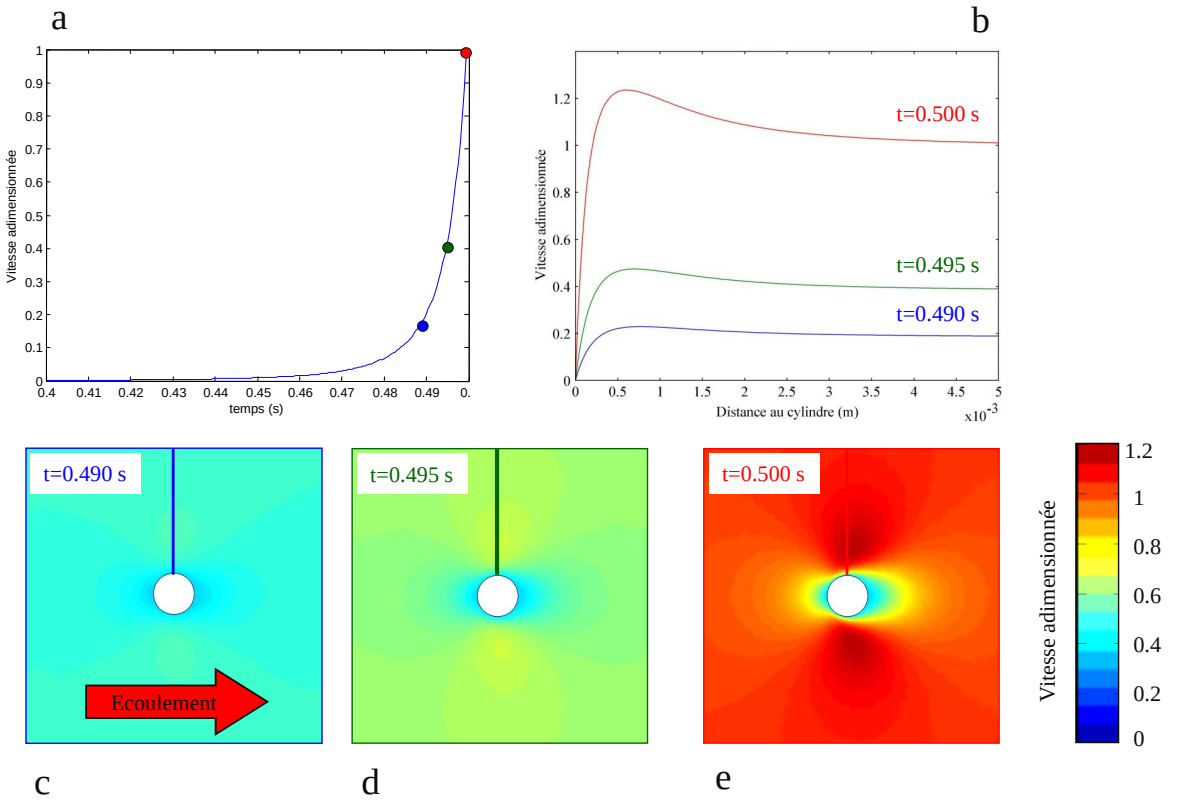

FIGURE 9.12: **Résultats de la détermination, par résolution numérique des équations de Navier & Stokes incompressibles par éléments finis, des vitesses dans une tranche bidimensionnelle de l'écoulement transitoire autour d'un obstacle cylindrique**. (a) Vitesse du fluide à la frontière du domaine de simulation en fonction du temps. Les 3 points, bleu , vert et rouge indiquent les temps auxquels seront tracés les profils de la figure 2.b et les coupes transversales 9.12.c, 9.12.d et 9.12.e. (b) Composante horizontale de la vitesse le long d'un profil spécifié par les lignes bleu, verte et rouge dans les figures 9.12.c, 9.12.d et 9.12.e respectivement. (c, d et e) Composante horizontale de la vitesse dans des coupes transversales de l'écoulement bidimensionnel transitoire autour du cylindre de 1mm, à t=490 ms, 495 ms et 500 ms.

fidèle de l'écoulement instationnaire nécessitera donc de prendre en compte cette divergence spatiale du flux généré par le prédateur.

Dans les résultats de l'écoulement instationnaire représentés sur la figure 9.12, on peut voir se développer, entre t=495 ms et t=500 ms, deux zones de fortes vitesses au dessus et au dessous du cylindre. Dans ces deux zones, le flux semble fortement spatialement accéléré par rapport à la vitesse de champ lointain. Ce phénomène est similaire à celui observé lors de l'interaction d'un écoulement oscillatoire avec un cylindre transversal (Holtsmark *et al.* (1954), Steinmann *et al.* (2006) Chapitre 3). Cette similarité est bien sûr complètement liée au caractère instationnaire de l'écoulement généré lors de l'approche d'un prédateur. C'est en effet le déphasage spatial constitutif aux phénomènes instationnaires qui va se propager dans les couches successives de fluide en s'amortissant exponentiellement. Comme dans le cas d'un flux oscillatoire, l'existence d'une dérivée temporelle de la vitesse dans la dérivée particulaire se traduira localement par des régions d'avancement de phase et des zones de forts gradients de vitesses (Guyon *et al.* (2012)). Ce phénomène, de dépassement local de la vitesse initiale d'un écoulement à proximité de la surface d'un obstacle, est également couramment visualisé lors de l'étude des écoulements stationnaires. Cependant, cet effet est beaucoup plus faible en stationnaire et il est dû à l'augmentation locale de pression, et non pas à l'instationnarité et au déphasage dans le fluide. Pour s'en convaincre, nous avons comparé, dans la figure 9.13, le champ de vitesse simulé dans un flux transitoire avec le champ de vitesses simulé dans un écoulement à vitesse constante $V_0 = 30$ cm/s. On peut constater ainsi, qu'outre la forte augmentation de la dissymétrie de l'écoulement, la simulation d'un écoulement stationnaire ne fait plus apparaître ces deux régions de grande vitesse.

Détermination des profils de vitesses dans les couches limites par décomposition de l'écoulement transitoire en série de Fourier

On suppose ici que la couche limite dans un écoulement transitoire à proximité de la structure qui supporte les poils peut aussi être décomposée en une série de Fourier de couches limites oscillatoires quasi-stationnaires de différentes fréquences. Connaissant les structures des couches limites dans des flux oscillatoires (Holtsmark *et al.* (1954), Humphrey *et al.* (1993), Steinmann *et al.* (2006) Chapitre 3), on en déduit facilement la couche limite totale. Avant de déterminer la forme des couches limites des différentes composantes de la série de Fourier, il convient d' exprimer la variation temporelle de la vitesse de l'écoulement $\mathbf{u}(t)$ comme sa série de Fourier. Comme initialement décrit dans Kant et Humphrey (2009) et dans le chapitre 8, nous pouvons décomposer le flux transitoire $\mathbf{u}(t)$ décrit par l'équation (9.8) en une série de Fourier $\boldsymbol{U}(\omega_m)$ de coefficients complexes de fréquences $\omega_m = 2\pi m \Delta f$, Δf étant le pas fréquentiel de la transformée de Fourier discrète de $\mathbf{u}(t)$. La somme des différentes sinusoïdes harmoniques va nous permettre d'obtenir l'égalité suivante :

$$\boldsymbol{u}(t) = \sum_{m=0}^{\infty} \boldsymbol{U}(\omega_m)\ e^{-i\omega_m t} \tag{9.9}$$

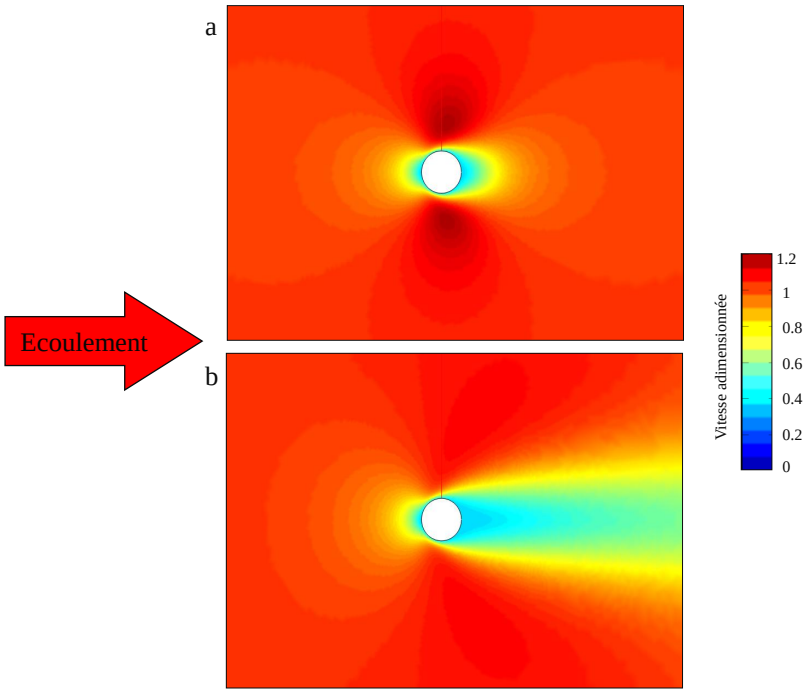

FIGURE 9.13: **Comparaison du champ de vitesses en flux transitoire avec le champ de vitesses en flux continu.** (a) Champ de vitesses autour d'un cylindre à t=0.5 s dans le flux décrit par $\boldsymbol{u}(t) = \frac{V_0(R)^3}{((t_{tot}-t)V_0+R)^3}$ avec $V_0 = 30$ cm/s, $t_{tot} = 0.5$ s et $R = 4$ mm. (b) Champ de vitesses autour d'un cylindre dans un écoulement stationnaire $V_0 = 30$cm/s.

Connaissant analytiquement $\boldsymbol{u}(t)$, on peut déterminer une relation analytique pour $\boldsymbol{U}(\omega_m)$:

$$\boldsymbol{U}(\omega_m) = \int_{-\infty}^{+\infty} \boldsymbol{u}(t)\, e^{-i\omega_m t} dt = \frac{iR\tau^2\pi\omega_m^2}{2} e^{i\omega_m \tau} \tag{9.10}$$

La vitesse $\boldsymbol{u}(t)$ et sa transformée de Fourier $\boldsymbol{U}(\omega_m)$ sont représentées sur la figure 4. La transformée de Fourier $\boldsymbol{U}(\omega_m)$ étant complexe, on peut l'écrire sous la forme :

$$\boldsymbol{U}(\omega_m) = \Re(\boldsymbol{U}(\omega_m)\ ) + i\Im(\boldsymbol{U}(\omega_m)\ ) \tag{9.11}$$

Le flux oscillant perpendiculairement à un cylindre a été décrit théoriquement par Holtsmark *et al.* (1954), Wang (1968), Humphrey *et al.* (1993) et mesuré expérimentalement par Steinmann *et al.* (2006) (Chapitre 3). Nous nous contenterons ici de l'approximation analytique du premier ordre de la solution des équations de Navier et Stokes. Cette approximation correspond à la partie oscillatoire de la solution complète. Nous avons adapté cette solution au cas où un flux oscillatoire harmonique peut être décomposé en deux parties, réelles et imaginaires. Cette décomposition complexe est équivalente à l'introduction d'un déphasage dans le temps décrit par $\phi_m = \text{atan}\left(\frac{\Im(\boldsymbol{U}(\omega_m)\ )}{\Re(\boldsymbol{U}(\omega_m)\ )}\right)$. Si on se focalise sur une seule fréquence, ω_m, on peut déterminer que la composante circonférentielle du flux perpendiculaire au cylindre sera :

$$\begin{aligned} {u_\theta}^m(y,t) = \Re(\boldsymbol{U}(\omega_m)\ ) &\left\{ cos(\omega_m t)\left(1+\left(1+\frac{1}{1+2\frac{y}{d/2}}\right)\right) - cos(\omega_m t-\beta y)\, e^{-}\beta y\left(2-\sqrt{2}\frac{y}{d/2}+\frac{3}{2}\sqrt{2}\left(\frac{y}{d/2}\right)^2\right)\right\} \\ - i\Im(\boldsymbol{U}(\omega_m)\ ) &\left\{ sin(\omega_m t)\left(1+\left(1+\frac{1}{1+2\frac{y}{d/2}}\right)\right) - sin(\omega_m t-\beta y)\, e^{-}\beta y\left(2-\sqrt{2}\frac{y}{d/2}+\frac{3}{2}\sqrt{2}\left(\frac{y}{d/2}\right)^2\right)\right\} \end{aligned} \tag{9.12}$$

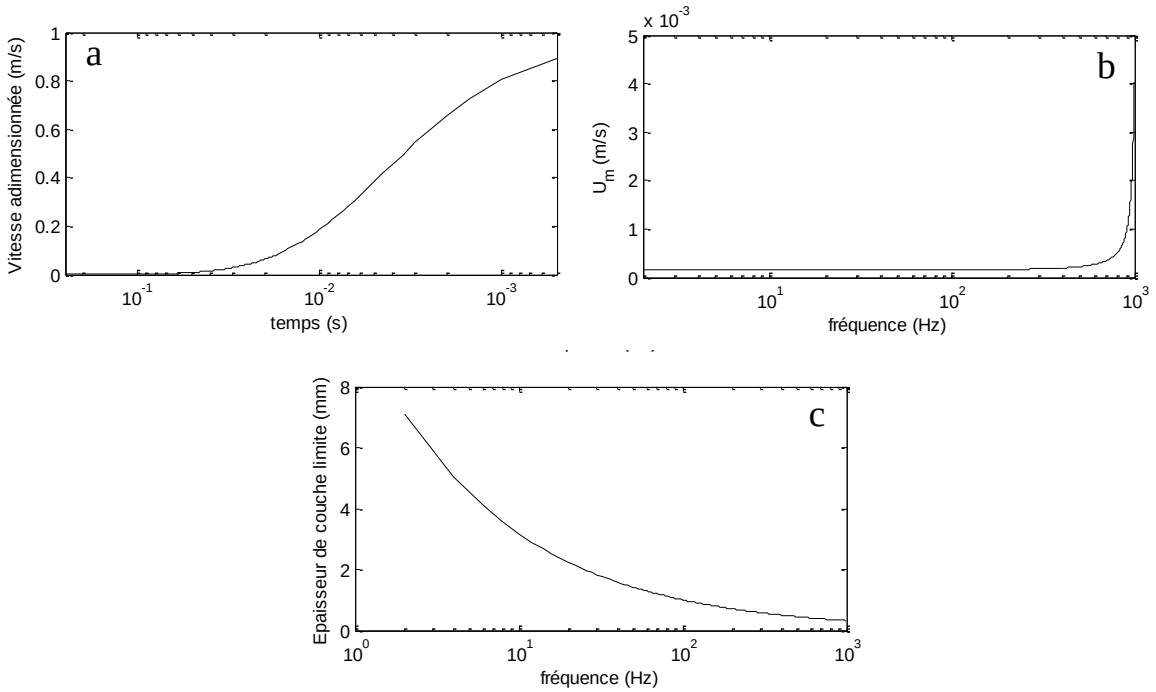

FIGURE 9.14: **Représentations temporelle et spectrale de la variation de la vitesse de l'écoulement très loin du cerque (champ lointain).** (a) Représentation graphique de u(t) comme décrit par l'équation (9.7). (b) Représentation spectrale de u(t), valeur absolue de $\boldsymbol{U}$ (ω_m), la transformée de Fourier de u(t). (c) Variation de l'épaisseur de la couche limite en fonction de la fréquence.

où y est la distance par rapport au cylindre (suivant l'axe perpendiculaire au flux pour simplifier), t est le temps, $\boldsymbol{U}(\omega_m)$ est l'amplitude du flux oscillatoire de champ lointain de fréquence ω_m, d est le diamètre du cylindre, $\beta = \sqrt{\frac{\omega_m}{2\nu}}$ et ν est la viscosité cinématique de l'air. L'équation (9.12) nous indique qu'à chaque fréquence dans le flux correspondra donc une longueur de couche limite donnée par $\delta = 4.5/\beta$. Cette couche limite sera d'une épaisseur de 7 mm pour un flux de 2 Hz, et son épaisseur peut descendre jusqu'à 300 μm pour un flux de 1000 Hz (voir figure 9.14.c). Ces épaisseurs de couches limites, leurs mesures et la comparaison avec la théorie sont décrites dans le chapitre 3 de ce mémoire (Steinmann *et al.* (2006)).

Le profil des vitesses horizontales, dans un axe perpendiculaire au cylindre et au fluide, peut être à présent décrit pour la somme des différentes harmoniques qui compose le flux $\mathbf{u}(t)$, auxquelles on aura affecté leur différentes couches limites. On peut ainsi déterminer la forme et l'évolution de la couche limite $\boldsymbol{u}(y,t)$:

$$\boldsymbol{u}(y,t) = \sum_{m=0}^{\infty} {u_\theta}^m(y,t) \tag{9.13}$$

Comparaison entre la résolution numérique et la décomposition de Fourier

Nous comparerons ici les profils de vitesses perpendiculaires à un cylindre, déterminés par la résolution numérique des équations de Navier & Stokes complètes, avec les profils déterminés par la méthode de décomposition de Fourier. Nous avons pour cela simulé le flux transitoire généré par l'arrivée d'un prédateur de diamètre $D = 8$ mm approchant à une vitesse $V_0 = 30$ cm/s.

Les profils de vitesses estimés autour du cylindre par les deux techniques sont assez similaires, et ceci quel que soit le temps auquel on les compare, comme le montre la figure 9.15. La résolution par série de Fourier semble cependant prédire des couches limites moins épaisses que celles calculées par résolution numérique complète des équations de Navier & Stokes. L'expression de la transformée de Fourier $\boldsymbol{U}(\omega_m)$ donnée par l'équation 9.11 et l'illustration de ses valeurs numériques dans la figure 9.14, nous indiquent que l'on peut décomposer $\mathbf{u}(t)$ en une somme de flux oscillatoires dont les composantes basses fréquences sont assez faibles. On peut estimer que 90 % de l'énergie du flux sera contenue dans la partie du spectre située entre 100 et 1000 Hz. Les couches limites dans des flux oscillatoires de 100 Hz à 1000 Hz auront une épaisseur comprise entre 300 μm et 1 mm. A l'inverse, on peut estimer l'épaisseur de la couche limite déterminée par la résolution numérique des équations de Navier & Stokes, celle ci s'élève à 400 μm.

Pour savoir comment ces différences de vitesses vont impacter différemment des poils placés sur ces cylindres, il faut déterminer les forces qui agissent sur un objet placé dans ces couches limites. Nous pouvons, à titre de comparaison, déterminer les moments de trainée $T(t)$ que subirait un poil dans ces couches limites. Ce moment, qui est l'intégrale de la force de trainée $F_D(t)$ le long du poil est décrit par l'expression suivante (Kant et Humphrey (2009)) :

$$T(t) = \int_0^L F_D(t) y dy = \int_0^L \frac{\pi\mu\ \boldsymbol{u}(y,t)}{2} y dy \tag{9.14}$$

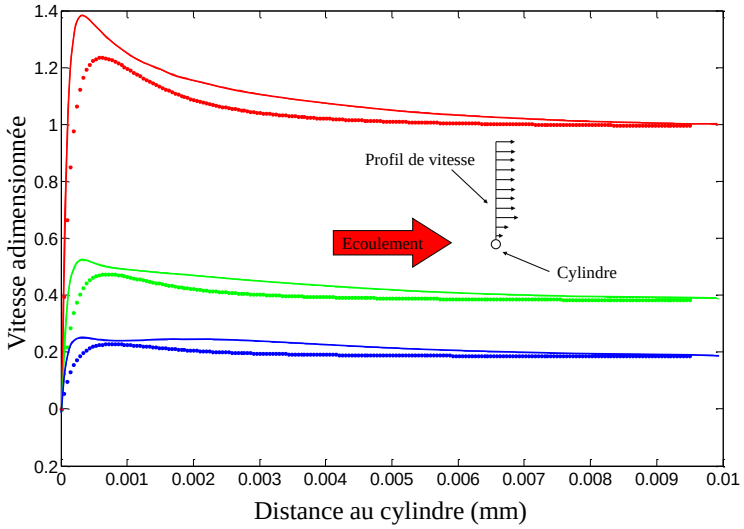

FIGURE 9.15: **Comparaison des composantes horizontales de la vitesse adimensionnée le long d'un profil long de 10 mm au dessus du cylindre et transversal au flux.** Les lignes correspondent à la décomposition en série de Fourier et les points représentent la résolution des équations de Navier & Stokes par éléments finis pour un flux transitoire. La couleur rouge représente les résultats à t=500 ms, en vert t=495 ms et en bleu t=490 ms.

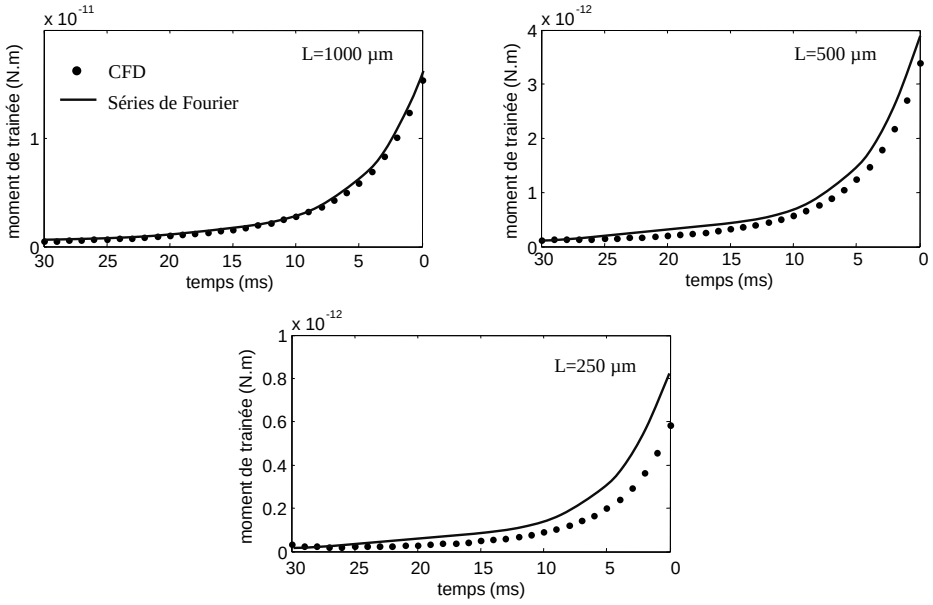

FIGURE 9.16: **Comparaison des moments de traînée**, calculés d'après les vitesses extraites des simulations numériques (les points / CFD) avec les moments calculés à l'aide des vitesses déterminées par série de Fourier (ligne / Fourier series), et ceci pour des longueurs de poils de 250 μm à 1000 μm.

où L est la longueur du poil et μ est la viscosité dynamique.

On constate sur la figure 9.16 que la grande différence des profils de vitesses dans les couches limites issus des résolutions numériques d'une part, et de l'approximation en série de Fourier

d'autre part ne se traduit pas forcément par une grande différence de l'intégrale des forces hydrodynamiques agissant sur les poils. Ainsi l'estimation de l'évolution temporelle de la force agissant sur un long poil de 1000 μm est la même avec les deux méthodes. On note cependant qu'elle peut être suréstimée par la décomposition de Fourier pour des petits poils, ceci étant dû au fait que les vitesses, dans les 500 premiers μm de l'écoulement, sont un peu suréstimées par la décomposition de Fourier.

Conclusions sur les couches limites instationnaires et les tailles des poils

La sommation de couches limites oscillatoires, qui est la supposition implicite de la méthode de Fourier, peut donc être validée si le but ultime est la modélisation du mouvement d'un poil. Nous aurions pourtant tendance à avoir une plus grande confiance dans la résolution complète des équations de Navier & Stokes incompressibles, cette méthode n'étant pas basée sur des suppositions implicites. Nous estimons ainsi que la résolution complète de l'écoulement est plus fidèle à la réalité. Cependant, ces deux méthodes nous permettent d'estimer l'épaisseur de ces couches limites comme étant similaires. Pour le cas particulier d'un flux transitoire provoqué par l'approche d'un prédateur à 30 cm/s, elle est de l'ordre de 400 μm, longueur assez proche de la taille des poils. Il a déjà été montré que ces poils filiformes étaient suffisamment longs pour atteindre l'extérieure des couches limites typiques des flux oscillatoires (Shimozawa et Kanou (1984b)). C'est ce qui leur assure une meilleure capacité à saisir le flux tout en restant assez courts et légers pour être capables de fléchir rapidement. La réalité biologique de ces fréquences typiques des écoulements oscillatoires n'a cependant jamais été vraiment justifiée. Ainsi, notre étude sur l'épaisseur des couches limites générées dans des écoulements instationnaires, dont la composition fréquentielle complexe est basée sur les mesures effectuées sur les prédateurs de ces grillons, nous a permis d'estimer l'adéquation entre longueur de poils et épaisseur de couche limite. L'étude plus systématique de la déflexion totale de ces poils dans les flux instationnaires, exposée dans le chapitre 8, nous a permis d'émettre des conclusions sur les tailles optimales des poils. Ces résultats, sur la longueur des récepteurs qui pourraient optimiser la capacité a détecter des changements dans des couches limites instationnaires, sont assez similaires aux conclusions avancées par Dickinson (2010). Cet auteur estime en effet que les tailles des poils présents sur les ailes des chauves-souris étaient aussi optimales compte tenu de l'épaisseur de la couche limite dans laquelle ils évoluent. Plus récemment, Dickinson *et al.* (2012) ont aussi modélisé les écoulements instationnaires autour d'une structure en mouvement non constant dans un fluide en résolvant les équations de Navier et Stokes. Ils ont ainsi déterminé les couches limites autour d'un demi cylindre représentant une aile de chauve souris lors d'une décélération. Ce cylindre avait un diamètre de 10 cm et l'écoulement maximal a été fixé à 8 cm/s, de tel sorte que le nombre de Reynolds de l'écoulement s'élevait à 500. Ces auteurs ont mis en valeur l'existence de zones de recirculation dans l'écoulement en aval du cylindre. Dans notre étude, l'écoulement était laminaire, le nombre de Reynolds décrivant le rapport entre les forces d'inertie et les forces visqueuses dans le fluide étant égal à 19. Des zones de recirculation n'ont pas été détectées jusqu'à ce jour et il ne semble pas que les poils filiformes des grillons soient soumis à de telles contraintes de cisaillement.

Perspectives : mesures PIV dans les écoulements transitoires autour de structures

Nous aboutissons, in fine, à de faibles différences concernant les forces de frottements hydrodynamiques sur les poils en utilisant l'une ou l'autre des méthodes de calculs de la couche limite. Il conviendrait cependant de valider entièrement la forme de cette couche limite instationnaire de manière expérimentale. Cette validation expérimentale de la forme de couches limites autour de cylindres ou toute autre structure en flux transitoire semble donc être la prochaine étape pour entièrement valider la simplification numérique de la sommation de série de Fourier. Il nous tient ainsi à cœur de développer prochainement un setup expérimental de mesures de vitesses par imagerie de particules (PIV) bidimensionnelle afin de déterminer la structure des écoulements transitoires. Cet écoulement pourra être généré par un piston/actionneur sur lequel nous fixerons des sphères de diamètre ajustable. L'utilisation d'un piston/actionneur programmable nous permettra de contrôler le mouvement de translation des sphères suivant l'axe horizontal à vitesse constante, afin de générer des changements de vitesses aux bornes du domaine de mesure proches de celles choisies pour la résolution numérique. Il semble cependant impossible de pouvoir imposer, sur toutes les frontières du domaine de mesure, les mêmes conditions de bords que celles spécifiées dans l'analyse numérique et la méthode de décomposition de Fourier présentée, la vitesse ne pouvant physiquement pas être constante le long des bords du champ de mesure. Une alternative pourrait être de déplacer le cylindre à la vitesse variable décrite par l'équation de u(t), ou comme proposé précédemment, prendre en compte cette divergence spatiale du flux généré par le prédateur dans le modèle numérique. Ces mesures permettraient bien sûr de valider les hypothèses simplificatrices de nos modèles de déflexion des poils filiformes des grillons. Mais comme on l'a vu dans le paragraphe précédent, les couches limites en flux instationnaires sont des phénomènes courants qui conditionnent le fonctionnement de nombreux réseaux de senseurs d'écoulement, de la ligne latérale des poissons (McHenry *et al.* (2008)), jusqu'aux matrices de poils sur les ailes de chauves souris (Sterbing-D'Angelo *et al.* (2011)). Le développement de ces mesures dans des flux transitoires trouverait des applications dans divers domaines de l'écologie sensorielle.

9.3.2 Vers la compréhension de la structure tridimensionnelle du flux autour de structures sensorielles complexes

Il apparaît, à la lumière des différents travaux effectués sur le fonctionnement des senseurs biomécaniques que les forces de viscosités du fluide sont souvent prédominantes sur celles de l'inertie, à l'échelle des insectes. Un mécanisme de localisation d'une source de modification de l'environnement (fluide ou air) sera donc complètement dépendant des effets visqueux, présents à ces petites échelles. La réponse biomécanique d'un senseur dépend, certes de ses caractéristiques intrinsèques, mais aussi fortement de la géométrie de son support qui va modifier, par sa simple existence, la quantité d'informations disponibles, et ceci de manière non linéaire avec la fréquence. Le positionnement de senseurs (soies filiformes, senseurs de pression tympanaux) sur toute la surface d'un corps ou d'un appendice peut permettre à un animal de tirer profit de la forte hétérogénéité spatiale des informations contenues dans le flux tridimensionnel autour de son corps (Steinmann *et al.* (2006), Dangles *et al.* (2008), Morley *et al.* (2012)).

Mesures préliminaires bidimensionnelles

Nous avons précédemment déterminé dans un plan bidimensionnel que l'orientation d'un flux oscillatoire différait fortement à la surface d'un cerque de son orientation initiale dans le champ lointain (Steinmann et Casas (2014) Chapitre 2). Plus spécifiquement, nous avons déterminé que la direction du flux est perturbée dans le sens anti-horaire sur le cerque gauche et dans le sens horaire sur le cerque droit, c'est à dire de façon opposée sur les deux appendices. Les conséquences sur la capacité d'un animal à déterminer la provenance d'un prédateur sont donc grandes, étant donné que ces deux effets peuvent s'annuler l'un l'autre ou s'amplifier selon le codage neuronal. Nous avons aussi observé que l'amplitude des flux était substantiellement plus réduite à proximité de l'abdomen du grillon qu'au bout des cerques, l'énergie disponible pour les poils étant ainsi comparativement réduite pour les poils situés à la base du cerque. Cet effet a cependant été considéré comme étant négligeable dans la partie 9.1 de la discussion, qui traitait de l'influence de la position du cerque sur la sensibilité des poils.

Les techniques expérimentales de vélocimétrie, utilisées jusqu'alors pour mettre en valeur ces effets, ont été purement bidimensionnelles, tandis que les cerques, supports des poils, et les flux d'airs émis par les prédateur ont bien souvent des géométries tridimensionnelles. La perspective de caractériser entièrement et localement un écoulement tridimensionnel à proximité d'un support de senseurs nous a contraint à développer des techniques innovantes de stereo-PIV et tomo-PIV.

La PIV tomographique autour d'objets tridimensionnels

En 2009, Scarano et Poelma (2009) ont prouvé la faisabilité de la mesure du flux tridimensionnel autour d'un cylindre à l'aide de la PIV tomographique. Cette technique, basée sur le principe de la reconstruction tomographique, permet la mesure instantanée des trois composantes de la vitesse dans un volume de mesure, ce volume étant illuminé à l'aide d'une optique volumique laser. Le champ tridimensionnel d'intensité lumineuse des particules éclairées, est réalisé lors d'une étape de reconstruction tomographique (Elsinga *et al.* (2006)). En utilisant la projection du volume, éclairé sur 4 plans images de 4 caméras disposées autour du champ de mesure, l'expérimentateur peut reconstituer la position des particules dans le volume illuminé autour de l'objet qui va perturber le flux, comme représenté dans la figure 9.17. Le point le plus délicat de cette mesure concerne le positionnement des caméras autour de l'objet tridimensionnel. La présence de cet objet va en effet obstruer le champ de vision des caméras de manière différente suivant leur point de vue, ne laissant subsister qu'une petite zone du volume de particules proche de l'objet reconstituable, comme illustré dans la figure 9.17.c. La configuration de placement des caméras, que ce soit sur un seul plan, en cercle, ou encore en opposition, aura elle aussi un impact important sur la qualité de la reconstruction tomographique (Thomas *et al.* (2014)). Les vecteurs vitesses dans le volume sont ensuite calculés par une technique itérative de corrélation croisée tridimensionnelle en utilisant les volumes d'interrogation (Scarano (2013)).

Il faudra être cependant capable d'augmenter ce volume de fluide reconstitué pour déterminer l'interaction entre structure et fluide tout autour du cerque. Pour ce faire, on peut envisager de changer l'orientation du flux, en plaçant le haut parleur qui générera un flux oscillatoire sur un

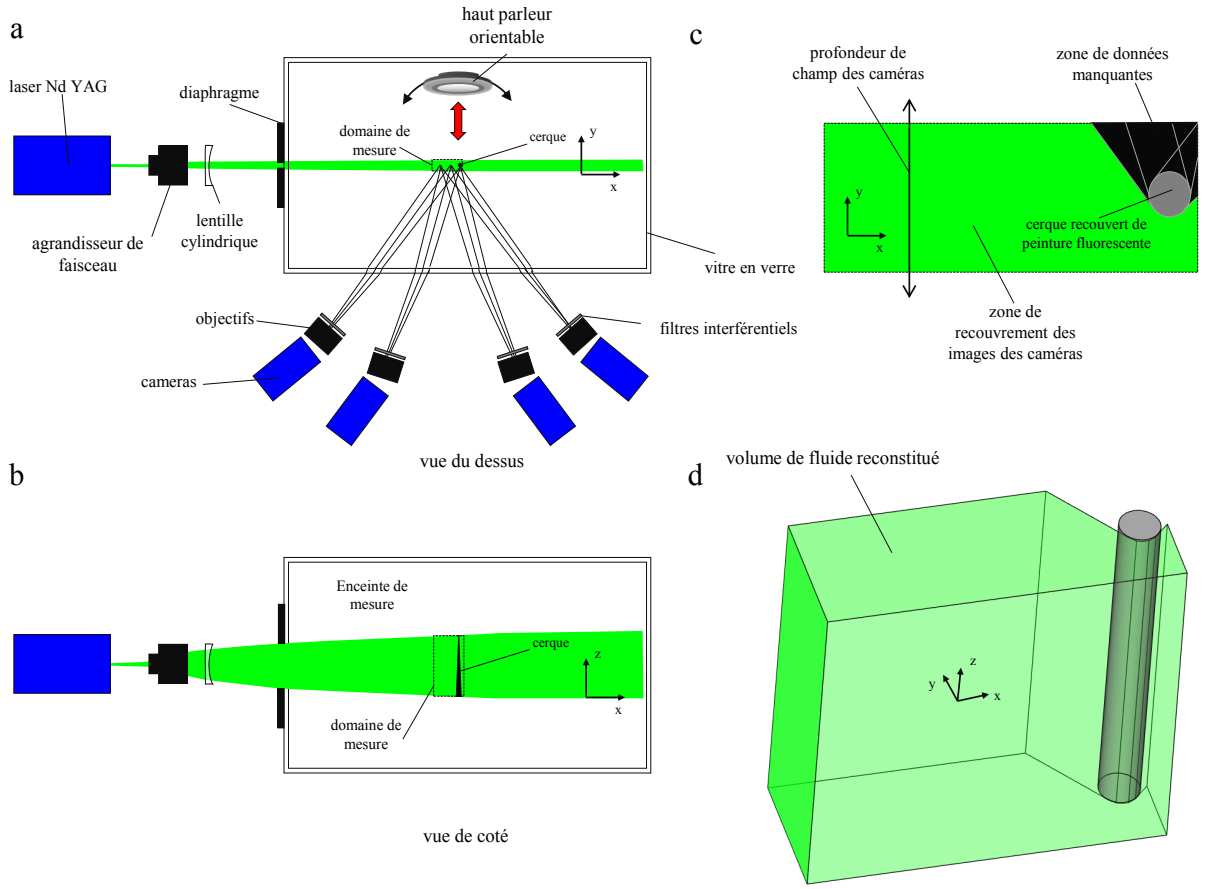

FIGURE 9.17: **Schéma conceptuel du setup expérimental de mesure par PIV tomographique des champs de vitesse dans un volume tridimensionnel autour d'un cylindre placé dans un flux oscillatoire.** (a) & (b) Un faisceau laser produit par un laser impulsionnel sera élargi par une optique d'agrandissement couplée à une lentille cylindrique réduisant la divergence des rayons lumineux. Le voulme de lumière laser ainsi créé passera ensuite par un diaphragme qui permettra de se débarasser des régions de faibles intensité lumineuse et d'assurer une délimitation franche et précise entre les volumes de fluide éclairé et sombre. Le volume éclairé sera ensuite projeté sur l'objet autour duquel l'écoulement doit être décrit. Quatre caméras, placées en dehors de l'enceinte de mesures, seront focalisées à l'aide d'objectifs macroscopiques sur ce domaine de mesure. Ces caméras seront dotées d'une monture permettant de régler indépendamment les angles des plans de la caméra (et de son capteur CMOS) et de l'objectif. Ceci permettra de régler la convergence des plans objet, lentille et images et de respecter la condition de Scheimpflug, nous assurant la netteté des particules imagées sur toute la longueur de l'image. (c) & (d) En ajustant la profondeur de champs des caméras de façon à être légèrement supérieur à la profondeur du domaine de mesure on s'assurera que toutes les particules illuminées seront nettes sur toutes les caméras. La présence d'un objet dans le volume à filmer générera des potentiels reflets. De plus la projection de cet objet sera différente sur les différentes caméras, et plus l'angle entre la première caméra (de droite) et la quatrième caméra (de gauche) sera grand plus la zone de recouvrement des images sera petite et le volume de fluide reconstitué réduit.

support muni d'un axe de rotation en z. Alternativement, il serait aussi envisageable d'utiliser un système de génération de flux, similaire à celui utilisé initialement par Mulder-Rosi *et al.* (2010). Afin de diminuer les réflexions parasites du laser sur la structure, il devrait être possible de recouvrir cette dernière avec une peinture fluorescente ayant la particularité d'absorber les photons à la longueur d'onde du laser ($\lambda = 532\ nm$) et de renvoyer la lumière à une longueur d'onde bien supérieure ($\lambda = 650\ nm$). Cette lumière réfléchie pourra ensuite être filtrée par l'intermédiaire de filtres interférentiels placés sur les objectifs des caméras.

9.3.3 Les réseaux de senseurs dans les couches limites instationnaires tridimenionnelles

Dans un autre contexte, celui du vol, et à une toute autre échelle à laquelle l'inertie dans le fluide domine les effets visqueux, Sterbing-D'Angelo et al. (Sterbing-D'Angelo *et al.* (2011) et Sterbing-D'Angelo *et al.* (2016)) ont montré que les poils filiformes situés sur les ailes de chauve souris leur permettaient de déterminer les écoulements. Ces auteurs ont prouvé que la perception des écoulements dans les couches limites le long des ailes était utile la la manœuvrabilité de l'animal. Dickinson *et al.* (2012) ont aussi montré que la juste représentation spatiale des motifs spatiotemporels des flux à la surface de cette aile (modélisée par un demi cylindre dans leur étude computationnelle) était primordiale pour comprendre les forces agissant sur ces poils. Ils ont aussi déterminé, que de par leur répartition homogène sur toute la surface de l'aile, ces poils pouvaient aider à la détection des zones de très fort cisaillement et de détachements de couches limites, caractéristiques de la présence de tourbillons de bout d'aile (LEV) (Phillips *et al.* (2015)). Un autre exemple de l'utilité d'un placement tridimensionnel des senseurs de flux concerne cette fois ci l'écologie de la fuite des poissons. Stewart *et al.* (2014) expliquent la réaction de fuite très rapide des larves de zebrafish lors d'une attaque de prédateur, par leur capacité à sentir une différence d'écoulement entre les deux cotés de leur corps. L'écoulement "de proue", généré en amont du prédateur, va soumettre l'un des côtés de la larve à des vitesses plus élevées. Après avoir été capté par les neuromastes de la ligne latérale du poisson, ce flux va déclencher la contraction des muscles sur le coté opposé du corps et diriger la fuite dans le sens opposé à l'arrivé du prédateur. Plus récemment, Axtmann *et al.* (2016)) ont aussi quantifié les éléments qui conditionnaient le fonctionnement d'un réseau de mécano-senseurs biomimétiques dans une couche limite. Ainsi la problématique du placement de réseau de senseurs à la surface tridimensionnelle d'une structure dépasse grandement le cadre de l'étude du grillon et trouve un vaste champs d'applications, depuis la biomécanique du maintien du vol instationnaire jusqu'à la conception des senseurs biomimétiques du futur. Les applications potentielles de ces senseurs biomimétiques sont déjà très nombreuses (Krijnen *et al.* (2006), Brücker *et al.* (2005) et Brücker et Rist (2014)). La mesure PIV des écoulements complexes proche de ces structures supportrices et la quantification des informations disponibles autour des senseurs sont essentielles à la compréhension du rôle fonctionnel de ces réseaux. Notre compréhension du fonctionnement et du couplage des senseurs biomimétiques nous a déjà permis de proposer un modèle linéaire de couplage visqueux, applicable à de larges réseaux de dizaines de poils mais restreint à deux dimensions. Ce modèle permettra de définir des critères d'optimisation des caractéristiques

d'implantations et de tailles des senseurs biomimétiques, par la mise en valeur d'espacements et de tailles optimaux, pour tirer profit du couplage aérodynamique visqueux positif existant entre senseurs biomimétiques. La caractérisation précise de la structure des écoulements instationnaires tridimensionnels pourrait en plus nous donner des lignes directrices pour le design et la fabrication de senseurs biomimétiques tridimensionnels. Un arrangement spatial adéquat de poils sensoriels biomimétiques sur un support tridimensionnel, mimant la morphologie du cerque de grillon, augmenterait par exemple considérablement la capacité d'un tel réseau de senseurs à déterminer la provenance et la directionnalité d'une perturbation (Krijnen *et al.* (2007)).

Bibliographie

Axtmann, G., Hegner, F., Brücker, C. et Rist, U. (2016). Investigation and prediction of the bending of single and tandem pillars in a laminar cross flow. *Journal of Fluids and Structures*, 66:110–126. 194

Barth, F. G. et Höller, A. (1999). Dynamics of arthropod filiform hairs. V. The response of spider trichobothria to natural stimuli. *Philosophical Transactions of the Royal Society B*, 354(1380):183–192. 174

Barth, F. G., Németh, S. S. et Friedrich, O. C. (2004). Arthropod touch reception : structure and mechanics of the basal part of a spider tactile hair. *Journal of Comparative Physiology, A.*, 190:523–530. 175

Barth, F. G., Wastl, U., Humphrey, J. A. C., Devarakonda, R., Trans, P. et Lond, R. S. (1993). Dynamics of arthropod filiform hairs . II . Mechanical properties of spider trichobothria (Cupiennius salei Keys .). *Philosophical Transactions of the Royal Society B : Biological Sciences*, 340:445–461. 29

Bathellier, B., Steinmann, T., Barth, F. G. et Casas, J. (2012). Air motion sensing hairs of arthropods detect high frequencies at near-maximal mechanical efficiency. *Journal of the Royal Society, Interface*, 9(71):1131–43. 18, 174

Bennet-clarck, H. C. (1984). A particle velocity microphone for the song of small insects and other acoustic measurements. *Journal of Experimental Biology*, 463:459–463. 26

Bleckmann, H., Borchardt, M. et Horn, P. (1994). Stimulus discrimination and wave source localization in fishing spiders (Dolomedes triton and D. okefinokensis). *Journal of Comparative Physiology, A.*, 174:305–316. 15

Bleckmann, H., Breithaupt, T., Blickhan, R. et Tautz, J. (1991). The time course and frequency content of hydrodynamic events caused by moving fish, frogs, and crustaceans. *Journal of Comparative Physiology, A.*, 168(6):749–57. 24

Bleckmann, H., Mogdans, J. et Coombs, S. L. (2014). *Flow sensing in air and water : Behavioral, neural and engineering principles of operation*. Springer Berlin Heidelberg. 15

Bleckmann, H. et Zelick, R. (2009). Lateral line system of fish. *Integrative Zoology*, 4:13–25. 15

Blickhan, R., Krick, C., Zehren, D. et Nachtigall, W. (1992). Generation of a vortex chain in the wake of a subundulatory swimmer. *Naturwissenschaften*, 221:220–221. 22

Bomphrey, R. J., Henningsson, P., Michaelis, D. et Hollis, D. (2012). Tomographic particle image velocimetry of desert locust wakes : instantaneous volumes combine to reveal hidden vortex elements and rapid wake deformation. *Journal of the Royal Society, Interface*, 9:3378–3386. 22, 23

Bomphrey, R. J., Lawson, N. J., Harding, N. J., Taylor, G. K. et Thomas, A. L. R. (2005). The aerodynamics of Manduca sexta : Digital particle image velocimetry analysis of the leading-edge vortex of the leading-edge vortex. *Journal of Experimental Biology*, 208:1079–1094. 22

Boyan, G. S., Ashman, S., Ball, E. E. et City, C. (1986). Initiation and modulation of flight by a single giant interneuron in the cercal system of the locust. *Naturwissenschaften*, 423:272–274. 15

Brücker, C. et Rist, U. (2014). Complex flow detection by fast processing of sensory hair arrays. *In* Bleckmann, H., Mogdans, J. et Coombs, S. L., éditeurs : *Flow Sensing in Hair and Water*, pages 489–498. Springer Berlin Heidelberg. 194

Brücker, C., Spatz, J. et Schröder, W. (2005). Feasability study of wall shear stress imaging using microstructured surfaces with flexible micropillars. *Experiments in Fluids*, 39(2):464–474. 194

Casas, J., Bacher, S., Tautz, J., Meyhöfer, R. et Pierre, D. (1998). Leaf vibrations and air movements in a leafminerparasitoid system. *Biological Control*, 11(2):147–153. 27

Casas, J. et Steinmann, T. (2014). Predator-induced flow disturbances alert prey, from the onset of an attack. *Proceedings of the Royal Society B*, 281(July):20141083–20141083. 163, 182, 183

Casas, J., Steinmann, T. et Dangles, O. (2008). The aerodynamic signature of running spiders. *PloS One*, 3(5):e2116. 110, 183

Catton, K. B., Webster, D. R., Brown, J. et Yen, J. (2007). Quantitative analysis of tethered and free-swimming copepodid flow fields. *Journal of Experimental Biology*, 210(Pt 2):299–310. 24, 25

Chagnaud, B. P., Bleckmann, H. et Engelmann, J. (2006). Neural responses of goldfish lateral line afferents to vortex motions. *Journal of Experimental Biology*, 209(Pt 2):327–42. 24

Dangles, O. et Casas, J. (2010). Physical ecology of fluid flow sensing in arthropods. *Annual review of entomology*, 55:505–525. 19, 20

Dangles, O., Casas, J. et Coolen, I. (2006a). Textbook cricket goes to the field : the ecological scene of the neuroethological play. *Journal of Experimental Biology*, 209(Pt 3):393–8. 19, 20

Dangles, O., Ory, N., Steinmann, T., Christides, J.-P. et Casas, J. (2006b). Spider's attack versus cricket's escape : velocity modes determine success. *Animal Behaviour*, 72(3):603–610. 20, 110, 163

Dangles, O., Pierre, D., Magal, C., Vannier, F. et Casas, J. (2006c). Ontogeny of air-motion sensing in cricket. *Journal of Experimental Biology*, 209(Pt 21):4363–70. 19, 163

Dangles, O., Steinmann, T., Pierre, D., Vannier, F. et Casas, J. (2008). Relative contributions of organ shape and receptor arrangement to the design of cricket's cercal system. *Journal of Comparative Physiology, A.*, 194(7):653–63. 16, 163, 191

Denissenko, P., Lukaschuk, S. et Breithaupt, T. (2007). The flow generated by an active olfactory system of the red swamp crayfish. *Journal of Experimental Biology*, 210(Pt 23):4083–91. 24, 25

Desutter-Grandcolas, L., Blanchet, E., Robillard, T., Magal, C., Vannier, F. et Dangles, O. (2010). Evolution of the cercal sensory system in a tropical cricket clade (Orthoptera : Grylloidea : Eneopterinae) : A phylogenetic approach. *Biological Journal of the Linnean Society*, 99(3):614–631. 16

Dickinson, B. T. (2010). Hair receptor sensitivity to changes in laminar boundary layer shape. *Bioinspiration & biomimetics*, 5(1):16002. 190

Dickinson, B. T., Singler, J. R. et Batten, B. A. (2012). Mathematical modeling and simulation of biologically inspired hair receptor arrays in laminar unsteady flow separation. *Journal of Fluids and Structures*, 29:1–17. 190, 194

Dickinson, M. H., Lehmann, F.-o. et Sane, S. P. (1999). Wing rotation and the aerodynamic basis of insect flight. *Nature*, 284:1954–1960. 22

Droogendijk, H., Casas, J., Steinmann, T. et Krijnen, G. J. M. (2014). Performance assessment of bio-inspired systems : fl ow sensing MEMS hairs. *Bioinspiration & Biomimetics*, 10(1):16001. 163

Drucker, E. G. et Lauder, G. V. (1999). Locomotor forces on a swimming fish : three-dimensional vortex wake dynamics quantified using digital particle image velocimetry. *Journal of Experimental Biology*, 202:2393–2412. 22, 23

Dupuy, F. (2009). La perception des mouvements d'air par le système cercal chez le grillon des bois Nemobius sylvestris. 16

Dupuy, F., Casas, J., Body, M. et Lazzari, C. R. (2011). Danger detection and escape behaviour in wood crickets. *Journal of insect physiology*, 57(7):865–71. 16, 163

Dupuy, F., Steinmann, T., Pierre, D., Christidès, J.-P., Cummins, G., Lazzari, C., Miller, J. et Casas, J. (2012). Responses of cricket cercal interneurons to realistic naturalistic stimuli in the field. *Journal of Experimental Biology*, 215(Pt 14):2382–9. 163, 174

Edwards, J. S. et Palka, J. (1974). The cerci and abdominal giant fibres of the house cricket , Acheta domesticus . I . anatomy and physiology of normal adults. *Proceedings of the Royal Society B : Biological Sciences*, 185:83–103. 16

Ellington C. P., van den Berg C., P., W. A. et R., T. A. L. (1996). Leading-edge vortices in insect flight. *Nature*, 384:626–630. 22, 23

Elsinga, G., Scarano, F., Wieneke, B. et Oudheusden, B. (2006). Tomographic particle image velocimetry. *Experiments in Fluids*, 41:933–947. 192

Engelmann, J., Hanke, W. et Bleckmann, H. (2002). Lateral line reception in still- and running water. *Journal of Comparative Physiology, A.*, 188(7):513–26. 24

Fletcher, N. H. (1978). Acoustical response of hair receptors in insects. *Journal of Comparative Physiology, A.*, 127:185–189. 18

Fraser, P. J. (1977). Cercal ablation modifies tethered flight behaviour of cockroach. *Nature*, 268:523–524. 16

Gnatzy, W. et Kämper, G. (1990). Digger wasp against crickets . II . An airborne signal produced by a running predator. *Journal of Comparative Physiology, A.*, 167:551–556. 27, 29

Gnatzy, W. et Tautz, J. (1980). Ultrastructure and mechanical properties of an insect mechanoreceptor : stimulus-transmitting structures and sensory apparatus of the cercal filiform hairs of Gryllus. *Cell Tissue Research*, 463:441–463. 16, 17

Göpfert, M. C., Briegel, H. et Robert, D. (1999). Mosquito hearing : sound-induced antennal vibrations in male and female aedes aegypti. *Journal of Experimental Biology*, 202:2727–2738. 27

Göpfert, M. C. et Robert, D. (2002). The mechanical basis of Drosophila audition. *Journal of Experimental Biology*, 205(Pt 9):1199–208. 27

Gras, H. et Hörner, M. (1992). Wind-evoked escape running of the cricket. *Journal of Experimental Biology*, 214:189–214. 16

Greendberg M. D. (1988). *Advanced Engineering Mathematics*. Prentice Hall, Upper Saddle River, NJ. 179

Guyon, E., Hulin, J. P. et Petit, L. (2012). *Hydrodynamique Physique*. CNRS editions - EDP Sciences. 185

Hanke, W., Brücker, C. et Bleckmann, H. (2000). The ageing of the low-frequency water disturbances caused by swimming goldfish and its possible relevance to prey detection. *Journal of Experimental Biology*, 203(Pt 7):1193–200. 24, 25

Hanke, W., Wieskotten, S., Niesterok, B., Miersch, L., Witte, M., Brede, M., Leder, A. et Dehnhardt, G. (2014). Hydrodynamic perception in pinnipeds. *In* Tropea, C. et Bleckmann, H., éditeurs : *Nature-Inspired Fluid Mechanics*, pages 255–270. 15

Hedenström, A. et Johansson, L. C. (2015). Bat flight : aerodynamics , kinematics and flight morphology. *Journal of Experimental Biology*, 218:653–663. 24

Henningsson, P., Michaelis, D., Nakata, T., Schanz, D., Bomphrey, R. J., Geisler, R. et Schro, A. (2015). The complex aerodynamic footprint of desert locusts revealed by large-volume tomographic particle image velocimetry. *Journal of royal society Interface*, 12:20150119. 24

Heys, J. J., Rajaraman, P. K., Gedeon, T. et Miller, J. P. (2012). A model of filiform hair distribution on the cricket cercus. *PloS One*, 7(10):e46588. 173

Holtsmark, J., Johnsen, I., Sikkeland, T. et Skavlem, S. (1954). Boundary layer flow near a cylindrical obstacle in Oscillating Incompressible Fluid. *The journal of the acoustical society of America*, 26(1952):26–39. 181, 185, 186

Humphrey, J. A. C., Devarakonda, R., Iglesias, I. et Barth, F. G. (1993). Dynamics of arthropod filiform hairs. I. Mathematical modelling of the hair and air motions. *Philosophical Transactions of the Royal Society of London. Series B : Biological Sciences*, 340:423–444. 18, 174, 178, 179, 181, 185, 186

Jacobs, G. a., Miller, J. P. et Aldworth, Z. (2008). Computational mechanisms of mechanosensory processing in the cricket. *Journal of Experimental Biology*, 211:1819–28. 163

Jacobs, G. a. et Theunissen, F. E. (1996). Functional organization of a neural map in the cricket cercal sensory system. *The Journal of neuroscience : the official journal of the Society for Neuroscience*, 16(2):769–784. 172, 173

Jiang, H. et Kiorboe, T. (2011). The fluid dynamics of swimming by jumping in copepods. *Journal of the Royal Society, Interface*, 8(61):1090–103. 19, 20

Jiang, H., Meneveau, C. et Osborn, T. R. (2002). The flow field around a freely swimming copepod in steady motion . Part II : Numerical simulation. *Journal of plankton research*, 24:191–213. 20

Joshi, K. et Miller, J. (2016). Biomechanical analysis of a filiform mechanosensory hair socket of crickets. *Journal of biomechanical Engineering*, 138(August):1–11. 174

Kämper, G. et Dambach, M. (1985). Low-frequency airborne vibrations generated by crickets during singing and agression. *Journal of insect physiology*, 31(12):925–929. 26

Kämper, G. et Kleindienst, H. U. (1990). Oscillation of cricket sensory hairs in a low-frequency sound field. *Journal of Comparative Physiology, A.*, 167(2):193–200. 18, 27

Kanou, M., Nawae, M. et Kuroishi, H. (2006). Cercal sensory system and giant interneurons in Gryllodes sigillatus. *Zoological Science*, 373:365–373. 16

Kant, R. et Humphrey, J. a. C. (2009). Response of cricket and spider motion-sensing hairs to airflow pulsations. *Journal of the Royal Society, Interface*, 6(40):1047–64. 181, 185, 188

Kjellerup, S. et Kiorboe, T. (2012). Prey detection in a cruising copepod. *Biology letters*, 8(3):438–41. 19, 20

Klopsch, C., Kuhlmann, H. C. et Barth, F. G. (2012). Airflow elicits a spider's jump towards airborne prey. I. Airflow around a flying blowfly. *Journal of the Royal Society, Interface*, page 10.1098/rsif.2012.0186. 29

Koehl, M. A. R. (2003). Physical modelling in biomechanics. *Philosophical Transactions of the Royal Society B*, 358:1589–1596. 19

Koehl, M. a. R. (2004). Biomechanics of microscopic appendages : functional shifts caused by changes in speed. *Journal of biomechanics*, 37(6):789–795. 26

Krijnen, G., Floris, A., Dijkstra, M., Lammerink, T. et Wiegerink, R. (2007). Biomimetic micromechanical adaptive flow-sensor arrays. *Proccedings of the Bioengineered and Bioinspired Systems III*, 6592:1–15. 195

Krijnen, G. J. M., Dijkstra, M., Baar, J. J. V., Shankar, S. S., Kuipers, W. J., Boer, R. J. H. D., Altpeter, D., Lammerink, T. S. J. et Wiegerink, R. (2006). MEMS based hair flow-sensors as model systems for acoustic perception studies. *Nanotechnology*, 17:S84–S89. 194

Kumagai, T., Shimozawa, T. et Baba, Y. (1998). Mobilities of the cercal wind-receptor hairs of the cricket, Gryllus bimaculatus. *Journal of Comparative Physiology, A.*, 183(1):7–21. 27

Landolfa, M. et Jacobs, G. (1995). Direction sensitivity of the filiform hair population of the cricket cercal system. *Journal of Comparative Physiology, A.*, 177:759–766. 163

Landolfa, M. A. et Miller, J. P. (1995). Stimulus-response properties of cricket cercal filiform receptors. *Journal of Comparative Physiology, A.*, 177:749–757. 16, 163

Levin, J. E. et Miller, J. P. (1996). Broadband neural coding in the cricket cercal sensory system enhanced by stochastic resonance. *Nature*, 380:165–168. 174

McConney, M. E., Anderson, K. D., Brott, L. L., Naik, R. R. et Tsukruk, V. V. (2009). Bioinspired material approaches to sensing. *Advanced Functional Materials*, 19(16):2527–2544. 175

McHenry, M. J., Strother, J. a. et van Netten, S. M. (2008). Mechanical filtering by the boundary layer and fluid-structure interaction in the superficial neuromast of the fish lateral line system. *Journal of Comparative Physiology, A.*, 194(9):795–810. 19, 26, 191

Meyhöfer, R., Casas, J. et Dorn, S. (1994). Host location by a parasitoid using leafminer vibrations : characterizing the vibrational signals produced by the leaf mining host. *Physiological Entomology*, 19:349–359. 27

Michaelis, D. (2014). Time resolved volumetric visualization of Zooplankton body and surrounding flow field using advanced masking in tomographic PIV. *In 16th International Symposium on Flow Visualization*, pages 1–15, Okinawa, Japan. 25

Michelsen, A., Kirchner, W. H. et Lindauer, M. (1986). Sound and vibrational signals in the dance language of the honeybee, Apis mellifera. *Behavioral Ecology and Sociobiology*, 18(3):207–212. 27

Michelsen, A. et Larsen, O. N. (1978). Biophysics of the ensiferan ear. *Journal of Comparative Physiology, A.*, 227:217–227. 27

Miller, J. P., Krueger, S., Heys, J. J. et Gedeon, T. (2011). Quantitative characterization of the filiform mechanosensory hair array on the cricket cercus. *PloS One*, 6(11):e27873. 16, 172, 173

Miller, K. B. et Bergsten, J. (2012). Phylogeny and classification of whirligig beetles (Coleoptera : Gyrinidae) : relaxed-clock model outperforms parsimony and time-free Bayesian analyses. *Systematic Entomology*, 37(4):706–746. 26

Morice, S., Pincebourde, S., Darboux, F., Kaiser, W. et Casas, J. (2013). Predator prey pursuit evasion games in structurally complex environments. *Integrative and Comparative Biology*, 53(5):767–779. 163

Morley, E. L., Steinmann, T., Casas, J. et Robert, D. (2012). Directional cues in Drosophila melanogaster audition : structure of acoustic flow and inter-antennal velocity differences. *Journal of Experimental Biology*, 215(Pt 14):2405–13. 191

Mulder-Rosi, J., Cummins, G. I. et Miller, J. P. (2010). The cricket cercal system implements delay-line processing. *Journal of neurophysiology*, 103(4):1823–32. 169, 194

Müller, U., Heuvel, B., Stamhuis, E. et Videler, J. (1997). Fish foot prints : morphology and energetics of the wake behind a continuously swimming mullet (Chelon labrosus Risso). *Journal of Experimental Biology*, 200(Pt 22):2893–906. 22

Murphy, D. W., Webster, D. R. et Yen, J. (2012). A high-speed tomographic PIV system for measuring zooplanktonic flow. *Limnology and oceanography : Methods*, 10:1096–1112. 26

Phillips, D. M., Ray, C. W., Hagen, B. J., Su, W., Baur, J. W. et Reich, G. W. (2015). Detection of flow separation and stagnation points using arti fi cial hair sensors. *Smart Materials and Structures*, 24:115026–10 pp. 194

Reidenbach, M. a., George, N. et Koehl, M. a. R. (2008). Antennule morphology and flicking kinematics facilitate odor sampling by the spiny lobster, Panulirus argus. *Journal of Experimental Biology*, 211(Pt 17):2849–58. 26

Roeder, K. D. (1966). Acoustic sensitivity of the noctuid tympanic organ and its range for the cries of bats. *Journal of insect physiology*, 12(7):843–859. 19

Roeder, K. D. (1970). Episodes in insect brains. How do animals select modes of behavior adapted to immediate circumstances ? A mechanism is sought by probing the brains of insects. *American Scientist*, 58(4):378–389. 19

Salençon, J. (2009). *Viscoélasticité pour le Calcul des structures*. 176

Scarano, F. (2013). Tomographic PIV : Principles and practice. *Measurement Science and Technology*, 24:012001–28pp. 192

Scarano, F. et Poelma, A. C. (2009). Three-dimensional vorticity patterns of cylinder wakes. *Experiments in Fluids*, 47:69–83. 192

Schaber, C. F. et Barth, F. G. (2015). Spider joint hair sensilla : adaptation to propriore-ceptive stimulation. *Journal of Comparative Physiology, A.*, 201:235–248. 175

Shimozawa, T. et Kanou, M. (1984a). The aerodynamics and sensory physiology of range fractionation in the cereal filiform sensilla of the cricket Gryllus bimaculatus. *Journal of Comparative Physiology, A.*, 155:495–505. 16, 18

Shimozawa, T. et Kanou, M. (1984b). Varieties of filiform hairs : range fractionation by sensory afferents and cercal interneurons of a cricket. *Journal of Comparative Physiology, A.*, 155:485–493. 18, 174, 178, 190

Shimozawa, T., Kumagai, T. et Baba, Y. (1998). Structural scaling and functional design of the cercal wind-receptor hairs of cricket. *Journal of Comparative Physiology, A.*, 183(2):171–186. 18, 174

Shimozawa, T., Murakami, J. et Kumagai, T. (2003). Cricket wind receptors : thermal noise for the highest sensitivity known. *In* Barth, F., Humphrey, J. et Secomb, T., éditeurs : *Sensors and Sensing in Biology and Engineering*, pages 145–157. Springer Vienna. 15, 18, 166, 173

Sirghi, L., Ponti, J., Broggi, F. et Rossi, F. (2008). Probing elasticity and adhesion of live cells by atomic force microscopy indentation. *European Biophysics Journal*, 37(6):935–945. 178

Spedding, G. et Rayner, J. (1984). Momentum and energy in the wake of a pigeon (Columba Livia) in slow flight. *Journal of Experimental Biology*, 111:81–102. 22, 23

Steinmann, T. et Casas, J. (2014). Laser-based optical methods for the sensory ecology of flow sensing : from classical PIV to micro-PIV and beyond. *In* Bleckmann, H., Mogdans, J. et Coombs, S. L., éditeurs : *Flow Sensing in Air and Water*, pages 31–62. Springer Berlin Heidelberg. 192

Steinmann, T., Casas, J., Krijnen, G. et Dangles, O. (2006). Air-flow sensitive hairs : boundary layers in oscillatory flows around arthropod appendages. *Journal of Experimental Biology*, 209(Pt 21):4398–408. 181, 185, 186, 188, 191

Sterbing-D'Angelo, S., Chadha, M., Chiu, C., Falk, B., Xian, W., Barcelo, J., Zook, J. M. et Moss, C. F. (2011). Bat wing sensors support flight control. *Proceedings of the National Academy of Sciences of the United States of America*, 108(27):11291–6. 191, 194

Sterbing-D'Angelo, S. J., Liu, H., Yu, M. et Moss, C. F. (2016). Morphology and deflection properties of bat wing sensory hairs : scanning electron microscopy , laser scanning vibrometry , and mechanics model. *Bioinspiration & biomimetics*, 11:056008. 194

Stewart, W. J., Mchenry, M. J., Stewart, W. J., Nair, A., Jiang, H. et Mchenry, M. J. (2014). Prey fish escape by sensing the bow wave of a predator. *Journal of Experimental Biology*, 217:4328–4336. 194

Strickler, J. R. (1977). Observation of swimming performances of planktonic copepods. *Limnology and oceanography*, 22:165–170. 24

Strickler, J. R. (1982). Calanoid copepodes, feeding currents, and the role of gravity. *Science*, 218:158–160. 24

Tauber, E. et Camhi, J. (1995). The wind-evoked escape behavior of the cricket Gryllus bimaculatus : integration of behavioral elements. *Journal of Experimental Biology*, 198(Pt 9):1895–907. 16

Tautz, J. (1979). Reception of particle oscillation in a medium - An unorthodox sensory capacity. *Naturwissenschaften*, 461:452–461. 18, 26

Tautz, J., Masters, W. M., Aicher, B. et Markl, H. (1981). A new type of water vibration receptor on the crayfish antenna - I. Sensory Physiology. *Journal of Comparative Physiology, A.*, 144:533–541. 25

Thomas, L., Tremblais, B. et David, L. (2014). Optimization of the volume reconstruction for classical Tomo-PIV algorithms (MART, BIMART and SMART) : synthetic and experimental studies. *Measurement Science and Technology*, 25(3):035303. 192

Visser, A. W. (2001). Hydromechanical signals in the plankton. *Marine Ecology Progress Series*, 222:1–24. 20

von der Emde, G. et Warrant, E. (2015). *The Ecology of Animal Senses*. Springer Berlin Heidelberg. 15, 19, 21

Wang, C.-Y. (1968). On high-frequency oscillatory viscous flows. *Journal of Fluid Mechanics*, 32:55–68. 186

Warrick, D. R., Tobalske, B. W. et Powers, D. R. (2009). Lift production in the hovering hummingbird. *Proceedings of the Royal Society B : Biological Sciences*, 276:3747–3752. 22, 23

Webster, D. R., Asce, M., Rahman, S. et Dasi, L. P. (2003). Laser-induced fluorescence measurements of a turbulent plume. *Journal of enginnering mechanics*, 129:1130–1137. 26

Webster, D. R. et Weissburg, M. J. (2009). The hydrodynamics of chemical cues among aquatic organisms. *Annual Review of Fluid Mechanics*, 41:73–90. 26

Wehner, R. (1987). 'Matched filters'-neural models of the external world. *Journal of Comparative Physiology, A.*, 161:511–531. 15, 19, 21

Weis-fogh, T. (1972). Energetics of hovering flight in hummingbirds and Drosophilia. *Journal of Experimental Biology*, 56:79–104. 22

Weissburg, M. J. (2000). The fluid dynamical context of chemosensory behavior. *Biological Bulletin*, 198:188–202. 25

Wiese, K. (1976). Mechanoreceptors for near-field water displacements in crayfish. *Journal of Neurophysiology*, 39(4):816–833. 15

Windmill, J. F. C., Fullard, J. H. et Robert, D. (2007). Mechanics of a simple ear : tympanal vibrations in noctuid moths. *Journal of Experimental Biology*, 210:2637–2648. 27

Windsor, S. P., Norris, S. E., Cameron, S. M., Mallinson, G. D. et Montgomery, J. C. (2010a). The flow fields involved in hydrodynamic imaging by blind Mexican cave fish (Astyanax fasciatus). Part I : open water and heading towards a wall. *Journal of Experimental Biology*, 213(Pt 22):3819–31. 24, 25

Windsor, S. P., Norris, S. E., Cameron, S. M., Mallinson, G. D. et Montgomery, J. C. (2010b). The flow fields involved in hydrodynamic imaging by blind Mexican cave fish (Astyanax fasciatus). Part II : gliding parallel to a wall. *Journal of Experimental Biology*, 213(Pt 22):3832–42. 24

Yu, Y. S. W., Graff, M. M., Bresee, C. S., Man, Y. B. et Hartmann, M. J. Z. (2016a). Whiskers aid anemotaxis in rats. *Science advances*, 2(8):e1600716. 15

Yu, Y. S. W., Graff, M. M. et Hartmann, M. J. Z. (2016b). Mechanical responses of rat vibrissae to airflow. *Journal of Experimental Biology*, 219(7):937–948. 15

INSTITUT DE RECHERCHE SUR LA BIOLOGIE DE L'INSECTE

Thomas STEINMANN

CENTRE NATIONAL DE LA RECHERCHE SCIENTIFIQUE

UNIVERSITÉ FRANÇOIS - RABELAIS TOURS
UNIVERSITÉ CONFÉDÉRALE LÉONARD DE VINCI

Métrologie optique en dynamique des fluides appliquée à l'écologie physique des insectes

Résumé

La capacité à percevoir des courants dans un fluide s'est développée chez de nombreuses espèces animales dans des contextes écologiques très variés. Les grillons détectent les écoulements d'air générés notamment lors de l'attaque de leurs prédateurs à l'aide de leurs cerques, situés à l'arrière de leur abdomen et recouverts de poils mécano-sensoriels. Ces senseurs sont considérés comme les détecteurs les plus sensibles du monde animal. Il leur suffit de capter l'énergie d'un dixième d'un photon pour déclencher un potentiel d'action au niveau du neurone sensoriel.

Ce manuscrit présente à la fois le développement des outils de mesures sans contact adaptés à ces questions d'écologie sensorielle ainsi que les méthodes numériques simulant les processus physiques à l'œuvre. L'étude du fonctionnement des senseurs a nécessité l'adaptation des méthodes de mesures non intrusives de très grande précision tel que la Vélocimétrie par Imagerie de Particules (PIV). La couche limite oscillante dans laquelle évoluent les poils a été visualisée et a servi à déterminer la réponse de poils modélisés par des systèmes oscillatoires du second ordre. Le couplage visqueux entre poils a été lui aussi caractérisé en adaptant la PIV à des mesures à très petites échelles sur des poils biomimétiques micro-electro-mécanique (MEMS). Les mesures des perturbations générées lors des attaques d'araignées, principales prédatrices des grillons, nous ont aidé à valider des modélisations numériques.

Ces résultats nous ont permis de revisiter la sensibilité extrême des poils filiformes et de placer ces mesures dans un contexte plus large, d'écologie sensorielle. En particulier, nous montrons que ces soies sont placées en groupe compact et exercent entre elles un fort couplage aérodynamique visqueux, qui réduit fortement leur sensibilité "de groupe". Ce fort couplage interroge l'intérêt d'avoir des récepteurs aussi performants individuellement, s'ils perdent leur sensibilité lorsqu'ils fonctionnent en réseau. Finalement, les réactions des poils à des mouvements de fluides générés par un piston mimant les attaques réelles d'araignées ont pu être déterminées à l'aide d'une caméra rapide, puis simulées et validées après avoir développé un modèle mécanique du poil répondant à des stimuli transitoires.

Mots clefs : écologie sensorielle, écologie physique, Vélocimétrie par imagerie de particules (PIV), poils filiformes, couches limites, biomimétisme, bioinspiration, écoulements visqueux, interaction proie-prédateur, biomécanique

Abstract

Flow sensing is used by a vast number of animals in various ecological contexts, from prey-predator interactions to mate selection, and orientation to flow itself. Crickets use hundreds of filiform hairs on two cerci as an early warning system to detect remote potential predators. Over the years, the cricket hairs have been described as the most sensitive sensor in the animal kingdom. The energy necessary for the emission of an action potential by its sensory neuron was estimated to be a tenth of the energy of a photon.

This PhD thesis aims to describe recent technological advances in the measurement and model of flows around biological and artificial flow sensors in the context of organismal sensory ecology. Non-contacting measurement methods such as and Particle Image Velocimetry (PIV) have been used to measure flows of biological relevance. The viscous oscillatory boundary layer surrounding filiform hairs has been visualized and used as input to model the mechanical response of these hairs, described as second order mechanical systems. The viscous hydrodynamic coupling occurring within hair canopy was also characterized using PIV measurements on biomimetic micro-electro-mechanical systems (MEMS) hairs, mimicking biological ones. We prove that the air flow upstream of hunting spiders is highly conspicuous aerodynamically and detectable up to several centimeters in front of the running predator. This disturbance of upstream air flows were also assessed by computational fluid dynamics (CFD).

This results allowed us to revisit the extreme sensitivity of cricket filiform hairs. We predicted strong hydrodynamic coupling within natural hair canopies and we addressed why hairs are packed together at such high densities, particularly given the exquisite sensitivity of a single hair. We also proposed a new model of hair deflection during the arrival of a predator, by taking into account both the initial and long-term aspects of the flow pattern produced by a lunging predator. We conclude that the length heterogeneity of the hair canopy mirrors the flow complexity of an entire attack, from launch to grasp.

Keywords : sensory ecology, physical ecology, Particle Image Velocimetry (PIV), filiform hairs, boundary layer flow, biomimetism, bioinspiration, viscous flow, prey-predator interaction, biomechanics